

# **AVIATION UTILIZATION OF GEOSTATIONARY SATELLITES FOR THE AUGMENTATION TO GPS: RANGING AND DATA LINK**

A DISSERTATION SUBMITTED TO THE DEPARTMENT OF AERONAUTICS AND  
ASTRONAUTICS AND THE COMMITTEE ON GRADUATE STUDIES OF  
STANFORD UNIVERSITY IN PARTIAL FULFILLMENT OF THE REQUIREMENTS  
FOR THE DEGREE OF DOCTOR OF PHILOSOPHY

Richard Andrew Fuller, II

May 2000

© Copyright 2000 Richard Andrew Fuller, II  
All Rights Reserved

I certify that I have read this thesis and that in my opinion it is fully adequate, in scope and in quality as a dissertation for the degree of Doctor of Philosophy.



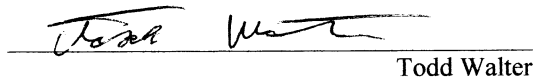
Per Enge  
(Principle Advisor)

I certify that I have read this thesis and that in my opinion it is fully adequate, in scope and in quality as a dissertation for the degree of Doctor of Philosophy.



J. David Powell

I certify that I have read this thesis and that in my opinion it is fully adequate, in scope and in quality as a dissertation for the degree of Doctor of Philosophy.



Todd Walter

Approved for the University Committee on Graduate Studies:

---





# Abstract

The Wide Area Augmentation System (WAAS) is a GPS-based navigation aid currently under development by the Federal Aviation Administration (FAA). WAAS will provide corrections to aviation users for the GPS clock, its ephemeris, and for the delay in its signal as it passes through the ionosphere. These corrections will be broadcast to users throughout the United States via geostationary satellites. A master station that combines data from a continental network of reference GPS receivers will create these messages. The geostationary satellites serve both as wide-area differential GPS data links as well as additional ranging sources. The data message stream of WAAS enhances the accuracy and integrity of the GPS signal for aviation. Simultaneously, the satellite ranging-source increases the percentage of time that the precise signal is available. In this way, WAAS provides needed improvements in four metrics over the standard GPS signal: accuracy, integrity, availability, and continuity.

The ranging function described above requires an estimate of the position of the geostationary satellite. This dissertation presents a novel technique for generating this position estimate. This technique is designed to provide high integrity performance in the user position domain and operates in real-time. As such, it contrasts classical orbit determination techniques that have no integrity requirement, are not designed to optimize performance in the user position domain, and usually have no real-time requirement. This estimator is evaluated using real data from the FAA's National Satellite Test Bed (NSTB).

The WAAS Signal-In-Space (SIS) has a limited data message bandwidth of 250 bits-per-second. This data bandwidth was chosen to balance two concerns. First, the power of the signal must not be so strong as to jam GPS. Second, the signal must provide the minimum amount of information necessary to ensure adequate accuracy and integrity for aviation users over the entire geostationary satellite footprint. The required message loss is specified not to exceed a rate of 0.001 (one loss per one-thousand messages) to ensure adequate system continuity and availability. The WAAS message structure is not particularly sensitive to independent message losses below the specified rate. Groups of missed messages (burst-mode) can prove to be a challenge in maintaining a continuous WAAS solution. The effects of burst-mode losses on the quality of the WAAS solution is presented and a Markov model for the burst message loss is developed. This research shows that WAAS availability can be achieved even with a message loss rate up to of 0.005 (i.e., five times the specification) even in the presence of burst-mode outages. This proves that the specification will ensure availability despite having been derived for independent message loss as opposed to burst losses.

Flight tests were conducted in California and Alaska to establish actual message loss profiles for aircraft. These flight test results were modeled and used in conjunction with NTSB reference station data to establish availability of WAAS solutions for various locations in the US. This research demonstrates that the GEO satellite fulfills its goals of providing accuracy, integrity, availability and continuity.

# Acknowledgments

First and foremost I would like to thank my research advisor Professor Per Enge. His contributions to this thesis are extensive and pervasive and this work could not have been completed without him. Professor Enge has an infectious enthusiasm that allows his advise to generate exceptional motivation in his students, including myself. It has been an honor and privilege to work with him over the past four years. The other members of my reading committee, Professor David Powell and Dr. Todd Walter, have also played a major role in this work and my academic development. Professor Powell helped steer my early academic career at Stanford and offered concise criticism of my work during its development to improve the clarity of my research and this thesis. Dr. Todd Walter has had a substantial impact on this work. My daily interaction with Dr. Walter has allowed this research to develop in ways that I had not originally envisioned. This interaction enabled this thesis and underlying research to achieve a higher quality and depth. I will continue to use Dr. Walter as a model for conduct in a technical leadership role.

The Federal Aviation Administration Satellite Program Office is the sponsor for this work. Their funding has provided an environment at Stanford University that has enabled true innovation that will contribute to the future of aviation and aviation aids. Without a doubt, this work would not be possible without their support.

This acknowledgement list would not be complete without recognition of my peers. These include my colleagues from the Wide-Area Differential GPS, the Local-Area

Augmentation System, and the Gravity Probe B Laboratories. Most notably Andrew Hansen, Andy Barrows, Roger Hayward, Demoz Gebre-Egziabher, Sherman Lo, Dong Hai Dai, Keith Alter, Chad Jennings, Yeou-Jyh Tsai, Sharon Houck, Gabriel Elkaim, and Jock Christie have helped me in many ways in the execution of this research and have added to both my academic and personal development. A special thanks goes out to Douglas Archdeacon who has kept the lab computer and network systems in a perpetually optimal configuration even with changing requirements. Additionally I would like to thank Sally Gressens, Student Services Manager for the department, whose ability to wade through and summarize the myriad of university regulations and requirements has been an invaluable aid throughout my career at Stanford.

Demoz Gebre-Egziabher and Sherman Lo are acknowledged for help in editing the contents of Chapter 1. Special thanks is given to Fiona Walter for both myself and for future readers of this work. Her detailed and insightful comments have made the final version of this thesis more clear and hopefully more of a pleasure to read.

I would like to thank my colleagues and supervisors from when I was employed at Space Systems/Loral namely: Carl Plescia, John Lehner, Kurt Brock, Earl Weiler, Len Furst, Al Tadros, Melvin Tse and most especially Dr. Wah Lim and Dr. Jack Rodden. Their encouragement while I was at SS/L helped lead me back to finish my degree.

On a personal level I would like to thank my parents, Richard and Marguerite Fuller, who supported my every effort growing up and taught me that almost nothing is impossible given adequate dedication and time. My wife's parents, Robert and Elvina Hoo, have been completely supportive and understanding throughout my research program. I also greatly appreciate Betty Wright who not only was my landlord for my first years at Stanford but also filled the role of surrogate grandmother.

The long hours of effort have been bearable only because I have someone to share my time-off. That someone is Tiffany, my wife. Her lasting support and dedication has made all of the work worthwhile. No one has touched my life more deeply than her. She continues to give me "All I Ask..."

# Table of Contents

<b>AVIATION UTILIZATION OF GEOSTATIONARY SATELLITES FOR THE AUGMENTATION TO GPS: RANGING AND DATA LINK.....</b>	<b>i</b>
<b>Abstract.....</b>	<b>v</b>
<b>Acknowledgments.....</b>	<b>vii</b>
<b>Table of Contents.....</b>	<b>ix</b>
<b>List of Figures.....</b>	<b>xv</b>
<b>Glossary of Terms.....</b>	<b>xxi</b>
<b>CHAPTER 1 .....</b>	<b>1</b>
INTRODUCTION .....	1
1.1 NAVIGATION HISTORY AND PERSPECTIVE: MARINE NAVIGATION.....	2
1.2 AVIATION NAVIGATION DEVELOPMENT AND HISTORY .....	9
1.2.1 EARLY RADIO NAVIGATION DIRECTION FINDERS .....	9
1.2.2 VOR AND DME.....	10
1.2.3 INSTRUMENT LANDING SYSTEM (ILS).....	12
1.2.4 LORAN/OMEGA.....	13
1.3 SATELLITE NAVIGATION HISTORY.....	14
1.3.1 THE TRANSIT SATELLITE PROGRAM .....	15
1.3.2 THE TIMATION AND 621B SATELLITE PROGRAMS .....	15
1.3.3 GLONASS .....	16
1.4 THE GLOBAL POSITIONING SYSTEM (GPS) .....	17

1.4.1 THE SPACE SEGMENT .....	17
1.4.2 THE CONTROL SEGMENT .....	21
1.4.3 THE USER SEGMENT .....	22
1.4.4 THE GPS OBSERVABLES .....	23
1.5 GPS ERROR SOURCES .....	23
1.6 LOCAL-AREA AND WIDE-AREA DIFFERENTIAL GPS .....	26
1.7 SPACE-BASED AUGMENTATION SYSTEMS (SBAS): THE WIDE AREA AUGMENTATION SYSTEM (WAAS) .....	27
1.8 THE NATIONAL SATELLITE TEST BED .....	29
1.9 LANDING ISSUES.....	30
1.10 CONTRIBUTIONS IN THIS THESIS .....	35
1.10.1 GEOSTATIONARY ORBIT DETERMINATION AND SATELLITE RANGING .....	36
ANALYSIS OF THE COVARIANCE DISTRIBUTION FOR A WIDE-AREA REFERENCE NETWORK .....	36
AUGMENTATION OF THE APPROACH USED FOR GPS EPHEMERIS ESTIMATION FOR THE MORE DIFFICULT GEOSTATIONARY PROBLEM .....	36
ADAPTIVE HIGH INTEGRITY REAL-TIME ORBIT ESTIMATOR .....	36
1.10.2 DATA LINK.....	37
EXPERIMENTAL VERIFICATION OF THEORETICAL MESSAGE LOSS RATES.....	37
DEMONSTRATION OF A NEW METHOD FOR THE CHARACTERIZATION OF BURST-MODE INFLUENCE ON MESSAGE LOSS.....	37
APPLICATION OF A BURST MESSAGE LOSS MODEL FROM ACTUAL AIRCRAFT DATA COLLECTION TO NSTB REFERENCE SITES .....	37
1.11 THESIS OUTLINE.....	37
<b>CHAPTER 2.....</b>	<b>39</b>
ORBIT DETERMINATION BACKGROUND.....	39
2.1 ORBITAL MECHANICS .....	39
2.2 THE TRAJECTORY EQUATION.....	42
2.3 DETERMINING THE ORBITAL ELEMENTS.....	48
2.4 ORBIT PROPAGATION TECHNIQUES .....	50
2.4.1 KEPLERIAN PROPAGATION .....	50
2.4.2 INTEGRATED PROPAGATION .....	52
2.4.3 KINEMATIC PROPAGATION .....	54
2.4.4 VINTI PROPAGATION.....	57
2.4.5 ERROR GROWTH FOR DIFFERENT METHODS .....	58
2.5 ORBIT TYPES .....	59
2.5.1 GPS ORBIT .....	60
2.5.2 GEOSTATIONARY ORBIT .....	61

2.6 MEASUREMENT PROCESSING FOR ORBIT DETERMINATION .....	63
2.6.1 SATELLITE RANGING .....	64
2.6.2 “SNAPSHOT” SOLUTION.....	66
<b>CHAPTER 3.....</b>	<b>69</b>
INFLUENCE OF ORBIT DETERMINATION TECHNIQUES ON WAAS USER PERFORMANCE .....	69
3.1 THREE PROPAGATION METHODS: NUMERICALLY INTEGRATED, ANALYTICALLY INTEGRATED AND KINEMATIC .....	70
3.2 WIDE-AREA MASTER STATION ARCHITECTURE .....	71
3.3 THE IGS AND PRECISE ORBITS .....	73
3.4 INFLUENCE OF PROPAGATION TECHNIQUE ON POSITIONING ACCURACY .....	76
3.5 USER RANGE ERRORS DUE TO EPHEMERIS ESTIMATE ERRORS .....	78
3.5.1 SATELLITE EPHEMERIS COVARIANCE MAPPING INTO USER RANGE DOMAIN .....	78
3.5.2 USER RANGE ERRORS USING NSTB DATA .....	82
3.6 GEOSTATIONARY ORBIT ESTIMATION: INITIALIZATION PROBLEM .....	87
<b>CHAPTER 4.....</b>	<b>89</b>
GEOSTATIONARY SATELLITE ORBIT DETERMINATION.....	89
4.1 THE GEOSTATIONARY ORBIT PROBLEM .....	89
4.1.1 CLOCK AND CLOCK RATE CONTROL.....	93
4.1.2 “SNAPSHOT” SOLUTION.....	95
4.1.3 <i>A-PRIORI</i> COVARIANCE ESTIMATION AND PROPAGATION .....	101
4.1.4 BATCH FILTER DESIGN .....	105
4.1.5 PSEUDORANGE RESIDUALS.....	109
4.1.6 GEOSTATIONARY UDRE .....	111
4.2 AVAILABILITY AND INTEGRITY .....	113
4.2.1 BASELINE AVAILABILITY CONFIGURATION .....	114
4.2.2 AVAILABILITY RESULTS WITH GEOSTATIONARY RANGING .....	116
<b>CHAPTER 5.....</b>	<b>119</b>
MESSAGING BACKGROUND.....	119
5.1 GPS ERRORS: TEMPORAL AND SPATIAL VARIATIONS .....	121
5.1.1 CLOCK AND EPHEMERIS (SA) ERRORS.....	122
5.1.2 IONOSPHERE ERRORS.....	126
5.1.3 USER UNIQUE ERRORS .....	128
5.2 WAAS MESSAGE CONTENT .....	128
5.2.1 MESSAGE TYPES.....	130
5.2.2 MESSAGE SEQUENCE AND TIMING .....	132

5.3 THEORETICAL AND SIMULATED MESSAGE LOSSES .....	136
5.3.1 THEORETICAL MESSAGE LOSS VERSUS SNR: CASCADE PLOT .....	136
5.3.2 SIMULATED MESSAGE LOSS VERSUS SNR: CASCADE PLOT .....	140
<b>CHAPTER 6.....</b>	<b>143</b>
WAAS MESSAGING PERFORMANCE IN THE PRESENCE OF BURST ERRORS .....	143
6.1 OBSERVED MESSAGE LOSSES .....	144
6.1.1 TEST SETUP AND EPOCH PROCESSING LOGIC .....	146
6.1.2 OBSERVED MESSAGE LOSSES VERSUS SNR.....	148
6.1.3 SNR FOR VARIOUS LOCATIONS ACROSS THE NSTB .....	150
6.2 FLIGHT MESSAGE LOSSES .....	152
6.2.1 IN-FLIGHT MESSAGE LOSS OBSERVATIONS.....	155
6.2.2 MODEL OF FLIGHT MESSAGE LOSSES (BURST-MODE ERRORS).....	157
6.2.3 BURST LOSS EFFECT ON INTEGRITY .....	161
6.3 MESSAGE LOSS IMPACT ON AVAILABILITY .....	163
6.3.1 INFLUENCE OF RANDOM MESSAGE LOSS .....	163
6.3.2 BURST LOSS EFFECT ON AVAILABILITY .....	166
<b>CHAPTER 7.....</b>	<b>169</b>
CONCLUSIONS AND SUGGESTIONS FOR FUTURE WORK .....	169
7.1 CONCLUSIONS .....	170
7.1.1 ORBIT DETERMINATION.....	170
7.1.2 MESSAGE LOSS .....	173
7.2 SUGGESTIONS FOR FUTURE WORK.....	177
7.2.1 PAYLOADS .....	177
7.2.2 SATELLITES WITH A SECOND TRANSPONDER .....	177
7.2.3 USE OF A NAVIGATION PAYLOAD RATHER THAN A BENT-PIPE TRANSPONDER .....	179
7.2.4 MULTIPLE FREQUENCY TRANSPONDERS.....	181
7.2.5 SATELLITE ORBITS.....	183
7.2.6 MESSAGE LOSS .....	185
7.2.7 SERVICE VOLUME MODEL.....	185
7.2.8 ANTENNA DESIGN.....	185
7.2.9 COPROBABILITY DISTRIBUTION .....	186
7.2.10 SBAS INTEROPERABILITY .....	187
7.2.11 AVIONICS .....	188
7.2.12 DATA SHARING.....	189
7.2.13 SHARED SATELLITES .....	189
<b>APPENDIX A.....</b>	<b>191</b>



MESSAGE LOSS PROBABILITY .....	191
A.1 RANDOM PROCESSES.....	191
A.2 CHARACTERIZATION OF A RANDOM PROCESS .....	192
A.3 CLASSIFICATION OF RANDOM PROCESSES.....	194
A.4 DISCRETE-PARAMETER MARKOV CHAINS.....	199
<b>BIBLIOGRAPHY.....</b>	<b>201</b>



# List of Figures

Figure 1.1: An Illuminated Mariner's Compass [Bowditch].....	4
Figure 1.2: A Sextant [Bowditch].....	7
Figure 1.3: VOR Receiver Diagram.....	11
Figure 1.4: DME System Architecture.....	11
Figure 1.5: The Instrument Landing System (ILS) [FarAim] .....	13
Figure 1.6: GPS Segments; Space, Control and User.....	18
Figure 1.7: GPS Ground tracks.....	19
Figure 1.8: C/A Code Spread Spectrum [Cohen] .....	21
Figure 1.9: Standard Positioning Solution variations .....	23
Figure 1.10: Components of the Unauthorized (SPS) User Ranging Error (SA Enabled)...25	
Figure 1.11: Example Differential GPS Architecture.....	26
Figure 1.12: Wide-Area Differential GPS Architecture .....	27
Figure 1.13: Comparison of Range Error Between Uncorrected GPS Range Error and WAAS Corrected Range Error.....	28
Figure 1.14: National Satellite Test Bed Receiver Sites.....	29
Figure 1.15: Historical Overview of Stanford University Involvement in WADGPS Development.....	30
Figure 1.16: Landing: Alert Limit, Protection Level, Decision Height and Accuracy.....	32
Figure 1.17: Chart to Evaluate Accuracy, Availability and Integrity.....	34
Figure 2.1: Relative Motion of Two Bodies .....	42
Figure 2.2: General Equation of Any Conic Section in Polar Coordinates.....	45

Figure 2.3: Keplerian Orbit Elements Referenced Against the Vernal Equinox [Bate] .....	46
Figure 2.4: Forces Acting on a GPS satellite.....	53
Figure 2.5: IGS GPS Reference Station Locations.....	54
Figure 2.6: Typical Satellite Position Errors of Precise Orbit Position Versus the Broadcast Ephemeris from the MCS .....	56
Figure 2.7: Satellite Position Error Estimation Process (Tsai).....	56
Figure 2.8: Representation of the Different Solution Methods.....	58
Figure 2.9: Divergence of Different Propagation Methods Versus the IGS Reference .....	59
Figure 2.10: Orbit Types .....	60
Figure 2.11: Influence of Slight Eccentricity and Inclination Errors On A Geostationary Satellite Position.....	62
Figure 2.12: Satellite Tracking Configuration and Coordinate System.....	65
Figure 2.13: Instantaneous “Snapshot” of Position Formed from Multiple Simultaneous Measurements.....	66
Figure 3.1: Orbit Propagation Methods .....	70
Figure 3.2: Testbed Master Station (TMS) Architecture .....	72
Figure 3.3: Example Perturbation Forces Acting on a Satellite.....	74
Figure 3.4: Processing of IGS in Preparation for Application to User Data.....	75
Figure 3.5: Final Stage of IGS Data Interpolation.....	75
Figure 3.6: Vertical Accuracy of Position Solutions for Various Orbit Determination Methods .....	76
Figure 3.7: Covariance of the Satellite Ephemeris Estimate Determined from Reference Stations and Represented in the User Range Domain.....	79
Figure 3.8: Flow-Diagram of the Computation of the User Range Domain Variance Due to Covariance of the Satellite Ephemeris Estimate .....	79
Figure 3.9: Pseudorange $1\sigma$ Error as a Function of SNR and Elevation .....	83
Figure 3.10: Satellite Covariance Map for a SV In View of the NSTB with Poor Tracking Geometry Between the Satellite and Reference Stations.....	84
Figure 3.11: Satellite Covariance Map for a SV In View of the NSTB with Good Tracking Geometry Between the Satellite and Reference Stations.....	85

Figure 3.12: Mapping of Pseudorange Confidence from Satellite Geometry to Users at 40 Degree Latitude Across Multiple Longitudes.....	87
Figure 3.13: Comparison Between the GPS Orbit Determination Process and the Geostationary Orbit Determination Process .....	88
Figure 4.1: Geostationary Satellite Orbital Variation Over Time .....	90
Figure 4.2: Fixed <i>a-priori</i> Approach to Orbit Filtering as Applied to GPS Satellites.....	91
Figure 4.3: Adaptive Orbit Filtering for Geostationary Satellites .....	92
Figure 4.4: Geostationary Satellite Clock Control for WAAS .....	94
Figure 4.5: GEO Orbit Position Variation From Mean Location.....	99
Figure 4.6: Snapshot Orbit Solution Residual. <i>A-priori</i> Covariance Used: $(10\text{ km})^2$ X, $(10\text{ km})^2$ Y, $(10\text{ km})^2$ Z and $(1\text{ km})^2$ for the Clock. ....	100
Figure 4.7: Covariance Real-Time Propagation Logic .....	104
Figure 4.8: Energy in the Perturbations As A Function of Orbital Harmonics.....	105
Figure 4.9: Flow-Diagram of the Batch-Fit Solution and Solution Propagation .....	107
Figure 4.10: Orbit Component Residuals After the Filter .....	109
Figure 4.11: Single Station Real-Time Pseudorange Residual After Orbit Solution.....	110
Figure 4.12: Pseudorange Residuals for All Tracking Stations.....	111
Figure 4.13: Example GEO $\sigma_{\text{UDRE}}$ . The Dark Line Represents the Value Returned by the $\sigma_{\text{UDRE}}$ Estimate Algorithm. The Light Line was an Adjustment based on the Observation of Lower Range Residuals. ....	113
Figure 4.14: WAAS Availability Before Inclusion of GEO-Ranging .....	115
Figure 4.15: WAAS Availability After Inclusion of GEO-Ranging.....	117
Figure 5.1: SBAS Architecture as a Data Source .....	120
Figure 5.2: GPS Errors Compared to WAAS .....	122
Figure 5.3: Time History of the Pseudorange Corruption Due to SA [Matchett, Enge97] .....	124
Figure 5.4: Error Growth Due to SA Over Time .....	125
Figure 5.5: Ionosphere Structure, Slant and Vertical Delays.....	127
Figure 5.6: WAAS Message Structure [RTCA159] .....	129
Figure 5.7: Error Growth with Fast Correction.....	130
Figure 5.8: WAAS Ionospheric Grid Definition [RTCA159, Walter00].....	131
Figure 5.9: FEC Convolutional Coding for WAAS.....	137

Figure 5.10: Probability of Message Failure without FEC and with FEC for $R_{tot}=250$ and $M=250$ .....	138
Figure 5.11: Theoretical Message Loss Rate for FEC Signal Versus SNR.....	139
Figure 5.12: Simulated Receiver Message Loss Rate versus SNR for 15 Hz NEB.....	141
Figure 6.1: Geostationary Satellites Utilized for Satellite Based Augmentation Systems (WAAS and EGNOS). Contours of the User Elevations for 5, 10, 15, and 20 Degrees.....	144
Figure 6.2: Rooftop Antenna Array Configuration .....	145
Figure 6.3: Epoch Processing Logic for GEO Messages .....	147
Figure 6.4: Static Station Message Loss Versus SNR.....	149
Figure 6.5: NSTB Locations Used with GEO Tracking .....	150
Figure 6.6: SNR Versus Elevation For Various Locations in the NSTB .....	151
Figure 6.7: Flight Test Aircraft Used by Stanford University .....	153
Figure 6.8: Flight Test System Diagram.....	153
Figure 6.9: Flight Test Data Link. Test Bed Master Station Located at Stanford University	154
Figure 6.10: Message Loss Histogram. The Locally-Level Flight ( $< 5$ degrees of bank) are All Contained in First Bar (Time Between Messages=1 sec).....	156
Figure 6.11: Burst Model Diagram.....	158
Figure 6.12: Flight Message Loss Compared to Burst Model Realization (3% of Data Including 60 Degree Bank Angles) .....	161
Figure 6.13: Comparison of Burst Model and Independent Loss Assumptions on the Probability that Three Successive Messages are Lost .....	162
Figure 6.14: WAAS Correction Unavailability for Independently Distributed Message Loss at Four NSTB Locations (Bernoulli Random Variable).....	165
Figure 6.15: WAAS Correction Unavailability Versus Burst Model Equivalent Total Message Loss Rate at Four NSTB Locations .....	167
Figure 7.1: Satellite Ephemeris Covariance Projections Upon Aircraft Users' Positions for Both Poor (Upper Plot) and Good (Lower Plot) Geometry Between the Satellite and Reference Stations.....	171
Figure 7.2: Improvement in WAAS Availability and Accuracy With GEO Ranging. Left: Without GEO Ranging; Right: With GEO Ranging.....	172

Figure 7.3: Orbit Error Covariance Propagation .....	173
Figure 7.4: Message Loss Rate Versus SNR from Actual Measurements.....	174
Figure 7.5: Message Loss From Flight Tests .....	175
Figure 7.6: Flight Message Loss Extended to NSTB Sites.....	176
Figure 7.7: Payload Sharing Between SBASs .....	178
Figure 7.8: Comparison between a Clock on the Ground versus on the satellite .....	180
Figure 7.9: Various Orbit Types .....	183
Figure 7.10: Ground Trace for a Molniya Orbit .....	184
Figure 7.11: Influence of Aircraft Maneuver (bank) on the Satellite Tracking Capability	186
Figure 7.12: Interoperability Options .....	187





## Glossary of Terms

<b>GPS</b>	
<b>AS</b>	Anti-Spoofing. The encryption of GPS “Y” Code which forms the “P” Code.
<b>Block I</b>	First generation of GPS satellites. These were launched from 1978 until 1985.
<b>Block II/IIA</b>	Follow-on to the first GPS satellite. These were launched from 1989 until 1996.
<b>Block IIR</b>	Replenishment satellites for the Block II/IIA. These were first launched in 1996 and will continue being launched until about 2005.
<b>Block IIF</b>	These are the follow-on satellites for the Block II/IIA constellation. These are due to begin launching in 2005.
<b>C/A Code</b>	Clear Acquisition Code. Code modulation of the GPS signal available to all users.
<b>CDMA</b>	Code Division Multiple Access
<b>DOP</b>	Dilution of Precision. A measure of the geometrical accuracy of a set of satellites. Examples of DOP are GDOP (geometric, position and time), PDOP (position-only), HDOP (horizontal), VDOP (vertical), and TDOP (time).
<b>GPS</b>	Global Positioning System

<b>HOW</b>	Hand-Over Word
<b>MCS</b>	Master Control Station. Central control facility for GPS operated by the JPO. Monitors and adjusts the performance of GPS worldwide.
<b>MHz</b>	Megahertz
<b>L1</b>	The frequency band for the primary GPS satellite signal referring to 1575.42 MHz.
<b>L2</b>	The frequency band for the secondary GPS satellite signal referring to 1227.6 MHz.
<b>P Code</b>	Precise Code modulation of the GPS signal available only to authorized (DoD and allied) users. This is an encrypted version of the Y Code that is implemented by AS.
<b>PRN</b>	Pseudorandom Noise
<b>PPS</b>	GPS Precise Position Service. The position solution available for authorized (DoD and allied) users.
<b>pseudorange</b>	The receiver measurement of the geometric range to the satellite with corruption from satellite and receiver clock errors, the atmosphere and receivers error.
<b>SA</b>	Selective Availability. The intentional degradation of the GPS signal by the DoD.
<b>SPS</b>	GPS Standard Position Service. The position solution available for all users.
<b>SV</b>	Space Vehicle. The GPS satellite.
<b>Y Code</b>	Precise Code modulation of the GPS signal available to all users. However, this code is usually encrypted by AS and the decryption is only available to authorized (DoD and allied) users.

<b>Organizations Related to GPS and Aviation</b>	
<b>DoD</b>	Department of Defense
<b>FAA</b>	Federal Aviation Administration
<b>ICAO</b>	International Civil Aviation Organization

<b>IGEB</b>	Interagency GPS Executive Board. Manages GPS and U.S. Government augmentations to GPS, consistent with national policy, to support and enhance U.S. economic competitiveness and productivity while protecting national security and foreign policy interests.
<b>IGS</b>	International GPS Service
<b>Inmarsat</b>	Inmarsat currently operates a global satellite system that is used by independent service providers to offer voice and multimedia. Provider of the geostationary satellites with navigation transponders.
<b>JPO</b>	Joint Program Office. In charge of the Global Positioning System administration for the DoD.
<b>MCS</b>	Master Control Station. Primary control of the GPS satellites, orbit and clock determination.
<b>RTCA</b>	Radio Technical Commission for Aviation Services
<b>RTCM</b>	Radio Technical Commission for Maritime Services
<b>USNO</b>	United States Naval Observatory

<b>Wide-Area DGPS</b>	
<b>Alert Limit</b>	The threshold above which a particular flight operation can no longer be conducted under instrument conditions
<b>C-Band</b>	The frequency band for the WAAS GEO uplink and downlink signal at 3630.42 MHz.
<b>CONUS</b>	Conterminous United States
<b>GBAS</b>	Ground Based Augmentation System
<b>GEO</b>	Geostationary satellite or Geostationary Earth Orbit
<b>GIVE</b>	Grid Ionospheric Vertical Error
<b>GUS</b>	Geostationary Uplink Station
<b>HAL</b>	Horizontal Alert Limit
<b>HPL</b>	Horizontal Protection Level
<b>MOPS</b>	Minimum Operational Performance Standard. Refers to RTCA159 specification for the Wide-Area Augmentation System (WAAS).

<b>NSTB</b>	National Satellite Test Bed. A prototype WAAS demonstration.
<b>Protection Level</b>	Broadcast indication of the bound on the accuracy of the state. This value is compared to the Alert Limit to determine if a flight operation can continue.
<b>SBAS</b>	Space Based Augmentation System
<b>SIS</b>	Signal in Space
<b>SVM</b>	Service Volume Model
<b>TMS</b>	Testbed Master Station (NSTB)
<b>TRS</b>	Testbed Reference Station (NSTB)
<b>UDRE</b>	User Differential Range Error
<b>VAL</b>	Vertical Alert Limit
<b>VPL</b>	Vertical Protection Level
<b>WAAS</b>	Wide-Area Augmentation System
<b>WADGPS</b>	Wide-Area Differential GPS
<b>WMS</b>	WAAS Master Station
<b>WNT</b>	WAAS Network Time
<b>WRS</b>	WAAS Reference Station

<b>Flight Phases</b>	
<b>Approach</b>	The approach phase begins at the acquisition of the landing aid and continues until the airport is in site or the aircraft is on the runway depending on the capabilities of the landing aid
<b>En Route</b>	The en route phase of flight leads from the origin to the destination and alternate destinations (an alternate destination is required for civil aircraft operating under instrument flight rules)
<b>Landing</b>	The landing phase begins at the decision height (when the runway is in sight) and ends when the aircraft exits the runway. Navigation during flare and decrab may be visual or the navigation set's electrical output may be coupled to an autopilot. A radio altimeter measures the height of the main landing gear above the runway for guiding the flare

<b>Missed Approach</b>	A missed approach is initiated at the pilot's option or at the traffic controller's request, typically because of poor visibility, poor alignment with the runway, equipment failure, or conflicting traffic
------------------------	--

<b>Aviation Navigation Aids and Terminology</b>	
<b>DME</b>	Distance Measuring Equipment
<b>ILS</b>	Instrument Landing System
<b>IM</b>	Inner marker
<b>Loran</b>	Long-Range Navigation system
<b>LNAV</b>	Lateral Navigation. This term is usually associated with en-route operations where high accuracy/integrity vertical navigation is not required.
<b>MM</b>	Middle marker
<b>Omega</b>	A world wide navigation system with relatively low accuracy.
<b>OM</b>	Outer marker
<b>VOR</b>	VHF Omnidirectional Range
<b>VNAV</b>	Vertical Navigation. This term is usually associated with approach operations where high accuracy/integrity vertical navigation is required.

<b>General</b>	
<b>dB</b>	Decibels
<b>dB-W</b>	Decibels in Watts
<b>GIPSY</b>	GPS-Inferred Positioning System, developed by the Jet Propulsion Laboratory
<b>km</b>	Kilometers
<b>LOS</b>	Line-Of-Sight. Vector from user or reference to a satellite; usually normalized.
<b>m</b>	Meters
<b>nmi</b>	Nautical miles (1.15 statute miles)
<b>RMS</b>	Root Mean Squared
<b>SNR</b>	Signal-to-Noise Ratio. Signal power divided by noise power in dB or dB-Hz.

<b>Celestial Mechanics</b>	
<b>Apoapsis/ Apogee</b>	The point in an orbit that a satellite is farthest from the central body. When orbiting the Earth this point is referred to as apogee.
<b>Eccentricity</b>	A parameter that specifies the shape of a conic section.
<b>Ephemeris</b>	A set of parameters that allow the position and velocity of the satellite to be determined. This may also include clock correction terms.
<b>GEO</b>	Geostationary Earth Orbit. Semi-major axis of 42,200 km. Altitude of 35,800 km.
<b>General Perturbations</b>	The solution of motion of satellite by analytical integration or series expansion of the perturbing forces or functions.
<b>LEO</b>	Low Earth Orbit. Altitudes ranging from 100 to 2000 km
<b>MEO</b>	Middle Earth Orbit. Range of altitudes between LEO and GEO
<b>Sidereal/ Sidereal time</b>	The measure of time defined by the apparent diurnal motion of the mean equinox; hence the measure of the rotation of the Earth with respect to the stars rather than the Sun.
<b>Semi-major axis</b>	Half the length of the major axis of the major axis of an ellipse; a standard element used to describe an elliptical orbit.
<b>Periapsis/ Perigee</b>	The point in an orbit that a satellite most closely approaches the central body. When orbiting the Earth this point is referred to as perigee.
<b>Inclination</b>	The angle between an orbital plane and the ecliptic plane at vernal equinox.
<b>Special Perturbations</b>	The use of direct numerical integration of the equations of motion to solve for the orbit of a satellite.
<b>Vernal Equinox</b>	The time when the apparent longitude of the Sun is $0^\circ$ .

# Chapter 1

*Oh, you may be sure that Columbus was happy not when he had discovered America, but when he was discovering it. Take my word for it, the highest moment of his happiness was just three days before the discovery of the New World, when the mutinous crew were on the point of returning to Europe in despair. It wasn't the New World that mattered, even if it had fallen to pieces.*

- Fyodor Dostoevsky

## Introduction

Navigation is key to national and international industry, commerce, and safety. Knowledge of position, both relative and absolute has been used throughout history to gain tactical advantage in both peaceful and not so peaceful pursuits. From the rudimentary techniques developed over two millennia ago, people all over the world have made both evolutionary and revolutionary progress in the business of knowing their position. Navigation progressed from simple piloting, the art of connecting known points, to satellite based navigation systems.

Today the premier worldwide navigation solution is the Global Positioning System (GPS). This satellite based navigation system was developed by the Department of Defense (DoD) to support a variety of military operations. As a military system, not all of the accuracy built into the system is available to civilian users. This lack of accuracy and absence of civilian signal control do not lend themselves easily to civilian aviation utilization. Even

with these restrictions, GPS has begun to make it into many cockpits as a navigation reference.

In recent years there has been widespread growth in the independent development of Satellite Based Augmentation Systems (SBASs). The Federal Aviation Administration's Wide Area Augmentation System (WAAS) will be the first such system designed to supplement the Global Positioning System (GPS).

The purpose of this thesis will be to develop the utility to aviation users of geostationary satellites for the augmentation of the Global Positioning System. To enhance appreciation for the current state of worldwide navigation systems, the following few sections give an overview of navigation throughout history. Next a brief sketch of the satellite navigation programs leading up to GPS is given. A summary of the Global Positioning System and its operation is subsequently provided. Contributions shown in the remainder of this thesis are listed at the end of this chapter.

## **1.1 NAVIGATION HISTORY AND PERSPECTIVE: MARINE NAVIGATION**

Since the beginning of recorded times, mariners have been among the first to utilize new navigation technology. The interest in such innovation is rooted in necessity. On the open sea, being uncertain of location or the direction to landfall can be fatal. Most early navigators kept sight of land at all times. Subtle clues such as the currents or presence of birds were also used to help get ships back on course.

The ancient Polynesians embraced the sea in their culture and lives. They navigated their canoes by the stars and other signs that came from the ocean and sky. "Navigation was a precise science, a learned art that was passed on verbally from one navigator to another for countless generations" [Clark00]. Some of their techniques are not completely understood and many are no longer practiced leaving modern navigators in amazement at their aptitude in navigating open water. They cast their observations of everything from the location of island neighbors to the prevailing direction of the swell with detailed maps of palm twigs and cowrie shells. The Polynesians watched the waves, whose direction and type yielded useful navigational secrets. They followed the faint gleam cast on the horizon by tiny islets



still out of sight below the horizon. However, these accomplishments are the exceptions that prove the rule: navigation at sea before the development of astronomical and timing aids was a most uncertain undertaking.

Early navigators may have followed clouds (which form over land) or odors (which can carry far out to sea). But what if land were nowhere nearby? The Phoenicians looked to the heavens. The sun moving across the commonly cloudless Mediterranean sky gave them their direction. [Calahan] suggests that Phoenician navigators may have used these subtle clues among others to navigate to the Americas in 500 BC to search for iron and steel. This journey is highly unlikely to have taken place; there are only a few artifacts to support this theory and the same evidence has been used to support Basque presence in the Americas during that period. However, known journeys by Phoenicians, Greeks, Egyptians, as well as others throughout the Mediterranean in ancient times suggest that these more 'intuitive' techniques worked; at least some of the time.

One of the greatest advances in navigation history came with the compass (Figure 1.1). The Chinese apparently knew about the powers of magnetism as early as the third millennium BC. However, the application of the compass for maritime use did not come into practice until early in the present millennium. The first mention of the compass in the West comes from the Englishman Alexander Neckham, who wrote in 1187 that "sailors use a magnetic needle which swings on a point and shows the direction of the north when the weather is overcast." Despite its usefulness, the compass took a long time to come into wide use, as many seamen thought it operated by black magic. Such concerns motivated the invention of the binnacle, in which sea captains could hide their recondite instrument from the suspicious eyes of the crew. In the meantime, sailors relied on natural forces they could readily comprehend.

One of the most apparent natural forces is currents. The western flowing currents of the Indian Ocean are possibly responsible for the Indonesian-based race of Madagascar, an African island 4,000 miles from the closest part of Indonesia. Similarly, the clockwise currents in the North Atlantic helped doom one of the greatest land frauds in history: Erik the Red's colonization scheme for the island he cleverly dubbed "Greenland." Of the 25

ships that sailed west from Norway in the year 990, the strong North Atlantic current, known as the Gulf Stream, foiled nine. The Gulf Stream was named by Benjamin Franklin when he was deputy Postmaster General of England in the 18<sup>th</sup> century when he noted that his mail ships to the American colonies took longer than whaling ships. From the whalers he learned of the strong prevailing current that originated in the Gulf of Mexico and swept into the North Atlantic.



**Figure 1.1: An Illuminated Mariner's Compass [Bowditch]**

Like currents, trade winds have always been important to mariners. Those blowing heads on yellowed old maps are not mere decoration. In the Indian Ocean, for example, Indian traders over the ages have ridden the northeast monsoon to Africa in the cool, dry winter

and taken the southwest monsoon back to the subcontinent in the hot, wet summer. To make their annual voyages from Tahiti to Hawaii, a journey of several thousand miles, the Polynesians hitched a ride on the prevailing southeasterly wind, setting a starboard tack and sailing northeast.

For millennia, as sailors from the Phoenicians to the Polynesians knew, the heavens remained the best way to find one's north-south position. Increasingly sophisticated devices were designed over the centuries to measure the height of the sun and stars over the horizon. The gnomon or sun-shadow disk operated like a sundial, enabling the user to approximate their latitude by the length of the sun's shadow cast on a disk floating level in water. The Arabian kamal was a rectangular plate that one moved closer or farther from one's face until the distance between the North star and the horizon exactly corresponded to the plate's upper and lower edges. The distance the plate lay away from the face -- measured by a string tied to the center of the plate and held at the other end to the tip of the nose -- determined latitude.

Charts have aided mariners ever since the Alexandrian astronomer Ptolemy created the first world atlas in the second century AD. Ptolemy's 27 maps that were part of his world atlas plotted latitude and longitude lines, though they became significantly less reliable the farther one was from the known world centered on the Mediterranean. Even before Ptolemy, there were sailing directions, that the Greeks called *periplus* or "circumnavigation," that were compiled from information collected from sailors' observations during their travels. One of these, "The Periplus of the Eritrean Sea," a document written in the first century by a Greek merchant living in Alexandria, described trading routes as far east as India. By the 10th century, Italian-made portolans supplied detailed directions, distances, depths, and coastal descriptions, and by the 13th century, sea maps with scale and bearings began to appear.

Around 200 BC, Appolonius of Pergus invented the astrolabe, a disc of metal that one held suspended by a small ring. The disc had a scale with degrees and a ruler for measuring the height of an astronomical body. The astrolabe came into common use by sailors in the Middle Ages. Other medieval mariners preferred the cross-staff, a T-shaped device whose

base was held up to the eye. One measured the sun's height by pulling the slidable top of the T toward one's eye until the sun lay at the top and the horizon at the bottom. Since blindness resulted from frequent use, the explorer John Davis invented the back-staff in 1595, which enabled one to get the same measurement with one's back to the sun. The sextant (Figure 1.2) was the most advanced of these devices, allowing users to determine their latitude to within a nautical mile or two, even from a swaying deck.

In the years after the sextant was invented in 1731, many held out hope that it would aid in east-west navigation as well -- that is, in finding longitude. Latitude is determined from the elevation of known stars. Polaris, or the North Star, is often employed in the Northern Hemisphere for determining latitude. However, to determine longitude, the rotation of the stars must be compensated for as they rotate overhead. This is a straightforward process if the exact time is known. Uncertainties of just one minute in time can cause longitudinal errors of over 4 km at the equator. Clocks of the day were not capable of working at sea with that accuracy. Instead of a clock, sailors could employ the sextant to figure longitude using the lunar-distance (lunars) method. The lunar process, with the astronomical tables of the 18th century, could take several hours to work out one's position -- not remotely good enough for sea travel. Several great prizes were announced in the late 1600s and early 1700s by Spain, France, and England to solve the longitude problem. It became the most significant scientific problem of the day with astronomers, mathematicians, and the greatest natural philosophers competing for fame and fortune. In the end, it was the resolute clockmaker, John Harrison, who solved the longitude problem with his chronometers.

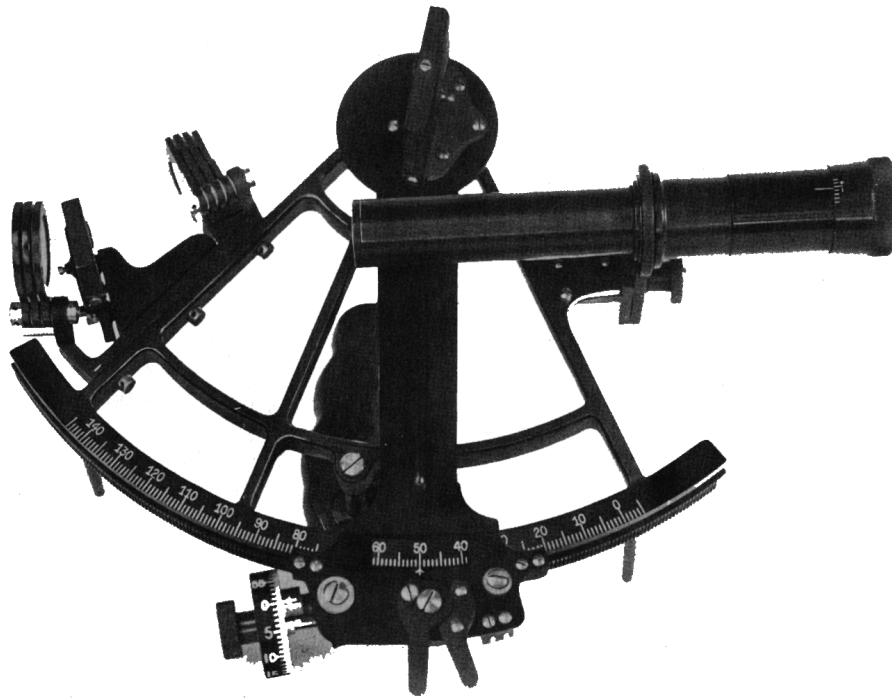


**Figure 1.2: A Sextant [Bowditch]**

John Harrison was not only scrutinized and delayed by his critics but also by his own perfectionism [Sobel]. He set out to win the greatest prize of his day; a handsome sum of 20,000 British pounds (several million dollars in today's U.S. currency) for a solution to the longitude problem. The pendulum clocks of the early 18<sup>th</sup> century were inadequate to meet the task of keeping time at sea. The pendulum gets disturbed by the sway of the ship, and the smallest changes in temperature and humidity cause the elements of the clock to shrink or expand slightly. This variation throws off the most careful calibration. Many astronomers and navigators of the day sought a method based on distances between the moon and the sun (lunars). Charts that were of sufficient accuracy to predict the position of the moon were not widely available until late in the 18<sup>th</sup> century.

Harrison's first timepiece, the H-1, was well received by the Board of Longitude, the review committee established to award the prize to a person or persons that delivered a 'useful and practical' method of determining longitude. H-1 was the most accurate timepiece ever built to that date. Clock designs of his day were sensitive to variations in

temperature because their parts expand and shrink. Harrison's clock was specially constructed of materials whose thermal expansion and contraction offset each other to keep the device in calibration. It could be wound while operating. It did not require lubrication. However, Harrison knew it could be better.

During the first review of his timepiece in 1737, Harrison convinced the board *not* to grant him the prize. Instead, he requested an advance on building another timepiece that removed many of the shortcomings of the first model. It was likely a disservice to Harrison that they accepted his proposal. When Harrison had completed the second and subsequent versions of his timekeeper, the atmosphere of acceptance had changed. The relatively friendly group of individuals that had greeted his first clock was replaced by persons that opposed the clock as a solution to longitude and preferred the more astronomical solution of lunars. [Sobel] described the incredulity that Harrison's various models of clocks faced:

In comparison, John Harrison offered the world a little ticking thing in a box [as a solution to the longitude problem]. Preposterous!

Worse, this device of Harrison's had all the complexity of the longitude problem already hardwired into its works. The user didn't have to master math or astronomy or gain experience to make it go. Something unseemly attended the sea clock, in the eyes of scientists and celestial navigators. Something facile. Something flukish. In an earlier era, Harrison might have been accused of witchcraft for proposing such a magic-box solution. As it was, Harrison stood alone against the vested navigational interests of the scientific establishment. He became entrenched in this position by virtue of his own high standards and the high degree of skepticism expressed by his opponents. Instead of the accolades he might have expected for his achievements, he was to be subjected to many unpleasant trials that began after the completion of his masterpiece, the fourth timekeeper, H-4, in 1759.

In spite of these struggles, the clock eventually gained acceptance as the solution to the longitude problem. By 1860 the British navy had about 200 ships on the high seas that employed over 800 chronometers.

## 1.2 AVIATION NAVIGATION DEVELOPMENT AND HISTORY

Much like the earliest mariners, early aircraft pilots navigated visually. While pilots had several aiding instruments including the compass for bearing, the barometer for altitude and

the anemometer for airspeed, they depended heavily on visual clues such as roads and landmarks for position location. During the 1920s, lighted beacons were added across the U.S. for airmail routes. The need to operate in non-visual conditions established the need for radio frequency based navigation aids which at first were direction indicators to radio beacons at known points.

### **1.2.1 EARLY RADIO NAVIGATION DIRECTION FINDERS**

In the 1930s leading up to World War II, medium and high frequency radio beacons served guidance and crude navigation functions for aircraft. By tracking a single beacon (usually collocated with an airport) a relative angular fix can be made between the axis of the aircraft and the beacon. By tracking two or more beacons, a crude position could be determined through triangulation. “Positive” navigation points were provided at some airports with vertical marker beacons. These vertical beacons were similar to the standard radio beacon except that their signals were directed upward. Tracking this beacon indicates to the pilot that they are directly above it giving them ‘positive’ feedback on their location. As more flights were made on a greater number of routes, the use of airport locations as beacons became undesired. Over time, directional beacons were set up along air travel routes around the world. These routes could take advantage of the lessons learned during World War II. During the war, it was shown that routes directed along prevailing winds (referred to as cyclonic) could cut travel time over the shortest distant method (great circle), thus saving fuel.

After World War II, VOR (VHF Omnidirectional Range) and ILS (Instrument Landing System) stations were developed and put into place. In the following decades, these systems have become the primary basis of air navigation in the western world. Starting in the 1960s, the former Russian republics used a system not standardized by the International Civil Aviation Organization (ICAO) that was an L-band angle/range system (known as RSN) that provided en-route navigation. A ground-based navigation precision approach radar (PAR) allowed Russian controllers to verbally assist landing aircraft. During the 1990s, the former Russian republics began to purchase and install western aviation aids. China used the Russian aiding system in the 1960s and early 1970s but began to install

western VOR, DME (Distance Measuring Equipment) and ILS aids in the late 1970s. According to [Kayton], outside of the developed world VOR/DME support is provided with the exceptions of the Polar Regions, the South Atlantic Ocean, and much of the Pacific and Indian oceans. Other methods such as celestial, inertial systems, Omega or GPS are necessary in these regions for navigation.

### 1.2.2 VOR AND DME

VOR broadcasts in a band between 108 and 118 MHz with channels 100 kHz apart. The ground broadcasts two signals modulated with a 30-Hz tone. The first is a fixed reference tone with an omnidirectional radiation pattern. The second signal is radiated with a cardioid pattern that rotates 30 rps. The receiver uses the relative phase of these two 30-Hz signals to determine bearing to the VOR (which is at a known location). Figure 1.3 shows a diagram of a VOR receiver. In addition to the 30-Hz modulation there is an audio channel broadcast modulated at 9660 Hz as well as Morse code identifier of the VOR with a 1020 Hz modulation. This system design was a U.S. standard by 1946 with later adoption by ICAO [Kayton]. The performance of this system is only limited by propagation effects and user equipment errors. High-end user equipment can usually achieve  $0.1^\circ$ - $10^\circ$  of angular resolution. This system only works well when the VOR and receiver are line of sight visible.

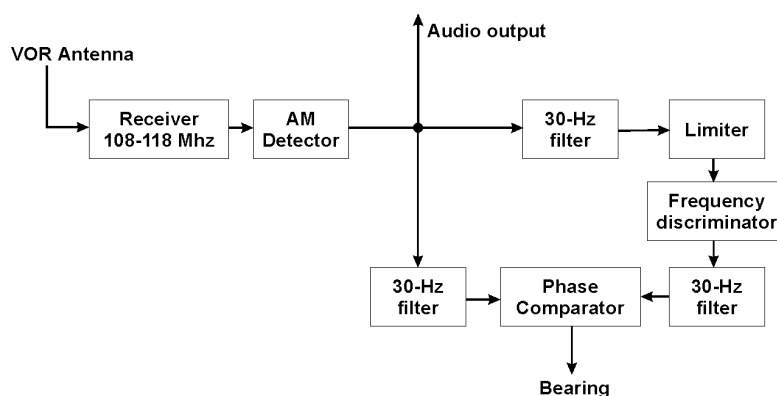
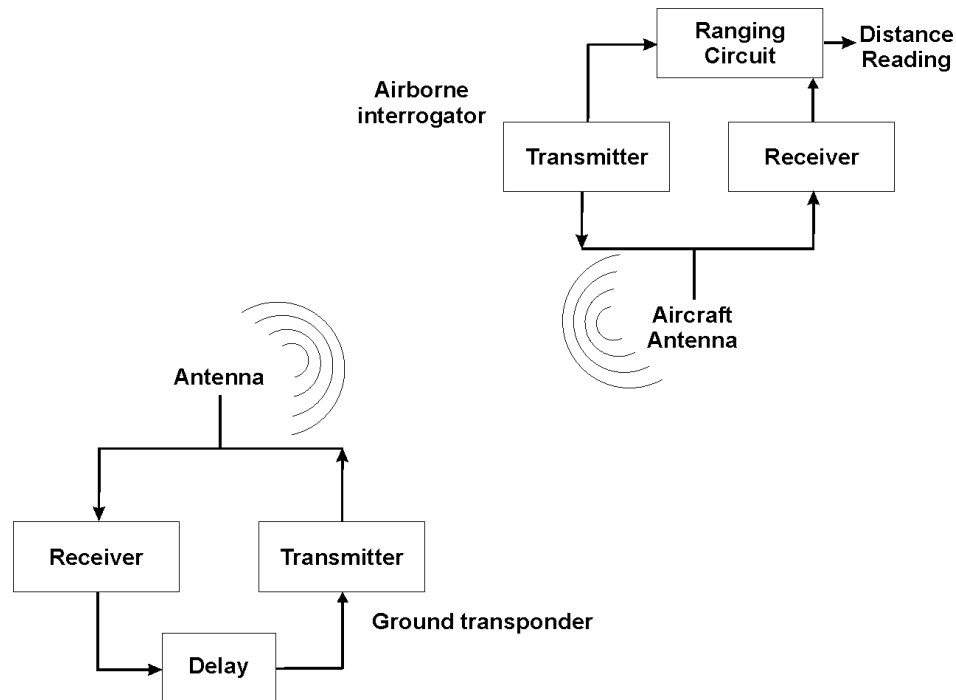


Figure 1.3: VOR Receiver Diagram



While VOR is a system designed for one-way (transmitter to receiver) angular measurement, Distance Measuring Equipment (DME) is a two-way system used for measuring range to a transponder. Figure 1.4 shows an overview of DME operation.



**Figure 1.4: DME System Architecture**

As represented in Figure 1.4, the airborne interrogator transmits pulses on one of the 126 designated frequencies for DME between 1025 and 1150 MHz (1 MHz bandwidth). The pulses are spaced 12  $\mu\text{sec}$  apart with each pulse lasting 3.5  $\mu\text{sec}$ . The pulse pairs are repeated between 5 and 150 times per second. The ground transponder receives these pulses and after a fixed 50  $\mu\text{sec}$  delay retransmits them either 63 MHz above or below the airborne transmit frequency. The airborne interrogator compares the receive time versus the transmit time, subtracts off the 50  $\mu\text{sec}$  delay and estimates the range as half of the residual round-trip time difference (12  $\mu\text{sec}$  represents a one nautical mile round-trip). Each transponder can support up to about 100 or more aircraft. Each airborne interrogator is made slightly unstable and the matching loop is designed to only recognize pulses that

correspond to its own signature. Unlike the VOR system, this transponder-based two way ranging has limited capacity.

### **1.2.3 INSTRUMENT LANDING SYSTEM (ILS)**

VOR and DME are designed to provide en route navigation. Figure 1.5 shows the Instrument Landing System (ILS) which is specifically designed for the approach and landing phases of flight. ILS consists of three signals: 1) the localizer (40 channels from 108-112 MHz); 2) the glide slope (40 channels from 329-335 MHz); and 3) marker beacons (single channel at 75 MHz). The localizer provides a radiation pattern that when received at the aircraft indicates lateral displacement from the centerline of the runway. The localizer array is usually placed 200-300 meters from the end of the stop line on the runway and can be 12 to 40 meters in length. In a similar fashion, the glide slope provides vertical guidance. The minimum coverage for the glide slope extends a minimum of 10 nmi and covers  $0.7^\circ$  (approximately) on either side of the nominal  $3^\circ$  slope. The marker beacons provide the pilot with two or three alerts points along the approach flight path. The outer marker (OM) is usually between 4-7 nmi from the landing threshold near the point of glide-path intercept. The middle marker (MM) is usually placed near the missed approach decision point. The inner marker (IM) is sometimes provided for precision approaches and is usually placed where the glide slope intersects 30 meters above the runway. ILS provides local information to aid approach and landing only.

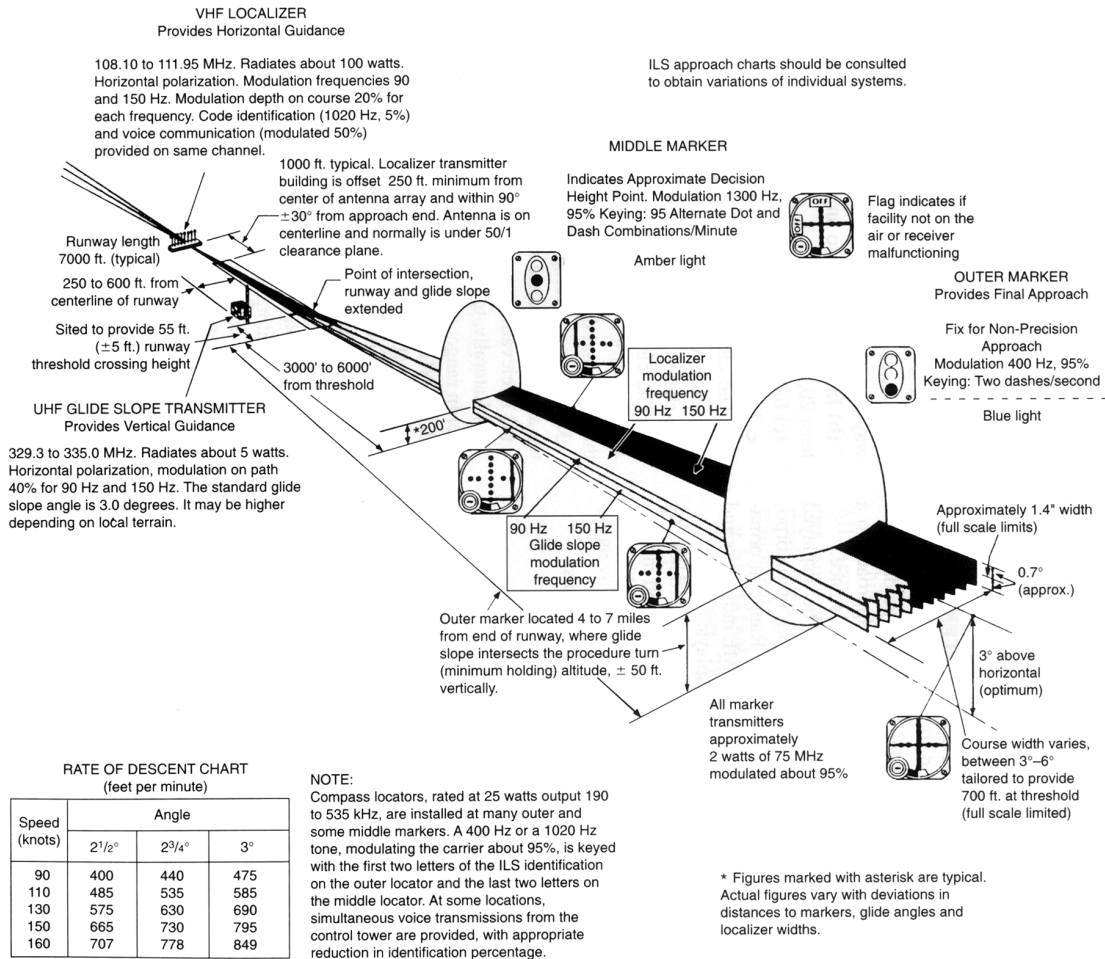


Figure 1.5: The Instrument Landing System (ILS) [FarAim]

## 1.2.4 LORAN/OMEGA

In comparison to VOR and DME systems that depend on radial lines and circles to measure distance and bearing, the Loran and Omega systems use hyperbolic lines of position. Loran (long-range navigation) and Omega systems are area navigation systems, which means that they allow continuous or near-continuous navigation without following arbitrary paths. Unlike VOR and DME where artificial airways interconnect various latitude/longitude points, Loran and Omega allow for navigation of arbitrary routes without using triangulation or trilateration [Kayton]. In the case of Loran at least three transmitting stations make up a chain. One station is designated as a master and the others are referred to as secondaries. Receivers can derive position, velocity (with differential operation), and

time states from the difference between the time of arrival of a radio wave from a secondary minus the time of arrival of a radio wave from the master. The repeatable and relative accuracy of Loran-C is usually between 18 and 90 meters. As of 1996, the Loran was supported along most of the Northern hemisphere's coasts as well as all of Conterminous United States (CONUS). However, much of the Southern hemisphere remained without support [Kayton].

In comparison, the Omega system in 1996 covered most of the Earth's surface. The system was comprised of eight transmitting stations around the world, each transmitting four common frequencies that are time shared between the stations so that only one station at a time is transmitting a given frequency. The transmission bands are in the very-low frequency range (VLF) and since the attenuation at these frequencies is very low, each station can reach ranges from 5,000 to 15,000 nmi. The distance between the receiver and transmitter is obtained from the signal phase. When used as a stand-alone system, an Omega receiver provides an accuracy of two to four nmi [USDOD&T, USDOT]. With differential corrections from a nearby reference receiver, the errors can be reduced to about 500 meters [Kayton]. However, due to multiple competing navigation methods the Omega system was phased out in 1998.

### **1.3 SATELLITE NAVIGATION HISTORY**

Each of the navigation systems presented so far have their individual strengths and weaknesses. VOR/DME and Loran support low to moderate accuracy area navigation (en route) over a wide geographic area (albeit not the entire surface of the Earth). ILS is a high accuracy system for local guidance during approach and landing but cannot be used for en route navigation. VOR/DME and ILS coverage are limited to line of sight from the transmitter to receiver requiring a large number of stations to cover a large geographical region. Loran chains cover significant regions of the globe but do not offer complete global coverage. Loran was a very effective and widely used system for marine applications. However, Loran never gained acceptance for aircraft under instrument conditions (IFR) due at least in part to a reputation for degraded performance in thunderstorms. By the 1960s, several programs were underway to overcome some of the

drawbacks of the navigation systems of the day by using satellites as one-way ranging sources for receivers.

### **1.3.1 THE TRANSIT SATELLITE PROGRAM**

Observations of the variations of Doppler shift of the Sputnik 1 satellite led researchers at the Applied Physics Laboratory (APL) of Johns Hopkins University to develop a computer program that determined the satellite's orbit. The researchers realized that the orbit of the satellite could be accurately estimated using Doppler measurements made by a receiver at a known (and fixed) location. Hence, one could use the Doppler and the knowledge of the satellite's orbit to determine the position of a receiver at an unknown location. This was the basis of the first satellite based navigational system called Transit. The Transit satellites broadcast two continuous signals at 150 and 400 MHz. Dual frequencies were used to remove ionospheric delay. They were in polar circular orbits of about 600 nmi altitude. The maximum rate of change of the Doppler shift was used to calculate the point of closest approach of the satellite. With the broadcast satellite position, along with a reference altitude (sea-level for ships), the computation of horizontal position was allowed to less than one hundred meters for a stationary receiver and several hundred meters for a moving receiver. Performance was sensitive to the user's velocity and thus was not particularly applicable to aircraft. However this program proved several important points for satellite navigation: 1) satellites could be very reliable (after early failures) with satellite life as long as 15 years; 2) satellite positions could be predicted very accurately for navigation use; 3) ionospheric effects could be compensated for by dual frequency signal design; and, 4) highly stable clocks could be utilized in orbit. The next programs would capitalize on these successes and overcome the shortcomings of the Transit system.

### **1.3.2 THE TIMATION AND 621B SATELLITE PROGRAMS**

The Timation satellite program was based on the idea of providing accurate time and three-dimensional position to users based on ranging, not on Doppler measurements. The ranging requirement meant that very stable clocks must be on the satellite and they must be synchronized to a master ground clock. Ranging was provided by a method known as side-

tone ranging that allowed users to resolve phase ambiguities to the satellite [Parkinson96]. This program developed the first atomic time clocks for space that proved critical for later satellite navigation progress.

The final precursor to GPS was the 621B satellite program which introduced the concept of pseudorandom noise (PRN) codes. These codes modulate the signal with a repeatable sequence of ones and zeros. An appropriate family of codes can be used to broadcast multiple channels of information at the same carrier frequency since they can be chosen to be nearly orthogonal (i.e., the cross-correlation between the codes are zero or very nearly so). The signal could be detected even if its power was below the ambient noise level and since the sequence was known and repeatable, the phase, and hence the range, of the satellite could be directly measured (plus any ambiguity added by the receiver clock, atmosphere, etc.). The precise clock of the Timation program was added to the 621B program to alleviate the reliance on continuous ground contact [Parkinson97].

### **1.3.3 GLONASS**

Before proceeding to a description of GPS, another satellite navigation system of note should be mentioned: GLObal'naya Navigatsionnay Sputnikovaya Sistema or GLONASS. GLONASS was developed by the Russian (Soviet) government beginning in the 1970s and went through many of the same development processes that led to GPS [Parkinson95]. Advancements and research in precise satellite orbit determination, stable clock architectures, satellite design, general relativity effects, and atmospheric effects on radio wave propagation led to the beginning GLONASS constellation in 1982. The signal architecture is similar to, but not compatible with, GPS. As with GPS, the signal design is open allowing for civilian use in navigation. While still in use today by many groups and countries around the world, the incompatible signal design with GPS has limited the manufacture of user equipment. Higher equipment costs and the lack of a complete constellation of satellites has kept this system from reaching true worldwide acceptance as a navigation standard. On-going work with dual GPS-GLONASS receivers as well as GLONASS constellation additions could raise the level of acceptance of this navigation system.

## 1.4 THE GLOBAL POSITIONING SYSTEM (GPS)

The concepts of the previous successful satellite programs were incorporated into a new system, conceived in 1973, and later named the Global Positioning System (GPS). This new system was supported by multiple military branches for worldwide precision navigation and ordnance delivery. It had two broadcast frequencies for ionospheric corrections as in Transit, and it used highly stable clocks as in Timation. It also used the PRN signal structure developed for 621B.

GPS is broken down into three basic segments as represented in Figure 1.6. These are: 1) Space, comprising the satellites; 2) Control, incorporating tracking and command centers; and 3) User, performing navigation functions based on ranging to the satellites.

### 1.4.1 THE SPACE SEGMENT

The GPS Space Vehicles (SV) are placed in circular orbits with  $55^\circ$  inclination, a semi-major axis of 26,560 km (20,182 km altitude) corresponding to an orbital period of 12 hours sidereal. There are six orbit planes (Table 1.1) placed at  $60^\circ$  offsets in longitude with nominally four satellites in each plane giving 24 satellites. Currently there are 28 active satellites in the planes as shown in Table 1.2. The slot numbers indicate orbit positions in the planes that are nominally separated by  $90^\circ$ . However the spacing is adjusted to achieve optimal coverage over regions of interest. Figure 1.7 shows the distribution of satellites and their ground tracks [TMSLIVE]. The lighter-colored ground tracks indicate the satellites that are in view of at least nine ground stations that are part of the National Satellite Test Bed (NSTB) which will be described later. The tracking stations are located in the conterminous United States (CONUS) as well as Alaska, Hawaii and Canada. The darkest satellite tracks are not in view of any tracking stations.

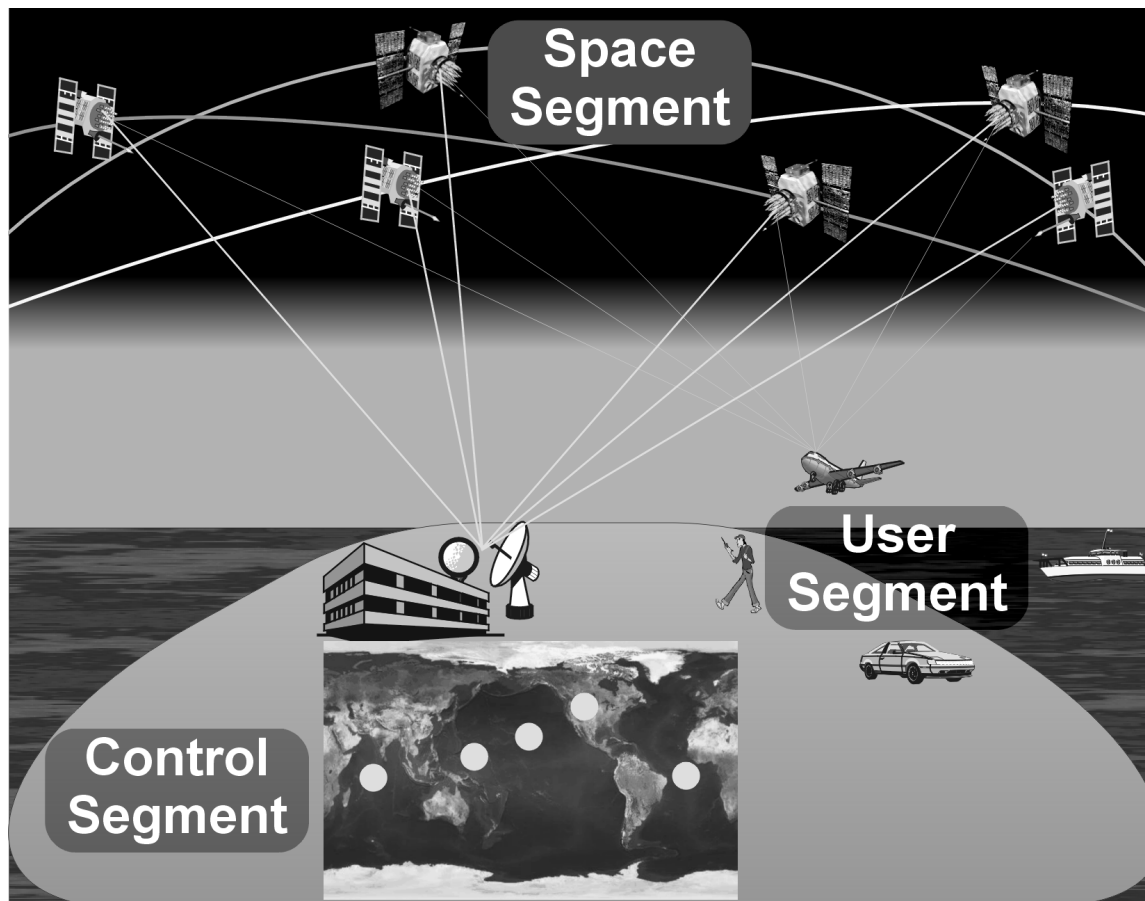


Figure 1.6: GPS Segments; Space, Control and User

Plane	Right Ascension of Ascending Node
A	55°
B	115°
C	175°
D	235°
E	295°
F	355°

Table 1.1: GPS SV Plane Locations on January 24, 2000



PRN	Plane	Slot Number
9	A	1
25	A	2
8	A	3
27	A	4
19	A	5
22	B	1
30	B	2
2	B	3
5	B	4
6	C	1
3	C	2
31	C	3
7	C	4
24	D	1

PRN	Plane	Slot Number
11	D	2
17	D	3
4	D	4
15	D	5
14	E	1
21	E	2
10	E	3
23	E	4
16	E	5
29	F	1
26	F	2
18	F	3
1	F	4
13	F	5

**Table 1.2: GPS SV Plane/Slot Allocation on January 24, 2000**

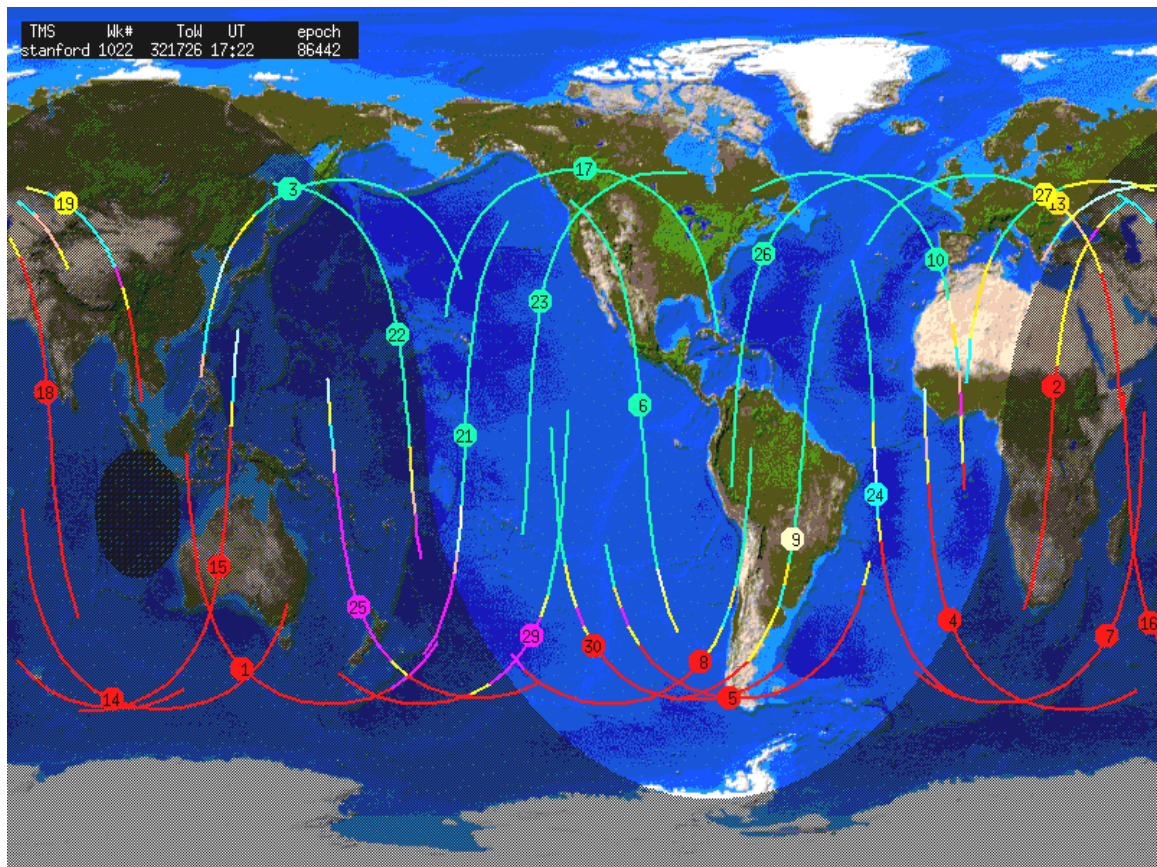


**Figure 1.7: GPS Ground tracks**

The satellites themselves are three-axis stabilized and use solar panels to provide power. Each satellite contains a pair of atomic clocks (for redundancy) which have a stability of 1 part in  $10^{13}$ . Each satellite broadcasts on two frequencies, 1575.42 MHz (L1) and 1278.6 MHz (L2). The L1 signal contains two separate PRN modulations: 1) the Clear Acquisition (C/A) code at bit or ‘chipping’ rate of 1.023 MHz (i.e., each millisecond there are 1023 modulated bits or ‘chips’ transmitted); and, 2) the so-called ‘P’ code which has a chipping rate of 10.23 MHz or 10 times that of the C/A code. The L2 signal only contains the P code. As in the 621B program, GPS uses a PRN coding sequence of bits that have a specified length but have the property that different codes do not strongly correlate with one another (i.e., they are orthogonal). The C/A code is 1023 chips long and thus repeats every 1 millisecond. The full P code length is 38 weeks but is truncated to 1 week.

As described by [Spilker], the C/A time-domain signal structure,  $s(t)$ , is represented by the following:

$$s(t) = A \cdot c(t) \cdot d(t) \cdot \sin(2\pi \cdot f \cdot t) \quad (1.1)$$

where

$A \doteq$  C / A signal amplitude

$f \doteq$  C / A signal frequency (1575.42 MHz)

$c(t) \doteq$  the predefined PRN code at 1.023 MHz

$d(t) \doteq$  a 50 bit - per - second data message

The effect of the C/A code modulation is to spread the modulated signal power over a frequency band equal to roughly twice the chipping rate as depicted in Figure 1.8. The corresponding spreading for P code is 10 times as wide.

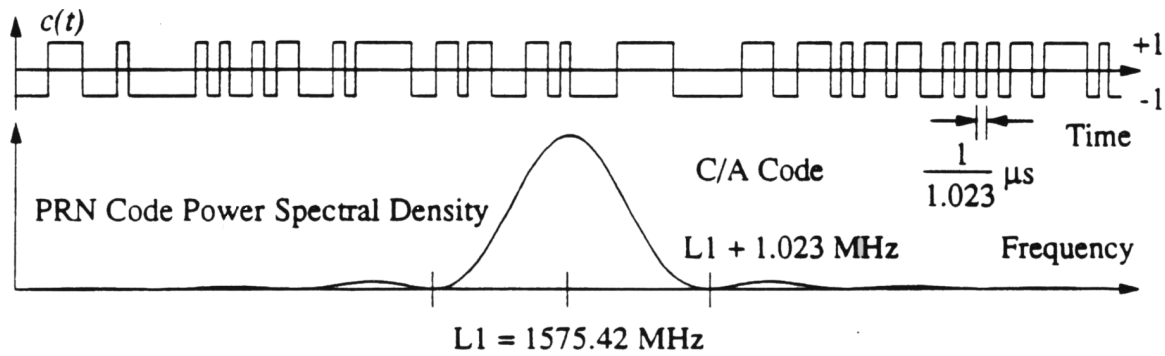


Figure 1.8: C/A Code Spread Spectrum [Cohen]

The data message,  $d(t)$ , is modulated onto the carrier signal at 50 bits-per-second (bps) [ICD200C]. The data message includes: 1) current GPS time to allow for the receiver to set its coarse clock (to about 50 milliseconds); 2) rough (compact) and precise (verbose) satellite ephemeris and clock drift rates (to calculate SV position); 3) a crude correction function for the ionosphere for receivers that do not use dual frequency compensation; 4) satellite health and user range accuracy estimates; 5) a hand-over-word (HOW) to give the relative phase between the C/A and P codes; and 6) the current offset between GPS time and Universal Time Coordinated (UTC) as determined by the United States Naval Observatory (USNO) [ICD200C].

#### 1.4.2 THE CONTROL SEGMENT

The control segment is responsible for the operation and maintenance of the Global Positioning System. There are five monitoring stations worldwide (inset, Figure 1.6) at Kwajalein, Hawaii, Colorado Springs, Diego Garcia and Ascension. These stations measure the discrepancies between the satellite state information (ephemerides and clock) as well as health of the satellites. The Master Control Station (MCS) in Colorado Springs formulates predicted values and uploads them to the satellites. This data is then included in the new message for broadcast to the users.

### 1.4.3 THE USER SEGMENT

The user segment comprises GPS receivers that decode the satellite messages and determine the ranges to at least four GPS SVs to determine 3D position and the receiver clock offset. Users breakdown into two main groups: authorized and unauthorized. Authorized users have full access to both the C/A and P codes. Authorized users are restricted to the military and other special groups or projects with special permission from the DoD. Unauthorized users generally cannot access the P codes as the code itself is encrypted before broadcast by a process known as anti-spoofing (AS). This makes the process of emulating a GPS signal to the authorized user more difficult. The encrypted modulated signal is known as Y code. Additionally the hand-over-word (HOW) between the C/A and Y code is also encrypted. Authorized users are given a 'key' that allows for the decryption of the HOW as well as the Y code. Authorized user receiver equipment with dual frequency code access utilizes what is known as the Precise Positioning Service (PPS).

Unauthorized users also suffer from an intentional effect known as Selective Availability or SA. With SA activated, the master control segment adds small intentional errors to the satellite clock or broadcast ephemeris to degrade the ranging accuracy of an unauthorized user. Unauthorized user receivers employing only L1 C/A code ranging utilize what is known as the Standard Positioning Service (SPS), which is available to all civilian users. The two axes of a position solution are shown in Figure 1.9, where the majority of the variation (140 meters vertically) is due to the degradation of SPS by SA. The DoD has specified that the SA degradation will not exceed 100 meters 2D RMS [ICD200C]. By presidential directive, SA was turned off on May 2<sup>nd</sup>, 2000. The balance of this thesis will always include the effects of SA on SPS since: 1) an insufficient period of time has elapsed to fully characterize GPS performance since the disabling of SA; and 2) conceivably SA could be re-enabled at any moment due to national security or international conflict concerns.

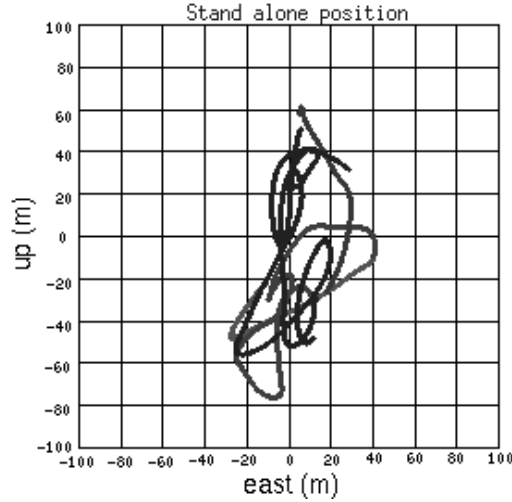


**Figure 1.9: Standard Positioning Solution variations**

#### 1.4.4 THE GPS OBSERVABLES

User receiver architectures vary widely and can supply a wide variety of measurements except the two primary measurements from GPS. Pseudorange,  $\rho_u^k$  from Equation (1.2), is the receiver measurement of the geometric range to the satellite with corruption from satellite and receiver clock errors, the atmosphere and receiver errors. The second basic measurement of the receiver is the continuous carrier phase,  $\phi_u^k$  in Equation (1.3). Continuous carrier phase shares the same degradation factors as the pseudorange, but an additional uncertainty is added since the wavelength of the carrier is only 19 centimeters and has an integer ambiguity that is difficult to resolve in real-time [Hofmann-Wellenhof].

#### 1.5 GPS ERROR SOURCES

As implied by Equations (1.2) and (1.3), a number of factors conspire to corrupt the pseudorange and carrier phase measurements for GPS. These errors are summarized in Figure 1.10 and below.

$$\rho_u^k = (\mathbf{r}_u^k \cdot \mathbf{1}_u^k) + b_u - B^k + I_u^k + T_u^k + v_u^k \quad (1.2)$$

$$\varphi_u^k = (\mathbf{r}_u^k \cdot \mathbf{1}_u^k) + b_u - B^k + I_u^k + T_u^k + N_u^k \lambda_{L1} + \xi_u^k \quad (1.3)$$

where

$\rho_u^k \doteq$  the pseudorange from the user receiver,  $u$ , to the  $k^{\text{th}}$  satellite

$\varphi_u^k \doteq$  the continuous carrier phase from the user receiver,  $u$ , to the  $k^{\text{th}}$  satellite

$\mathbf{1}_u^k \doteq$  the line - of - sight from the user receiver,  $u$ , to the  $k^{\text{th}}$  satellite

$\mathbf{r}_u^k \cdot \mathbf{1}_u^k \doteq$  the calculated range from the user receiver,  $u$ , to the  $k^{\text{th}}$  satellite

$b_u \doteq$  the user receiver clock offset from GPS time

$B^k \doteq$  the  $k^{\text{th}}$  satellite clock offset from GPS time

$I_u^k \doteq$  the ionospheric delay along the line - of - sight from the user receiver,  $u$ , to the  $k^{\text{th}}$  satellite

$T_u^k \doteq$  the tropospheric delay along the line - of - sight from the user receiver,  $u$ , to the  $k^{\text{th}}$  satellite

$N_u^k \doteq$  the continuous phase cycle ambiguity from the user receiver,  $u$ , to the  $k^{\text{th}}$  satellite

$\lambda_{L1} \doteq$  the L1 carrier phase wavelength, 0.1903 meters

$v_u^k \doteq$  the pseudorange measurement error

$\xi_u^k \doteq$  the carrier phase measurement error

Clock errors are mostly due to the degradation of SA, introduced in Section 1.4.3 and discussed further in Chapter 4. The GPS specification [ICD200C] states that degradation due to SA may be due to perturbations in satellite ephemeris or from intentional clock dithering. [Tsai95a] noted that SA does not seem to be applied to the ephemeris. [Dai99] showed that with data collected over 311 days in 1998 and 1999, the 3D RMS error of the ephemeris was less than 5 meters. Therefore, it is reasonable to assume that the overwhelming majority of SA errors are from clock perturbations.

Ionospheric delay is caused when the GPS signal encounters the ionosphere. The carrier wave is advanced while the code phase is delayed. These effects are partially corrected for the single-frequency user by the Klobuchar ionospheric parameters broadcast in the GPS message itself (estimated at 60% by [Klobuchar86]). Dual frequency receivers can, for the most part, remove these effects directly.

Tropospheric delay can be up to 30 meters for low elevation satellites due to GPS signal propagation through the lower atmosphere (troposphere) [Parkinson96]. There are two

primary components of the tropospheric delay, dry and wet. The dry component makes up about 90% of the total delay and can be modeled well with surface pressure data. The wet component is much more difficult to model and not well correlated with surface conditions. The wet term can add as much as 2-3 meters of uncorrected error on the GPS measurements [Parkinson96].

Ephemeris errors occur when the reported satellite position does not match the actual position. The component of these errors along the line of sight to the user is usually less than a few meters [Dai99].

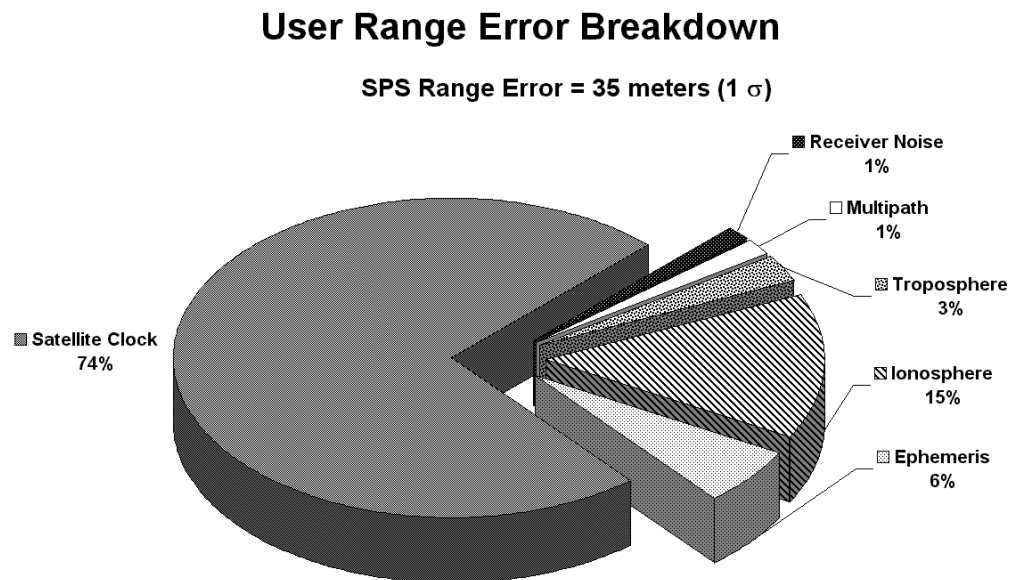


**Figure 1.10: Components of the Unauthorized (SPS) User Ranging Error (SA Enabled)**

Multipath errors are due to local reflections of the signal near the receiver and are tracked with delay, corrupting the range and phase measurements.

Receiver noise is comprised of thermal noise, signal and modeling quantization. These errors are usually limited to about 1 meter for pseudorange and 1 mm for carrier phase.

## 1.6 LOCAL-AREA AND WIDE-AREA DIFFERENTIAL GPS

Since many of the errors of the previous section are common-mode for receivers that are nearby, it is possible to use measurements from one GPS receiver at a known reference location to correct the measurements of the nearby rover. At the limit, for two receivers that share the same antenna, the only residual errors that would remain are due to receiver noise. Figure 1.11 shows this concept, called differential GPS (DGPS). Local-Area Differential GPS consists of a reference station at a known location measuring the errors in the pseudorange and broadcasting the pseudorange corrections to users via a data link.

Differential GPS can reduce position errors to as little as 0.5 meters (with smoothing). However, differential GPS systems suffer from a high sensitivity to the proximity of the user to the reference station. Beyond a separation of 100 km the solution degrades. For DGPS corrections to be available over the entire CONUS over 500 stations are required [Christie98, Christie99, Kee93b].

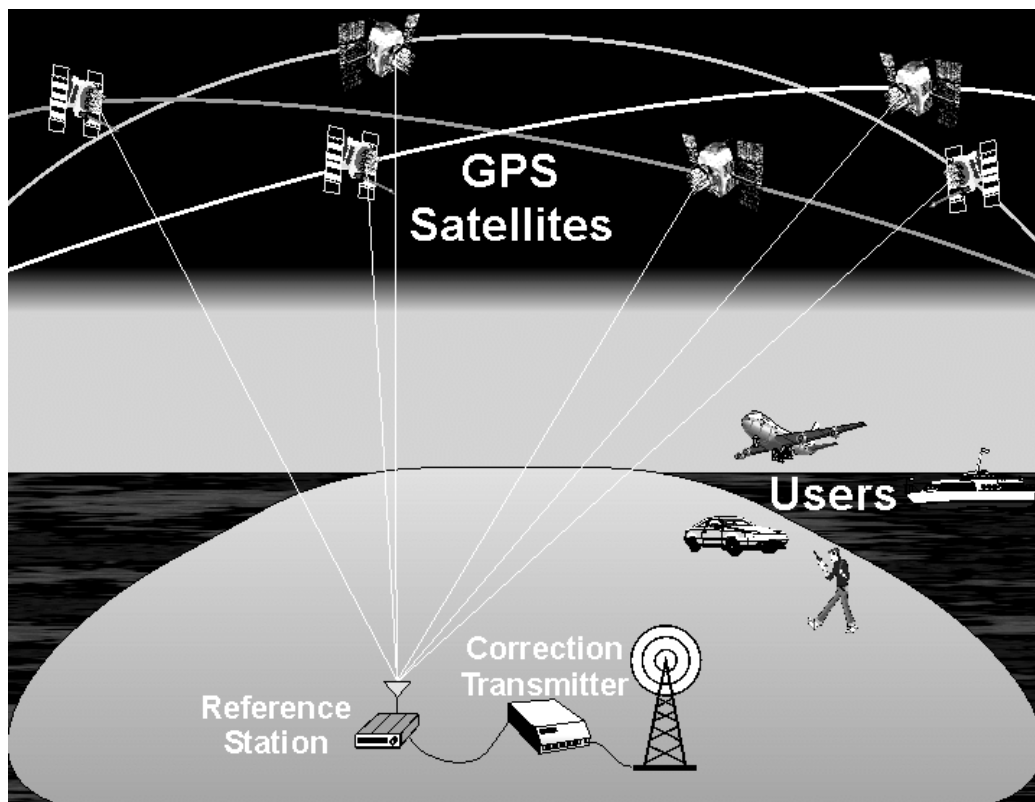
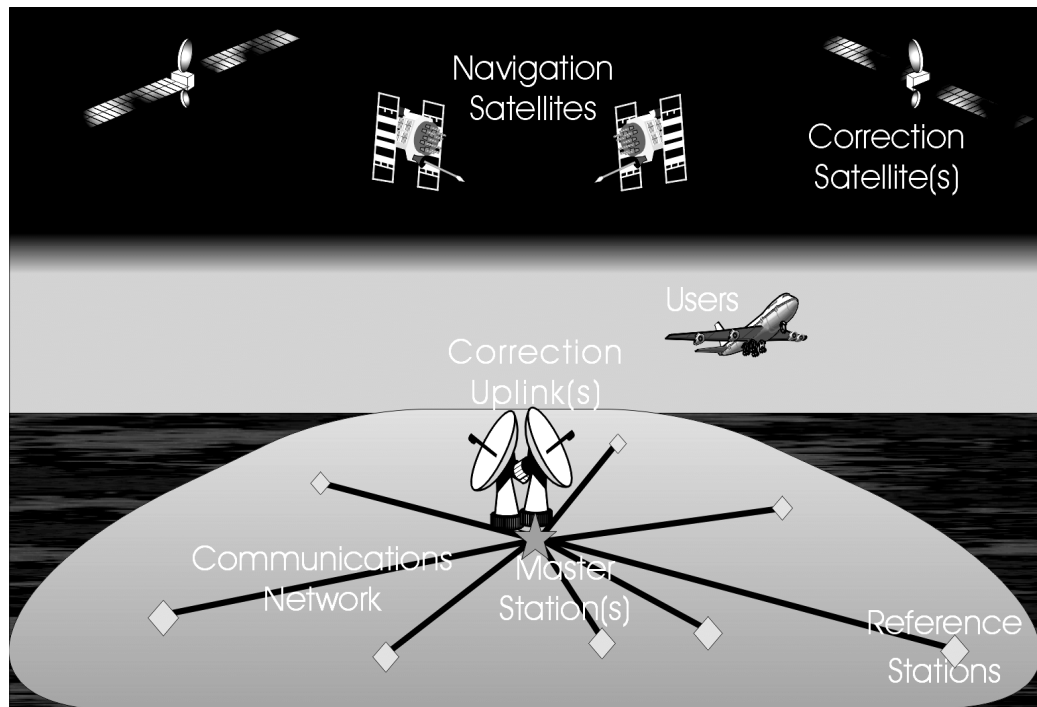


Figure 1.11: Example Differential GPS Architecture





**Figure 1.12: Wide-Area Differential GPS Architecture**

In the early 1990s, [Kee90, Kee91, Kee92, Kee93a, and Kee93b] proposed using a network of reference stations to solve for the GPS ephemeris, clock and ionospheric errors directly. This would require far fewer stations than for standard differential GPS. Figure 1.12 shows the components of a wide area differential GPS system. It includes a network of reference stations connected to a master station that computes the corrections and transmits those corrections via data link. The reference stations each employ an atomic standard for timing stability and the ability to track both GPS frequencies (using cross or other special correlation techniques) for real-time ionospheric corrections.

### **1.7 SPACE-BASED AUGMENTATION SYSTEMS (SBAS): THE WIDE AREA AUGMENTATION SYSTEM (WAAS)**

The use of wide area differential GPS for the aviation community is currently under development by the FAA and is called the Wide Area Augmentation System (WAAS). The major elements of this system are shown in Figure 1.12. The data link employed by this system uses a geostationary satellite, which has a semi-major axis of 42,000 km and a

nearly zero degree inclination. The major advantage of this satellite orbit configuration is that it is synchronous with the rotation of the Earth and, therefore, is in a practically fixed position all of the time relative to users and reference stations. Not only must the accuracy be improved by this system but it must constantly monitor and verify the GPS satellite signals to ensure integrity [Enge96].

Figure 1.13 shows the reduction in ranging errors when the WAAS correction messages are applied.

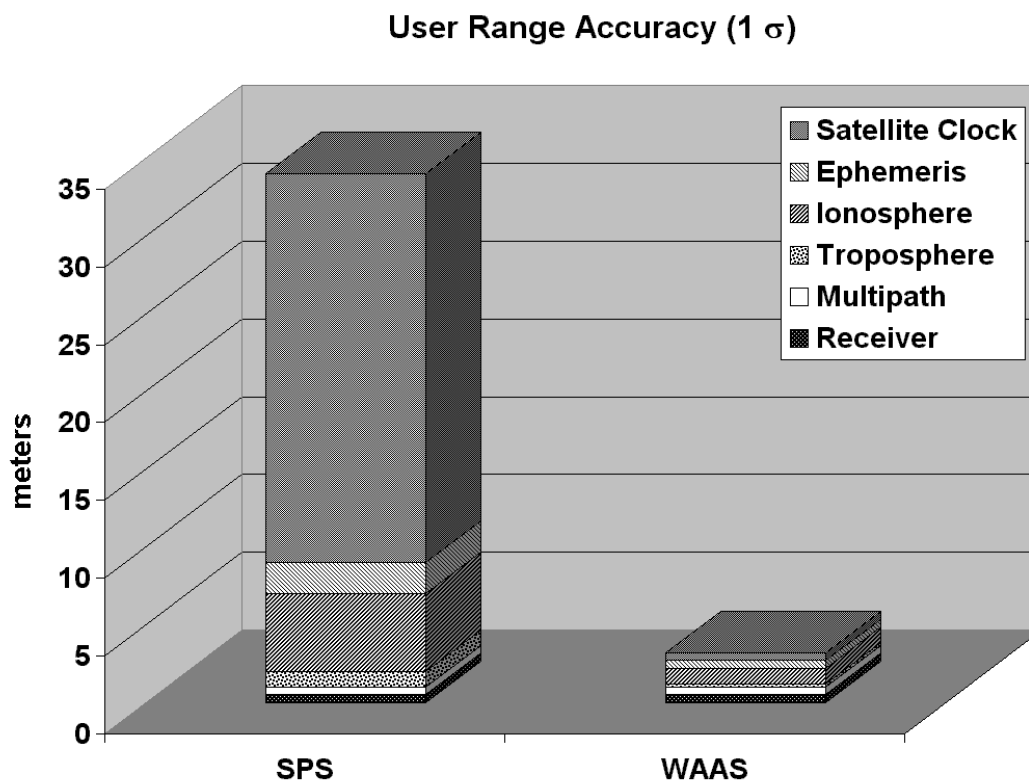


**Figure 1.13: Comparison of Range Error Between Uncorrected GPS Range Error and WAAS Corrected Range Error**

## 1.8 THE NATIONAL SATELLITE TEST BED

To evaluate algorithms for WAAS, the FAA implemented the National Satellite Test Bed (NSTB) as a prototype. Figure 1.14 shows the permanent site locations in the NSTB. This network of receivers employs over 30 sites in CONUS, Canada, Alaska, and Hawaii on a

permanent basis and several other stations worldwide. The CONUS stations are linked in real-time through 56K leased lines back to the FAA Technical Center in Atlantic City, New Jersey. A T1 line links Stanford University to the NSTB through the Technical Center.



**Figure 1.14: National Satellite Test Bed Receiver Sites**

Stanford University has played a major role in the development and deployment of the NSTB since its inception. Figure 1.15 shows a brief history of Stanford University's involvement in the NSTB and WAAS progress. Stanford University has developed prototype WAAS master station software [Walter94]. This software collects data in real-time from the NSTB, computes the corrections for ephemeris, clock and ionospheric errors and can broadcast corrections using geostationary, Ethernet, serial, or modem data links to users. This software can also emulate users in the system by setting certain stations in the NSTB as 'passive'. These passive stations do not contribute information to the correction calculations. This software system has been used to support algorithm development, GPS error characterization, and perform flight tests.

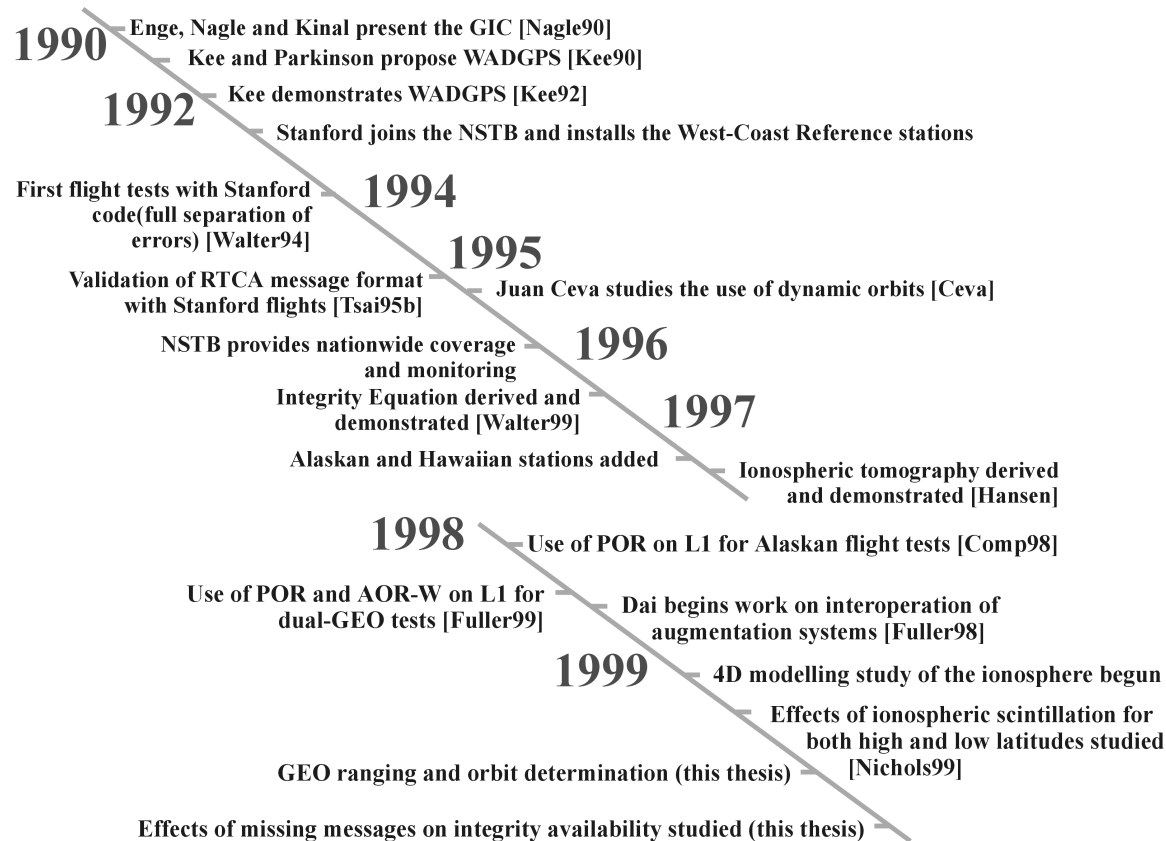


**Figure 1.15: Historical Overview of Stanford University Involvement in WADGPS Development**

## 1.9 LANDING ISSUES

There has been continual advancement in aircraft navigation and guidance over the past 70 years. All of the navigation solutions for aviation prior to the introduction of GPS lacked at least one of two critical features: coverage and capacity. GPS navigation solutions are ubiquitous; available worldwide, including the Northern and Southern Poles, without the addition of any additional infrastructure on the ground or the air. GPS has limitless capacity; supporting all users without any signal degradation. However, even with all of its strengths, GPS does require augmentation for aviation application. The reasons for augmentation of GPS for aviation are fourfold: 1) accuracy; 2) integrity; 3) availability; and 4) continuity. The rest of this section will introduce the concepts and discuss the issues related to improving these four metrics for GPS utilization by aviation.

As depicted in Figure 1.16, an aircraft is approaching an airport under inclement weather, or other poor environmental conditions. Without adequate visibility, the pilot must trust in instrument readings for part or all of the landing phase. The instruments represent the current position and attitude and this representation is the ‘virtual’ aircraft that is some unknown distance and orientation from the true aircraft. For these discussions, the difference between the position indicated by the instruments and the true position of the aircraft is the error (for a detailed description of flight errors see [Kayton]).

The difference between the measured position and the actual or true position is also referred to as accuracy. The ability of a system to provide timely warnings to users or shut itself down when it should not be used for navigation is integrity. The fraction of time that the service for precise navigation is capable of providing a signal with integrity is availability. If the system supports the required accuracy and integrity throughout a maneuver then continuity is achieved.

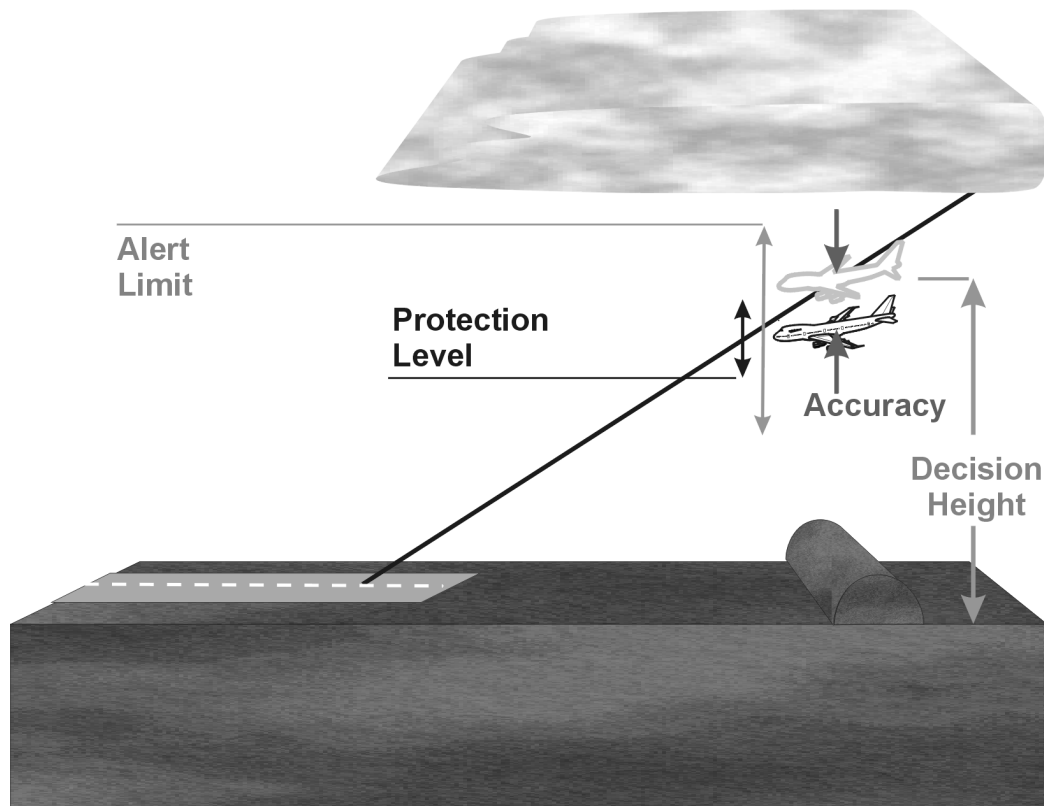


**Figure 1.16: Landing: Alert Limit, Protection Level, Decision Height and Accuracy**

Smaller errors represent better accuracy of the instruments. However, higher accuracy instruments will not always bring about better integrity; in other words, statistically lower errors will not lower the possibility of instrument errors causing a dangerous situation during landing. To ensure integrity, a bound on the position must accompany the position to establish the maximum excursion that the estimate could be from the true position.

Figure 1.16 shows an obstacle underneath the desired flight path of the aircraft. The protection level illustrates a bound on the position accuracy of the system. While the accuracy of the current position is not known by the pilot, the protection level gives an indication of the maximum variation that the position estimate can be from the reported position.

During landing, the modes of operation (e.g. Precision Approach, Non-Precision Approach, etc.) are differentiated from one another using runway visibility at the decision height and a protection threshold known as the alert limit.

If the runway is not clearly visible at the mandated decision height then a missed-approach must be executed. If the protection level (the dynamic calculation of the position error bound) exceeds the alert limit, then the missed-approach also must be executed. The calculation of the protection level for WAAS is based on multiple factors [Walter99]. These factors are:

- The broadcast bounds from the WAAS master station on the ephemeris/clock (UDRE) and the ionosphere (GIVE);
- The geometry between the airplane and the satellites tracked by the receiver;
- The tropospheric model errors;
- The multipath error; and,
- The receiver error.

This calculation is specified in Minimum Operational Performance Standards for Global Positioning System/Wide Area Augmentation System Airborne Equipment (MOPS) [RTCA159].

These factors lead to a given protection level which must be compared to the specified alert limit that is appropriate for the given approach procedure. As the protection level increases to the point where it exceeds the alert limit, the approach can no longer be conducted. This negatively impacts availability. However the protection level must be sufficiently large to cover the actual error in the solution. Therefore these factors, the protection level and the alert limit, lead to a trade-off between availability and integrity for a given approach operation type.

## Accuracy, Availability, and Integrity Triangle Chart

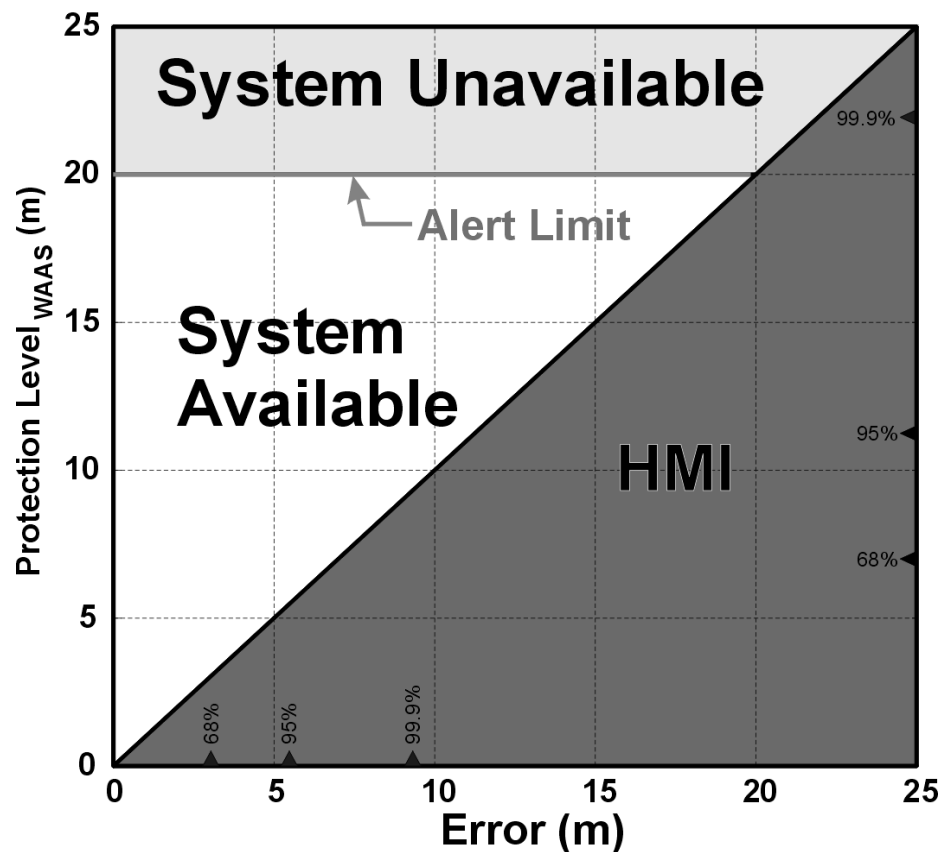


Figure 1.17: Chart to Evaluate Accuracy, Availability and Integrity

Figure 1.17 elucidates the relationship between accuracy, availability and integrity. The vertical axis shows the protection level for the user error and the horizontal axis shows the

measured user error. While in flight, the pilot cannot know the true instantaneous position error (shown on the horizontal axis) without an independent navigation system. The pilot does have access to the Protection Level (shown on the vertical axis). The protection level calculation is specified in the WAAS MOPS [RTCA159]. In the air the pilot makes the decision to proceed with an operation based on the current value of the protection level. Because we have an independent truth reference system on the ground, we can establish the relationship between the true error and the protection level with chart like Figure 1.17.

The desired operational region, marked as ‘System Available’ in Figure 1.17, indicates that the position error has not exceeded the protection level. A threshold for this operation, known as the alert limit, is set at 20 meters in this example. There are thresholds for both the vertical and horizontal dimensions. The vertical threshold is known as the Vertical Alert Limit (VAL), while the horizontal threshold is known as the Horizontal Alert Limit (HAL). There can be multiple alert limits shown on this chart. The values of the single or multiple alert limits are a function of the current flight mode.

If the current protection level exceeds the alert limit then the system cannot support that flight mode, as indicated by the ‘System Unavailable’ region in Figure 1.17. If the position error exceeds the protection level there is an integrity failure and this is marked as the ‘HMI’ region. HMI stands for Hazardously Misleading Information, and indicates that the current position error exceeds the protection level set by the WADGPS master station.

Performance of a WADGPS system can be easily confirmed when plotted in form of Figure 1.17. Figure 1.17 assumes that the position error can be independently determined or known *a-priori* (i.e., a stationary receiver at a surveyed location). Performance is verified by first checking that no epochs have violated the HMI region and second checking that the required availability is met for the current flight mode. Small triangular tick marks are placed along the horizontal and vertical axes to indicate the 68, 95 and 99.9 percent values for the errors and protection levels of the data being displayed.



## **1.10 CONTRIBUTIONS IN THIS THESIS**

This thesis will demonstrate the utility and performance of the geostationary satellite as a ranging source as well as a data link.

### **1.10.1 GEOSTATIONARY ORBIT DETERMINATION AND SATELLITE RANGING**

#### **ANALYSIS OF THE COVARIANCE DISTRIBUTION FOR A WIDE-AREA REFERENCE NETWORK**

This contribution will show the relationship between a satellite location and its covariance projection upon a user. This is critical in establishing the orbit determination accuracy required the satellite to be useful in user position computations.

#### **AUGMENTATION OF THE APPROACH USED FOR GPS EPHEMERIS ESTIMATION FOR THE MORE DIFFICULT GEOSTATIONARY PROBLEM**

In order to provide a valid ranging measurement to the user, an ephemeris solution must be developed for the geostationary satellite. Once this ephemeris is established, the geostationary satellites can be used in the same manner as the GPS satellite.

[Tsai99] showed how a kinematically smoothed orbit determination technique could be applied to GPS orbits. However, the GPS orbits nominally only vary by several meters from the broadcast ephemeris projected along the Line-of-Sight (LOS) between the satellite and the user. This helps to linearize the system. This method degrades gracefully when the ephemeris errors exceed the linear region. In fact, they cannot be corrected by the WAAS messages and therefore have to be removed from ranging consideration. This technique will be extended to handle the geostationary satellite location variation that exceeds the linear limit assumed in Tsai's work.

#### **ADAPTIVE HIGH INTEGRITY REAL-TIME ORBIT ESTIMATOR**

This dissertation presents a novel technique for generating this position estimate. This technique is designed to provide high integrity performance in the user position domain and

operates in real-time. As such, it contrasts classical orbit determination techniques that have no integrity requirement, are not designed to optimize performance in the satellite position domain, and usually have no real-time requirement. Our estimator is evaluated using real data from the FAA's National Satellite Test Bed (NSTB).

### **1.10.2 DATA LINK**

Even more important than the geostationary satellite as an additional ranging source, the satellite data link must remain in near constant contact with the user to ensure that the GPS corrections are valid and that alert conditions are received. This work will evaluate the data link under a variety of airborne operations as well as at different geographic locations.

#### **EXPERIMENTAL VERIFICATION OF THEORETICAL MESSAGE LOSS RATES**

Substantial work has been done on establishing the theoretical and simulated loss rate expected for a WAAS user [Enge97, Schnaufer]. This contribution will verify and demonstrate the theoretical message loss rates for given signal power levels by using a stationary reference receiver. Once the theoretical basis is established, the following contributions will extend the results to a variety of stationary and in flight conditions.

#### **DEMONSTRATION OF A NEW METHOD FOR THE CHARACTERIZATION OF BURST-MODE INFLUENCE ON MESSAGE LOSS**

Aircraft maneuvers, such as a bank away from a satellite, will cause message losses. Losses tend to be grouped together for multiple seconds during these maneuvers. Therefore, the loss characteristics will have a 'burst mode' behavior. Flight data will be collected and a method for modeling the losses will be developed to predict the burst nature of the dropped messages and their impact on WAAS performance.

#### **APPLICATION OF A BURST MESSAGE LOSS MODEL FROM ACTUAL AIRCRAFT DATA COLLECTION TO NSTB REFERENCE SITES**

The burst model formed from data collected during flight tests will be applied to data from stationary reference sites around CONUS to predict WAAS integrity and availability in flight for a wide geographic region.

## 1.11 THESIS OUTLINE

Chapter 2 gives the background information on orbit determination and the type of orbit propagation methods available. The discussion in Chapter 3 develops a sensitivity analysis that relates satellite position errors to errors in the user range and user position domains. Chapter 4 details the design of a geostationary orbit determination method that allows for precise user ranging. This ranging is incorporated into user position solutions to elucidate the improvements in performance with geostationary range measurements. Chapter 5 develops the background for the message loss observed for a binomial as well as a burst loss model. Chapter 6 shows the results from ground and flight tests as well as a technique for applying these loss models to an arbitrary user. Chapter 7 summarizes the results of this thesis and looks at potential future work with the geostationary satellite for WADGPS applications.



# Chapter 2

## Orbit Determination Background

The launch of Sputnik in 1958 inaugurated the “Space Age.” Over the last 40 years many artificial satellites of the Earth and even other planets have been produced. They have served many applications from military to planetary resource exploration. As previously mentioned, satellite navigation has been around almost as long. However, it is only recently that the aviation community has begun to adopt this technology. For this reason, the concepts of satellite orbits and orbit determination may not be a familiar subject to most aviation experts. This chapter is a brief introduction to the history and methods of satellite orbit determination.

### 2.1 ORBITAL MECHANICS

Some of the techniques applied today to determine the position and movement of heavenly bodies and satellites can be traced to the Greeks. These investigations date back as far as 500 BC. While Pythagoras, Oenipodes, Eudoxus, Aristotle, and Erathosthenes each made contributions to the philosophy of the scientific approach, they developed astronomical principles and were often more concerned with the search for perfection. This led them to reduce the universe into simple shapes and forms. The Greeks and their successors often put aside the confirmation of scientific and mathematical principles to observe this desired perfection [Berry]. Aristotle held that the perfect circle was the true path for heavenly

bodies. This belief held for nearly two millennia. However, between 1601 and 1606, Johann Kepler tried to correlate observations made by Tycho Brahe for the orbit of Mars with circular orbit tracks. The observations and orbits agreed within 8 minutes of arc. A less scrupulous man would have declared victory and moved on. Tycho Brahe's observations were the most accurate measurement of the positions of the stars and planets ever made. The 8 minutes of arc were in excess of the uncertainties in the data. The careful Kepler realized this and searched for a realizable orbit that was both circular and within the tolerances of measurement. No circular solution was found after years of work. He would later refer to this period as his "war with Mars." After exhausting the circular hypothesis, he struck upon the idea of an ellipse. Kepler's elliptical orbit and Brahe's observation agreed within the tolerance of the measurements. This may have been the first explicit use of the concept of observational error, although Brahe's own meticulous calibration of his instruments may have suggested this approach. From this, Kepler's first two laws of planetary motion were born (a third would follow 10 years later):

First Law	The orbit of each planet is an ellipse, with the sun at a focus
Second Law	The line joining the planet to the sun sweeps out equal areas in equal times
Third Law	The square of the period of a planet is proportional to the cube of its mean distance from the sun

**Table 2.1: Kepler's Laws of Planetary Motion**

The relationship between Kepler's mathematical description of the motion of the planets and the physical world would not be worked out for 50 years, and the results would not be published for nearly 80 years. Isaac Newton was a student at Cambridge University when it shut down in 1665 and 1666 due to an outbreak of the plague. During this break, he conceived of the physical explanation for Kepler's laws. Also in this period he established the foundations for differential and integral calculus. These were independently developed by Leibniz several years. Newton put aside his discoveries of the motion of the planets and gravity for 20 years due to differences between his calculations and observations of the moon [Bate]. However, when he did publish his work on planetary motion, it brought together and simplified many of the approaches of the day. This work resulted in Newton's three famous laws of motion:

First Law	Every body continues in its state of rest or uniform motion in a straight line unless it is compelled to change that state by forces impressed upon it
Second Law	The rate of change of momentum is proportional to the force impressed and is in the same direction of that force
Third Law	To every action there is always opposed an equal reaction

**Table 2.2: Newton's Laws of Motion**

Newton also extended these concepts with a law of gravity that stated that two bodies are attracted to one another with a force that is proportional to their masses and the inverse square of their distances. As depicted in Figure 2.1, Newton formulated the motion of mass  $m$  due to the attraction of mass  $M$  as:

$$\ddot{\mathbf{r}}_m = -\frac{GM}{r^2} \frac{\mathbf{r}_{mM}}{r} \quad (2.1)$$

Conversely, the motion of mass  $M$  due to the influence of mass  $m$  as:

$$\ddot{\mathbf{r}}_M = \frac{Gm}{r^2} \frac{\mathbf{r}_{mM}}{r} \quad (2.2)$$

In the case where  $M \gg m$ , then the motion of mass  $M$  can be considered nearly zero and we can solve for the resultant relative equation of motion:

$$\begin{aligned} \ddot{\mathbf{r}}_{mM} &= -\frac{G(M+m)}{r^3} \mathbf{r}_{mM} \\ \mathbf{r} &\equiv \mathbf{r}_{mM} \quad \text{and} \quad (M+m) \approx M \\ \ddot{\mathbf{r}} &= -\frac{GM}{r^3} \mathbf{r} \end{aligned} \quad (2.3)$$

where  $G$  is referred to as the gravitational constant. After simple substitution in Equation (2.3), the familiar equation for two-body motion results in Equation (2.4). The gravitational constant of the Earth,  $\mu$ , is defined as  $\mu \equiv GM$ . After substitution into Equation (2.3) we get:

$$\ddot{\mathbf{r}} + \frac{\mu}{r^3} \mathbf{r} = 0 \quad (2.4)$$

This is the common representation of the equation of motion for the two-body problem.

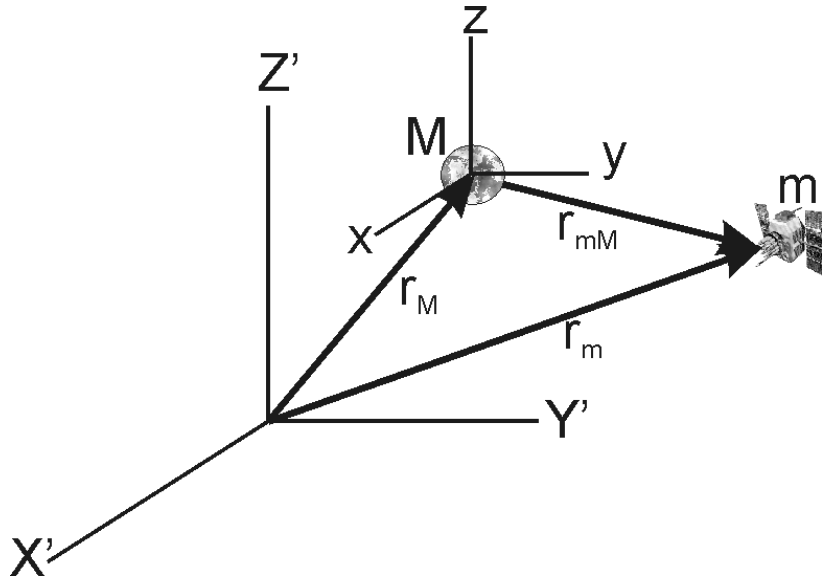


Figure 2.1: Relative Motion of Two Bodies

The next section will deal with solving this equation in a form that is useful for position propagation of a satellite. The section following will allow for an arbitrary position and velocity state vector to be propagated from the time of measurement to a future time.

## 2.2 THE TRAJECTORY EQUATION

The equation of motion, Equation (2.3), is in a reasonably simple form but the shape of an orbit is not readily apparent. There is no easy way to solve for its complete solution. However, a partial solution can yield the orbit size and shape [Bate]. The starting point is the principle of conservation of angular momentum. The angular momentum vector,  $\mathbf{h}$ , is unchanged over time if not disturbed by an external force:

$$\begin{aligned}\mathbf{h} &= \mathbf{r} \times \dot{\mathbf{r}} = \text{constant} \\ \ddot{\mathbf{r}} \times \mathbf{h} &= \frac{\mu}{r^3} \mathbf{h} \times \mathbf{r}\end{aligned}\tag{2.5}$$

Since the angular momentum of the orbit,  $\mathbf{h}$ , is constant, we can rewrite the left-hand side of Equation (2.5) as:



$$\begin{aligned}
\ddot{\mathbf{r}} \times \mathbf{h} &= \frac{d\dot{\mathbf{r}}}{dt} \times \mathbf{h} + 0 \\
&= \frac{d\dot{\mathbf{r}}}{dt} \times \mathbf{h} + \dot{\mathbf{r}} \times \frac{d\mathbf{h}}{dt} \\
&= \frac{d}{dt}(\dot{\mathbf{r}} \times \mathbf{h})
\end{aligned} \tag{2.6}$$

Rewriting the right-hand side of Equation (2.5), we get:

$$\begin{aligned}
\frac{\mu}{r^3} \mathbf{h} \times \mathbf{r} &= \frac{\mu}{r^3} (\mathbf{r} \times \dot{\mathbf{r}}) \times \mathbf{r} = \frac{\mu}{r^3} [\dot{\mathbf{r}}(\mathbf{r} \cdot \mathbf{r}) - \mathbf{r}(\mathbf{r} \cdot \dot{\mathbf{r}})] \\
&= \frac{\mu}{r} \dot{\mathbf{r}} - \frac{\mu \dot{r}}{r^2} \mathbf{r} \\
&= \mu \frac{d}{dt} \left( \frac{\mathbf{r}}{r} \right)
\end{aligned} \tag{2.7}$$

Combining both the left and right sides from Equations (2.6) and (2.7), then integrating the equation we get:

$$\dot{\mathbf{r}} \times \mathbf{h} = \mu \frac{\mathbf{r}}{r} + \mathbf{B} \tag{2.8}$$

where  $\mathbf{B}$  is a vector constant of integration. If we dot-multiply Equation (2.8) by  $\mathbf{r}$ :

$$\begin{aligned}
\mathbf{r} \cdot \dot{\mathbf{r}} \times \mathbf{h} &= \mathbf{r} \cdot \mu \frac{\mathbf{r}}{r} + \mathbf{r} \cdot \mathbf{B} \\
(\mathbf{r} \times \dot{\mathbf{r}}) \cdot \mathbf{h} &= \mu \frac{\mathbf{r} \cdot \mathbf{r}}{r} + \mathbf{r} \cdot \mathbf{B}
\end{aligned} \tag{2.9}$$

Substitute the properties:

$$\begin{aligned}
\mathbf{a} \cdot \mathbf{b} \times \mathbf{c} &= \mathbf{a} \times \mathbf{b} \cdot \mathbf{c} \\
\mathbf{a} \cdot \mathbf{a} &= a^2 \\
\mathbf{a} \cdot \mathbf{b} &= ab \cos \nu
\end{aligned} \tag{2.10}$$

where the definition of the angle  $\nu$  is shown in Figure 2.2. Combining Equations (2.9) and (2.10) yields:

$$h^2 = \mu r + r B \cos v \quad (2.11)$$

Solving for  $r$  we obtain:

$$r = \frac{h^2/\mu}{1 + (B/\mu) \cos v} \quad (2.12)$$

Define the following:

$$\begin{aligned} p &\equiv h^2/\mu \\ e &\equiv B/\mu \end{aligned} \quad (2.13)$$

Substitute these definitions into Equation (2.12) to yield:

$$r = \frac{p}{1 + e \cos v} \quad (2.14)$$

which is the equation for a conic section in polar coordinates. The type of conic section is based on the parameter  $e$ , eccentricity as indicated by Figure 2.2. The solution has both closed (repeating) and open orbits. For satellites of the Earth, which are the concern here, the conic type will be a circle or an ellipse which are closed orbits. The parabolic orbit offers a border case between open and closed orbits. For the case of the hyperbola, the orbit is open and the satellite does not have a periodic passage around the central body [Bate].

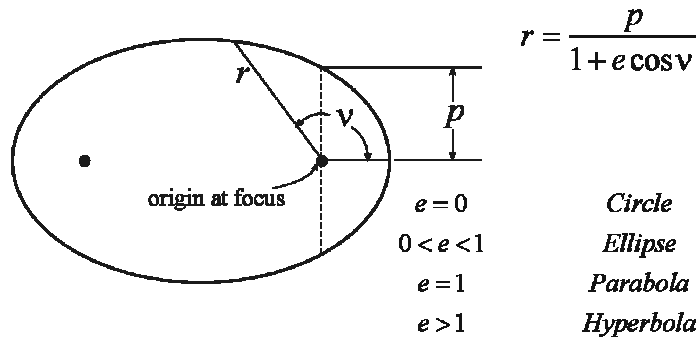


**Figure 2.2: General Equation of Any Conic Section in Polar Coordinates**

The most popular way to represent an orbit is with six parameters known as the Keplerian orbit elements. The normal vectors  $\mathbf{I}$ ,  $\mathbf{J}$ , and  $\mathbf{K}$  (see Figure 2.3) form the inertial reference frame and are defined relative to the position of the sun at vernal equinox [Seidelmann]. The vernal equinox is the time when the apparent longitude of the Sun is  $0^\circ$ .

The first of the Keplerian elements is,  $a$ , or semi-major axis, and it represents the size of the conic orbit. The next element is the eccentricity,  $e$ , which is a constant that describes the shape of the conic orbit, as indicated in Figure 2.2. The inclination,  $i$ , is the angle between the normal vector  $\mathbf{K}$  and the angular momentum vector,  $\mathbf{h}$ .  $\Omega$  is the right ascension of the ascending node and is defined as the angle between the principle axis,  $\mathbf{I}$ , and the point where the satellite crosses into the Northern Hemisphere of the orbit (ascending node). The angle in the plane of the satellite's orbit between the ascending node and the periapsis point measured in the direction of the satellite's motion is referred to as the argument of periapsis,  $\omega$ . The final element to represent the orbit system is the time of periapsis passage,  $T$ , which is the time that the satellite was at periapsis.

The following discussions are limited to the case when the orbit is circular or elliptical and has a non-zero inclination. Even these conditions can produce singularities in the Keplerian orbit set that are treated in a limited fashion by [Bate, Ceva] and more fully by [Vinti].

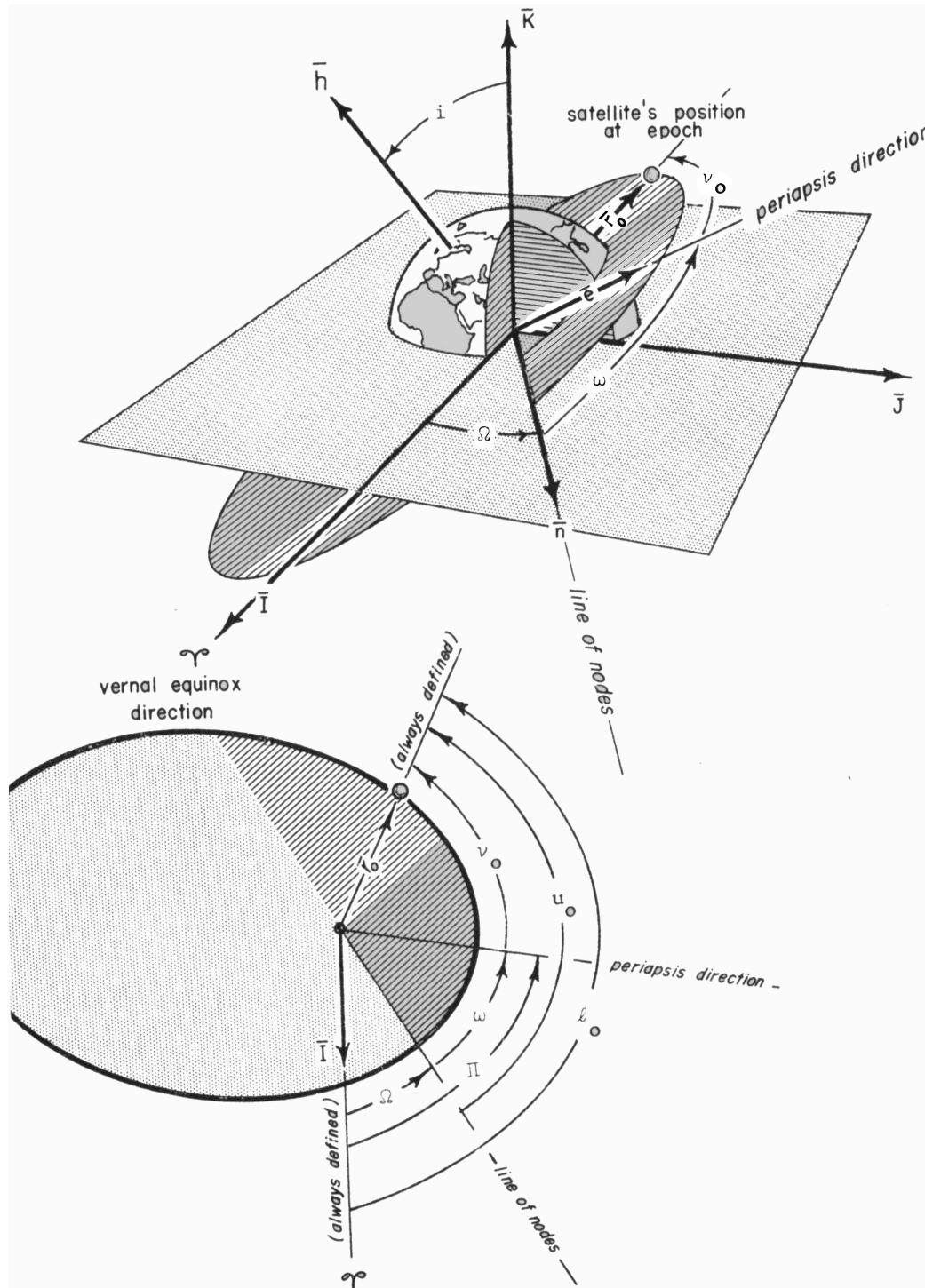


Figure 2.3: Keplerian Orbit Elements Referenced Against the Vernal Equinox [Bate]

To project the position,  $\mathbf{r}$ , to an arbitrary time,  $t$ , the first step is to use the Keplerian elements and to employ “Kepler’s Equation” as derived in [Bate]:

$$\begin{aligned}
n &\equiv \sqrt{\mu/a^3} \\
M &= n(t - T_k) = E_t - e \sin E_t
\end{aligned}
\tag{2.15}$$

where  $M$  is referred to as the mean anomaly,  $E_t$  is the eccentric anomaly, and  $T_k$  is the time of periapsis passage. This cannot be solved explicitly for  $E_t$ , so this equation is usually solved for iteratively. The next step is to utilize the eccentric anomaly to solve for the position in the plane of the orbit:

$$\begin{aligned}
v &= 2 \tan^{-1} \left( \tan \left( \frac{E_t}{2} \right) \sqrt{\frac{1+e}{1-e}} \right) \\
r &= p / (1 + e \cos(v)) \quad \text{from Eq. (2.10)} \\
p &= a(1 - e^2) \\
r &= a(1 - e^2) / (1 + e \cos(v)) \\
\mathbf{r}_0 &= \begin{bmatrix} r \cos(v) \\ r \sin(v) \\ 0 \end{bmatrix}
\end{aligned}
\tag{2.16}$$

Now rotate the planar solution into the inertial frame:

$$\begin{aligned}
\mathbf{R}_\Omega &= \begin{bmatrix} \cos \Omega & -\sin \Omega & 0 \\ \sin \Omega & \cos \Omega & 0 \\ 0 & 0 & 1 \end{bmatrix} \quad \mathbf{R}_i = \begin{bmatrix} 1 & 0 & 0 \\ 0 & \cos i & -\sin i \\ 0 & \sin i & \cos i \end{bmatrix} \quad \mathbf{R}_\omega = \begin{bmatrix} \cos \omega & -\sin \omega & 0 \\ \sin \omega & \cos \omega & 0 \\ 0 & 0 & 1 \end{bmatrix} \\
\mathbf{r} &= [\mathbf{R}_\Omega][\mathbf{R}_i][\mathbf{R}_\omega]\mathbf{r}_0
\end{aligned}
\tag{2.17}$$

This now allows the calculation of the position vector,  $\mathbf{r}$ , from the Keplerian elements. The following section will show how to reverse the process and compute the elements from a known orbital position and velocity.

### 2.3 DETERMINING THE ORBITAL ELEMENTS

In many cases, the current position,  $\mathbf{r}$ , and velocity,  $\dot{\mathbf{r}}$ , are available at a given time and the Keplerian elements are needed for propagation to a future time. In order to perform the propagation, the Keplerian elements need to be determined. These can be solved for using manipulations of the three basic vectors of the system,  $\mathbf{h}$ ,  $\mathbf{n}$ , and  $\mathbf{e}$ , presented in Figure 2.3. The first of these vectors, the angular momentum vector,  $\mathbf{h}$ , is defined in Equation (2.5). The vector  $\mathbf{n}$  is defined as the cross product between  $\mathbf{h}$  and the reference frame vector  $\mathbf{K}$ .

$$\mathbf{n} \equiv \mathbf{K} \times \mathbf{h} \quad (2.18)$$

The eccentricity vector,  $\mathbf{e}$ , can be solved from the constant vector of integration,  $\mathbf{B}$ , from Equation (2.8):

$$\begin{aligned} \mathbf{B} &= \dot{\mathbf{r}} \times \mathbf{h} - \mu \frac{\mathbf{r}}{r} \\ \mathbf{e} &= \frac{\dot{\mathbf{r}} \times \mathbf{h}}{\mu} - \frac{\mathbf{r}}{r} \\ \mathbf{h} &\equiv \mathbf{r} \times \dot{\mathbf{r}} \\ \mu \mathbf{e} &= \dot{\mathbf{r}} \times (\mathbf{r} \times \dot{\mathbf{r}}) - \mu \frac{\mathbf{r}}{r} \end{aligned} \quad (2.19)$$

By expanding the vector triple product we get:

$$\begin{aligned} \mu \mathbf{e} &= (\dot{\mathbf{r}} \cdot \dot{\mathbf{r}}) \mathbf{r} - (\mathbf{r} \cdot \dot{\mathbf{r}}) \dot{\mathbf{r}} - \mu \frac{\mathbf{r}}{r} \\ \mu \mathbf{e} &= \left( \dot{r}^2 - \frac{\mu}{r} \right) \mathbf{r} - (\mathbf{r} \cdot \dot{\mathbf{r}}) \dot{\mathbf{r}} \end{aligned} \quad (2.20)$$

The semi-major axis can be derived from Equations (2.5), (2.14), and (2.16) as:

$$a = \frac{h^2}{\mu(1 - e^2)} \quad (2.21)$$

From Equation (2.20) the eccentricity is derived:

$$e = |\mathbf{e}| \quad (2.22)$$

Given that  $i$  is the angle between  $\mathbf{K}$  and  $\mathbf{h}$ :

$$\cos i = \frac{\mathbf{h} \cdot \hat{\mathbf{K}}}{h} \quad (2.23)$$

Since  $\Omega$  is the angle between  $\mathbf{I}$  and  $\mathbf{n}$ :

$$\cos \Omega = \frac{\mathbf{n} \cdot \hat{\mathbf{I}}}{n} \quad (2.24)$$

The angle between the vectors  $\mathbf{e}$  and  $\mathbf{n}$  is  $\omega$  which can be found from:

$$\cos \omega = \frac{\mathbf{n} \cdot \mathbf{e}}{ne} \quad (2.25)$$

To find the time of periapsis passage,  $T$ , it is first necessary to solve for the angle  $\nu$ , which is the angle between  $\mathbf{e}$  and  $\mathbf{r}$ :

$$\cos \nu = \frac{\mathbf{e} \cdot \mathbf{r}}{er} \quad (2.26)$$

Finally, we can find the time of periapsis passage by combining the results from Equation (2.26) and Kepler's Equation (2.15):

$$\begin{aligned} n &\equiv \sqrt{\mu/a^3} \\ M &= n(t - T_k) = E_t - e \sin E_t \\ \cos E_t &= \frac{e + \cos \nu}{1 + e \cos \nu} \\ T_k &= t - \frac{E_t - e \sin E_t}{n} \end{aligned} \quad (2.27)$$

Section 2.2 formulated a propagation using Keplerian parameters that describe a conic section. This section described how to formulate the Keplerian elements from a given position and velocity at a given time. The following sections will examine the usage of propagation techniques and outline the most popular methods.

## 2.4 ORBIT PROPAGATION TECHNIQUES

The techniques presented in Sections 2.1, 2.2 and 2.3 apply where the attracting body is a point mass or a perfect homogeneous sphere. Precise orbit determination requires taking into account small perturbations in the orbit due to force deviations from this idealization. The following sections will outline different methods for dealing with these perturbations.

### 2.4.1 KEPLERIAN PROPAGATION

Section 2.2 showed how the two-body problem could be solved in a simplified form to yield a set of Keplerian parameters that generates a position solution over time. The form of this propagation method is:

$$\begin{aligned}\bar{\mathbf{r}}(t) &= f(a, e, i, \omega, \Omega, T_k, t) \\ \bar{\mathbf{r}}(t) &= \begin{bmatrix} r_x(t) & r_y(t) & r_z(t) & \dot{r}_x(t) & \dot{r}_y(t) & \dot{r}_z(t) \end{bmatrix}\end{aligned}\tag{2.28}$$

Given parameters at any specific time, a position vector can be found for any other point in time. The procedure examined in Section 2.3 allows one to solve for the parameters given an initial state vector. Later sections will deal with the solution for the initial estimate that will be propagated.

This technique diverges from the true path of the satellite over time, even with perfect knowledge of the parameters at initialization. This divergence is due to the influence of perturbing forces on the satellite that were not taken into account in the solution of the equation of motion that resulted in the Keplerian parameters. These forces include Earth gravity deviations from the perfect sphere, other gravitational sources such as the Sun and the Moon, and to a lesser extent other planets. Drag of the satellite as it passes through the extremely thin upper atmosphere and the interplanetary medium is another source of



deviation from perfect Keplerian motion. Also included in the perturbations are pressure terms due to solar wind and light reflecting off of the Earth. The most significant disturbing force is caused by the fact that the Earth is not a homogeneous sphere, and therefore has spatial variations of the gravitational potential over its surface. These forces are the largest factor in causing the propagated position to depart from the true position over time.

A great deal of work has gone into extending the simplicity of the Keplerian system to include these perturbation influences. The earliest known method for calculating the variations of the Keplerian parameters due to perturbations were developed by Euler in 1748. A description of this method is given in [Bate].

Variation of parameters is an approach to determine how the parameter sets change over time, whether they are the classical Keplerian elements or another equivalent set [Baker]. This is achieved by determining the time-rate of change of the parameters in terms of the perturbations. These rates can be numerically or analytically integrated to solve for position over time. Methods that employ analytical integration of the equations of motion are referred to as ‘general perturbations.’ [Battin] and [Vinti98] give detailed information on general perturbation methods. General perturbation methods offer a very precise solution for a modeled disturbance. However, in many cases an analytical solution does not exist for an exact model and simplifications must be made to enable the solution [Rosborough]. As a result, no general perturbation method has yet been synthesized that takes into account all perturbation forces. Section 2.4.4 outlines one of the most advanced general perturbation methods that has been developed to date.

Another approach to incorporating the perturbing forces is to explicitly model all of the forces acting on a body. Analytical solutions exist only for a limited set of circumstances which do not include general forces or functions. Since an analytical solution is not possible for such a general case, numerical integration is always involved. Methods that apply direct numerical integration are referred to as ‘special perturbations.’ The advantage of special perturbation solutions is that forces and functions of unlimited complexity, and non-linearity, can usually be incorporated. A major disadvantage of these methods is the

computational efficiency, where numerical integration generally requires higher computational loads compared to analytically integrated solutions. In addition, the code size tends to be large in comparison to general perturbation methods. The following section gives an overview of the integrated methods, with an example system that employs very detailed models to determine the orbits of the GPS satellites.

### 2.4.2 INTEGRATED PROPAGATION

One of the most used formulations of special perturbations (numerically integrated) is Cowell's Method. This was developed early in the 20<sup>th</sup> century and first applied to the orbit of Jupiter's moon Pasiphae. For the two-body problem presented in Equation (2.4) the perturbations are added as follows:

$$\ddot{\mathbf{r}} + \frac{\mu}{r^3} \mathbf{r} = \mathbf{F}(\mathbf{r}, \dot{\mathbf{r}}, t) \quad (2.29)$$

where  $\mathbf{F}$  is a function that describes the perturbations as a function of satellite position, velocity, and time. Figure 2.4 depicts some of the perturbing forces that can be modeled by the functional form in Equation (2.29). In order to formulate a step-by-step integration scheme by Cowell's Method we have:

$$\begin{aligned} \dot{\mathbf{r}} &\equiv \mathbf{v} \\ \dot{\mathbf{v}} &= -\frac{\mu}{r^3} \mathbf{r} + \mathbf{F}(\mathbf{r}, \mathbf{v}, t) \end{aligned} \quad (2.30)$$

and:

$$\begin{aligned} \mathbf{r}(t_0 + \Delta t) &= \mathbf{r}(t_0) + \left[ \frac{d\mathbf{r}}{dt} \right]_{t_0} \Delta t \\ \mathbf{v}(t_0 + \Delta t) &= \mathbf{v}(t_0) + \left[ \frac{d\mathbf{v}}{dt} \right]_{t_0} \Delta t \end{aligned} \quad (2.31)$$

The values of  $\mathbf{r}(t_0)$  and  $\left[\frac{d\mathbf{r}}{dt}\right]_{t_0}$  are given as initial conditions and the terms,  $\mathbf{v}(t_0)$  and

$\left[\frac{d\mathbf{v}}{dt}\right]_{t_0}$  can be obtained from Equation (2.30).

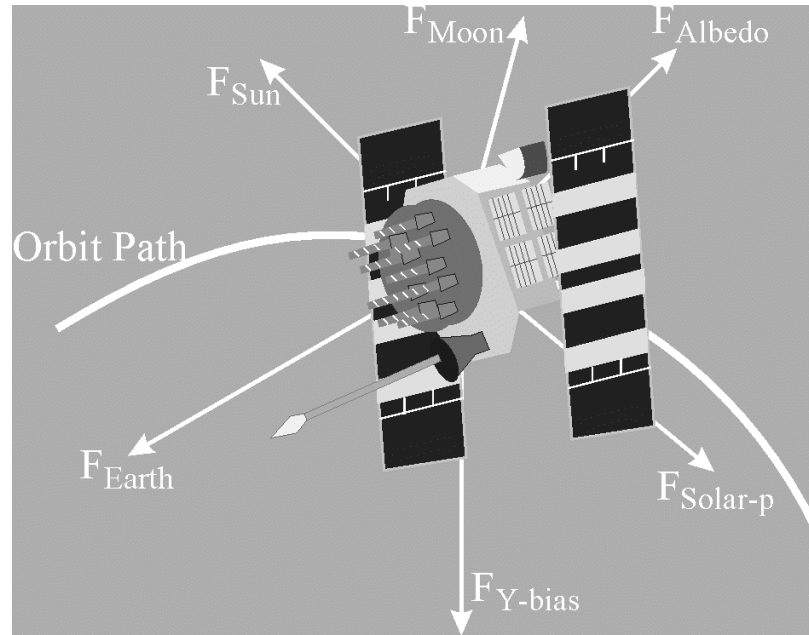


**Figure 2.4: Forces Acting on a GPS satellite**

A related numerically integrated technique is called Enke's Method which integrates the difference between the primary acceleration and the perturbing accelerations. This method is fully described in [Battin, Bate].

The International GPS Service (IGS) provides precise orbit and clock solutions for GPS satellites based on numerically integrated methods. The IGS utilizes a network of GPS reference stations that currently number 200 (Figure 2.5). [Zumberge, Davis, Ceva] report that the precision of the orbit solutions can reach 10 cm by utilizing measurements from the IGS worldwide network.

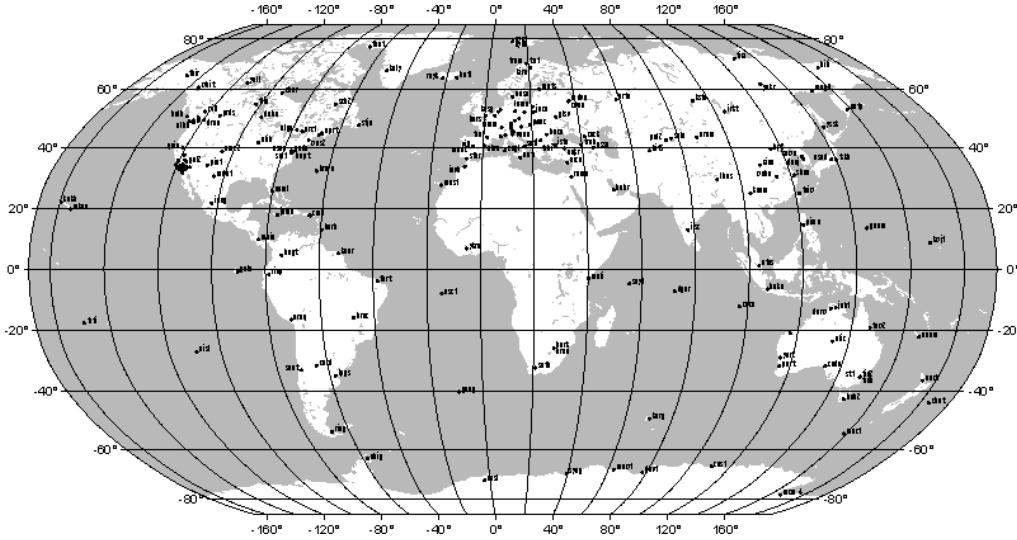


**Figure 2.5: IGS GPS Reference Station Locations**

While the performance is impressive, the code used to produce the results, GPS-Inferred Positioning System (GIPSY), has in excess of 50,000 lines of code [Yunck, Pogorelc97a]. While this code is not huge by modern computational or storage standards, it is a formidable task to certify a codeset of this size to flight-safety standards. The advantages of analytically integrated techniques (Sections 2.4.1 and 2.4.4) are that they employ much smaller codesets and are not nearly as sensitive to numerical errors in the computation. Numerically integrated techniques have superior precision, as evidenced by the IGS performance, but must have extensive coding to implement the most accurate models.

### 2.4.3 KINEMATIC PROPAGATION

The simplest model for the propagation of a position vector is to use the instantaneous velocity to extrapolate the position over time. This is actually just a simplified form of numerically integrated solution that employs a simple kinematic model of the orbit motion. [Tsai99] synthesized a kinematic propagator as part of a solution for small variations between the true GPS satellite positions and those broadcast by the MCS. The form of Tsai's propagator is:

$$\mathbf{X}(k+1) = \Phi\mathbf{X}(k) + \Gamma\mathbf{w}_d(k) \quad (2.29)$$

where  $T$  is the sampling interval and  $\mathbf{w}_d$  is the discrete process noise and:

$$\begin{aligned}\Phi &= \begin{bmatrix} 1 & 0 & 0 & T & 0 & 0 \\ 0 & 1 & 0 & 0 & T & 0 \\ 0 & 0 & 1 & 0 & 0 & T \\ 0 & 0 & 0 & 1 & 0 & 0 \\ 0 & 0 & 0 & 0 & 1 & 0 \\ 0 & 0 & 0 & 0 & 0 & 1 \end{bmatrix} \\ \Gamma &= \mathbf{I} \\ \mathbf{X} &= [\Delta X^k \quad \Delta Y^k \quad \Delta Z^k \quad \Delta \dot{X}^k \quad \Delta \dot{Y}^k \quad \Delta \dot{Z}^k]^T\end{aligned}\tag{2.30}$$

The state vector  $\mathbf{X}$  is made up of the small differences between the current orbit estimate and the broadcast ephemeris. These perturbation values are typically very small versus the satellite position components. Figure 2.6 shows the perturbations for GPS Satellite Vehicle 31 (SV31) over 24 hours on July 27, 1997. These results were obtained by comparing the ephemeris solution broadcast by the MCS over the satellite signal to the one obtained by the IGS. As presented previously, the precision of the IGS orbit estimates are on the order of 10 cm, which places the variation of the MCS estimates on the order of a few meters. A longer period of comparison was explored in [Dai99] where the 3D RMS position error was less than 5 meters. It appears that these errors are likely due to residual errors in the estimation process of the MCS and not due to intentional corruption due to SA [Parkinson96, Chap. 16].

Tsai's estimation process, as depicted in Figure 2.7, contains a Kalman filter that makes successive estimates of the state vector  $\mathbf{X}$ . Since the errors in the MCS orbits are usually small, the filter was designed for a narrow linear region for the state vector  $\mathbf{X}$  with a correspondingly small *a-priori* covariance matrix. As the WAAS MOPS [RTCA159] is only capable of sending corrections for the GPS satellite position of  $\pm 128$  meters, this narrow region of applicability is not an issue. The narrow linear region of the kinematic filter is complementary to the WAAS MOPS requirements since any large broadcast position errors that would cause filter non-linearities to be a problem would be too large for broadcast in a WAAS message.

## Error in Ephemeris for GPS SV31 on July 27, 1997

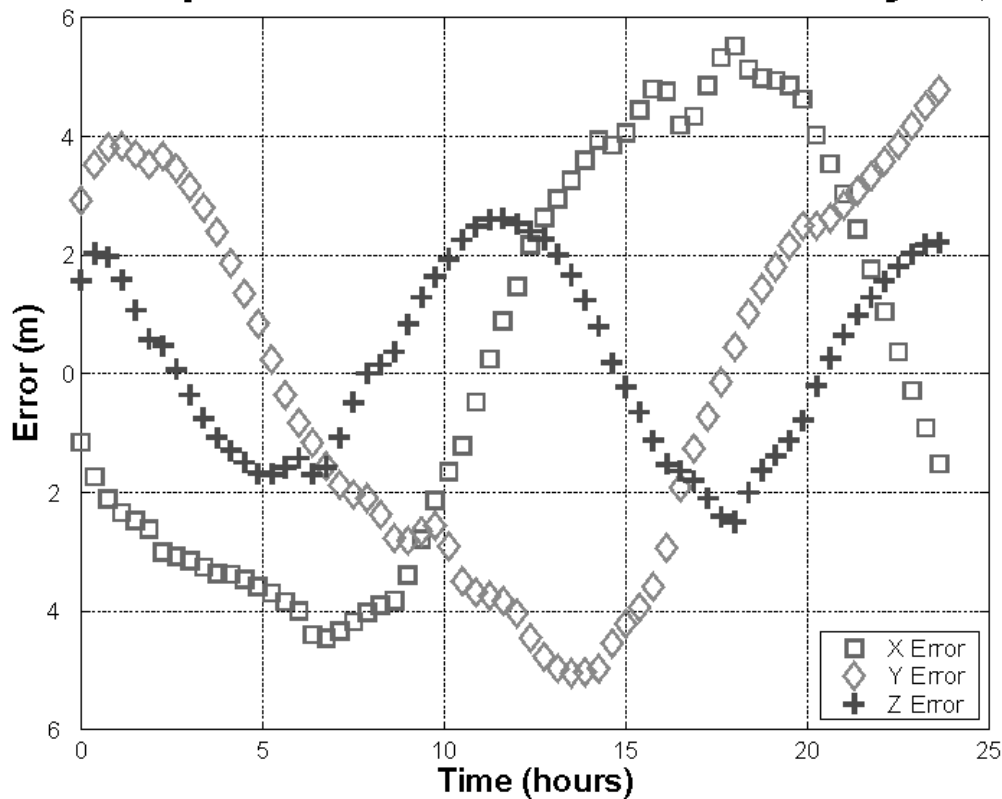


Figure 2.6: Typical Satellite Position Errors of Precise Orbit Position Versus the Broadcast Ephemeris from the MCS

### GPS Satellite Position Estimation Process (Tsai)

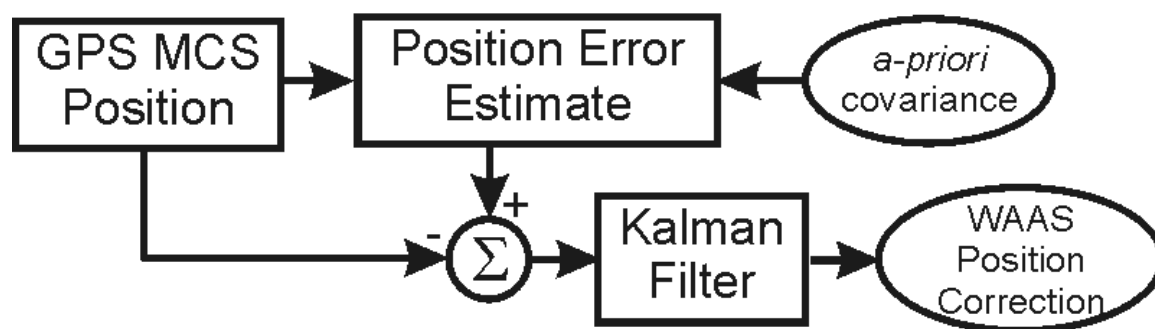


Figure 2.7: Satellite Position Error Estimation Process (Tsai)

#### 2.4.4 VINTI PROPAGATION

Vinti propagation is another analytically integrated technique which is related to the Keplerian propagation method. As noted, Kepler and Newton provided the simplest analytic solution for the unperturbed problem. These equations are reduced to a single homogeneous second-order ordinary differential equation in vector format, from Equation (2.4). [Brouwer] performed successive canonical transformations and analytic term-by-term integration using the von Zeipel averaging technique. A Brouwer method often encounters numerical difficulties in the neighborhood of the singularities of zero eccentricity, zero inclination, or critical inclination.

[Vinti98] formulated the equations of motion with the oblate spheroidal coordinate system. Since the primary perturbing forces on a satellite are due to the gravitational variation of the spheroidal shape of the Earth, an accurate model for this disturbance is critical [Colombo, Rosborough]. By using a spheroidal coordinate system, Vinti was able to take advantage of separation of variables to solve analytically the Hamilton-Jacobi partial differential equations while simultaneously satisfying the Laplace equation as discussed in [Vinti98, Chapter 8]. Even though Vinti's method includes only the second, third and about 70% of the fourth-order zonal gravitational harmonics [Kaula] in the perturbed accelerations, his method is computationally efficient in both numerical complexity and accuracy.

Figure 2.8 represents the relative accuracy of the numerically integrated propagation and Vinti propagation in comparison to Keplerian propagation. Further details on Vinti's method are given in [Vinti98, Chapter 8].

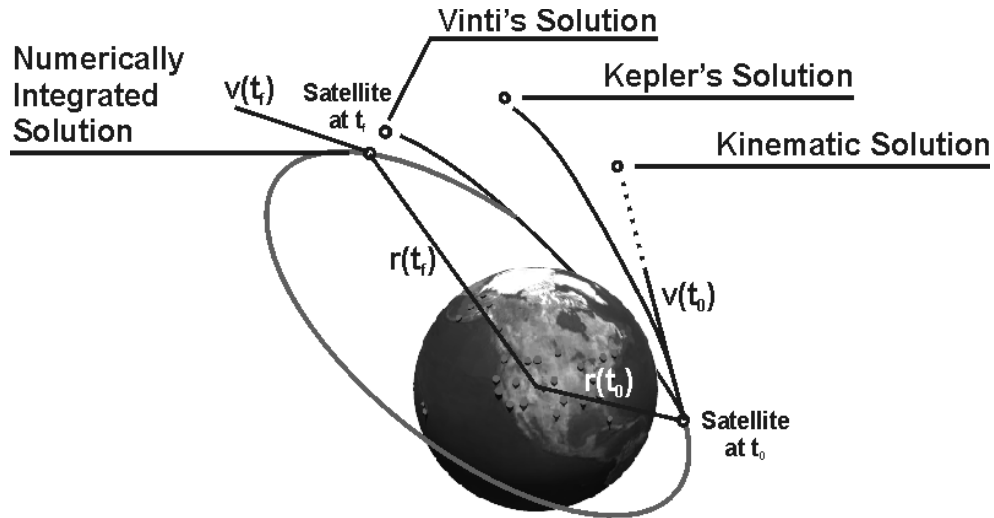


Figure 2.8: Representation of the Different Solution Methods

#### 2.4.5 ERROR GROWTH FOR DIFFERENT METHODS

Figure 2.9 shows typical error growth calculated with the different propagation methods discussed in this chapter. The orbital data from Figure 2.6 was used as a reference trajectory. Initial conditions from this data were propagated with kinematic, Keplerian, and Vinti methods. The kinematic propagation method performed relatively poorly because the divergence was calculated from the total position, not the divergence of the residual position of Equation (2.30). The total position error was used for comparison in this case in anticipation of the application of these methods to geostationary Earth orbit (GEO) determination where a meter-level precision broadcast orbit will not be available. For the Kepler and Vinti methods, the performance is nearly the same up to 10 seconds in duration. After 10 seconds, the performance of the Keplerian method diverges faster than the Vinti method. After 10,000 seconds (2.8 hours), the Vinti method is 10 times more accurate.



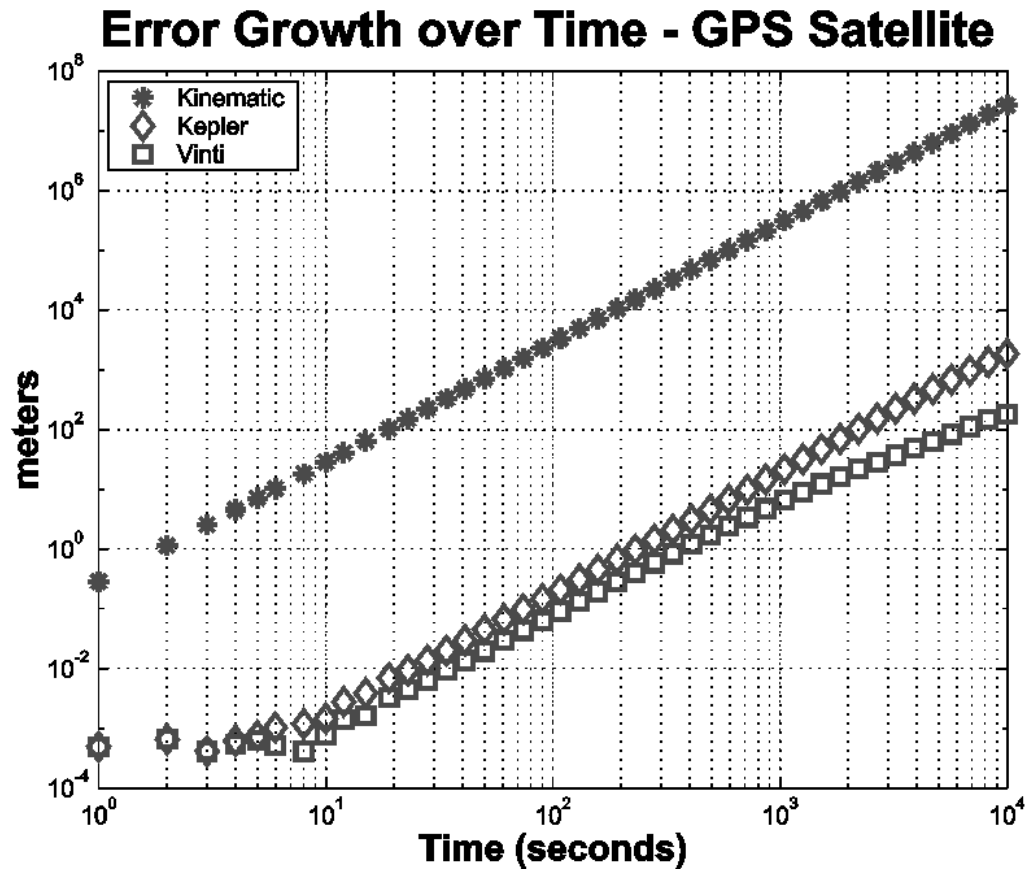


Figure 2.9: Divergence of Different Propagation Methods Versus the IGS Reference

## 2.5 ORBIT TYPES

Many types of orbits exist for different applications (Figure 2.10). Low-Earth Orbits (LEO) are designed for ease of launch and lower power since less broadcast signal strength is required to get a message to and from such a close satellite. At a higher altitude, Medium-Earth Orbit, MEO, is used to get better coverage of the Earth from the satellite's vantage-point. The major advantage of a geostationary orbit (GEO) is that it remains fixed relative to a point on the Earth. This is due to the fact that the GEO orbital period is specified to be exactly matched to the rotation of the Earth and have zero inclination angle.

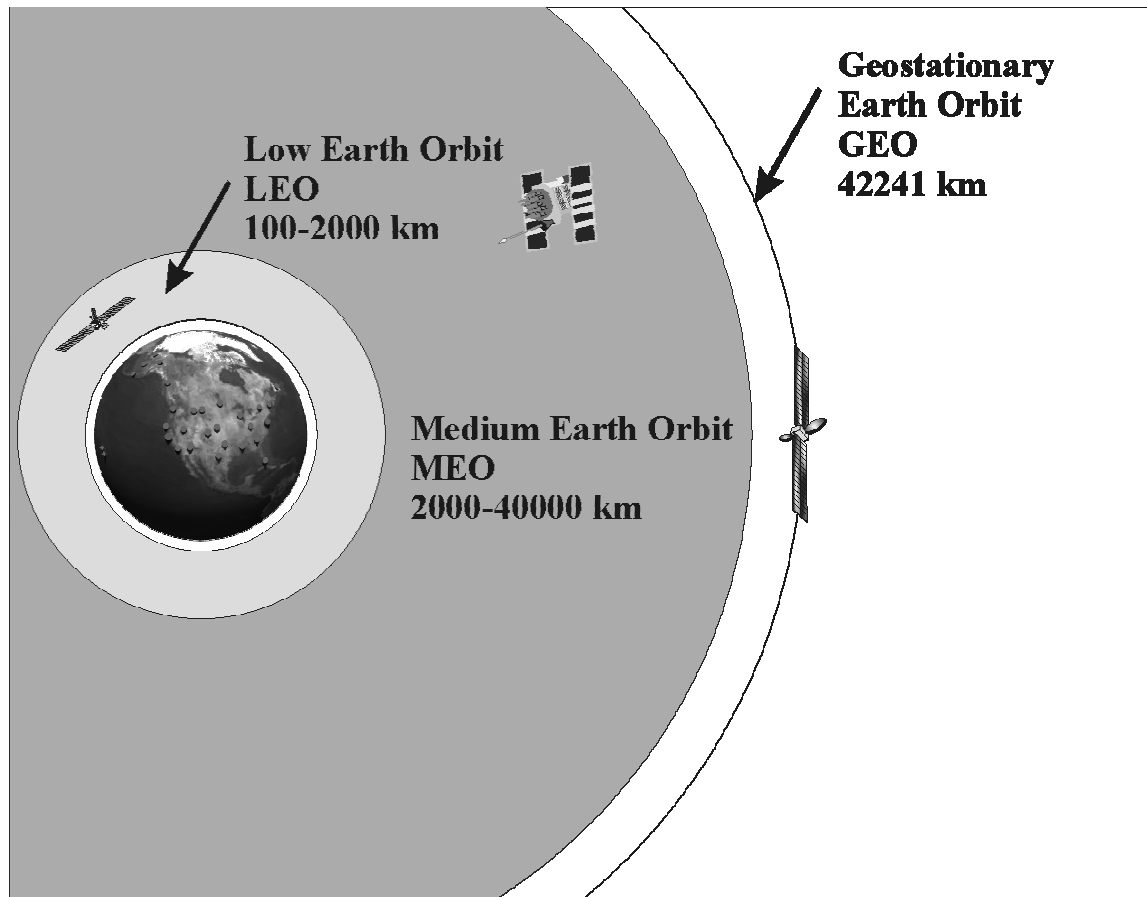


Figure 2.10: Orbit Types

### 2.5.1 GPS ORBIT

As stated in Chapter 1, the GPS constellation is comprised of at least 24 satellites arranged in six orbital planes spaced evenly in right ascension. The GPS satellites' orbits are classified as MEO. MEO orbits, as compared to LEO, trade higher altitude and a larger coverage region, against extra power required to broadcast the signal. The MEO design allows for far fewer GPS satellite vehicles (SVs) as compared to a LEO constellation. This is critical when considering the fact that at least four SVs are required to be in view of a user receiver to solve for instantaneous position and receiver clock. As the signal power requirements for the receiver are relatively low at  $-161$  dB-Watts [ICD200C], the added altitude could be afforded with a reasonable power budget [Parkinson96, Wertz]. The satellites have the following nominal orbital parameters:

Element	Value
Semi-major axis	26,600 km
Inclination	55°
Eccentricity	< 0.01
Right ascension of the ascending node	See Table 1.1
Argument of perigee Time of perigee passage	Poorly Defined

**Table 2.3: GPS Orbital Elements**

As indicated in Table 2.3, the argument of perigee and time of perigee passage are poorly defined because orbits with very small or non-existent eccentricities do not have a well defined perigee. Perfectly circular orbits ( $e=0$ ) do not have a perigee or an apogee.

### 2.5.2 GEOSTATIONARY ORBIT

The most advantageous attribute of a geostationary satellite is the fact that it remains at near-constant location relative to a fixed point on the surface of the Earth. This is achieved by placing the satellite above the equator with zero inclination and eccentricity (circular) as well as a semi-major axis that has the period of the orbit exactly synchronous with that of the rotation of the Earth. Typical geostationary orbital parameters are given in Table 2.4.

Element	Value
Semi-major axis	42,200 km
Inclination	< 0.1°
Eccentricity	< 0.01
Right ascension of the ascending node Argument of perigee Time of perigee passage	Undefined

**Table 2.4: Geostationary (GEO) Orbital Elements**

Table 2.4 indicates that the right ascension of the ascending node, the argument of perigee and the time of perigee passage are undefined. With zero inclination the satellite does not

have an ascending node and therefore its right ascension is not defined. As mentioned, an orbit with zero eccentricity has no defined perigee or apogee. As a result, the argument of perigee and time of perigee pass are undefined.

While the geostationary satellite may remain near a fixed position in the sky, it is not truly stationary. Slight disturbances such as those discussed in Section 2.4 produce small variations of the orbital elements. These cause the inclination and eccentricity to wander from zero. Figure 2.11 shows the influence for non-zero inclination and eccentricity parameters on a geostationary orbit. The control scheme for geostationary orbits usually tries to place a satellite within a latitude/longitude box of approximately 0.1 degrees on a side around the desired nominal location. This corresponds to a relative position variation of over 50-km from the desired satellite position.

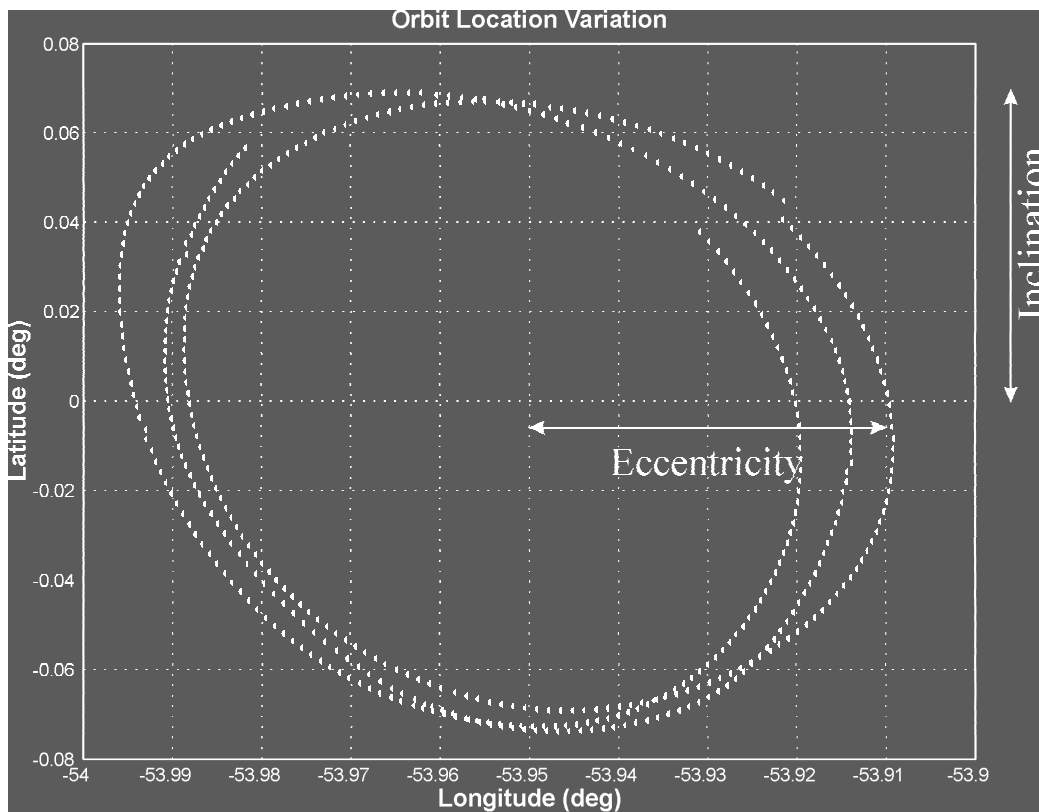


**Figure 2.11: Influence of Slight Eccentricity and Inclination Errors On A Geostationary Satellite Position**

Over time, the perturbations cause the variation of the position from the desired point to grow. This necessitates occasional orbit maneuvers to keep the satellite within the design limits [Wertz].

## 2.6 MEASUREMENT PROCESSING FOR ORBIT DETERMINATION

Three major types of orbit determination techniques are presented here: 1) analytically integrated (general perturbations); 2) numerically integrated (special perturbations), and 3) kinematic, which is a sub-class of numerically integrated. For further discussion on the variety and complexity of the methods available see [Battin, Bate, Ceva].

Section 2.4.4 and [Vinti98, Chapter 8] provide the foundations for an analytically integrated approach. The process starts with an estimate of the position and velocity at a given time. Next propagate this solution forward in time using the technique presented in Section 2.4. Once a new position is estimated, it can be compared to a computed value for the satellite and the estimate-propagate cycle can be continued. The following chapter outlines the application of a filter for geostationary orbit determination based on this method. This method is strongly dependent on the input measurement accuracy and sampling. Observation geometry plays a major role in the overall accuracy of an analytically integrated method. This is due to the fact that precise model knowledge is not available, making measurement accuracy extremely important. With good geometry and very precise measurements, satellite orbit determination with precision less than 10 m is certainly achievable in real-time.

Numerically integrated methods utilize detailed knowledge of the forces acting on the satellite. The discussion in Section 2.2 developed the two-body model assuming that all forces on the satellite are from a main body that is a homogeneous sphere. In actuality, there are many forces acting on a satellite. These forces act to ‘perturb’ the satellite from the simple Keplerian/Newtonian prediction of the orbit. These forces can cause the position uncertainty for both the kinematic and analytic approaches to grow rapidly in the absence of measurements. With extremely precise knowledge of the forces acting on the satellite, it is possible to predict the position of a satellite many hours or even days in

advance without measurement update [Vinti]. The disadvantage of the dynamic method is the complexity of the solution. This method often requires very detailed numerical integration along with complicated potential models for forces to be carried out by a computer. The best methods available can create orbit solutions with a precision of roughly 10 cm.

The kinematic method is very similar to the numerically integrated method except that it uses a simple linear model for the orbit propagation (usually just the slope and bias). This method is discussed in detail in [Tsai99]. Like analytically integrated methods, these solutions are highly dependent on the type and accuracy of the input measurements. However, in a GPS-based system they can be better than 10 m.

### **2.6.1 SATELLITE RANGING**

The primary means of determining position and velocity for the majority of satellites in orbit today employs radar ranging and range rate data. Many times, the radar data is coupled with optical or laser sensors to get the most accurate data [Bate]. Until the late 1980s, ground based measurements for satellite ranging were noisy and sparse. This led to the adoption of batch-filtering techniques for precise orbit determination [Davis]. The continuing development of GPS in the 1980s led to new techniques employing numerically integrated methods and sequential filtering.

Installations located on the surface of the Earth can measure the position and velocity of a satellite relative to the radar site (Figure 2.12). However, the radar site is not located at the center of the Earth, so the position vector measured is not the  $\rho$  that is required.

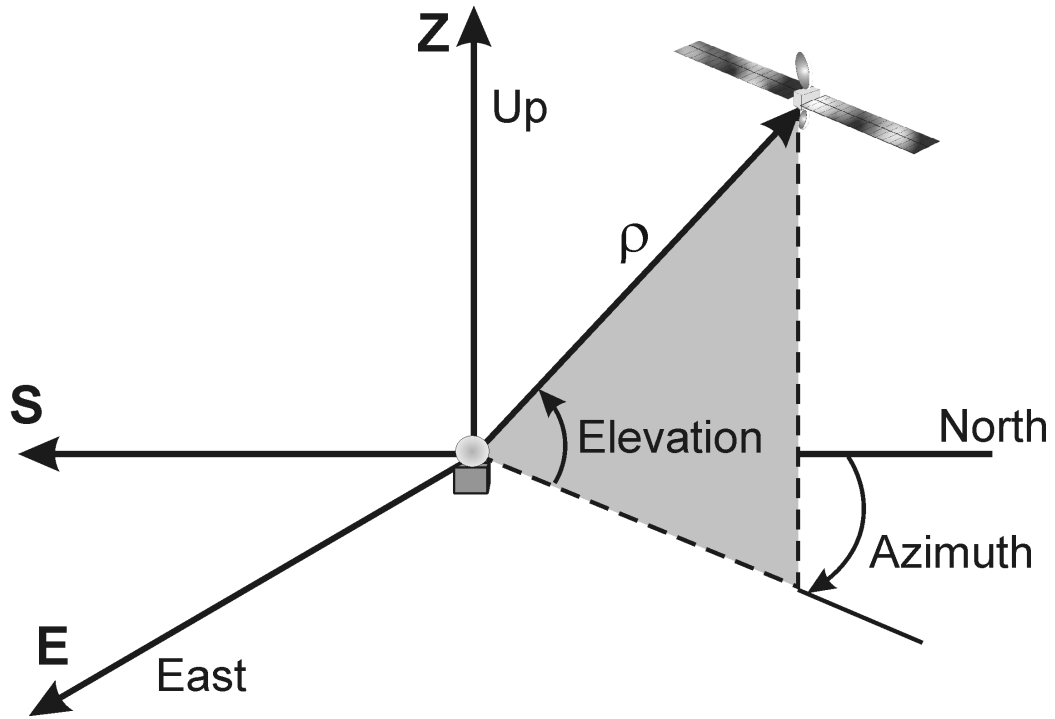


Figure 2.12: Satellite Tracking Configuration and Coordinate System

The radar makes its measurements in the topocentric-horizon coordinate system as shown in Figure 2.12. The origin of the topocentric-horizon system is the point on the surface of the Earth (called the “topos”) where the radar is located. The fundamental plane is the horizon and the **S**-axis points south. The **E**-axis is east and the **Z**-axis points up towards the zenith of the sky. The radar records the range and range rate as well as the azimuth and elevation to the satellite in this **SEZ** frame. Additionally it records the local **SEZ** elevation and azimuth angles. The following relationships can then be established:

$$\begin{aligned}
 \rho_S &= -\rho \cos(Elevation) \cos(Azimuth) \\
 \rho_E &= \rho \cos(Elevation) \sin(Azimuth) \\
 \rho_Z &= \rho \sin(Elevation)
 \end{aligned}
 \tag{2.31}$$

Since the position of the radar station is known (from a survey or another method), then the position of the satellite can be determined.

A similar expression for velocity determination from the range-rate is developed in [Bate], which takes into account the rotation of the Earth as well as Coriolis acceleration.

With an estimate of the position and velocity, the methods discussed in the previous sections can be applied to propagate the position and velocity forward in time. While this method is very robust, the measurements are particularly noisy and require dedicated and expensive ground equipment properly placed in the satellite ground track.

### 2.6.2 “SNAPSHOT” SOLUTION

The snapshot solution is an extension of the satellite ranging concept where a single station adds measurements to an orbit estimation process. As represented in Figure 2.13, the snapshot approach uses multiple parallel measurements to make the instantaneous estimate of the satellite position [Tsai99].

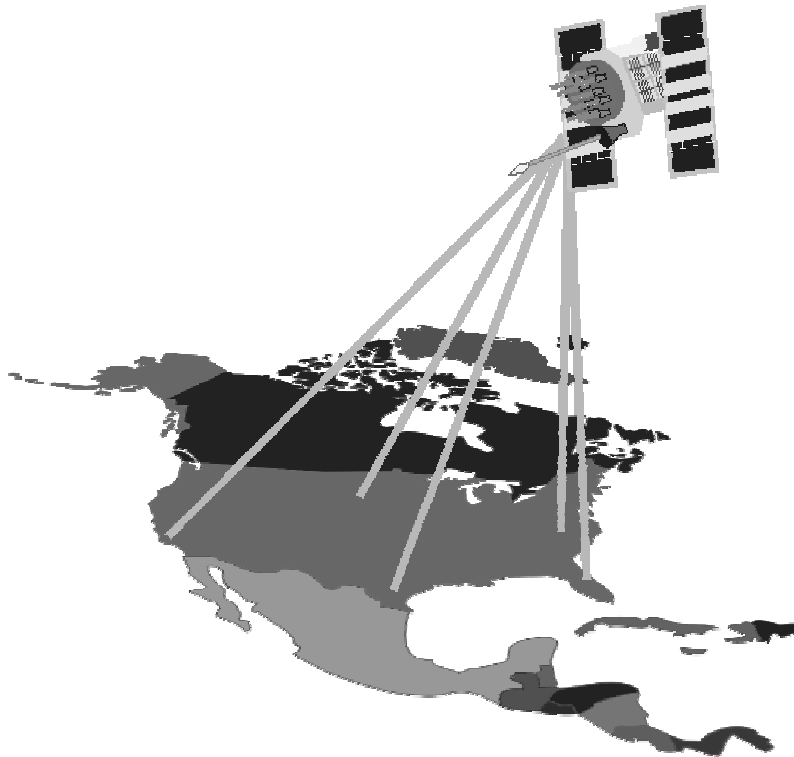


**Figure 2.13: Instantaneous “Snapshot” of Position Formed from Multiple Simultaneous Measurements**



This technique usually employs a range and a range-rate for the satellite position determination. The azimuth and elevation are not necessary for the solution. The method is, in essence, an “inverse-GPS” solution where the satellite position becomes the unknown and the reference station locations are very well known. This method will be further explored in Chapter 4.



# **Chapter 3**

## **Influence of Orbit Determination Techniques on WAAS User Performance**

The previous chapter introduced the orbit determination problem and outlined different approaches to solve that problem. This chapter looks at the influence of three of orbit determination techniques on user position error.

This development starts by reviewing the techniques of orbit determination. Three examples of orbit determination techniques are used to derive user position solutions from the Stanford University Testbed Master Station (TMS). The results from the three techniques are compared for their overall accuracy in the user position domain. They show that while different techniques have widely different orbit determination accuracy the resultant user position domain solutions are very similar. This highlights the point that high accuracy and integrity for the user domain position solution is not determined by accurate satellite ephemeris estimation.

The chapter concludes with the development of a sensitivity analysis to show the influence of the satellite ephemeris estimate covariance on the aircraft user range accuracy.

### 3.1 THREE PROPAGATION METHODS: NUMERICALLY INTEGRATED, ANALYTICALLY INTEGRATED AND KINEMATIC

The orbit estimation process takes individual estimates of a satellite position (from any source that produces a XYZ inertial position) and propagates this to an arbitrary time. Chapter 2 presented various methods for orbit propagation including their relative accuracy and decorrelation in time. Figure 3.1 summarizes the previously described techniques.

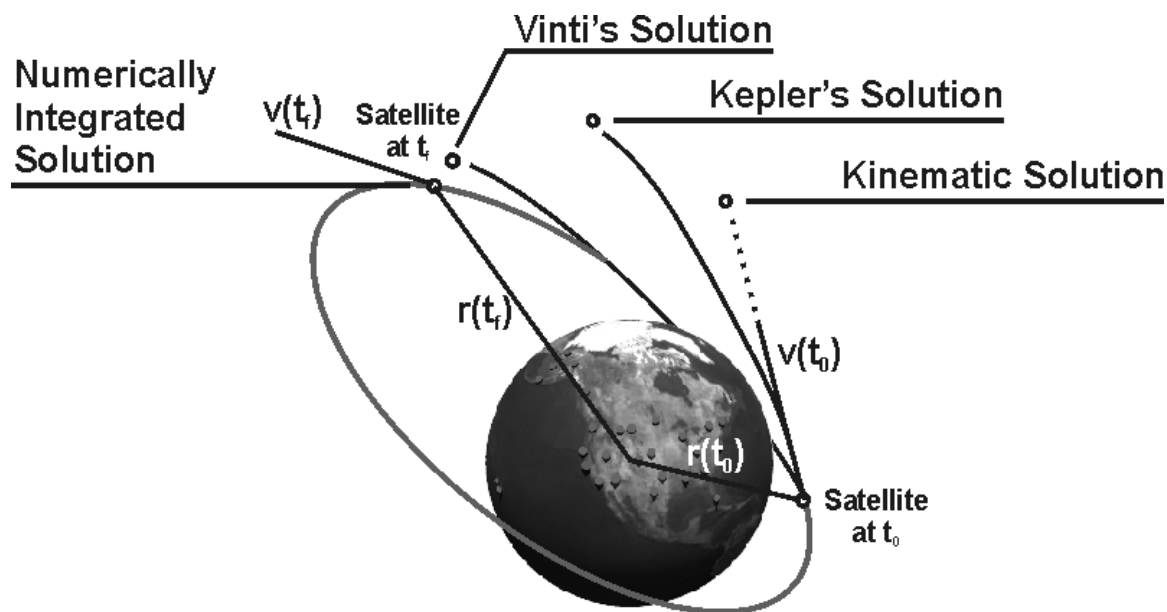


Figure 3.1: Orbit Propagation Methods

To evaluate the influence of the orbit determination methods on user domain position and ranging accuracy, we must first establish the framework in which the orbit determination is to be used. This framework is the wide-area master station where the GPS reference station data is combined into corrections for ephemeris, clock and ionosphere. The next step is to establish a reference orbit against which all other techniques will be judged. Once the reference trajectory is established, then the different orbit determination techniques are compared in the user range and position domains.

### 3.2 WIDE-AREA MASTER STATION ARCHITECTURE

The flow diagram for processing GPS data with a wide-area network of receivers is shown in Figure 3.2. This is the design of Stanford University's Testbed Master Station (TMS). The thick lines in the diagram represent multiple parallel channels of data, either for multiple satellites or multiple receivers. A thin line represents a single scalar measurement. This reference architecture is fully described in [Tsai99].

GPS measurements in the form of pseudorange and carrier phase for both L1 and L2 frequencies are collected by a wide-area network of reference stations. The pseudorange measurements are corrupted by ephemeris errors, satellite clock errors, station clock errors, atmospheric (ionosphere and troposphere), measurement noise, etc. as discussed in Chapter 1. However, the ionospheric delay estimation is handled separately. The pseudorange residuals passed to the routines for ephemeris and clock errors are:

$$\begin{aligned}\Delta\rho_i^k &\doteq \text{pseudorange residual for station } i \text{ and satellite } k \\ \Delta\rho_i^k &= \Delta r^k \bullet 1_i^k + \Delta b_i - \Delta B^k + v\end{aligned}\tag{3.1}$$

where:

$$\begin{aligned}\Delta\rho_i^k &\doteq \text{pseudorange residual for station } i \text{ and satellite } k \\ \Delta r^k &\doteq \text{ephemeris error for satellite } k \\ 1_i^k &\doteq \text{normalized Line - Of - Sight (LOS) from station } i \text{ to satellite } k \\ \Delta b_i &\doteq \text{clock offset from GPS time for station } i \\ \Delta B^k &\doteq \text{clock offset from GPS time for satellite } k \\ v &\doteq \text{pseudorange measurement error}\end{aligned}$$

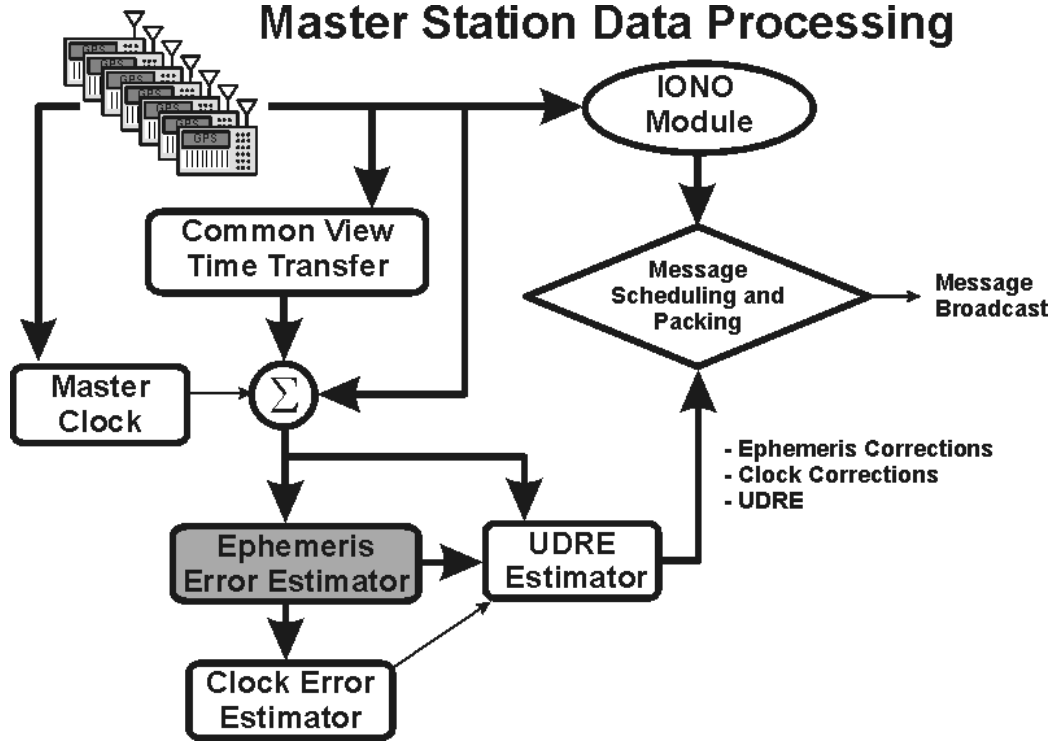


Figure 3.2: Testbed Master Station (TMS) Architecture

The first processing stage is the Common View Time-Transfer (CVTT) algorithm. This routine calculates the relative clock offsets between each of the receiver clocks versus a single station designated as the ‘master’ clock. While each reference station has a stable atomic clock, the offset between these clocks is not known *a-priori*. A master clock estimator is running in parallel to determine the offset between the master clock and GPS time. The master clock is a smoothed estimate of GPS time without the influence of SA. Further information on the CVTT and master clock algorithms are given in [Chao97].

After the summing junction in Figure 3.2, where the CVTT, master clock and original measurements are combined, the resultant pseudorange residuals are:

$$\Delta\tilde{\rho}_i^k = \Delta r^k \cdot 1_i^k - \Delta B^k + e_i^k \quad (3.2)$$

Equation (3.2) combines all noise terms and estimation errors for CVTT and the master clock in the term  $e_i^k$ . The resultant term,  $\Delta\tilde{\rho}_i^k$ , leaves only ephemeris and satellite clock uncertainties. These residuals are passed onto the clock, ephemeris and UDRE estimators.

UDRE stands for the User Differential Range Error, which is designed to place a bound on the pseudorange error component due to the clock and ephemeris terms after correction from the WAAS message stream [RTCA159]. An algorithm for the computation of the UDRE for GPS is given in [Tsai99].

The results from the UDRE, ephemeris, and clock estimation routines are passed onto the algorithm that prepares the data for transmission to the user aircraft. These ephemeris, clock and UDRE estimation routines will be covered in more detail in Chapter 4. Of critical interest at this point is that the ephemeris estimation module could be modified to user different orbit estimation methods without dramatically impacting the system design. Three different methods were utilized for the ephemeris estimation (the shaded box in Figure 3.2). These methods were used to establish the efficacy of each of the various approaches.

The first approach taken was the standard kinematic method described in [Tsai99]. This formed the baseline to which all subsequent results would be compared. The next approach taken was to remove the ephemeris estimation routine entirely leaving only the broadcast ephemeris. This placed all of the weight for the corrections in the clock estimate. Finally, the IGS precise orbital solution introduced in Chapter 2 and described in the following section was substituted for the ephemeris estimation routine.

### **3.3 THE IGS AND PRECISE ORBITS**

The IGS produces orbital solutions with repeatable precision of 10 cm per axis [Zumberge]. The principle of this method is that the perturbation forces, shown in Figure 3.3, are integrated numerically to solve for the instantaneous position solution. The IGS utilizes measurements from up to 200 ground stations (Figure 2.5) to determine the deviations of the actual GPS satellite paths from broadcast orbits created by the MCS.

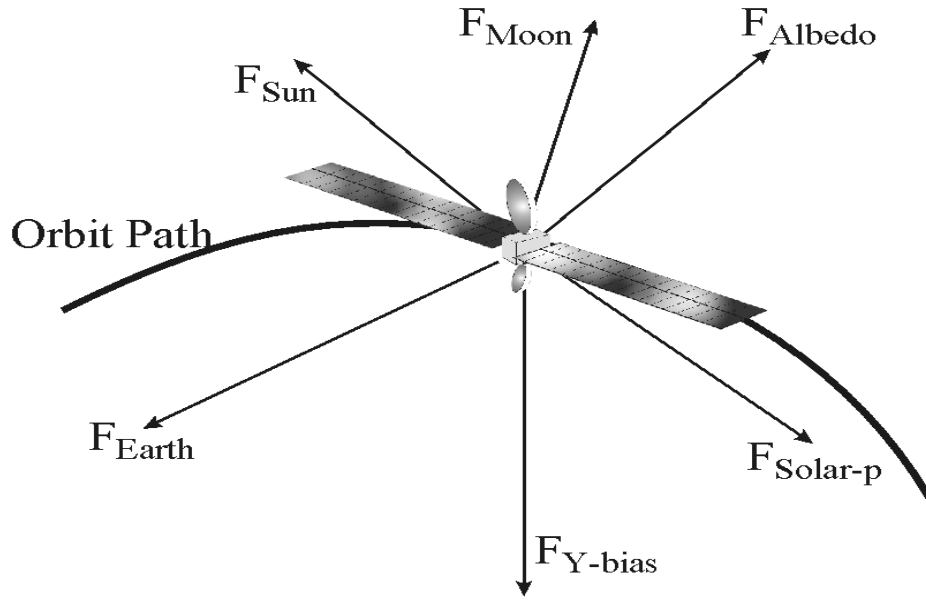


Figure 3.3: Example Perturbation Forces Acting on a Satellite

The precise GPS orbits are saved in one-day long files placed on the internet on a weekly basis. While the data is very precise, it is stored only at 15-minute intervals. This made interpolation of these orbits necessary for the inclusion in the standard TMS, which utilized data at one-second intervals. To achieve this, a two-step technique was developed for interpolating from the IGS data to the information employed by the TMS. The first step, shown in Figure 3.4, takes the difference between the broadcast orbits (from the MCS) and the IGS solutions. Care was taken to make sure that the IODE (Issue of Data Ephemeris) was recorded for synchronization (the IODE is used as a unique identifier of a broadcast ephemeris set).

The orbit XYZ time histories are not conducive to simple fitting functions such as lines or polynomials [Hofmann-Wellenhoff]. For this reason, the smoothly varying difference between the broadcast orbit and precise IGS orbit was fit by a polynomial curve of order 5 and sub-sampled at 30-second intervals. This result was stored to file for inclusion into the TMS process. The sampling interval was chosen as a compromise between file size and fit residuals. Sub-sampling of the data at intervals lower than 30 seconds did not substantially reduce fit errors in the subsequent step. The TMS software was modified to read in the curve-fit IGS data and linearly interpolate it to the one-second intervals necessary to match



the incoming GPS data epochs. Figure 3.5 shows this final step in replacing the default ephemeris processing.

### IGS Orbit Profile Generation

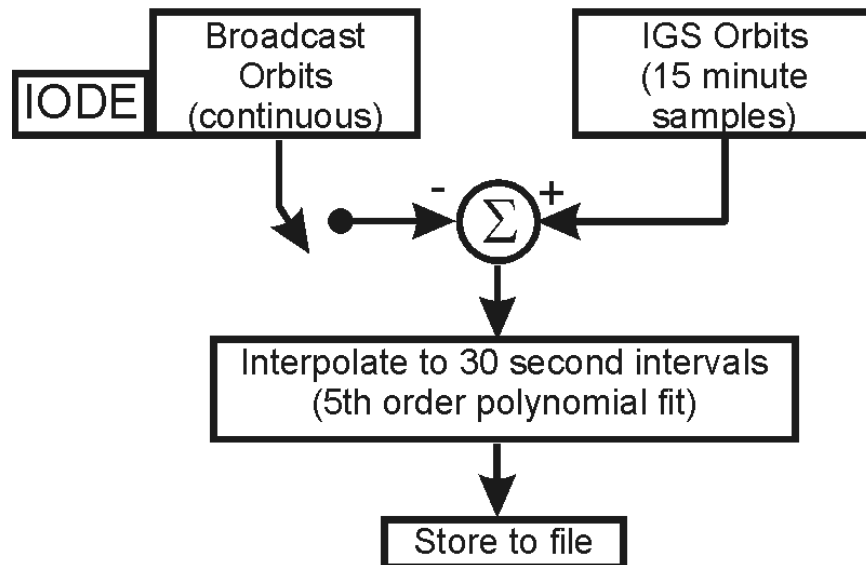


Figure 3.4: Processing of IGS in Preparation for Application to User Data

### Using the IGS Orbit Profile

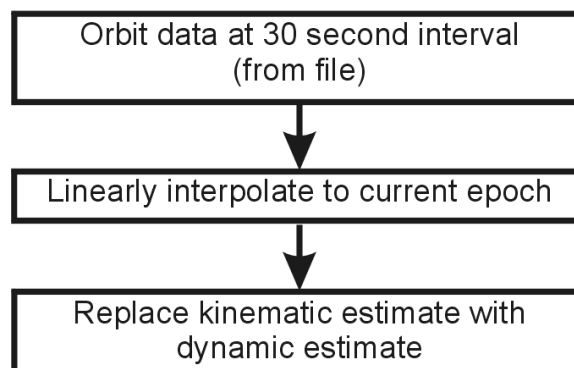


Figure 3.5: Final Stage of IGS Data Interpolation

The substitution of the IGS data into the TMS processing, together with the standard kinematic processing and results with no ephemeris processing are compared in the user position domain in the following section.

### 3.4 INFLUENCE OF PROPAGATION TECHNIQUE ON POSITIONING ACCURACY

Utilizing data over four days from the National Satellite Test Bed (NSTB), the position solution was calculated at the FAA Technical Center in Atlantic City, New Jersey. This site is one of the NSTB reference station sites and, for these tests, it was used as a passive station. A passive station is a reference station that is not providing any data for the computation of the wide-area differential GPS solution. Figure 3.6 shows the results in terms of vertical accuracy over those four days. Here the vertical accuracy is defined to be the error, in meters, that is not exceeded for a given percentage of the time. For instance, the chart below shows 99.9% accuracy. This indicates that 99.9% of the time over those four days, the errors did not exceed the values shown on the chart.

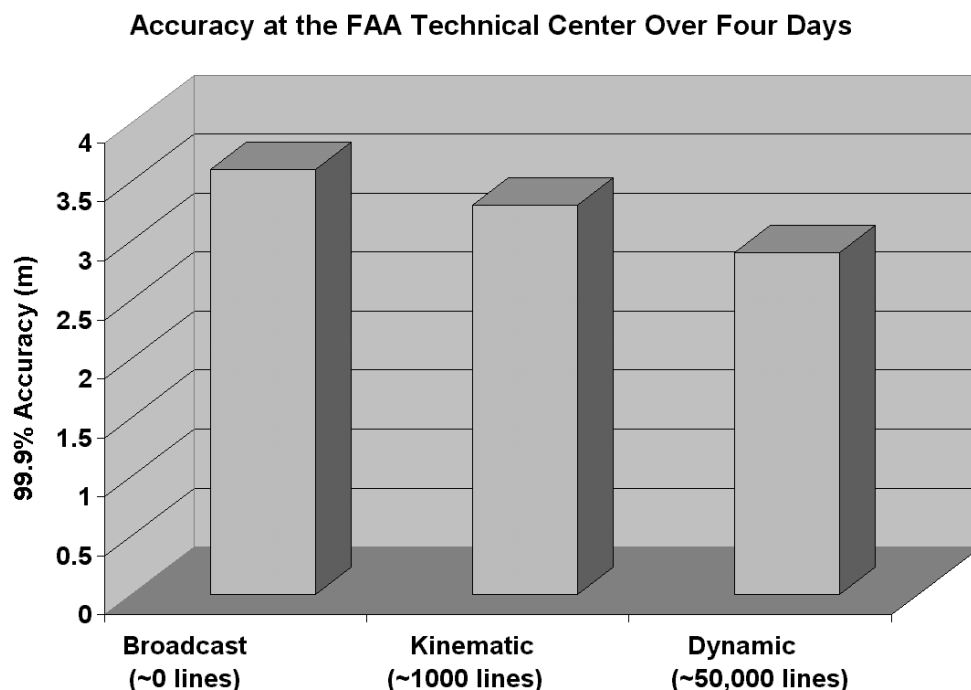


Figure 3.6: Vertical Accuracy of Position Solutions for Various Orbit Determination Methods

As illustrated in Figure 3.6, the orbit determination method producing the best vertical accuracy was that of the numerically integrated technique employed by IGS. Note that the user position accuracies of these three methods are remarkably close, despite the large difference in their orbital estimation precision. The IGS reports ephemeris precision on the order of 10 cm, yet the results in the position domain vary by only 60 cm from best to worst among the three different applied methods.

With regard to code size, the IGS method is reported to be well in excess of 50,000 lines of code [Pogorelc97a]. The default kinematic model in the TMS is approximately 1,000 lines of code and the use of the broadcast orbits did not require any additional lines of code. Therefore, to secure roughly 60 cm over doing nothing at all (a 20% improvement in user position accuracy) the substantial effort of developing a numerically integrated solution had to be made. This becomes critical when evaluating the costs of developing and *certifying* flight software that comes under the highest scrutiny through validation testing.

Considering the dramatic disparity of the code sizes, the distinction between the three results seems insignificant. This is particularly true in light of the fact that the 95% vertical accuracy specification is 7.6 meters [RTCA159], more than twice as much as large as the greatest observed 99.9% vertical accuracy.

These results point to numerically integrated orbit determination methods when the principle goal is user position accuracy but at a cost of increased code size and complexity. However, since both user position accuracy *and* the protection level are of primary concern for the aviation user, a clear choice cannot be made on these results alone. The next section performs a sensitivity analysis that relates the measurement uncertainties at the wide-area reference stations to the components of the ephemeris errors seen by users of the wide-area corrections. This is accomplished by mapping the covariance ellipsoid of the satellite's position into the user range domain (i.e., along the LOS between the satellite and the user). The satellite position covariance ellipsoid is derived based on measurements from a network of reference receivers with known pseudorange error means and variances.

### 3.5 USER RANGE ERRORS DUE TO EPHEMERIS ESTIMATE ERRORS

As shown in Figure 2.9, error growth in kinematic orbit propagation presented in Section 3.4 is bounded within a few meters over several seconds. Analytically integrated methods (Kepler and Vinti) show errors on the order of a few centimeters in several seconds and less than a meter for a propagation time of 200 seconds. The reference orbit of Figure 2.9 from the IGS implementation of numerically integrated orbit propagation is the most accurate and can have errors much less than a meter over many hours [Vinti98]. Since instantaneous measurement errors for reference stations tracking GPS satellites can be on the order of 1-10 meters, it is clear that measurement errors dominate the short-duration precision problem. This is of critical concern for time-to-alarm consideration. Time-to-alarm is the time difference between the start of a satellite ephemeris (or clock) problem and the moment that the user is made aware of the problem with an alert message. The time-to-alarm for WAAS is six seconds [RTCA159] and is one of the essential components of aviation user integrity.

Since measurement errors are so critical, the relationship between the reference station measurement errors and the resultant user domain range errors is explored in the next sections.

#### 3.5.1 SATELLITE EPHEMERIS COVARIANCE MAPPING INTO USER RANGE DOMAIN

Figure 3.7 shows how the measurement errors, as seen by the reference stations, map into a covariance ellipse describing the orbital estimation uncertainties and in turn project into confidence bounds for the user. This is done by first establishing the covariance of the satellite estimate based on measurements from a ground-based network of reference receivers as indicated in Figure 3.8. The covariance matrix from the satellite ephemeris estimate is then mapped to users at different locations within the satellite footprint (users in view of the satellite). Thus, the relationship between satellite ephemeris errors and user range error can be determined for a fixed network of reference receivers.

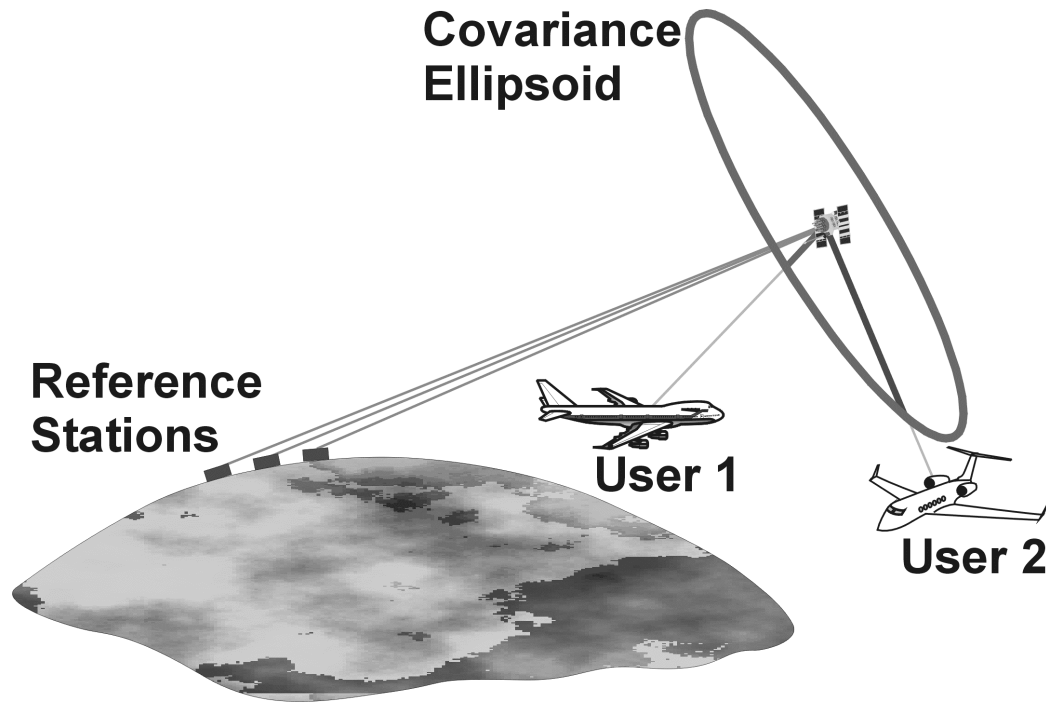


Figure 3.7: Covariance of the Satellite Ephemeris Estimate Determined from Reference Stations and Represented in the User Range Domain

### Covariance Mapping from Satellite Ephemeris Estimate to User Range Domain

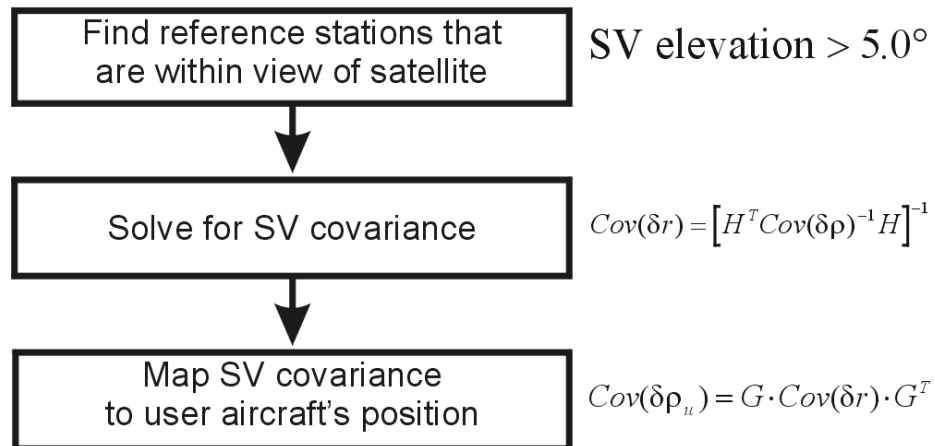


Figure 3.8: Flow-Diagram of the Computation of the User Range Domain Variance Due to Covariance of the Satellite Ephemeris Estimate

The reference stations collect GPS observables (in this case the codephase pseudorange measurements). To relate the uncertainty in the measurement data to the uncertainty in the satellite position, we look at a small variation of the  $k^{\text{th}}$  satellite from its broadcast position,  $\Delta r^k$ , which, projected into the reference station pseudorange domain, is:

$$\begin{bmatrix} \Delta \rho_1^k \\ \Delta \rho_2^k \\ \vdots \\ \Delta \rho_n^k \end{bmatrix} = \begin{bmatrix} 1_1^k \\ 1_2^k \\ \vdots \\ 1_n^k \end{bmatrix} \bullet [\Delta r^k] + \varepsilon \quad (3.3)$$

$$\delta \rho = \mathbf{H} \delta r + \varepsilon$$

where  $1_i^k$  is the normalized LOS between the  $k^{\text{th}}$  satellite and the  $i^{\text{th}}$  reference station,  $\mathbf{H}$  is the projection matrix formed along the LOS between the satellite and the  $i^{\text{th}}$  reference station, and  $\varepsilon$  is the measurement error.

Satellite position error can be estimated with the normalized pseudoinverse [Strang]:

$$\delta r = (\mathbf{H}^T \mathbf{H})^{-1} \mathbf{H}^T \delta \rho \quad (3.4)$$

The desired result is the covariance matrix relating the measurement error covariance to the covariance satellite position estimate. To achieve this, we solve for the covariance of  $\delta r$ :

$$\begin{aligned} \text{Cov}(\delta r) &= E[\delta r \cdot \delta r^T] \\ &= E\left[(\mathbf{H}^T \mathbf{H})^{-1} \mathbf{H}^T \delta \rho \cdot ((\mathbf{H}^T \mathbf{H})^{-1} \mathbf{H}^T \delta \rho)^T\right] \\ &= E\left[(\mathbf{H}^T \mathbf{H})^{-1} \mathbf{H}^T \delta \rho \cdot \delta \rho^T \mathbf{H} (\mathbf{H}^T \mathbf{H})^{-1}\right] \end{aligned} \quad (3.5)$$

Since the projection matrix is deterministic, the expected value operator,  $E[\ ]$ , can be taken inside the equation:

$$\begin{aligned} \text{Cov}(\delta r) &= (\mathbf{H}^T \mathbf{H})^{-1} \mathbf{H}^T (E[\delta \rho \cdot \delta \rho^T]) \mathbf{H} (\mathbf{H}^T \mathbf{H})^{-1} \\ &= \mathbf{H}^{-1} (\text{Cov}(\delta \rho)) (\mathbf{H}^T)^{-1} \end{aligned} \quad (3.6)$$

After bringing the inversion outside of the expression:

$$Cov(\delta r) = [\mathbf{H}^T Cov(\delta \rho)^{-1} \mathbf{H}]^{-1} \quad (3.7)$$

Equation (3.7) gives us an expression to relate the pseudorange covariance,  $Cov(\delta \rho)$ , to the satellite position covariance,  $Cov(\delta r)$ . This creates the satellite covariance ellipsoid of Figure 3.7.

The next step is to map this satellite position covariance into the user range domain. The error in the satellite position is projected to the user pseudorange as follows:

$$\begin{aligned} \delta \rho_u &= 1_u^k \cdot \delta r \\ \delta \rho_u &= \mathbf{G} \delta r \end{aligned} \quad (3.8)$$

where  $1_u^k$  is the normalized LOS between the  $k^{\text{th}}$  satellite and a user receiver. The user range residual,  $\delta \rho_u$ , is due to the satellite position perturbation,  $\delta r$ . To determine the covariance in the user range from the ephemeris we have:

$$\begin{aligned} Cov(\delta \rho_u) &= E[\delta \rho_u^2] = E[\mathbf{G} \delta r \delta r^T \mathbf{G}^T] \\ &= \mathbf{G} \cdot E[\delta r \delta r^T] \cdot \mathbf{G}^T \\ &= \mathbf{G} \cdot Cov(\delta r) \cdot \mathbf{G}^T \end{aligned} \quad (3.9)$$

Combining Equations (3.7) and (3.9) we get:

$$Cov(\delta \rho_u) = \mathbf{G} [\mathbf{H}^T Cov(\delta \rho)^{-1} \mathbf{H}]^{-1} \mathbf{G}^T \quad (3.10)$$

Equation (3.10) relates the measurement covariance from the network reference stations,  $Cov(\delta \rho)$ , to the covariance of the user range domain perturbation,  $Cov(\delta \rho_u)$ . This is the sensitivity of the user range domain errors to the measurement errors at the reference stations for a given satellite location relative to a user location.

This final covariance gives the mapping of the satellite covariance to the user's range domain covariance due to ephemeris errors. Since the ephemeris error covariance was caused by the measurement error of the reference stations, this allows for the reference station measurement uncertainties to be mapped into the user range domain error.

The application of Equation (3.10) is shown in Figure 3.8. The initial reference station measurement uncertainty determines the satellite covariance. Subsequently, the satellite covariance is mapped into the user aircraft's range domain. Thus, a satellite's ephemeris and clock uncertainty can be individually mapped into the user aircraft's position.

### 3.5.2 USER RANGE ERRORS USING NSTB DATA

The covariance of the reference station measurements that is needed for Equation (3.7) is derived from NSTB reference station data. Dual-frequency carrier-smoothed pseudorange measurements are utilized for satellite orbit determination. A description of the dual-frequency carrier smoothing algorithm is given in [Chao97]. Dai gives a description of the carrier-smoothed pseudorange stochastic distribution as a function of bounding SNR values [Dai97]. He showed that the dominant error residual in the measurement, multipath and receiver noise could be calibrated versus the receiver L1 SNR. This calibration profile can be combined with a nominal SNR versus elevation curve to form a relationship between the pseudorange variance and elevation. These calibrations are performed on a station-by-station basis. There were a variety of accuracies recorded based primarily on antenna site selection and secondarily on receiver type. Multipath errors are highly dependent on antenna site selection. For this study, it was assumed that the reference receiver sites for WAAS would be better chosen than some unfortunate sites for the NSTB. An average for all of the NSTB profile parameters was used for the pseudorange error function. The assumption is that an attempt will be made across the WAAS network to mitigate potential multipath problems at the reference stations such that these parameters represent a conservative bound. The error distributions resulting from the average parameters are shown in Figure 3.9. Preliminary information from the WAAS network [McHugh] indicates that the Figure 3.9 error bound is conservative.



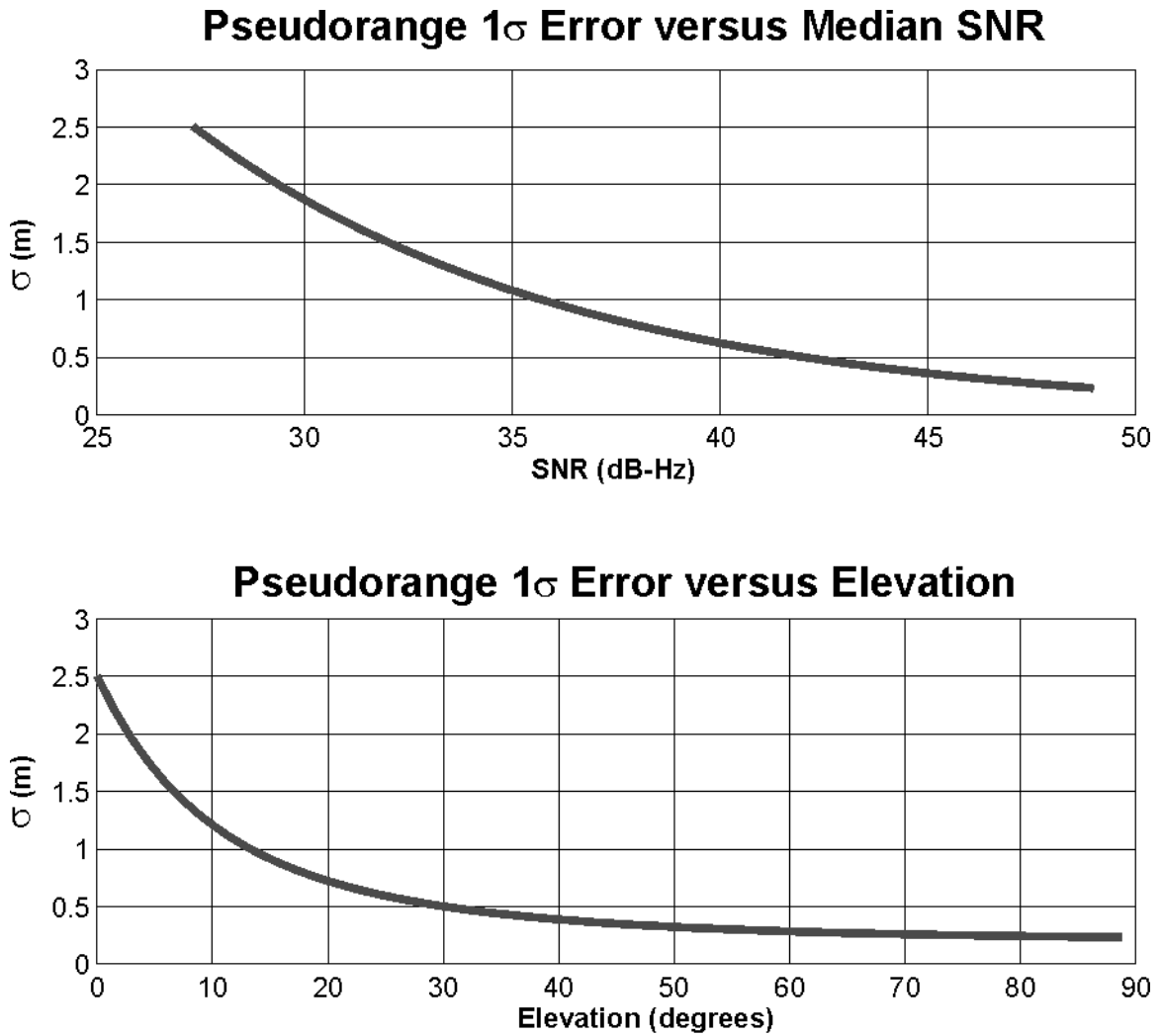
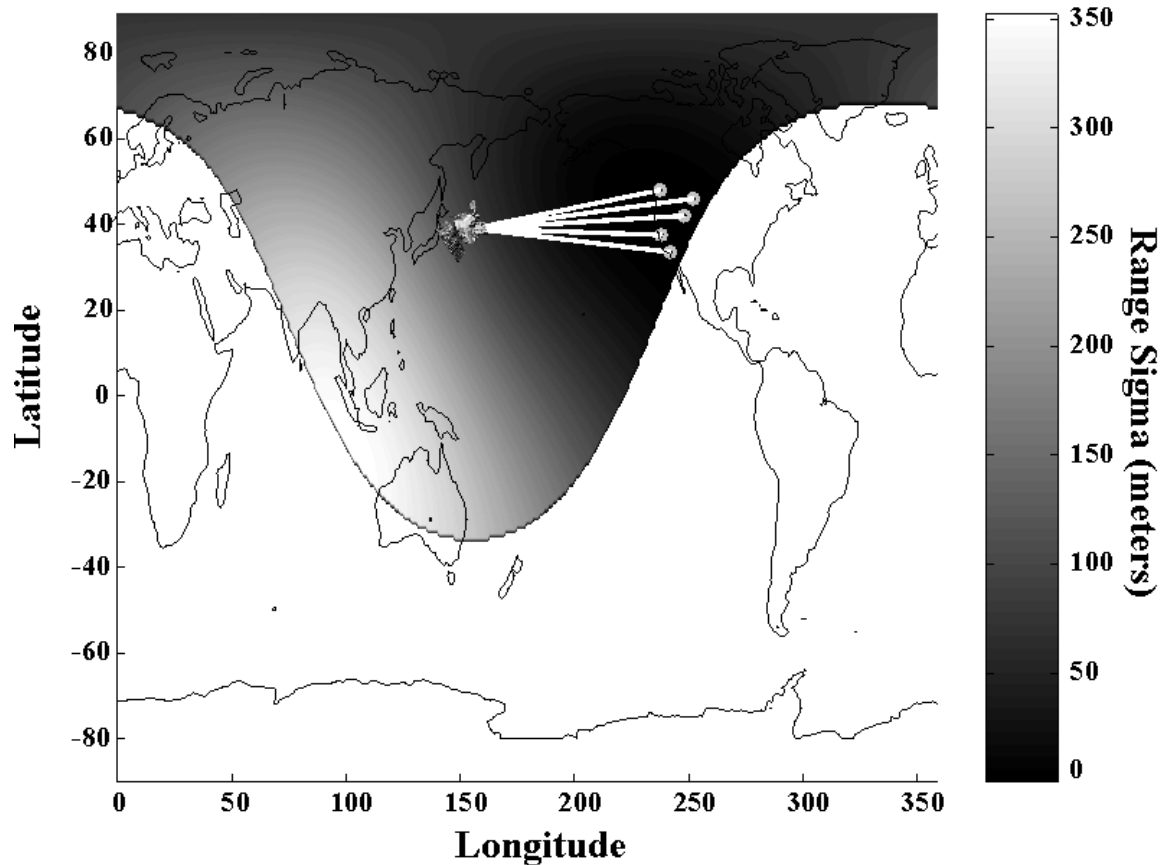


Figure 3.9: Pseudorange  $1\sigma$  Error as a Function of SNR and Elevation

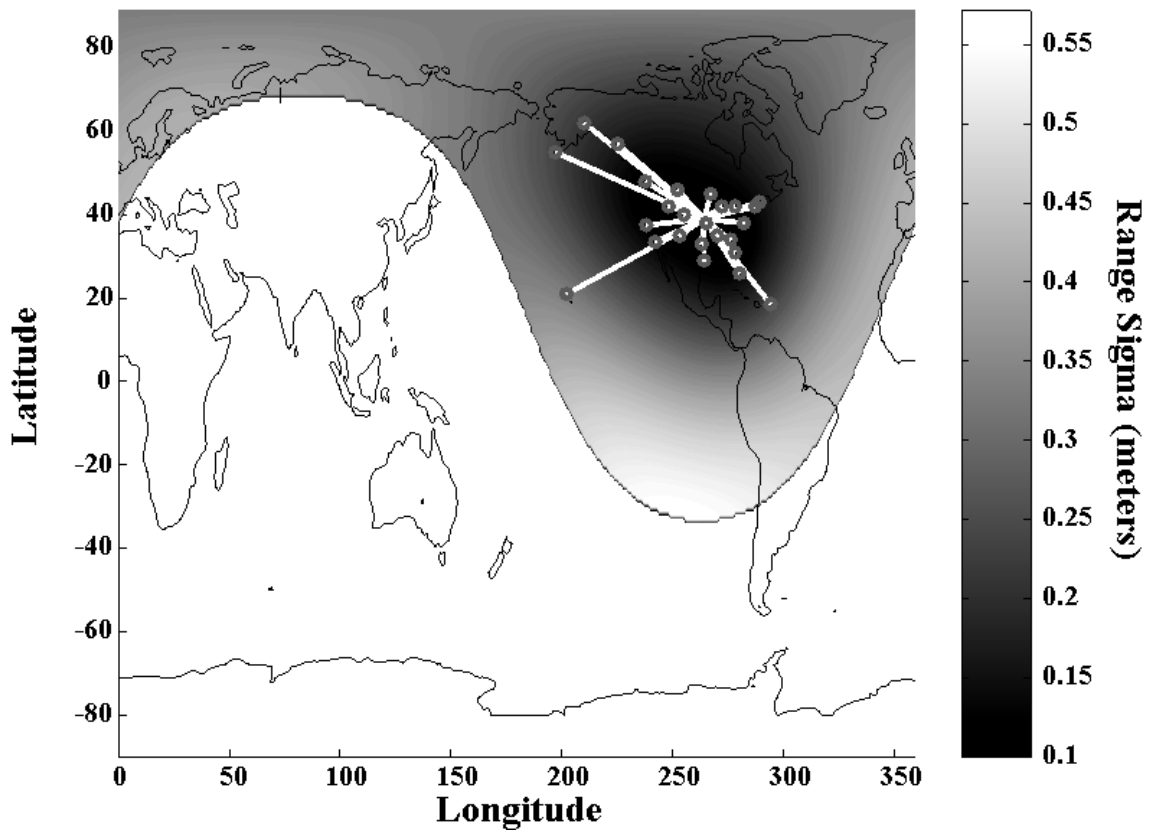
Figure 3.10 shows the mapping of the satellite uncertainties onto the footprint of a GPS satellite located at a latitude of 39N and a longitude of 156E. Errors are large for users far from the reference network and small for nearby users.

### User Worst-Case Sigma (m) for SV Located at Lat=39N, Lon=156E



**Figure 3.10: Satellite Covariance Map for a SV In View of the NSTB with Poor Tracking Geometry Between the Satellite and Reference Stations**

Figure 3.11 shows the mapping of the satellite uncertainties onto the footprint of a GPS satellite located at a latitude of 39N and a longitude of 246E. In comparison to Figure 3.10, the overall errors are significantly smaller. As in Figure 3.10, the projected errors near the reference stations are the smallest, while farther out on the satellite footprint there are larger errors. However, the beneficial geometry is very apparent. Regardless of the maximum errors of the projection of the satellite covariance matrix, the lowest satellite covariance projection is always near the reference stations. Thus, a user at or near the vicinity of the reference station centroid is at the minimum of the satellite ephemeris covariance projection.

**User Worst-Case Sigma (m) for SV Located at Lat=39N, Lon=264E**

**Figure 3.11: Satellite Covariance Map for a SV In View of the NSTB with Good Tracking Geometry Between the Satellite and Reference Stations**

Since the kinematically smoothed orbit determination technique is formed directly from the instantaneous reference station measurements, the uncertainties of that method is closest to the covariance technique presented here. Thus, covariance projection forms the basis for the confidence bounds associated with the kinematic solution.

In Figure 3.12, the results from Figure 3.11 were taken at 40N latitude and plotted across the longitudes in the satellite footprint. Chapter 4 will show that the instantaneous kinematic solution can be represented by Equation (3.7). Therefore, the line derived from Figure 3.11 in Figure 3.12 can be denoted as a bound on the kinematic solution. The broadcast result is taken from [Dai99] where the 3D RMS value is assumed to be less than five meters. The broadcast ephemeris range is not known to be variable at different parts of the orbit. Finally, the performance for the IGS orbits is based on the precision performance

from [Zumberge]. This 10-cm bound is based on the reported post-processed precision of the IGS orbits. This line assumes a worldwide network of stations to ensure constant measurements of the satellite observables. If a geographically restricted network is employed, like WAAS operating only in the CONUS, then these results will degrade away from the reference station network towards the kinematic solution.

As shown in Figure 3.12, there is a dramatic difference in the confidence between the corrected solutions (kinematic and integration) versus the uncorrected ephemeris errors (broadcast). The kinematic solution approaches the overall availability levels that are achievable by integrated methods. The advantage of the kinematic method is that it provides an instantaneous solution that can be used to bound errors with very fast time constants (a few seconds) from the satellite and help ensure time-to-alarm for WAAS.

### Range Confidence versus Longitude at Latitude=40 degrees

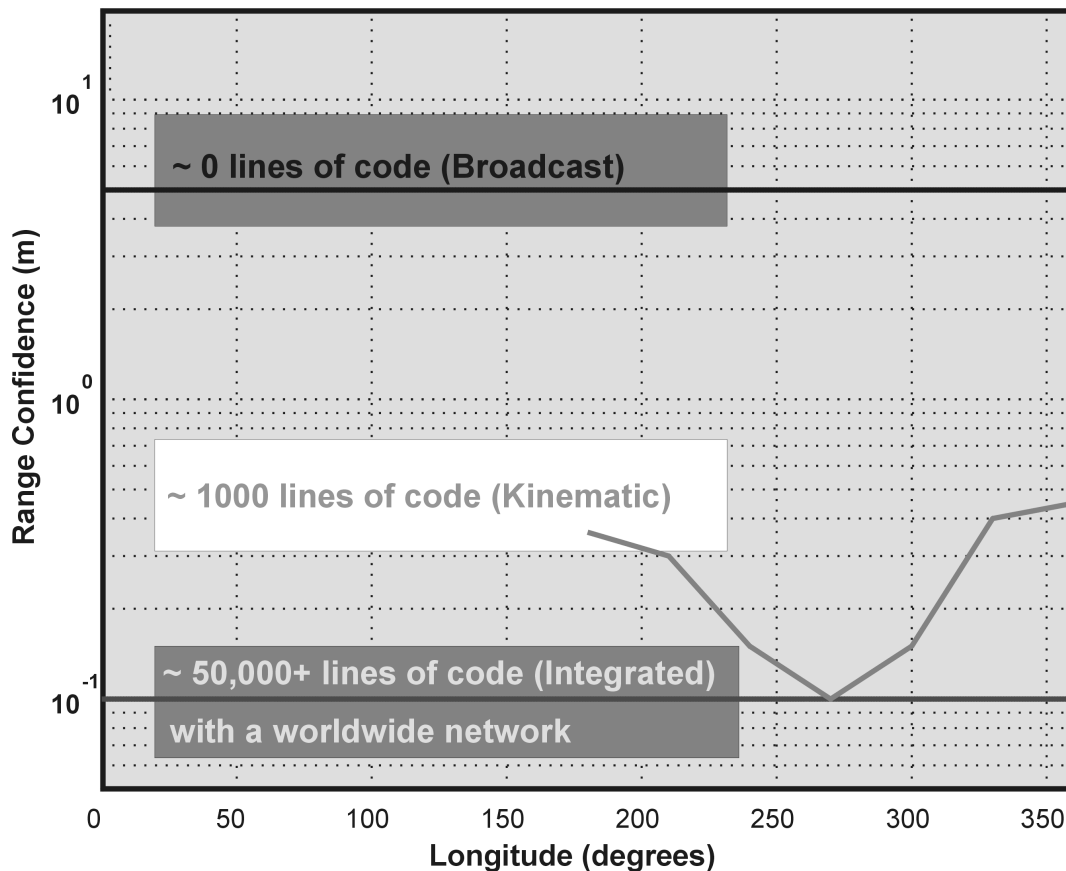


Figure 3.12: Mapping of Pseudorange Confidence from Satellite Geometry to Users at 40 Degree Latitude Across Multiple Longitudes

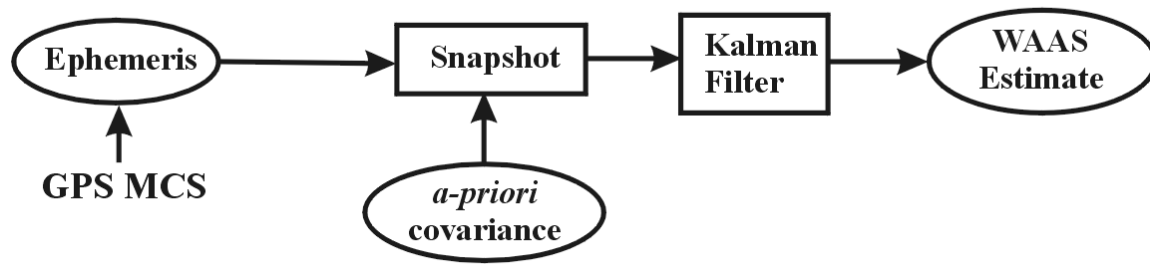
Measurement errors for users can be on the order of one meter. The kinematic and integrated solutions have range domain errors that are much smaller than the measurement errors for the case in Figure 3.12. Therefore, when evaluating differences between the expected range and the measured pseudorange, the residuals will be dominated by the measurement noise, not the ephemeris estimate error.

Integrated solutions provide accurate results for very long time constants but require some sort of kinematic residual to detect and isolate effects with short time constants when ephemeris, or clock errors develop. Although the integrated solution may be able to solve for very precise orbits over time, integrity will always require a kinematic solution. Comparing the integrity results with the relative complexity of the integrated solutions yields the obvious choice of a kinematic solution method.

### 3.6 GEOSTATIONARY ORBIT ESTIMATION: INITIALIZATION PROBLEM

This chapter has concentrated on the issues surrounding GPS satellites. While geostationary Earth Orbit (GEO) satellites have many of the same issues there are distinct problems dealing with the GEO satellites in WAAS. As shown in Figure 2.11, the GEO satellite position can vary substantially from the linear range designed into the kinematic filter used by Tsai for GPS orbit determination. Figure 3.13 shows an overview of the GPS and geostationary orbit estimation processes. The switch added at the snapshot stage allows for quicker convergence of the satellite position at initialization. This is due to the fact that the initial uncertainty of the geostationary satellite position can be as much as 50 km. Once the initial convergence is complete, the switch is turned to the full estimation process. This computes not only the real-time position estimate but also provides an update for the *a-priori* covariance. The following chapter will examine this issue and develop a method for dealing with the issue of highly uncertain initial conditions for the satellite orbit as well as the estimation of the *a-priori* covariance.

### GPS Estimation Process (Tsai)



### Geostationary Estimation Process (Fuller)

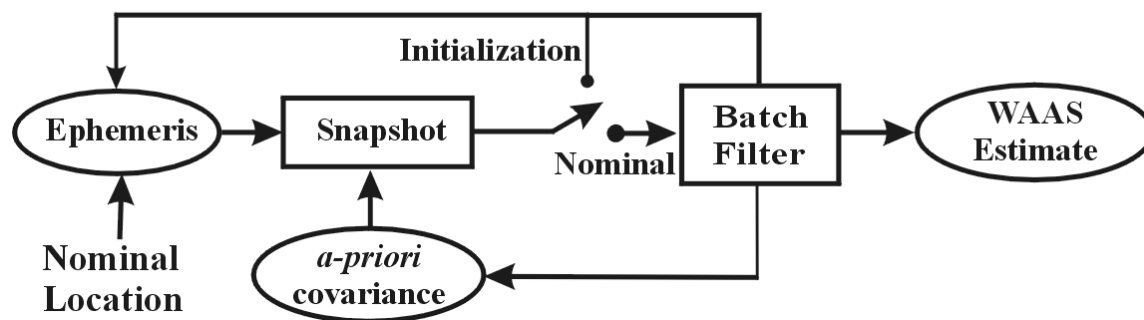


Figure 3.13: Comparison Between the GPS Orbit Determination Process and the Geostationary Orbit Determination Process

# Chapter 4

## Geostationary Satellite Orbit Determination

This chapter extends preceding chapters to geostationary (GEO) satellite orbit determination. First, this chapter presents a detailed description of the orbit estimation and filtering algorithm. Following this, it looks at the performance of the filter for GEO satellite position estimation. Emphasis is placed upon the most important factor in the orbit determination problem: minimizing user range error. As presented in Chapter 3, range error can be small (less than a meter) even when the satellite position is not precisely known (several meters or larger). Since the user accuracy requirement was shown to be satisfied, further increases in satellite position accuracy is only necessary if it leads to increases in availability. The work presented in this chapter supports the assertion that small range error in the user domain is more important than precise GEO satellite position knowledge. The chapter concludes with a study on the improvement in precision and non-precision approach availability using the results from GEO ranging.

### 4.1 THE GEOSTATIONARY ORBIT PROBLEM

Figure 4.1 shows the variation of the GEO satellite position from a mean location. The North-South (latitude) and East-West (longitude) variation is about  $\pm 0.07$  and  $\pm 0.04$  degrees, respectively. While the goal is to keep the satellite fixed at a specific location, the reality is that this goal is achieved only within a bounding box around the desired point.

Disturbing forces, primarily from the Sun, Moon and solar pressure, cause the satellite to drift over time from its specified location. Occasional corrections, usually in the form of thruster firings are required to adjust the position the satellite to a certain tolerance around a given point. These corrections are referred to as “station keeping maneuvers” [Kaplan].

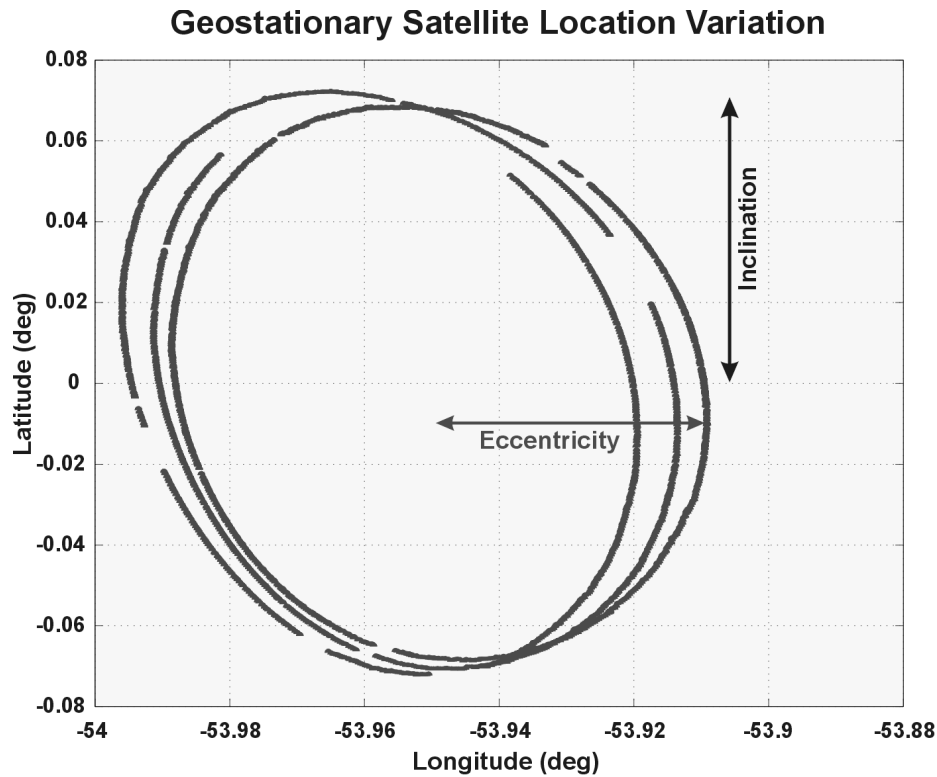


Figure 4.1: Geostationary Satellite Orbital Variation Over Time

The variation in Figure 4.1 from the mean position is as much as 50 km. The estimation process for the GEO orbit needs to be able to accommodate the uncertainty of position up to that 50 km. The goals of the estimation process are:

- Create an orbit estimate that has a user range residual on the order of one meter;
- Formulate a bound (UDRE) on this estimate;
- Make this estimate in real-time; and,
- Tolerate and accommodate large initial uncertainties in both position and covariance.



The design must be able to handle four to five orders of magnitude of residual error from initialization to convergence which is remarkably different from the method used for GPS satellites in WAAS. The approach for GPS satellites, as presented in [Tsai99], need only handle up to a maximum 256 meters of error (roughly two orders of magnitude) from the broadcast ephemerides. Satellites were assumed to always be operating in a region where the kinematic linear extrapolation of the orbit error estimate would be valid, which is correct for GPS satellites [Dai97, Tsai99]. Should the orbit error exceed the linear region of the estimation process, no valid correction may be broadcast as the WAAS MOPS [RTCA159] does not support transmitting such a large correction. The linear region of the estimation process and the WAAS message structure are highly correlated. The WAAS message structure does not support values as large as the magnitude of the orbit errors when they begin to exceed the linear region of the GPS orbit estimator. When the values exceed the maximum correction value for the WAAS specification the GPS satellite is marked as *don't use*. Therefore, the estimation process for GPS satellites degrades gracefully by specification.

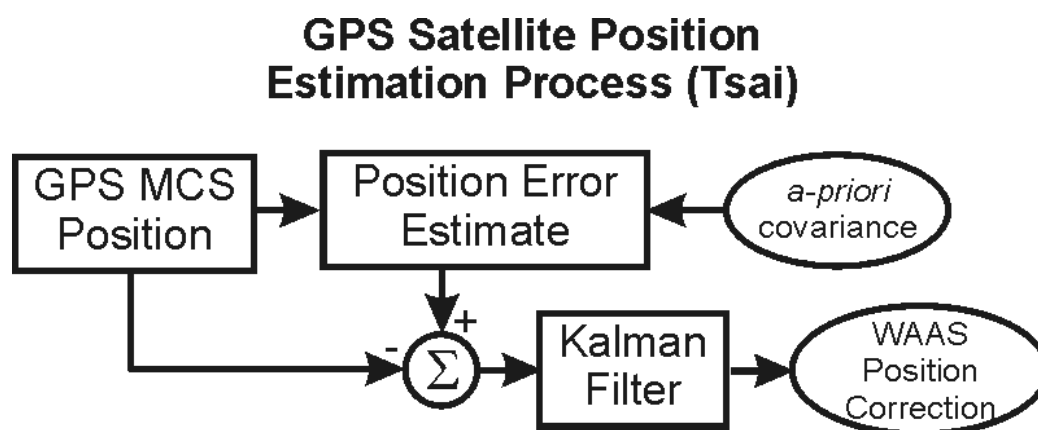


**Figure 4.2: Fixed *a-priori* Approach to Orbit Filtering as Applied to GPS Satellites**

The position error estimate used by Tsai and shown in Figure 4.2 is formed from the instantaneous ‘snapshot’ of the satellite position error which is described in Section 4.1.2. The *a-priori* covariance value was the largest that produced smooth residuals after the snapshot [Tsai99]. The *a-priori* covariance value used in [Tsai99] was  $(2\text{ m})^2$  in the radial

direction (from the center of the Earth to the satellite),  $(6 \text{ m})^2$  along the path of the orbit and  $(4 \text{ m})^2$  in the axis perpendicular to the orbit path. These values are in good agreement with historically observed differences between the broadcast ephemerides and post-processed precise orbits [Dai99]. This estimation process is an effective solution for the first three goals shown above.

In contrast, Figure 4.3 shows an estimation process block diagram that can also accommodate the fourth goal above. While the position snapshot remains unchanged, the logic has been modified to support a switch to formulate an initial orbital guess at startup, a ring-buffer batch fit of the orbital solution, and an *a-priori* covariance feedback term. These modifications are implemented to facilitate the large range of position uncertainty from the initialization process. The ring-buffer batch fit to the orbit was adopted to capture the periodic nature of the disturbance forces acting on the satellite. The *a-priori* covariance feedback term was added to take into account the varying uncertainties of the position estimate over time.

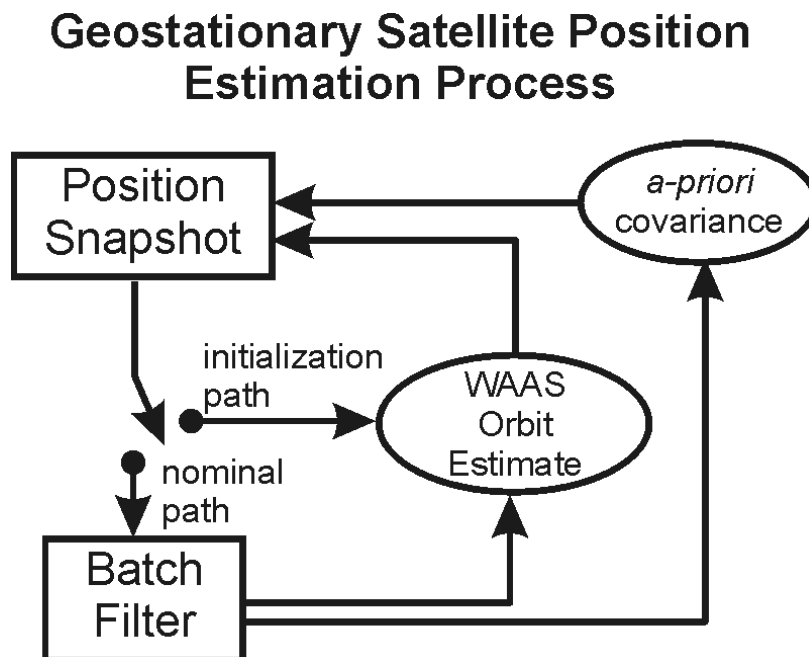


Figure 4.3: Adaptive Orbit Filtering for Geostationary Satellites

Section 4.1.1 discusses how, the satellite clock is removed from the geostationary orbit determination problem. The following sections explore the details of the filter design: 1) orbit snapshot; 2) estimation and smoothing; and 3) the batch filter. The pseudorange residuals are presented followed by the solution availability.

#### 4.1.1 CLOCK AND CLOCK RATE CONTROL

The Geostationary satellite Uplink Sub-system (GUS) is the part of the WAAS architecture responsible for the estimation and control of the various sources of divergences between code and carrier of the WAAS signal. It also synchronizes the GEO code phase to WAAS Network Time (WNT) [RTCA159]. This system has been developed and tested for the FAA by the Raytheon Systems Company. The disturbances in the WAAS signal include ionospheric delay, satellite Doppler and frequency translation errors due to the satellite transponder (C-Band to GPS-L1). The control algorithm utilizes feed-forward corrections of the code phase, carrier phase and carrier frequency to maintain code-carrier coherency [Grewal99]. Figure 4.4 shows the major aspects of the GUS control loop algorithm. The control loop contains both hardware and algorithm components. The hardware components are the WAAS GPS Receiver, GEO satellite and the GUS signal generator. Two GUS installations are in Santa Paula, California and Clarksburg, Maryland.

The downlink ionospheric delay is estimated with the Ionosphere Delay and Rate Estimator in Figure 4.4 using pseudorange measurements from the WAAS GPS Receiver on L1 and L2. A two-state Kalman filter [Grewal97] estimates the ionospheric delay and delay rate.

At each measurement epoch, a range measurement is taken and processed by the Range, Rate and Acceleration Estimator. Equation (4.1) represents the measurement passed into the Range, Rate and Acceleration Estimator [Van Dierendonck94]. The input values include the reference pseudorange from the GUS Signal Generator ( $\rho_{L1}^{SIGGEN}$ ) and the received pseudorange from the WAAS receiver ( $\rho_{L1}^{GEO}$ ). These values are adjusted for the ionospheric delay on L1 ( $\tilde{\rho}_{IONO}^{GEO}$ ). The residual term includes biases from the Signal Generator and WAAS receiver ( $\delta p_{BIAS}$ ).

$$z = \frac{(\rho_{L1}^{GEO} - \tilde{\rho}_{IONO}^{GEO}) + \rho_{L1}^{SIGGEN}}{2} - \delta\rho_{BIAS} \quad (4.1)$$

The bias term,  $\delta\rho_{BIAS}$ , is made up of the C-Band uplink delay and the L1 receiver delay of the GUS WAAS receiver. These values are determined by bench calibration and are known *a-priori* to the estimation process. The Range, Rate and Acceleration Estimator employs a three state Kalman filter that provides input data for the frequency and code control loops. The Code Control Loop is a second order control system that regulates the code phase generation in the GUS signal generator to the WNT. The error signal for this control system is the difference between the WAAS pseudorange ( $\rho_{L1}^{SIGGEN}$ ) and the estimated pseudorange from the Kalman filter. The loop output is code rate adjustments to the GUS Signal Generator.

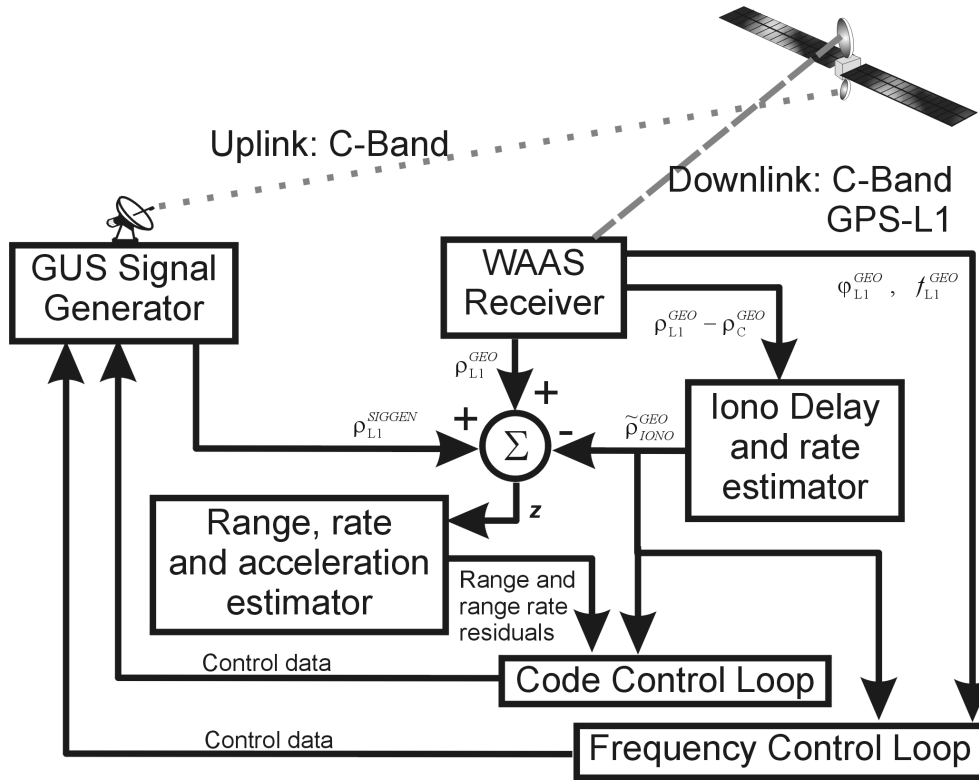


Figure 4.4: Geostationary Satellite Clock Control for WAAS

The Frequency Control Loop regulates the GUS signal generator clock to compensate for code/carrier divergence and keep synchronization with WNT. This loop has two modes. First, it adjusts the signal generator frequency to compensate for the uplink Doppler effects by using a first-order control system. The error signal input is the difference between the L1 Doppler frequency from the WAAS GPS Receiver and the estimated range rate converted to a Doppler frequency from the Kalman filter. Once the frequency error is below a threshold value, the carrier phase is controlled by using a second order control system. The error signal input to the system is the difference between the L1 carrier phase and a carrier phase estimate based on the Kalman filter output. This estimated range is converted to carrier cycles using as a reference the range estimate at the time the carrier phase control starts. This allows for fine synchronization with WNT. Fine adjustments are made to the signal generator carrier frequency to maintain phase coherence [Grewal99, FAA97, NAVSYS].

The GUS control loop estimates the ionospheric delay contribution of the GEO C-Band uplink to maintain code-carrier coherency of the broadcast signal-in-space. The ionospheric delay is calculated with the following equation:

$$\text{Iono Delay} = \frac{\rho_{L1}^{GEO} - \rho_C^{GEO} - \tau_{L1} + \tau_C}{1 - (f_{L1}/f_C)^2} \quad (4.2)$$

where  $\tau_{L1}$  is the GPS-L1 downlink delay in meters,  $\tau_C$  is the C-Band downlink delay in meters,  $f_{L1}$  is the GPS-L1 frequency, and  $f_C$  is the C-Band frequency.

#### 4.1.2 “SNAPSHOT” SOLUTION

The snapshot method uses multiple pseudorange measurements to estimate the position of the satellite. In essence, this is the inverse of the GPS problem where the position solution is for the satellite not for the receiver.

[Stengel] states that when the statistics of the measurement error can vary from measurement to measurement, as in this case, it is desirable in an estimator to weight the good data more heavily than the poor data.

A weighted least-squares estimator can be derived by minimizing a quadratic cost function of a normalized measurement residual. This estimator will be used to determine ephemeris error. First, examine the linear system defined by:

$$\begin{aligned}\mathbf{z} &= \mathbf{H}\mathbf{x} + \mathbf{v} \\ &= \mathbf{y} + \mathbf{v}\end{aligned}\tag{4.3}$$

where  $\mathbf{x}$  is the state vector of the system,  $\mathbf{y}$  and  $\mathbf{z}$  are the error-free output vectors,  $\mathbf{H}$  is the observation matrix, and  $\mathbf{v}$  is the measurement error vector. If an estimate of the state is denoted by  $\hat{\mathbf{x}}$ , then an estimate of the output is:

$$\hat{\mathbf{y}} = \mathbf{H}\hat{\mathbf{x}}\tag{4.4}$$

The error between the estimate and the state value (the state residual,  $\tilde{\mathbf{x}}$ ) is given as:

$$\tilde{\mathbf{x}} \doteq \mathbf{x} - \hat{\mathbf{x}}\tag{4.5}$$

A weighted quadratic cost function for this linear system is given as:

$$J_{WLS} = \frac{1}{2}(\mathbf{z} - \mathbf{H}\hat{\mathbf{x}})^T \mathbf{W}^{-1}(\mathbf{z} - \mathbf{H}\hat{\mathbf{x}})\tag{4.6}$$

where  $\mathbf{W}$  is the weighting matrix. The minima of the cost function corresponding to the weighted least squares estimator is derived by setting  $\partial J_{WLS} / \partial \hat{\mathbf{x}}$  equal to zero.

$$\partial J_{WLS} / \partial \hat{\mathbf{x}} = \frac{1}{2}(\mathbf{H}^T \mathbf{W}^{-1} \mathbf{H} \hat{\mathbf{x}} - \mathbf{H}^T \mathbf{W}^{-1} \mathbf{z})^T = \mathbf{0}\tag{4.7}$$

Solving for  $\hat{\mathbf{x}}$  we get:

$$\begin{aligned}
 \hat{\mathbf{x}}_{WLS} &= (\mathbf{H}^T \mathbf{W}^{-1} \mathbf{H})^{-1} \mathbf{H}^T \mathbf{W}^{-1} \mathbf{z} \\
 &= \mathbf{x} + (\mathbf{H}^T \mathbf{W}^{-1} \mathbf{H})^{-1} \mathbf{H}^T \mathbf{W}^{-1} \mathbf{v}
 \end{aligned} \tag{4.8}$$

There are a number of possible weighting matrices that can be defined [Stengel, Gelb]. For example, the measurement error covariance can be used:

$$\begin{aligned}
 \mathbf{W} &= E[(\mathbf{z} - \mathbf{y})(\mathbf{z} - \mathbf{y})^T] \\
 &= E[(\mathbf{z} - \mathbf{H}\mathbf{x})(\mathbf{z} - \mathbf{H}\mathbf{x})^T] \\
 &= E[\mathbf{v}\mathbf{v}^T] \\
 &= \text{Cov}(\mathbf{v})
 \end{aligned} \tag{4.9}$$

thus showing that the example is an appropriate choice for a weighting matrix.

This result can be utilized in an orbit estimation method. The measurement,  $\mathbf{z}$ , of this problem is the synchronized pseudorange residual, Equation (3.2). From the synchronized pseudorange residual, the linear formulation of the snapshot position solution is:

$$\begin{aligned}
 \begin{bmatrix} \Delta \tilde{\rho}_1^{GEO} \\ \Delta \tilde{\rho}_2^{GEO} \\ \vdots \\ \Delta \tilde{\rho}_n^{GEO} \end{bmatrix} &= \begin{bmatrix} \mathbf{1}_1^{GEO} & -1 \\ \mathbf{1}_2^{GEO} & -1 \\ \vdots & \\ \mathbf{1}_n^{GEO} & -1 \end{bmatrix} \bullet \begin{bmatrix} \Delta \mathbf{r}^{GEO} \\ \Delta B^{GEO} \end{bmatrix} \\
 \mathbf{z} &= \begin{bmatrix} \Delta \tilde{\rho}_1^{GEO} \\ \Delta \tilde{\rho}_2^{GEO} \\ \vdots \\ \Delta \tilde{\rho}_n^{GEO} \end{bmatrix} \\
 \mathbf{H} &= \begin{bmatrix} \mathbf{1}_1^{GEO} & -1 \\ \mathbf{1}_2^{GEO} & -1 \\ \vdots & \\ \mathbf{1}_n^{GEO} & -1 \end{bmatrix} \\
 \mathbf{x} &= \begin{bmatrix} \Delta \mathbf{r}^{GEO} \\ \Delta B^{GEO} \end{bmatrix} \\
 \mathbf{z} &= \mathbf{H}\mathbf{x}
 \end{aligned} \tag{4.10}$$

where  $\Delta\tilde{\rho}_n^{GEO}$  is the synchronized pseudorange residual,  $\mathbf{1}_n^{GEO}$  is the LOS vector from  $n^{\text{th}}$  reference station to the GEO satellite,  $\Delta\mathbf{r}^{GEO}$  is the XYZ position offset between the predicted and actual satellite location, and  $\Delta B^{GEO}$  is the satellite clock error. Even though the clock is stabilized by the loops described in the previous section, the absolute clock offset from GPS time is not known by the reference stations. The clock term in Equation (4.10) allows for the computation of that offset. This snapshot approach has often been referred to as ‘Inverse GPS’ because unlike the GPS solution that uses multiple satellites to solve for a receiver position and clock, the snapshot solution utilizes multiple receivers to estimate the position and clock of a single satellite.

Tsai asserts that the weighted least squares result in Equation (4.8) is not the best candidate for GPS ephemeris due to high sensitivity to poor geometry experienced in GPS snapshot orbit determination [Tsai99]. While it does bound the errors, it is too noisy in general to fit into the 250 bit WAAS message structure. The same holds true of the GEO satellite position estimator.

Bryson proposed a form of the weighted least squares solution that combined a weighting on both the state residual error,  $(\mathbf{x} - \hat{\mathbf{x}})$ , as well as the measurement error,  $(\mathbf{z} - \mathbf{H}\hat{\mathbf{x}})$  [Bryson]. This places constraints on the state estimate error as well as the measurement error. [Tsai99] refers to this formulation of the weighted least squares solution as the minimum-variance estimator. The basis of the minimum-variance estimator is the cost function:

$$J_{MV} = \frac{1}{2}(\mathbf{x} - \hat{\mathbf{x}})^T \Lambda^{-1}(\mathbf{x} - \hat{\mathbf{x}}) + \frac{1}{2}(\mathbf{z} - \mathbf{H}\hat{\mathbf{x}})^T \mathbf{W}^{-1}(\mathbf{z} - \mathbf{H}\hat{\mathbf{x}}) \quad (4.11)$$

where the term  $\Lambda^{-1}$  is referred to as the *a-priori* covariance that is the expected error in the state estimate. The corresponding minimum-variance estimate is determined by:

$$\hat{\mathbf{x}}_{MV} = (\Lambda^{-1} + \mathbf{H}^T \mathbf{W}^{-1} \mathbf{H})^{-1} \mathbf{H}^T \mathbf{W}^{-1} \mathbf{z} \quad (4.12)$$



As mentioned in previous sections, the *a-priori* covariance is assumed small for the GPS satellite position estimate since the observed errors are usually small and the corrections that the WAAS message format [RTCA159] supports is limited to  $\pm 128$  meters. A numerically small *a-priori* covariance limits the sensitivity of the estimate to poor geometry.

Figure 4.5 shows a GEO orbit snapshot time history with a fixed *a-priori* covariance set at  $(10 \text{ km})^2$  for each of the XYZ axes and  $(1 \text{ km})^2$  for the clock. The measurement covariance was the same as that used in Section 3.5.2 (Figure 3.9). The only difference is that instead of using an average parameter set across all receivers, the model used individual receiver characteristics to model the measurement covariances. Figure 4.5 is the orbital variation from the average on each axis. The initial convergence period of roughly 1 minute (60 measurement epochs) is not shown. Over this period a ‘walk-in’ from up to 40 km of initial error occurs for each axis.

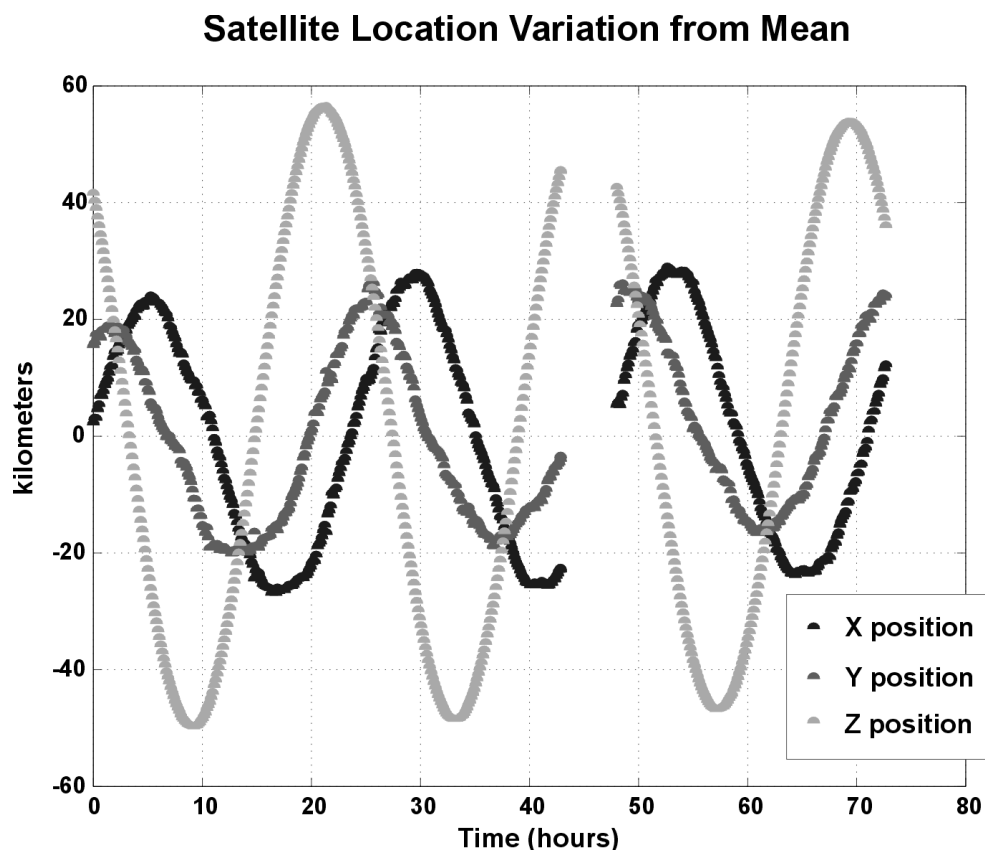
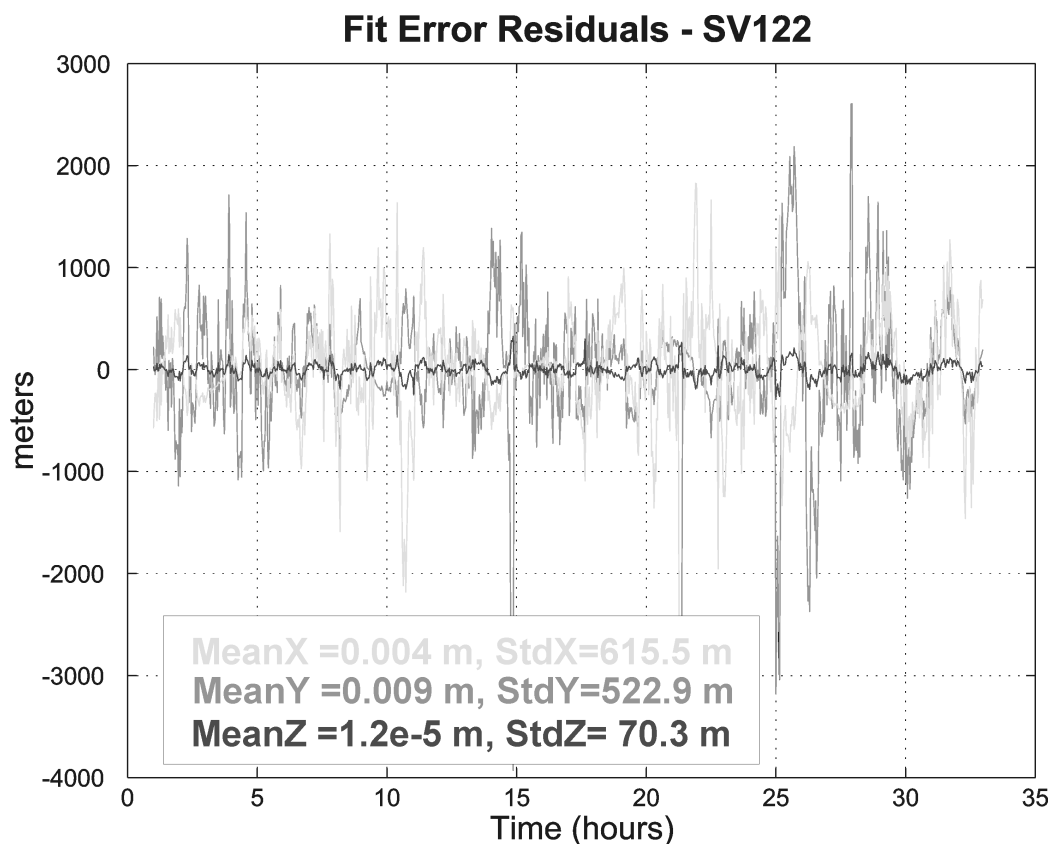


Figure 4.5: GEO Orbit Position Variation From Mean Location

Of particular note in Figure 4.5 is the variation of the satellite about the nominal orbital path. By using a simple orbit path fit, which will be discussed later in this chapter, the nominal orbital path can be subtracted from the path in Figure 4.5. The data outages in Figure 4.5 are due to reference stations going off-line for short periods. The residual between the snapshot and the orbit fit is shown in Figure 4.6. The residuals are very large due to the nearly unbounded *a-priori* covariance used in the snapshot solution. The next section details an algorithm for the adaptive solution for the *a-priori* covariance.



**Figure 4.6: Snapshot Orbit Solution Residual. *A-priori* Covariance Used:  $(10 \text{ km})^2$  X,  $(10 \text{ km})^2$  Y,  $(10 \text{ km})^2$  Z and  $(1 \text{ km})^2$  for the Clock.**

In contrast to GPS orbits, the variation of the orbit for a GEO satellite combined with the lack of precise reference orbit information limits the usefulness of a fixed, small *a-priori* covariance value. The variations in satellite position indicated by Figures 4.1 and 4.5 can

span 50-100 kilometers in each axis under nominal conditions. This motivated the development of the adaptive *a-priori* covariance estimator.

#### 4.1.3 A-PRIORI COVARIANCE ESTIMATION AND PROPAGATION

The first step in establishing an *a-priori* estimate and propagation is to find the satellite position and velocity state estimate error covariance matrix. The state estimate error covariance matrix,  $\mathbf{P}_{MV}$ , which describes the sensitivity of the solution for  $\hat{\mathbf{x}}_{MV}$  to measurement errors is:

$$\begin{aligned} P_{MV} &= E\left[(\mathbf{x} - \hat{\mathbf{x}}_{MV})(\mathbf{x} - \hat{\mathbf{x}}_{MV})^T\right] \\ &= (\Lambda^{-1} + \mathbf{H}^T \mathbf{W}^{-1} \mathbf{H})^{-1} \mathbf{H}^T \mathbf{W}^{-1} E[\mathbf{v} \mathbf{v}^T] \mathbf{W}^{-1} \mathbf{H} (\Lambda^{-1} + \mathbf{H}^T \mathbf{W}^{-1} \mathbf{H})^{-1} \\ &= (\Lambda^{-1} + \mathbf{H}^T \mathbf{W}^{-1} \mathbf{H})^{-1} \mathbf{H}^T \mathbf{W}^{-1} \text{Cov}(\mathbf{v}) \mathbf{W}^{-1} \mathbf{H} (\Lambda^{-1} + \mathbf{H}^T \mathbf{W}^{-1} \mathbf{H})^{-1} \end{aligned} \quad (4.13)$$

Again, selecting the weighting matrix,  $\mathbf{W}$ , as the covariance of the measurement errors,  $\text{Cov}(\mathbf{v})$ , we have:

$$\begin{aligned} P_{MV} &= (\Lambda^{-1} + \mathbf{H}^T \mathbf{W}^{-1} \mathbf{H})^{-1} (\mathbf{H}^T \mathbf{W}^{-1} \mathbf{H}) (\Lambda^{-1} + \mathbf{H}^T \mathbf{W}^{-1} \mathbf{H})^{-1} \\ &= (\Lambda^{-1} + \mathbf{H}^T \mathbf{W}^{-1} \mathbf{H})^{-1} \end{aligned} \quad (4.14)$$

The form of Equation (4.13) contains a combination of the measurement error covariance ( $\mathbf{W}$ ) and the *a-priori* covariance,  $\Lambda^{-1}$ . The estimate of the *a-priori* covariance can be obtained by looking at the orbit determination problem as a discrete-time linear system:

$$\mathbf{x}_k = \Phi_{k-1} \mathbf{x}_{k-1} + \Gamma_{k-1} \mathbf{w}_{k-1} \quad (4.15)$$

where  $\mathbf{x}_k$  is the state vector at epoch  $k$ ,  $\Phi_{k-1}$  is the state transition matrix, and  $\mathbf{w}_{k-1}$  is known as the process noise. It is assumed that  $\Phi$  and  $\Gamma$  are known and that the initial state,  $\mathbf{x}_0$ , is an unknown Gaussian random variable prescribed by its mean value and the initial covariance matrix,  $\mathbf{P}_0$ :

$$\begin{aligned}
E[\mathbf{x}_0] &= \mathbf{m}_0 \\
E[(\mathbf{x}_0 - \mathbf{m}_0)(\mathbf{x}_0 - \mathbf{m}_0)^T] &= \mathbf{P}_0
\end{aligned} \tag{4.16}$$

The process noise is assumed to be a zero-mean Gaussian random sequence:

$$\begin{aligned}
E[\mathbf{w}_k] &= \mathbf{0} \\
E[\mathbf{w}_k \mathbf{w}_k^T] &= \mathbf{Q}_k'
\end{aligned} \tag{4.17}$$

The disturbance input covariance matrix,  $\mathbf{Q}_k'$ , could be symmetric, implying instantaneous cross-correlation of disturbances. However, if  $\mathbf{Q}_k'$  is diagonal, then components of the disturbance input are uncorrelated with each other.

The expected value of the state at the  $k^{\text{th}}$  epoch is:

$$\begin{aligned}
E[\mathbf{x}_k] &= E[\Phi_{k-1}\mathbf{x}_{k-1} + \Gamma_{k-1}\mathbf{w}_{k-1}] \\
&= \Phi_{k-1}E[\mathbf{x}_{k-1}] + \Gamma_{k-1}E[\mathbf{w}_{k-1}] \\
&= \Phi_{k-1}\mathbf{m}_{k-1}
\end{aligned} \tag{4.18}$$

The result in Equation (4.18) demonstrates that, in this case, the known mean values are indistinguishable from deterministic values. The equation propagates the expected value of the state, with the understanding that random perturbations from the expected value are likely to occur [Stengel].

The covariance of the state errors can be propagated in a similar manner. From Equations (4.15) and (4.18) the outer product of the state errors at the  $k^{\text{th}}$  epoch is:

$$\begin{aligned}
(\mathbf{x}_k - \mathbf{m}_k)(\mathbf{x}_k - \mathbf{m}_k)^T &= [\Phi_{k-1}(\mathbf{x}_{k-1} - \mathbf{m}_{k-1}) + \Gamma_{k-1}\mathbf{w}_{k-1}] \cdot \\
&\quad [\Phi_{k-1}(\mathbf{x}_{k-1} - \mathbf{m}_{k-1}) + \Gamma_{k-1}\mathbf{w}_{k-1}]^T
\end{aligned} \tag{4.19}$$

Take the expected values of both sides:

$$\begin{aligned}
 E[(\mathbf{x}_k - \mathbf{m}_k)(\mathbf{x}_k - \mathbf{m}_k)^T] &= \mathbf{P}_k \\
 &= E[\Phi_{k-1}(\mathbf{x}_{k-1} - \mathbf{m}_{k-1})(\mathbf{x}_{k-1} - \mathbf{m}_{k-1})^T \Phi_{k-1}^T \\
 &\quad + \Gamma_{k-1} \mathbf{w}_{k-1} \mathbf{w}_{k-1}^T \Gamma_{k-1}^T \\
 &\quad + \Phi_{k-1}(\mathbf{x}_{k-1} - \mathbf{m}_{k-1}) \mathbf{w}_{k-1}^T \Gamma_{k-1}^T \\
 &\quad + \Gamma_{k-1} \mathbf{w}_{k-1} (\mathbf{x}_{k-1} - \mathbf{m}_{k-1})^T \Phi_{k-1}^T] \\
 &= \Phi_{k-1} \mathbf{P}_{k-1} \Phi_{k-1}^T + \Gamma_{k-1} \mathbf{Q}'_{k-1} \Gamma_{k-1}^T \\
 &\quad + \Phi_{k-1} \mathbf{M}_{k-1} \Phi_{k-1}^T + \Gamma_{k-1} \mathbf{M}_{k-1}^T \Gamma_{k-1}^T
 \end{aligned} \tag{4.20}$$

where the cross-correlation between state errors and disturbance input:

$$\mathbf{M}_{k-1} = E[(\mathbf{x}_{k-1} - \mathbf{m}_{k-1}) \mathbf{w}_{k-1}^T] \tag{4.21}$$

is identically zero if  $\mathbf{w}_{k-1}$  is a white-noise sequence. This leaves the result for the propagation of the state error covariance as:

$$\mathbf{P}_k = \Phi_{k-1} \mathbf{P}_{k-1} \Phi_{k-1}^T + \Gamma_{k-1} \mathbf{Q}'_{k-1} \Gamma_{k-1}^T \tag{4.22}$$

This result gives a formulation for propagation of the state error covariance. The process noise term,  $\Gamma_{k-1} \mathbf{Q}'_{k-1} \Gamma_{k-1}^T$ , is the contributing covariance to the *a-priori* state estimate. Equation (4.22) can be used to propagate the real-time *a-priori* state estimate covariance,  $\Lambda_k$ , as shown in Equation (4.23).

$$\begin{aligned}
 \mathbf{P}_k &= \Lambda_k \\
 \Lambda_k &= \Phi_{k-1} \Lambda_{k-1} \Phi_{k-1}^T + \Gamma_{k-1} \mathbf{Q}'_{k-1} \Gamma_{k-1}^T
 \end{aligned} \tag{4.23}$$

The process noise term,  $\Gamma_{k-1} \mathbf{Q}'_{k-1} \Gamma_{k-1}^T$ , is due to the influence of unmodeled measurement residual terms on the pseudorange measurement. As discussed in [Dai97], the overwhelming majority of the residual error in the pseudorange measurement is multipath and receiver noise. While the receiver noise can mostly be modeled assuming that the errors are a Gaussian random variable [Leon-Garcia] (i.e., the process is white), the multipath errors are much more difficult to model. Multipath errors are correlated in time

and vary by the antenna type, the surroundings of the antenna, and the tracking loops inside the receiver. All of these factors make multipath one of the most difficult error sources to model in GPS. The process noise term,  $\Gamma_{k-1} \mathbf{Q}'_{k-1} \Gamma_{k-1}^T$ , is used to compensate for multipath measurement uncertainty without directly modeling the source of multipath.

Figure 4.7 shows the application of the covariance propagation method, including the position solution estimate. Included in this figure is the initial covariance which is based on an initial mean value as described by Equation (4.16). The assumed initial mean value for the position is 10 km. The assumed initial mean value for the clock term is 1 km.

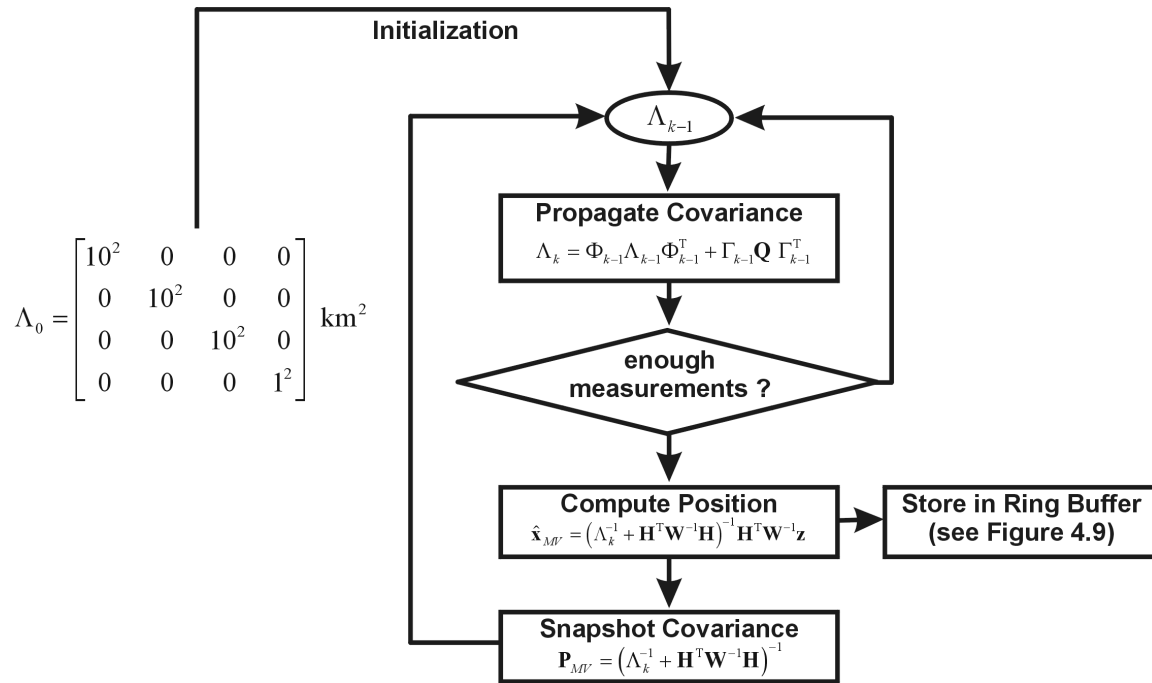


Figure 4.7: Covariance Real-Time Propagation Logic

The major factors in the size of the *a-priori* covariance matrix are the values of the measurement covariance,  $\mathbf{W}$ , and the uncertainties of the residual station errors,  $\mathbf{Q}'_k$ .

#### 4.1.4 BATCH FILTER DESIGN

GEO pseudorange residuals can be fit with simple functions to remove most of the systematic errors introduced by orbit and clock variations [Davidson]. A combination of pseudorange bias, slope, and harmonic terms was used for the fit. The reasoning behind this result is that the clock variation should be roughly linear over time, due to the utilization of atomic clocks at the GPS reference stations. This suggests that a fit with simple harmonic and linear functions in the satellite position domain should also be feasible.

The orbital characteristics can be captured in the first few harmonics of the orbital period. Figure 4.8 shows the Power-Spectral-Density of a representative orbit (GPS from IGS). This figure indicates that most of the orbital energy is contained within the first few orbital harmonics. By the 5<sup>th</sup> orbital harmonic, the energy level is roughly one-billionth of the total.

**Normalized Power Spectral Density of GPS Satellite (Source:IGS)**

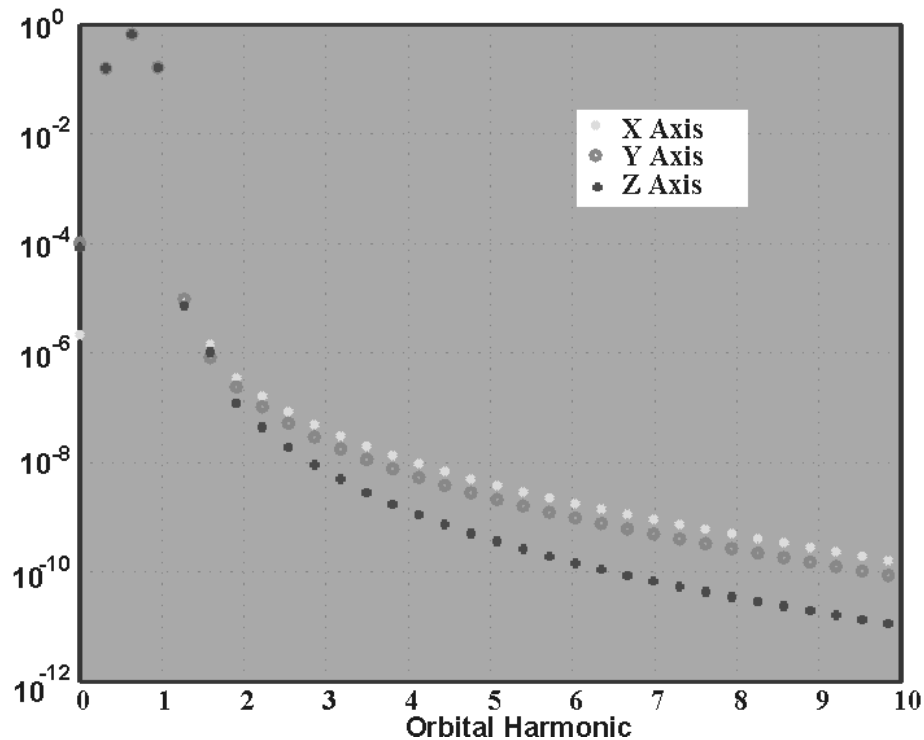


**Figure 4.8: Energy in the Perturbations As A Function of Orbital Harmonics**

Extending this result to the GEO position solutions, the time-history of each of the position components (XYZ) were fit to the following function:

$$f(t) = a_0 + a_1 t + a_2 \sin(\omega t) + a_3 \cos(\omega t) + a_4 \sin(2\omega t) + a_5 \cos(2\omega t) + a_6 \sin(3\omega t) + a_7 \cos(3\omega t) + a_8 \sin(4\omega t) + a_9 \cos(4\omega t) \quad (4.24)$$

Where  $f(t)$  is the functional fit of one of the XYZ orbital elements and  $\omega$  is the orbital period of the satellite. After determining coefficients for Equation (4.24), the velocity can be determined by differentiating the equation:

$$\begin{aligned} \dot{f}(t) = & a_1 + a_2 \omega \cos(\omega t) - a_3 \omega \sin(\omega t) + 2a_4 \omega \cos(2\omega t) - 2a_5 \omega \sin(2\omega t) \\ & + 3a_6 \omega \cos(3\omega t) - 3a_7 \omega \sin(3\omega t) \\ & + 4a_8 \omega \cos(4\omega t) - 4a_9 \omega \sin(4\omega t) \end{aligned} \quad (4.25)$$

This gives two linear equations to relate the orbital harmonics with linear drift to the XYZ position and velocity orbital terms. This solution can be used to initiate a propagation of the orbit as described in Chapter 2.

The batch fit approach has been used in this research both as a method for determining the ‘true’ orbital path and as part of the filter for estimating the position. There was no independent source used to evaluate the accuracy of the orbit. This is consistent with the approach used when the primary goal of the GEO position solution is to minimize the range errors of the user.

Figure 4.9 shows the flow of calculations from position estimate to the next epoch. The first step of this batch-fit process is to collect GEO position snapshot estimates to form a time history. This time-history is stored in a ring-buffer. A ring-buffer is a storage technique that contains a time-history with a fixed number of memory locations. Once all of the locations are filled, new data replaces the oldest data at the ‘head’ (see Figure 4.9). After each update in the ring buffer, both the head and the tail are incremented.



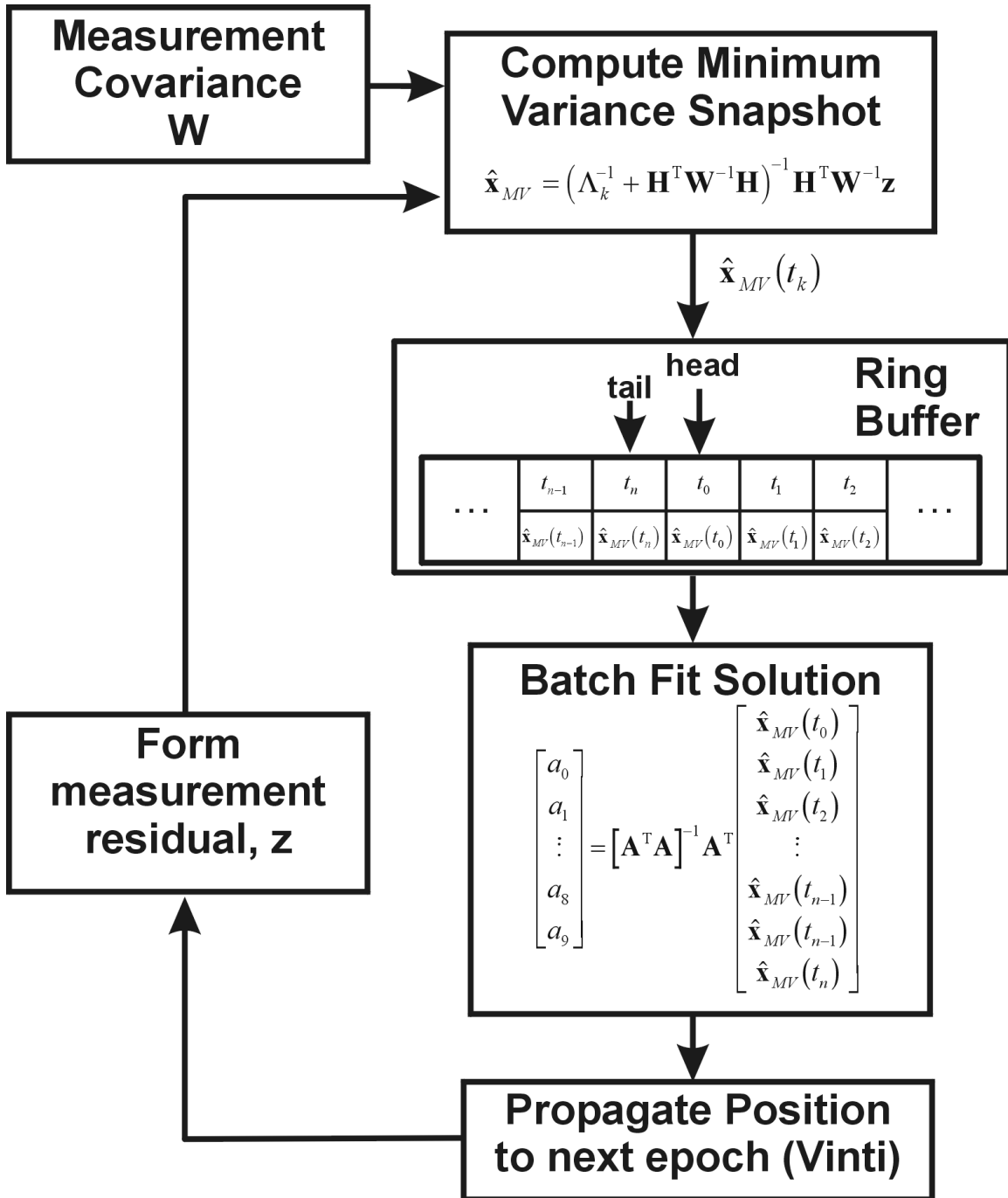


Figure 4.9: Flow-Diagram of the Batch-Fit Solution and Solution Propagation

Data lengths between one and 24 hours were used in a least-squares fit. The minimum amount of data necessary was approximately 4 hours based on sufficient observation of the orbit harmonics. Nominally, a 12-hour batch length was used to fit the orbital positions.

The goal of the batch fit procedure is to determine the parameters,  $[a_1, a_2, \dots, a_8, a_9]$ . The least squares matrix  $\mathbf{A}$  (Figure 4.9) is used in a least squares fit to solve for the parameters. Matrix  $\mathbf{A}$  is derived from the linear equation in Equation (4.24) as:

$$\mathbf{A} = \begin{bmatrix} 1 & t_0 & \sin(\omega t_0) & \cos(\omega t_0) & \cdots & \sin(4\omega t_0) & \cos(4\omega t_0) \\ 1 & t_1 & \sin(\omega t_1) & \cos(\omega t_1) & \cdots & \sin(4\omega t_1) & \cos(4\omega t_1) \\ \vdots & \vdots & \vdots & \vdots & \vdots & \vdots & \vdots \\ 1 & t_n & \sin(\omega t_n) & \cos(\omega t_n) & \cdots & \sin(4\omega t_n) & \cos(4\omega t_n) \end{bmatrix} \quad (4.26)$$

Once the fit parameters are determined, a current-epoch position and velocity solution is determined from Equations (4.24) and (4.25). This solution is propagated to a future epoch using the Vinti analytically integrated method described in Section 2.4.4 and Appendix A.

Figure 4.10 shows the progressive reduction of the residuals between the propagated solution and the batch solution over time. Not only are the slowly varying orbit parameters ( $> 1$  hour time-scale) reduced over this period, but the high-frequency terms are reduced as well. This is due to the reduction of the *a-priori* covariance term. The process noise term,  $\Gamma_{k-1} \mathbf{Q}'_{k-1} \Gamma_{k-1}^T$ , controls the rate of the *a-priori* state covariance reduction. If the *a-priori* covariance decreases too quickly, the low-frequency terms converge more slowly since the measurement variance exceed the actual position knowledge. The balancing of the *a-priori* covariance convergence rate is critical in the batch-fit process. If the rate is set too steep then the fit will track local biases. If the rate is too shallow, then the estimates will be dominated by measurement noise.

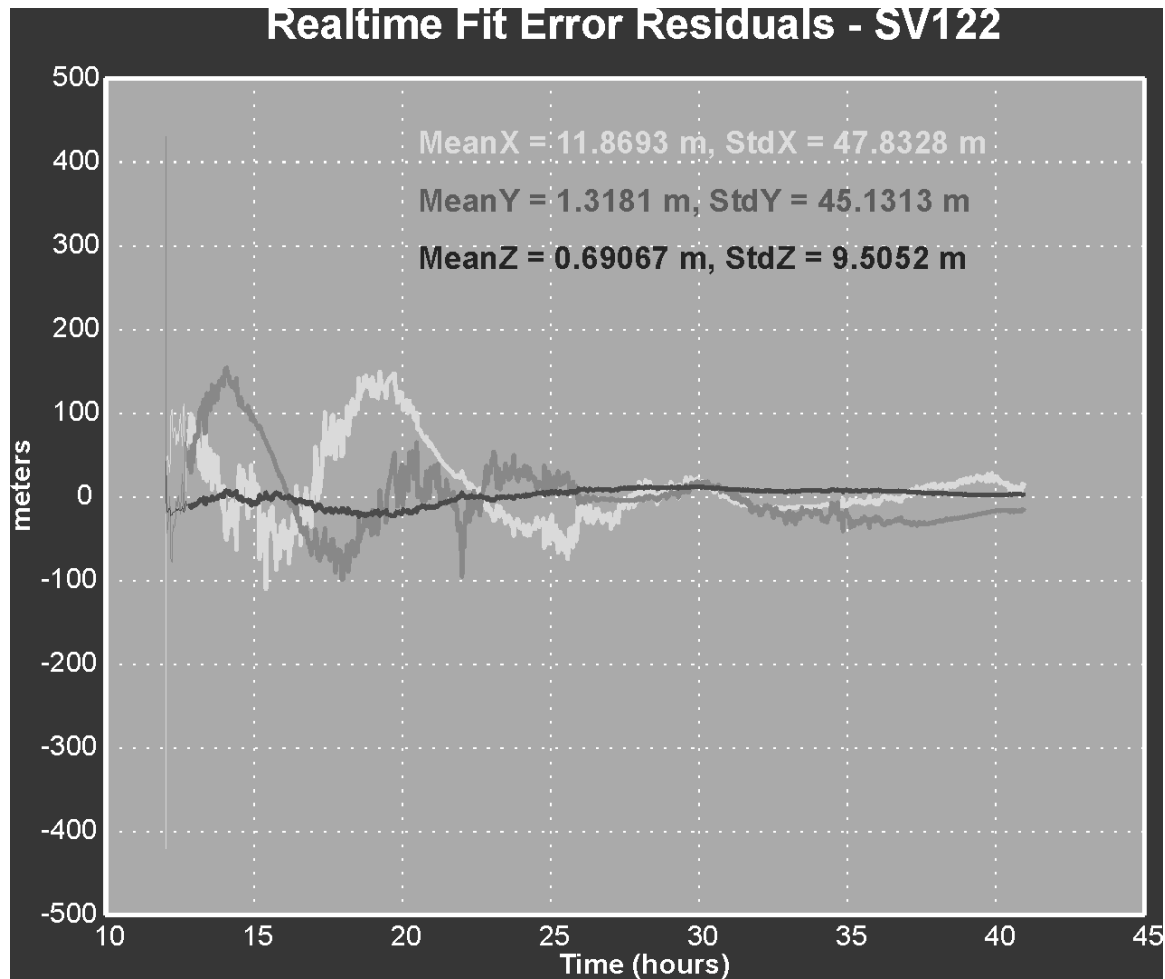


Figure 4.10: Orbit Component Residuals After the Filter

#### 4.1.5 PSEUDORANGE RESIDUALS

Based on results from the previous section, the post-orbit fit pseudorange residuals can be determined. The synchronized pseudorange residuals of Equation (3.2) were corrected for the orbit and clock residuals solved with estimation routines detailed in previous sections. The residuals shown in Figure 4.11 were taken from a single station over a 30-hour period with the dual GPS/GEO receiver in Bangor, Maine. The beginning of this data segment was taken after the initial batch-fit period of 12 hours. The statistics of the pseudorange have a standard deviation less than two carrier wavelengths. The solution is for the satellite SV122 located at 54 degrees of West Longitude.

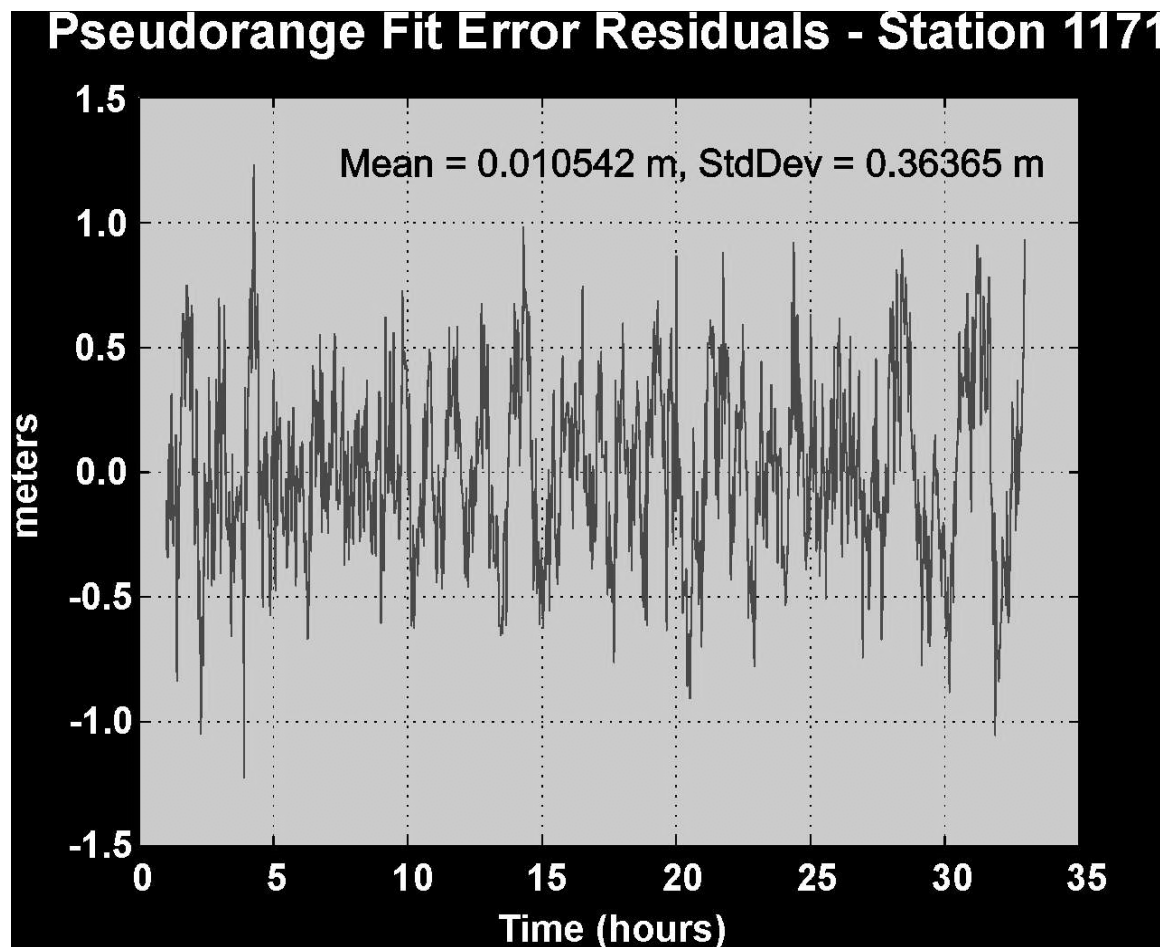


Figure 4.11: Single Station Real-Time Pseudorange Residual After Orbit Solution

Figure 4.12 are the fit residuals for all of the dual GPS/GEO stations in the NSTB. Some of the poorly placed antennae (in terms of multipath disruption) in the network cause large variations from the results seen in Figure 4.11. However, the overall error distributions are contained within roughly 2 meters with standard deviation less than 1 meter. It is critical to note now that even with 10-100 meter snapshot satellite orbit residuals (Figure 4.10) the pseudorange residuals are generally smaller than two meters (Figures 4.11 and 4.12). This observation supports the hypothesis put forth at the beginning of this chapter that small range residuals can be achieved without providing the minimum satellite position error.

## Pseudorange Residuals (m) - SV122 at 6 Stations

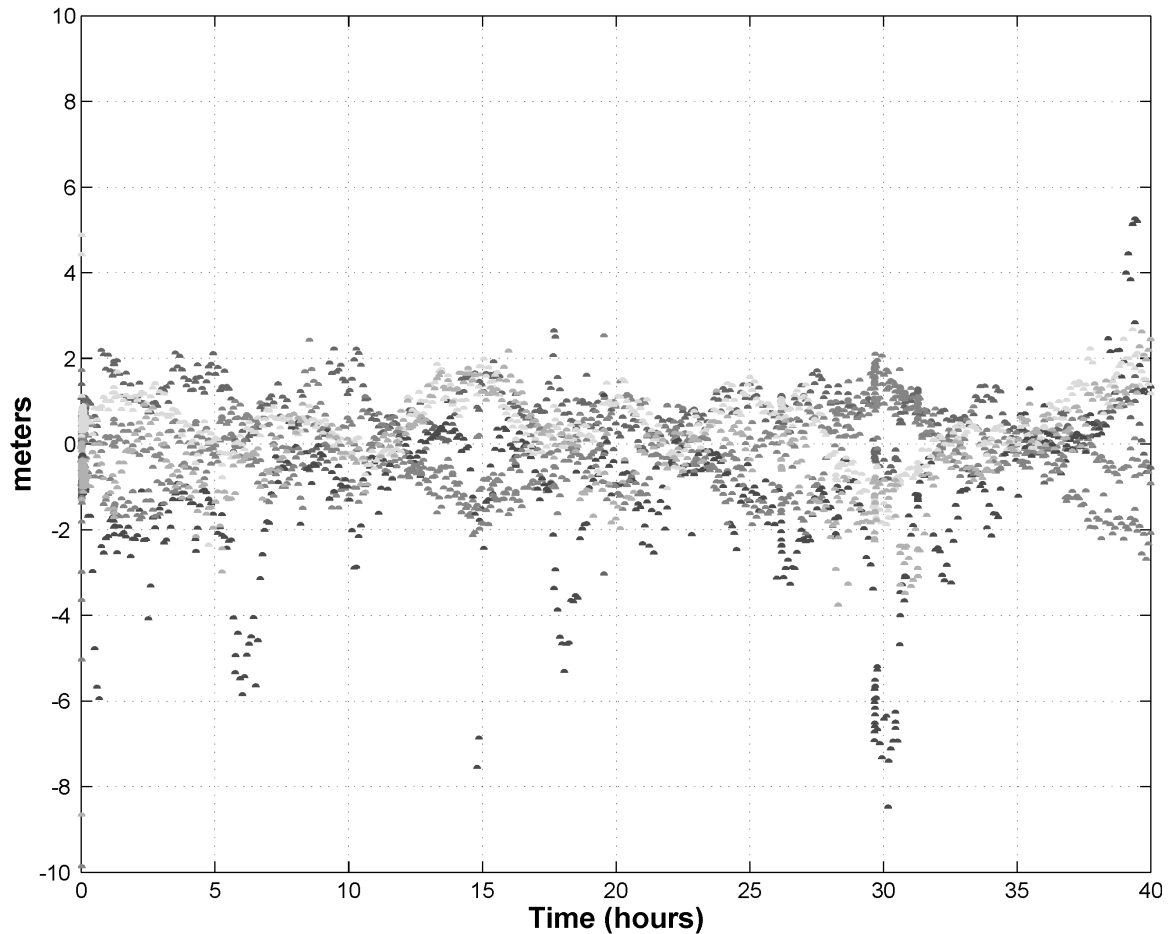


Figure 4.12: Pseudorange Residuals for All Tracking Stations

Figure 4.12 shows that the GEO satellite orbit estimation routine described here provides ranging accuracies good to within a few meters.

### 4.1.6 GEOSTATIONARY UDRE

Along with the position of the GEO satellite and the offset of its clock, the WAAS message broadcasts the confidence of combined satellite and clock as the User Differential Range Error (UDRE). The UDRE is a single number but it must be valid for any user inside the coverage region of WAAS. The discussion here is adapted from the approach taken for GPS satellites in [Tsai99]. The coverage region considered herein is bounded by the extent of the network of reference stations. To determine the UDRE, first the satellite and clock

estimate covariance,  $\mathbf{P}_{UDRE}$ , is projected onto each of the reference station's Line-of-Sight (LOS) to the satellite:

$$\sigma_{UDRE,i}^2 = \mathbf{1}_i^T \cdot \mathbf{P}_{UDRE} \cdot \mathbf{1}_i \quad (4.27)$$

where  $\mathbf{1}_i$  is the LOS from the  $i^{\text{th}}$  reference station to the satellite and  $\sigma_{UDRE,i}^2$  is the projected variance at the  $i^{\text{th}}$  reference station. The UDRE variance is found as the maximum value across all of the reference stations:

$$\sigma_{UDRE}^2 = \max(\sigma_{UDRE,1}^2, \sigma_{UDRE,2}^2, \sigma_{UDRE,3}^2, \dots, \sigma_{UDRE,n-1}^2, \sigma_{UDRE,n}^2) \quad (4.28)$$

where  $n$  is the number of reference stations tracking the given GPS satellite.

In the same fashion, the UDRE for the GEO satellite is formed. The snapshot covariance of Equation (4.14) is used for the source of the satellite and clock estimate covariance,  $\mathbf{P}_{UDRE}$ . This is not the approach taken in [Tsai99] where the measurement covariance from the reference stations is combined with a smoothed satellite and clock covariance. The smoothed covariance takes into account the time-correlation of the satellite and clock estimates and is significantly smaller than the snapshot covariance used for the GEO satellite. As a result, the UDRE values for the GEO satellite are much larger than the ones using the GPS estimation technique.

Figure 4.13 shows the UDRE values calculated with Equation (4.28) for a GEO satellite from the satellite and clock estimate covariance of Equation (4.14). The dark line represents the UDRE values straight from Equation (4.28). These values proved to be overly conservative due to the snapshot covariance magnitude. These values were adjusted downward by a factor of eight to closely correspond to the pseudorange residuals shown in Figures 4.11 and 4.12. The lower UDRE values were used for evaluating performance in Section 4.2. It is certain that lower UDRE values could be achieved by adopting a method closer to [Tsai99] where a smoothed estimate of the satellite and clock covariance dramatically reduces the UDRE variance.

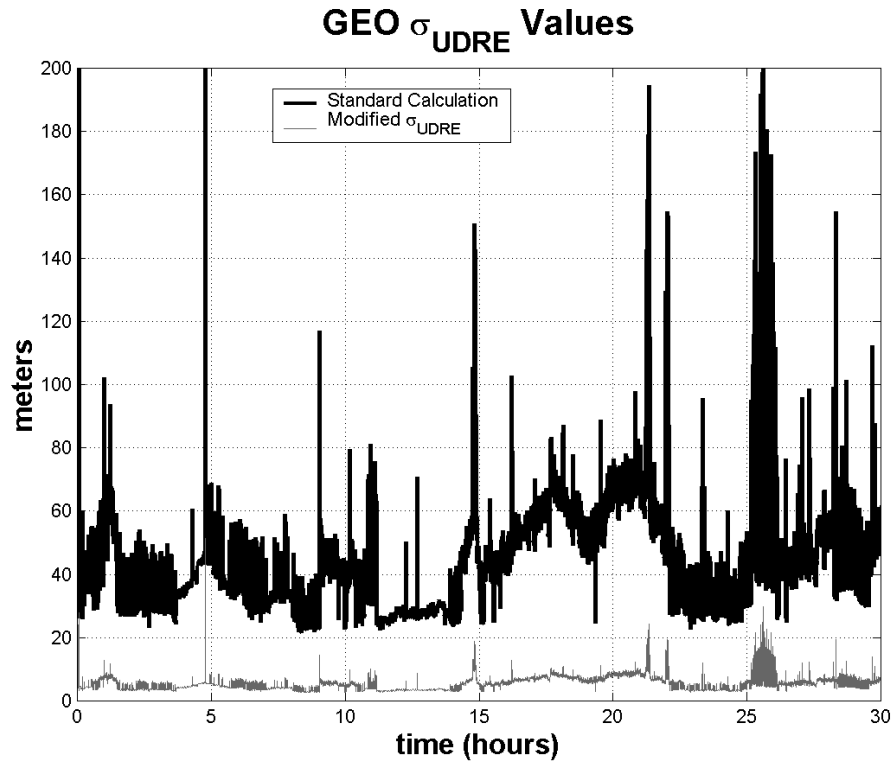


**Figure 4.13: Example GEO  $\sigma_{UDRE}$ .** The Dark Line Represents the Value Returned by the  $\sigma_{UDRE}$  Estimate Algorithm. The Light Line was an Adjustment based on the Observation of Lower Range Residuals.

The following sections apply the results of GEO ranging to users in the NSTB reference network to evaluate system improvement.

## 4.2 AVAILABILITY AND INTEGRITY

As introduced in Chapter 1, there exists a quantitative relationship between system accuracy, integrity and availability. Section 1.9 describes in detail this relationship.

The following sections will compare the WAAS solution availability for users without GEO ranging against with GEO ranging. The Stanford TMS is used to process NSTB reference stations data for these results. First, baseline availability performance is established without GEO ranging for users using NSTB data. These availability results are compared to the same users utilizing GEO ranging. It is also demonstrated that the solution provides integrity for all cases (i.e., no HMI).

### 4.2.1 BASELINE AVAILABILITY CONFIGURATION

At the time of publication of this work, there are 28 active and healthy GPS satellites on-orbit. This exceeds the specified nominal architecture of 21 primary satellites plus three active spares [ICD200C]. These extra satellites are due to several Block II satellites exceeding their design lifetimes. In March of 1999, [GPSWorld99] reported that at least six satellites had reached 10 years in-orbit, from a mean-mission projected goal of 6 years. The extra satellites are of great benefit to the user community providing favorable geometry from users to satellites almost all of the time. In this environment where the number of GPS satellites exceed the specifications there is little or no need for GEO ranging. It has been shown that WAAS availability and integrity requirements can be met without a GEO ranging solution [Tsai99, Hansen99, Walter99].

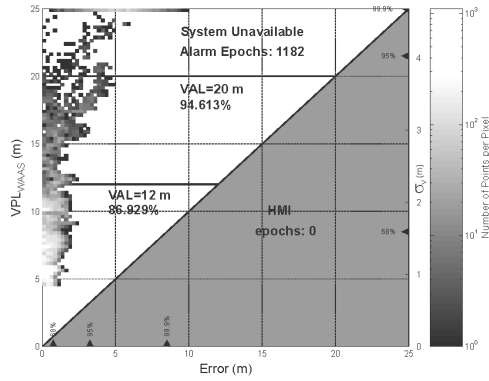
However, the DoD and the JPO have not guaranteed these excess satellites in the future. Therefore, it is assumed for the availability studies in this chapter that the nominal satellite configuration will be available with a single satellite failure. This nominal-minus-one satellite configuration was achieved by removing five satellites from the constellation of 28. The remaining satellites were chosen to be evenly distributed so that no periods with poor satellite geometry would remain in the solution.

The availability charts in Figure 4.15 utilize a nominal-minus-one satellite configuration (i.e., 23 satellites) with actual NISTB data over six hours. The results in Figure 4.15 do not include any GEO satellite ranging information for the user position solution. The results are from all of the dual GPS-GEO reference stations in the NISTB that are visible to the satellite SV122 (AOR-W). The availability is broken into two different levels. The first availability is defined with a 12-meter vertical alert limit. The second availability is defined with a 20-meter vertical alert limit. The 12-meter vertical alert limit has been used as a possible candidate for precision approach landings with a 200 foot decision height equivalent to current Category Phase I requirements [Kayton]. The 20-meter vertical alert limit is a more modest precision approach capability that may be better matched to WAAS. The availability results of Figure 4.15 are summarize in Tables 4.1 and 4.2. Table 4.1

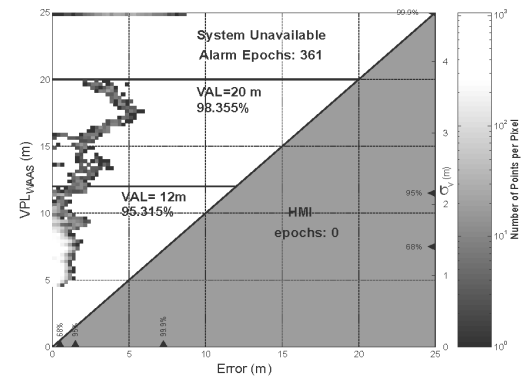


recaps the availability results with a VAL=20 meters and Table 4.2 gives the results with a VAL=12 meters.

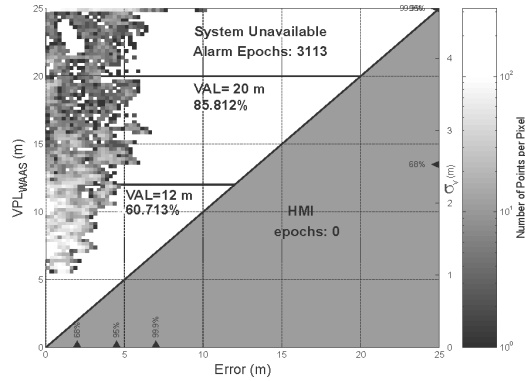
Vertical Performance at Anderson, SC 0x0A71 (21941 seconds)



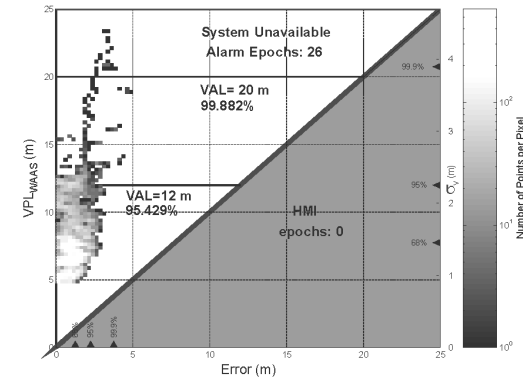
Vertical Performance at Dayton, OH 0x0E71 (21941 seconds)



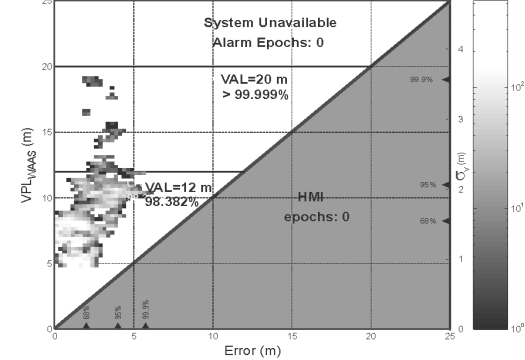
Vertical Performance at Miami, FA 0x0F71 (21941 seconds)



Vertical Performance at Bangor, ME 0x1171 (21941 seconds)



Vertical Performance at Gander, Newfoundland 0x1F71 (21941 seconds)



Vertical Performance at Winnipeg, Manitoba 0x2071 (21940 seconds)

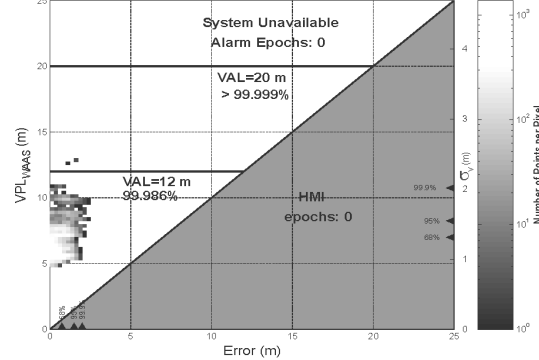


Figure 4.14: WAAS Availability Before Inclusion of GEO-Ranging

Station	VAL=20 meters (%)
Anderson, SC (0x0A71)	94.613
Dayton, OH (0x0E71)	98.355
Miami, FL (0x0F71)	85.812
Bangor, ME (0x1171)	99.882
Gander, Newfoundland (0x1F71)	>99.999
Winnipeg, Manitoba (0x2071)	>99.999

**Table 4.1: Availability Before Inclusion of GEO-Ranging with a VAL=20 meters**

Station	VAL=12 meters (%)
Anderson, SC (0x0A71)	86.929
Dayton, OH (0x0E71)	95.315
Miami, FL (0x0F71)	60.713
Bangor, ME (0x1171)	95.429
Gander, Newfoundland (0x1F71)	98.382
Winnipeg, Manitoba (0x2071)	99.986

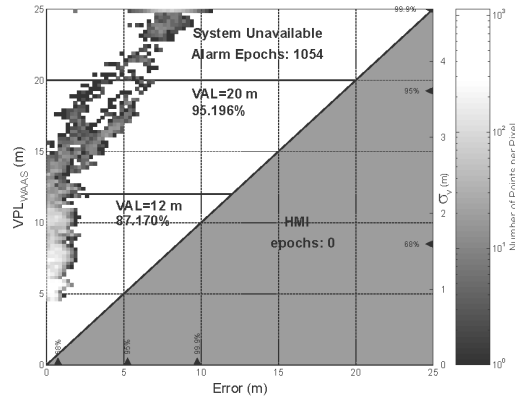
**Table 4.2: Availability Before Inclusion of GEO-Ranging with a VAL=12 meters**

The following section will add GEO ranging to the TMS calculation and determine its influence on the availability of the WAAS.

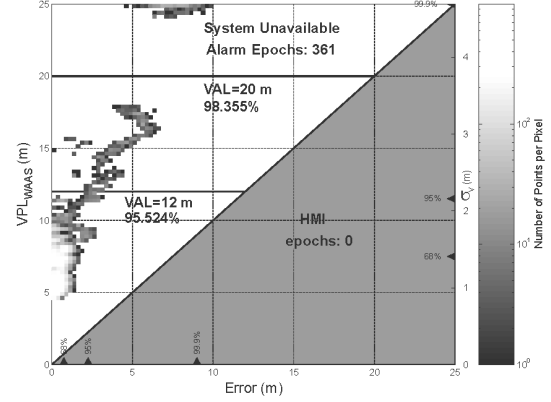
#### 4.2.2 AVAILABILITY RESULTS WITH GEOSTATIONARY RANGING

The availability charts in the previous section detailed the results of a nominal satellite-minus-one configuration. The set of results in Figure 4.16 includes the use of GEO satellite ranging. Again, the GPS satellites removed from processing consideration were chosen in such a way to maintain an even distribution across the constellation. However, the GEO satellite ranges were included in the position processing.

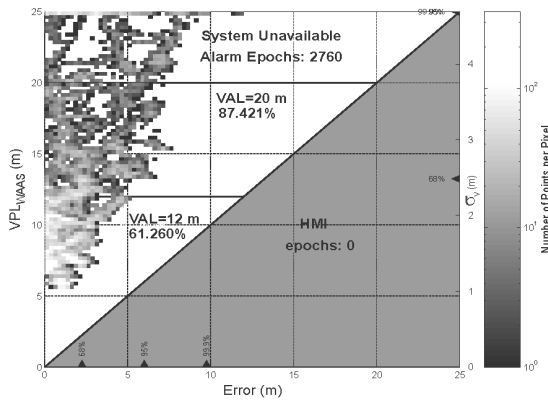
Vertical Performance at Anderson, SC 0x0A71 (21941 seconds)



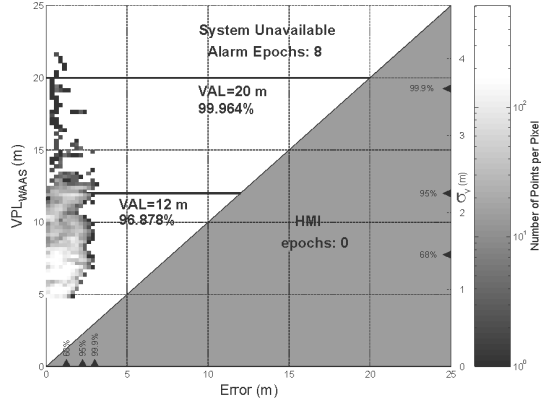
Vertical Performance at Dayton, OH 0x0E71 (21941 seconds)



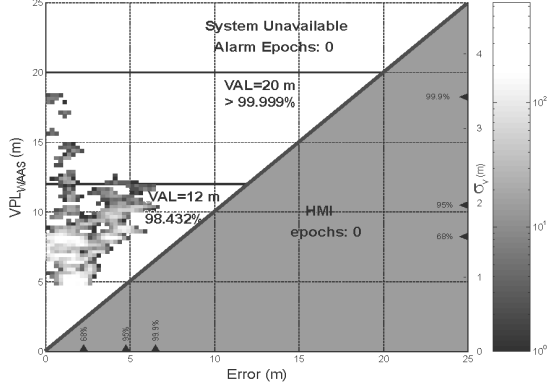
Vertical Performance at Miami, FA 0x0F71 (21941 seconds)



Vertical Performance at Bangor, ME 0x1171 (21941 seconds)



Vertical Performance at Gander, Newfoundland 0x1F71 (21941 seconds)



Vertical Performance at Winnipeg, Manitoba 0x2071 (21940 seconds)

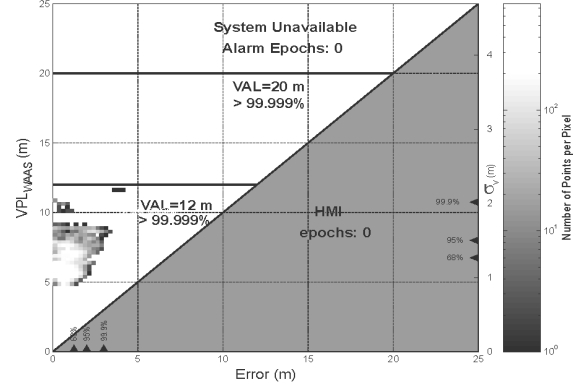


Figure 4.15: WAAS Availability After Inclusion of GEO-Ranging

Station	VAL=20 meters (%)		
	Ref	GEO	$\Delta$
Anderson, SC (0x0A71)	94.613	95.198	0.585
Dayton, OH (0x0E71)	98.355	98.355	0.000
Miami, FL (0x0F71)	85.812	87.421	1.609
Bangor, ME (0x1171)	99.882	99.964	0.082
Gander, Newfoundland (0x1F71)	>99.999	>99.999	0.000
Winnipeg, Manitoba (0x2071)	>99.999	>99.999	0.000
Maximum Improvement			1.609

**Table 4.3: Availability After Inclusion of GEO-Ranging for a VAL=20 meters**

Station	VAL=12 meters (%)		
	Ref	GEO	$\Delta$
Anderson, SC (0x0A71)	86.929	87.170	0.241
Dayton, OH (0x0E71)	95.315	95.524	0.209
Miami, FL (0x0F71)	60.713	61.260	1.087
Bangor, ME (0x1171)	95.429	96.878	1.449
Gander, Newfoundland (0x1F71)	98.382	98.432	0.050
Winnipeg, Manitoba (0x2071)	99.986	>99.999	0.014
Maximum Improvement			1.449

**Table 4.4: Availability After Inclusion of GEO-Ranging for a VAL=12 meters**

Table 4.3 shows the availability improvement between the case with no GEO ranging (Ref column) to the case with GEO ranging (GEO column) for a VAL=20 meters. Table 4.4 is the same comparison for the VAL=12 meters. As summarized in Tables 4.3 and 4.4, there is improvement in adding the GEO ranging to the user aircraft's position solution. As indicated from the data in the table, the additional ranging source improves the availability of all but the very highest (>99.99%) of the availability cases. Also implied by these results is that the GEO satellite provides a time-invariant ranging source which will improve the availability of solutions over a wide geographic range. Integrity (i.e., no HMI) was maintained for all cases with and without GEO ranging.

# Chapter 5

## Messaging Background

As mentioned earlier, the primary reason for the GEO satellite is as a data link. This data link delivers messages which provide information to enhance the accuracy, integrity, availability and continuity of the GPS satellite signals. Utilizing a network of reference stations to estimate the errors in GPS, WAAS forms corrections to GPS and broadcasts these corrections in messages to improve accuracy for the user. Along with corrections, error bounds of those corrections are also broadcast providing integrity over standalone GPS. WAAS is expected to provide service for all phases of flight as described in [Loh, Kayton]. Figure 5.1 shows the GPS reference network, the master station that computes the GPS corrections and the data channel to the aircraft users through the GEO. The aircraft user will track GPS satellites and at least one GEO satellite. Ranging measurements to the GPS and GEO satellites are combined with differential corrections and confidence bounds broadcast in the GEO messages and processed to form the navigation solution. This chapter focuses on the GPS errors that the messages will correct as well as the design of the data link exploited by WAAS.

The WAAS Signal-In-Space (SIS) has a limited data message bandwidth of 250 bits-per-second. This data bandwidth was chosen to balance two issues. The power of the signal must be sufficient to ensure reception over the geostationary satellite footprint without jamming the GPS signal. Additionally, the signal must provide the minimum amount of

information necessary to ensure adequate accuracy and integrity for aviation users [Enge97]. The required message loss rate is specified not to exceed one part-per-thousand (0.001 or  $10^{-3}$  probability of occurrence) to ensure adequate system continuity and availability [RTCA159]. The message loss rate was chosen based on the requirement that the probability that a *safety-critical* message loss is less than  $10^{-8}$ . Safety-critical messages are broadcast when an error is detected in a GPS satellite or there are changes in the correction bounds (UDRE, GIVE). When safety-critical messages need to be broadcast they are repeated three times. The message loss rate was chosen to keep the probability of losing three messages in a row below  $10^{-8}$ . Assuming that message losses are independently distributed (see Appendix A) the probability that all three messages are lost is:  $(10^{-3} \cdot 10^{-3} \cdot 10^{-3} = 10^{-9}) < 10^{-8}$  [Enge97].

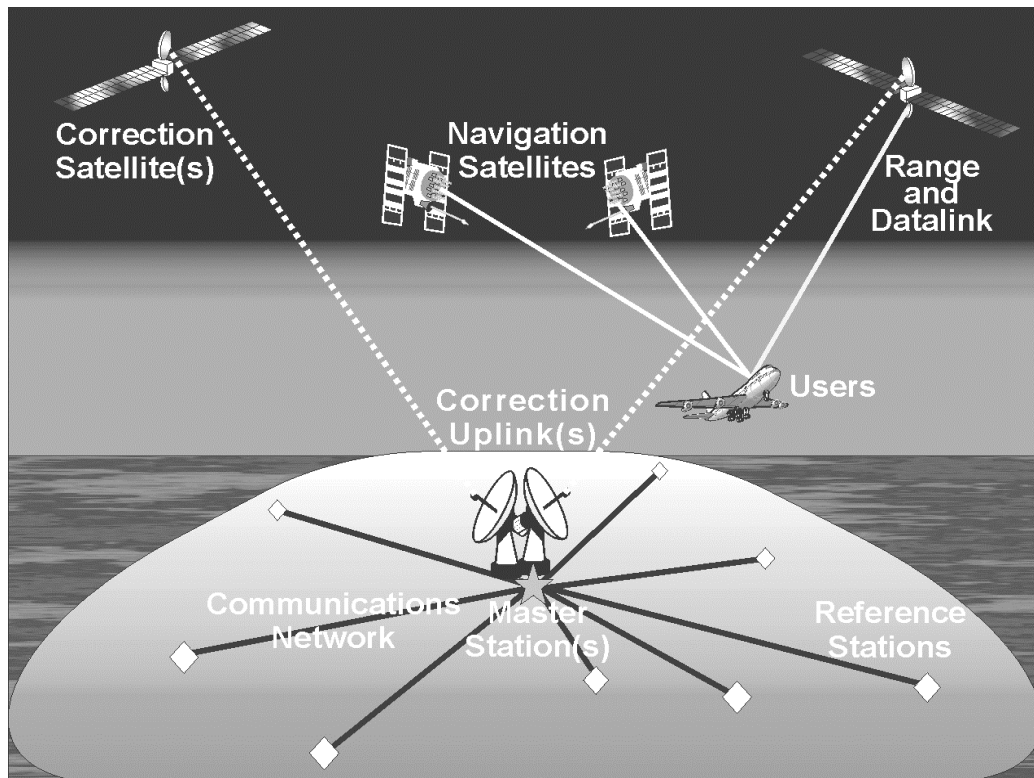


Figure 5.1: SBAS Architecture as a Data Source

The purpose of this chapter is to give an overview of the GEO as a data link. The WAAS signal design presented in previous work is delineated. This chapter briefly reviews the GPS errors and their distribution over time and space. The spatial and temporal variability of these terms ultimately set the required WAAS message bandwidth. This chapter concludes with a discussion of WAAS message content and structure followed by the theoretical and simulated message loss rates for the GEO signal.

## 5.1 GPS ERRORS: TEMPORAL AND SPATIAL VARIATIONS

The GPS errors that will be corrected by the WAAS messages have both spatial and temporal components. Spatial variations are due to error components with very little or no variation in time. An example of a spatial variation is the ephemeris errors with XYZ components. An important feature of spatial variations in this case is that they are sensitive to both the position of the satellite as well as the position of the aviation user. Temporal variations have only a time component.

The left-hand bar of Figure 5.2 is representative of the mean RMS errors that are seen on the GPS SPS pseudorange. The right-hand bar in Figure 5.2 represents the mean RMS errors expected for the WAAS receiver. The most dramatic improvement is in the satellite clock. However, there is a significant reduction in ionospheric errors as well. Reductions in the other error components are assumed because of the utilization of WAAS. When clock, ephemeris and ionospheric errors are reduced, the tropospheric, multipath and receiver noise errors have a higher proportion of the total error. Since tropospheric, multipath and receiver errors are not corrected by WAAS these can be grouped together as “user unique errors.” These user unique errors are handled either by a model implemented in the receiver or limited by the receiver designs themselves. Design issues include: Delay Lock Loop (code tracking) and Phase Lock Loop (phase tracking) bandwidths; correlator spacing; as well as other concerns [Parkinson96, Chapter 8].

Antenna design and placement on an aircraft can dramatically influence both ranging accuracy and message loss rate. These antenna design elements are beyond the scope of this thesis and are included as topics for future work in Chapter 7.

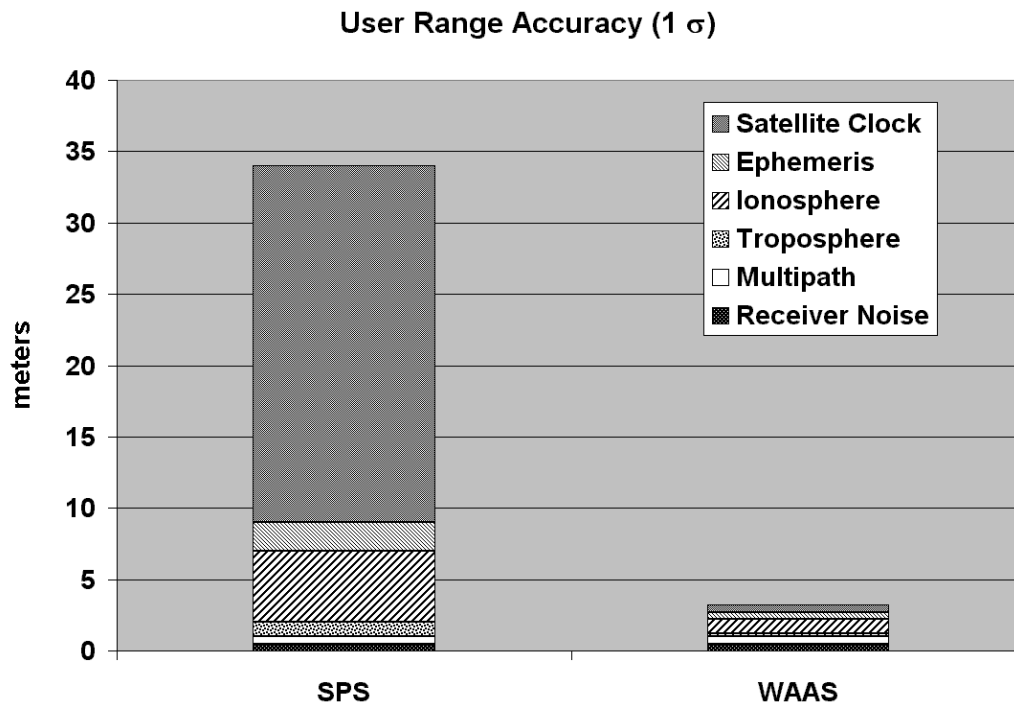


Figure 5.2: GPS Errors Compared to WAAS

The following sections will give a brief description of the observed spatial and temporal variations in the nominal GPS signals.

### 5.1.1 CLOCK AND EPHEMERIS (SA) ERRORS

The satellite clock for an unauthorized user is corrupted by an intentional degradation factor known as selective availability, or SA. This variation can be up to a few dozen meters. The satellite clock error does not have a spatial component and is therefore independent of satellite and user position. However, it has a temporal component with a correlation time of about 200 seconds.

SA is intentionally introduced by the DoD to limit the accuracy of the unauthorized user position to 100 meters, 2D RMS [ICD200C, Ceva]. Based on observations summarized in



[Tsai95a, Ceva, Dai99], it is apparent that this variation is overwhelmingly due to clock errors. Ephemeris errors are nominally a few meters as shown in Chapter 2 (Figure 2.6).

Multiple models have been developed for SA over the past decade [Matchett, Chou]. These models are based on linear autoregressive moving-average (ARMA) linear systems. The ARMA models characterize the statistical distribution of the errors; however, no truly predictive model for SA has been demonstrated.

The time history for SA was described in [Enge97] as:

$$\mathbf{s}(t+1) = \Phi \begin{bmatrix} \mathbf{s}(t) \\ \dot{\mathbf{s}}(t) \end{bmatrix} + \mathbf{G}\mathbf{w}(t+1) \quad (5.1)$$

where  $\mathbf{s}(t)$  is the current state of the SA range and range-rate values,  $\Phi$  is the state transition matrix, and the component  $\mathbf{G}\mathbf{w}(t+1)$  is added at each time step. The noise vector,  $\mathbf{w}(t+1)$ , is uncorrelated noise from one time step to the next with a normal distribution. [Matchett] developed the following set of parameters to match the SA distribution. Figure 5.3 shows the SA distribution using these parameters.

$$\begin{aligned} \Phi &= \begin{bmatrix} 0.9999312900 & 0.9952953944 \\ -0.0001372025 & 0.9905826798 \end{bmatrix} \\ \mathbf{G} &= \begin{bmatrix} 0.01551014 & 0.026737569 \\ 0.0 & 0.0534755539 \end{bmatrix} \end{aligned} \quad (5.2)$$

## Example SA Range and Range Rate Disturbance

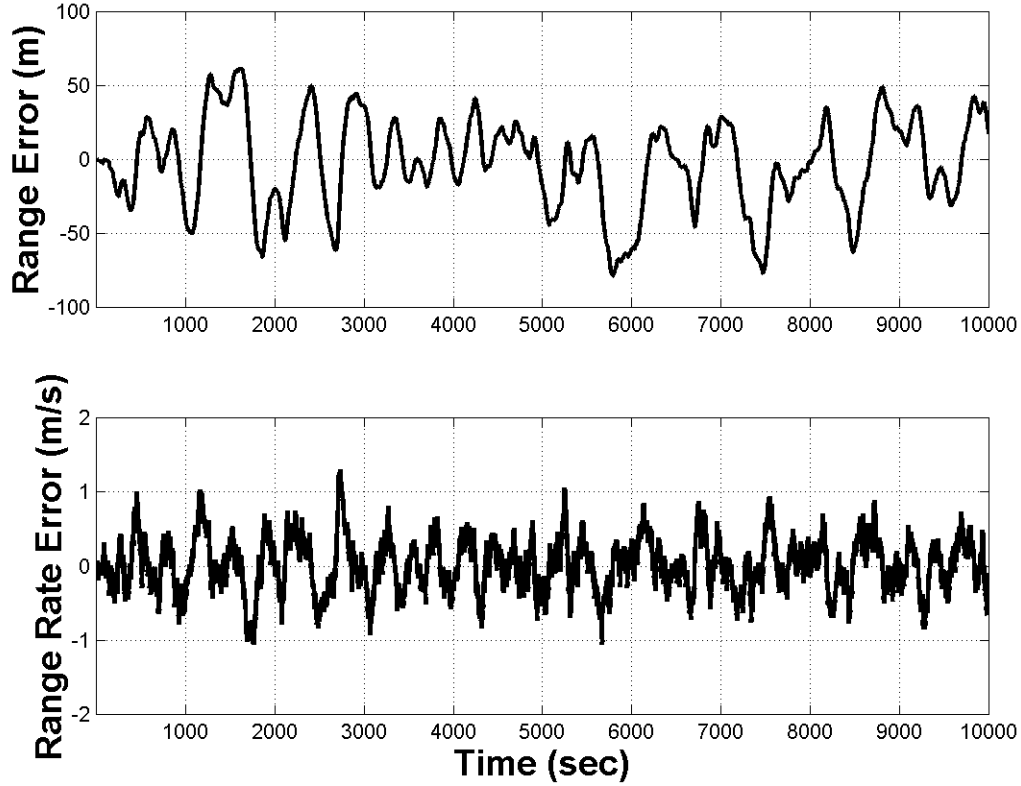


Figure 5.3: Time History of the Pseudorange Corruption Due to SA [Matchett, Enge97]

Using Equation (5.1) with the parameters in Equation (5.2), future values of SA can be predicted. The covariance propagation of the distribution is presented in [Enge97]:

$$\mathbf{P}(t+1) = \Phi \mathbf{P}(t) \Phi^T + \mathbf{G} \mathbf{Q}_{SA} \mathbf{G}^T \quad (5.3)$$

where the process noise is defined in [Matchett] as:

$$\mathbf{G} \mathbf{Q}_{SA} \mathbf{G}^T = \begin{bmatrix} 9.5546127e-4 & 1.4298059e-3 \\ 1.4298059e-3 & 2.8596331e-3 \end{bmatrix} \quad (5.4)$$

The square-root of the covariance for SA range is shown in Figure 5.4. Equation (5.1) is used as the generating function after an update from a differential correction. The limit at the minimum correction latency is set as the quantization level of the differential

correction. The limit at the maximum correction latency is due to the correlation time, which is roughly 180 seconds for this model.

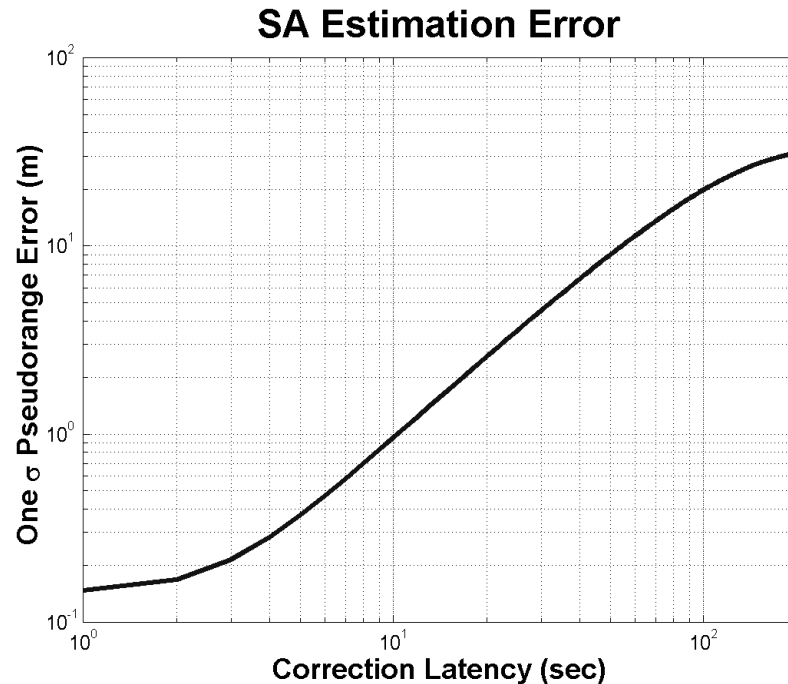


Figure 5.4: Error Growth Due to SA Over Time

Corrections for differential and wide-area differential GPS will primarily be designed to overcome SA errors since these are the most dominant errors with time-scales less than a few minutes [Enge97]. While SA degradation has recently been disabled by the DoD under the direction of the President, it remains a capability built into the GPS constellation and may be re-enabled under certain circumstances. At the press conference announcing the SA shut-off, the following answer was given when asked if SA could or would be re-enabled in the future:

*We will not deny that unless we're in a conflict somewhere where we need to protect U.S. forces and/or coalition forces.*

-Arthur L. Money, Assistant Secretary of Defense, May 1<sup>st</sup>, 2000

This statement combined with the capabilities still available in the GPS satellites indicate the possibility, albeit remote, that SA may be re-enabled in the future. Some capability for

dealing with the deleterious effects of SA should and most likely will remain in the WAAS message design.

### 5.1.2 IONOSPHERE ERRORS

Ionospheric errors are caused by the free electron content of the upper atmosphere. The modulation on the signal is delayed in proportion to the number of free electrons encountered and is also (to first order) proportional to the inverse of the carrier frequency squared ( $1/f^2$ ). The phase of the radio frequency carrier is advanced by the same amount because of these effects [Chao97, Klobuchar86, Parkinson96, Hansen00]. This effect has both temporal and spatial distributions. Ionospheric corrections are broadcast on the GPS message to correct these errors to within 2-10 meters. However, these do not include temporal variations that are highly localized within the ionosphere.

As represented in Figure 5.5, the maximum vertical delay produced by this phenomenon is on the order of 20-30 meters and occurs at 2 pm local time (2 hours after the Sun reaches its highest point). The vertical delay values during the night are between 3-6 meters. Dual frequency receivers can eliminate most of the delay. Single frequency receivers can eliminate 60% of the delay by using the GPS broadcast parameters [Klobuchar86]. Even with the recent elimination of SA, the second GPS frequency is still not available to civilian users.

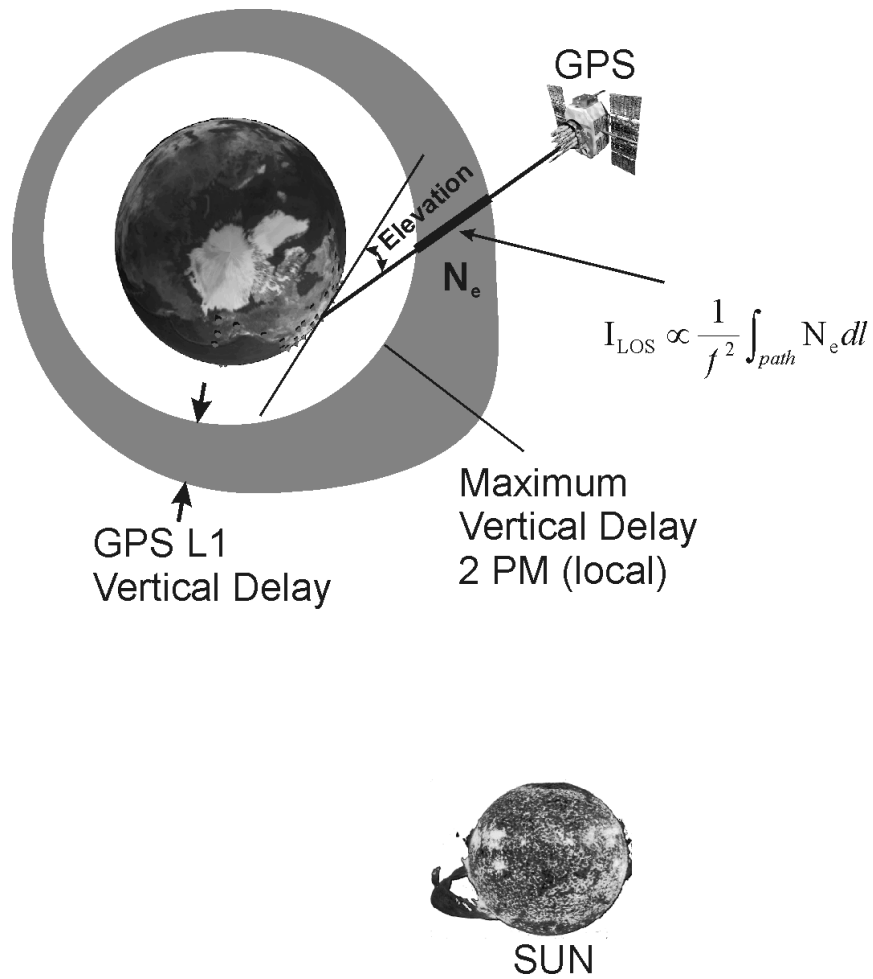


**Figure 5.5: Ionosphere Structure, Slant and Vertical Delays**

The ionosphere is assumed to be wide-sense stationary (WSS) in a Solar-Magnetic (SM) frame [Hansen99]. The WSS assumption makes the ionosphere temporally invariant over periods of minutes to hours. While this is generally true, occasional ionospheric disturbances or ‘storms’ have both temporal and spatial effects on the user. These irregular ionospheric disturbances happen occasionally, but most often during solar maximum which occurs every 11 years. The next solar maximum should occur sometime in the year 2000 or early 2001.

### 5.1.3 USER UNIQUE ERRORS

Another deviation in the signal is caused the troposphere. Variations in temperature, pressure, and humidity all contribute to variations in the speed of light of radio waves. Both code and carrier will have the same delays, and these effects are highly localized.

Multipath is the error caused by reflected signals entering the front end of the receiver and masking the real correlation peak. These effects are most pronounced for a stationary receiver near large reflecting surfaces. Ranging errors of 15 meters or more can be found in extreme cases [Parkinson96, Chapter 13]. Multipath is a major concern for WAAS and GPS reference stations and can dominate the error residuals. Careful placement of reference station antennas away from potential reflection sources is the easiest way to mitigate this effect. The relative obstruction-free surface of the top of an aircraft, in addition to reasonable care taken in the placement of an antenna, will minimize the impact of multipath for an aircraft user.

Receiver errors include thermal noise quantization errors in the pseudorange measurements. This error has no spatial component, and it is on the order of one (1) meter for pseudorange code and one (1) mm for the carrier [Kee93b]. Carrier-smoothing can dramatically reduce pseudorange code phase error [Chao97] as it is uncorrelated in time.

## 5.2 WAAS MESSAGE CONTENT

As the previous section indicated, there are various temporal and spatial scales that are present in GPS error sources. The WAAS correction message structure is built around supporting the different scales present in the GPS errors. The temporal components of the message are handled by ‘fast’ and ‘slow’ message types. The spatial components are corrected by ‘slow’ messages and conveyed via vector corrections for the ephemeris and a grid of vertical delays for the ionosphere.

Table 5.1 contains a summary of the temporal and spatial variations. The first column contains error sources. The next three columns indicate if the error sources have temporal or spatial components. The spatial components are broken down into two sub-categories:

spatial contributions from SV motion and those from user location. The last column indicates the source of each of the GPS error corrections. As stated previously, the WAAS correction messages are designed for satellite clock, satellite ephemeris, and ionospheric errors. Variations in the troposphere are relatively small but so highly dependent on user position (as well as other variables). A receiver model, specified in [RTCA159], is adequate to remove most of the troposphere's influence so explicit corrections are not broadcast. Both multipath and receiver errors are user phenomena and must be minimized or eliminated by receiver design.

Error Source	Temporal	Spatial-SV	Spatial-User	Correction
Satellite Clock	High	None	None	WAAS
Satellite Ephemeris	Low	High	Moderate	
Ionosphere	Moderate	High	High	
Troposphere	Low	Moderate	High	Receiver Model
Multipath	Low	Moderate	High	Receiver Design
Receiver Measurement	High	None	None	

Table 5.1: Error Sources and Their Temporal and Spatial Association

The structure of the WAAS 250 bit message is shown in Figure 5.6. This shows the message preamble, identifier, and parity overhead bits as well as the 212 available bits in each frame.

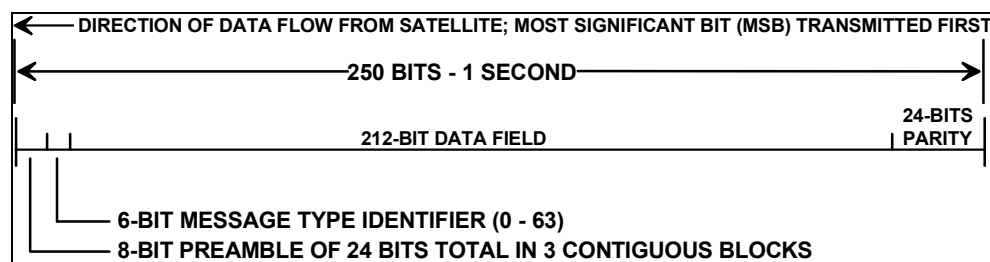


Figure 5.6: WAAS Message Structure [RTCA159]

The following sections of this chapter detail the types of WAAS messages defined in the WAAS Minimum Operational Performance Standards for Global Positioning System/Wide Area Augmentation System Airborne Equipment (MOPS) [RTCA159].

### 5.2.1 MESSAGE TYPES

Fast correction messages carry the quickly varying components of the pseudorange errors for each satellite [Tsai95b]. As mentioned, the majority of this error is due to SA clock variations. These fast corrections will also include integrity information on each GPS satellite. This integrity information is formulated as a protection level that is formed from clock and ephemeris (UDRE) as well as the ionosphere (GIVE) and user specific errors. When errors cannot be bounded within the limits specified in [RTCA159] a *don't use* message is sent. The integrity content must be sent much more quickly than any other type of data (less than 6 seconds) because positive integrity is required (i.e., a satellite can only be used if a recent UDRE has been received).

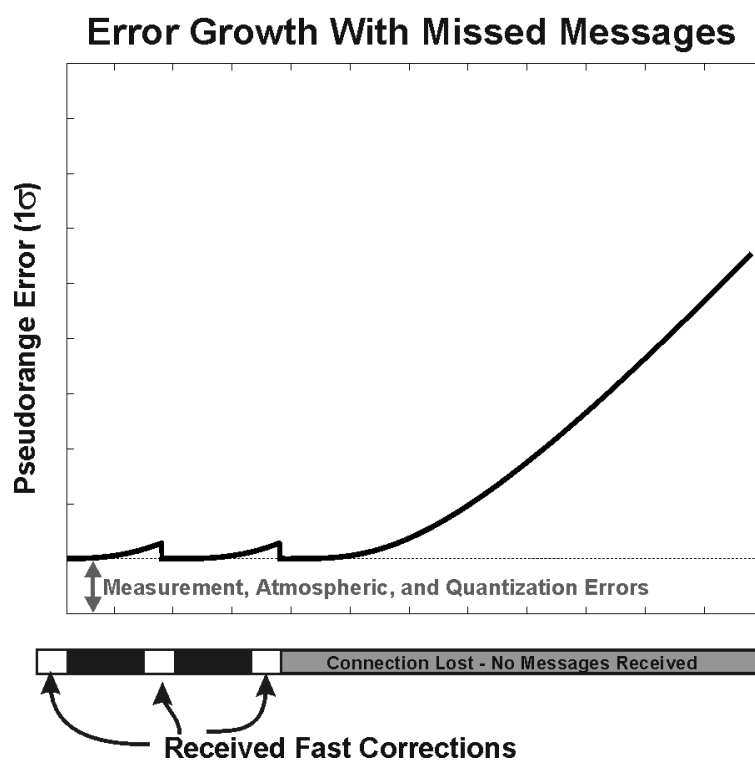


Figure 5.7: Error Growth with Fast Correction



Figure 5.7 shows the qualitative error growth over time. The fast corrections decorrelate, as shown in Figure 5.4, after the correction is applied. The baseline error in Figure 5.7 is due to the residual errors in the atmosphere (ionosphere and troposphere), measurement error of the receiver, and quantization effects of the correction. Fast correction message types are required by integrity as well as this temporal error growth. Even though SA has been disabled by the DoD, satellite monitoring integrity is still a fast message [Enge97], because of the required time to alarm for aviation applications.

The result from Figure 5.7 indicates the influence of missing messages on the errors seen by user aircraft. With lost messages over time, these errors and their corresponding error bounds will reduce the availability of aircraft operation modes. This is the motivation for understanding the performance of the airborne data link.

Slow message types include satellite masks, ionospheric masks, GPS ephemeris corrections, ionospheric vertical delays, geostationary satellite almanacs and precise geostationary ephemeris.

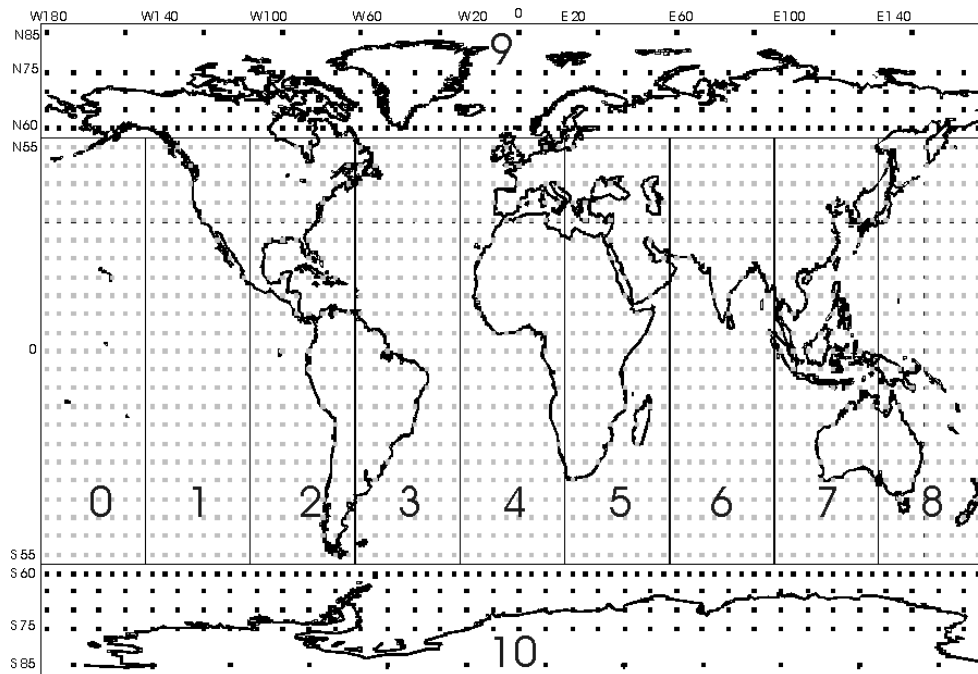


Figure 5.8: WAAS Ionospheric Grid Definition [RTCA159, Walter00]

A mask is used to conserve bits in message transmission. Instead of identifying a particular satellite for a fast correction or a latitude/longitude combination for an ionospheric correction, a slot reference is given into the mask. For the ephemeris, the mask is used to designate which satellite belongs to which slot in the fast correction messages. By using this slot mechanism, a satellite identifier does not have to be sent with every correction. The ionospheric mask is used to associate each slot in the ionospheric correction with a geographic location (Figure 5.8). This use of masks reduces the overall data throughput requirement.

The GPS ephemeris corrections are designed to correct the relatively small and slowly varying errors in the position estimate of the SV.

The ionospheric vertical delays are specified at particular reference points. These ionospheric reference points form a grid when mapped to the surface of the Earth as shown in Figure 5.8. These grid vertical delays are mapped onto the LOS from the satellite to the aircraft user by computing the slant delay as described in [El-Arini, RTCA159, Chao97].

To support the extra ranging signal from the geostationary satellite described in Chapter 4, there are almanac and precise ephemeris messages for the GEO. Since the satellite ephemeris is generated by the WAAS Master Station and it is not degraded (as with SA on GPS), there is little or no requirement to send slow corrections to the GEO ephemeris.

### 5.2.2 MESSAGE SEQUENCE AND TIMING

Table 5.2 gives a summary of WAAS message types from [RTCA159]. The first column indicates the kind of data being transmitted. The second column contains the message types that send the associated data. The third column provides the maximum spacing in time that should exist between consecutive messages of that type. The fourth and fifth columns give time-outs, or the maximum validity times, for different modes of aircraft operation [Kayton, RTCA159]. The sixth column shows the minimum number of messages that are required every 5 minutes to support continuous WAAS corrections.

Data	Associated Message Types	Maximum Update Interval (seconds)	En Route, Terminal, NPA Time-Out (seconds)	Precision Approach Time-Out (seconds)	Minimum Messages Every 5 min	BW %
WAAS in Test Mode	0	6	N/A	N/A	N/A	N/A
PRN Mask	1	120	600	600	2	0.6
UDREI	2 to 6, 24	6	18	12	--	--
Fast Corrections	2 to 5, 24	60	18-180	2-120	150	50.0
Long Term Corrections	24, 25	120	360	240	14	4.7
GEO Navigation Data	9	120	360	240	2	0.6
Fast Correction Degradation	7	120	360	240	2	0.6
Degradation Parameters	10	120	360	240	2	0.6
Ionospheric Grid Mask	18	300	1200	1200	10	3.2
Ionospheric Corrections	26	300	600	600	10	3.2
UTC Timing Data	12	300	86,400	86,400	1	0.3
Almanac Data	17	300	None	None	1	0.3
Service Level	27	300 (if used)	86,400	86,400	1	0.3
Total BW						64.4

**Table 5.2: Message Definitions and Timing [RTCA159]**

The seventh and final column of Table 5.2 is the percentage bandwidth required to transmit the message types. This is the total bandwidth over time. The sixth and seventh columns were defined with an assumption of 27 satellites for message types 2-6, 24 and 25. These columns were also defined with the assumption that the ionospheric grid covered CONUS only. As shown in the table, the total bandwidth required with the nominal message stream is only 64.4% of the total bandwidth available. This means that roughly 36% residual bandwidth exists. This leaves additional bandwidth to transmit messages on a larger number of satellites (up to 51 maximum) or a larger number of ionospheric grid points. Conversely, increasing the number of GPS satellites or the ionospheric grid coverage would decrease the residual bandwidth.

GPS Time of Week (sec)	Message Type	Objective
...	...	...
203402	1	PRN Mask assignments
203403	63	Null message, no other message required
203404	3	Fast corrections, slots 14-26 in mask
203405	26	Ionosphere vertical delays and accuracy
203406	2	Fast corrections, slots 1-13 in mask
203407	24	Six fast corrections, one long-term correction
203408	26	Ionosphere vertical delays and accuracy
203409	26	Ionosphere vertical delays and accuracy
203410	3	Fast corrections, slots 14-26 in mask
203411	26	Ionosphere vertical delays and accuracy
203412	2	Fast corrections, slots 1-13 in mask
...	...	...
203423	17	GEO almanac data
203424	3	Fast corrections, slots 14-26 in mask
203425	18	Definitions of ionospheric grid points (mask)
203426	2	Fast corrections, slots 1-13 in mask
203427	24	Six fast corrections, one long-term correction
203428	18	Definitions of ionospheric grid points (mask)
203429	18	Definitions of ionospheric grid points (mask)
203430	3	Fast corrections, slots 14-26 in mask
203431	18	Definitions of ionospheric grid points (mask)
203432	2	Fast corrections, slots 1-13 in mask
...	...	...
203439	24	Six fast corrections, one long-term correction
203440	26	Ionosphere vertical delays and accuracy
203441	26	Ionosphere vertical delays and accuracy
203442	3	Fast corrections, slots 14-26 in mask
203443	18	Definitions of ionospheric grid points (mask)
203444	2	Fast corrections, slots 1-13 in mask
...	...	...
203455	12	UTC/WAAS network time offset
203456	2	Fast corrections, slots 1-13 in mask
203457	24	Six fast corrections, one long-term correction
203458	9	GEO navigation message
203459	7	Fast correction degradation parameter and timeout for fast corrections
203460	3	Fast corrections, slots 14-26 in mask
203461	10	Fast and long-term degradation parameters
203462	2	Fast corrections, slots 1-13 in mask
203463	24	Six fast corrections, one long-term correction
203468	24	Six fast corrections, one long-term correction
203469	63	Null message, no other message required
...	...	...

Table 5.3: Sample Message Sequence

As shown in Table 5.2, the majority of the required message bandwidth is the fast corrections (50%). Increasing the ionospheric coverage region quickly expands the relative percentage of message types 18 and 26.

Table 5.3 shows a sample sequence of messages that a WAAS user would receive. The table shows the sequence at an arbitrary time in the GPS week with repetitive messages omitted to show a full message sequence. The general flow of events in the message stream is: 1) send the masks necessary for the fast and slow correction messages; 2) send the GEO almanac and ephemeris messages; 3) update the slow and fast correction messages (plus integrity messages); 4) update system availability and timing packets; and 5) repeat the process with fast correction messages taking up the majority of the message bandwidth.

### 5.3 THEORETICAL AND SIMULATED MESSAGE LOSSES

The WAAS message channel employs several techniques for improving the likelihood of successful bit decoding. This section will review the transmission channel used for WAAS and examine the theoretical performance for this channel. Simulation of this channel will then be compared to its theoretical performance. Initially, this analysis assumes that the message losses are independent.

#### 5.3.1 THEORETICAL MESSAGE LOSS VERSUS SNR: CASCADE PLOT

WAAS messages are broadcast in repeat cycles to minimize the chances that an update is lost. The assumption is that three repeats are used for critical alert messages or changes in the correction bounds (UDRE, GIVE). With three repeats, the probability of an individual message failure can be approximately,  $1-p=10^{-3}$ , where  $p=0.999$  is the probability that any single message is received successfully. The probability of message success is estimated by:

$$p \approx [1 - \Pr(\epsilon)]^M \quad (5.5)$$

where  $\Pr(\epsilon)$  is the probability of a single independent bit error in the message of length,  $M(=250 \text{ bits})$ .

The probability of a bit error in the absence of forward error correction (FEC) is approximately [Enge97, Clark81]:

$$\Pr_{NoFEC}(\epsilon) = Q_{\text{Gauss}} \left[ \sqrt{\frac{2C}{R_{\text{tot}} N_0}} \right] \quad (5.6)$$

$$p_{NoFEC} \approx [1 - \Pr_{NoFEC}(\epsilon)]^M$$

where:

$$Q_{\text{Gauss}}[\alpha] = \frac{1}{\sqrt{2\pi}} \int_{\alpha}^{\infty} \exp\left[-\frac{\beta^2}{2}\right] d\beta \quad (5.7)$$

In Equation (5.6),  $C/N_0$  is the carrier-to-noise ratio in dB-Hz and  $R_{\text{tot}} = 250$  is the total data rate in bits per second. This establishes a theoretical relationship between the probability of bit error and the received carrier-to-noise ratio. The total message error is still approximated by Equation (5.5).

WAAS uses FEC with the probability of a bit error bounded by:

$$\Pr_{FEC}(\epsilon) \leq 36Q_{\text{Gauss}} \left[ \sqrt{\frac{10C}{R_{\text{tot}} N_0}} \right] + 211Q_{\text{Gauss}} \left[ \sqrt{\frac{12C}{R_{\text{tot}} N_0}} \right] + 1404Q_{\text{Gauss}} \left[ \sqrt{\frac{14C}{R_{\text{tot}} N_0}} \right] \quad (5.8)$$

$$p_{FEC} \approx [1 - \Pr_{FEC}(\epsilon)]^M$$

where this equation employs a  $1/2$  rate convolutional code of constraint length 7 and  $R_{\text{tot}} = 250$  [Enge97, Clark81]. A diagram of the FEC convolutional coding scheme for WAAS is shown in Figure 5.9. There are multiple user options for decoding this signal.

Viterbi decoding is the most popular scheme for retrieving the data from the broadcast symbols [Heller, Clark81].

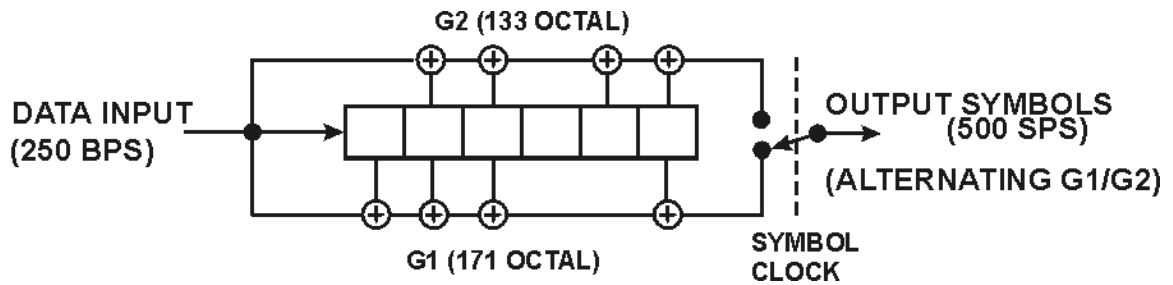


Figure 5.9: FEC Convolutional Coding for WAAS

Equations (5.6) and (5.8) assume that the code and carrier of the signal have been recovered perfectly such that the only channel disturbance is white Gaussian noise. A further assumption is that the receiver employs a soft decision decoder [Clark81].

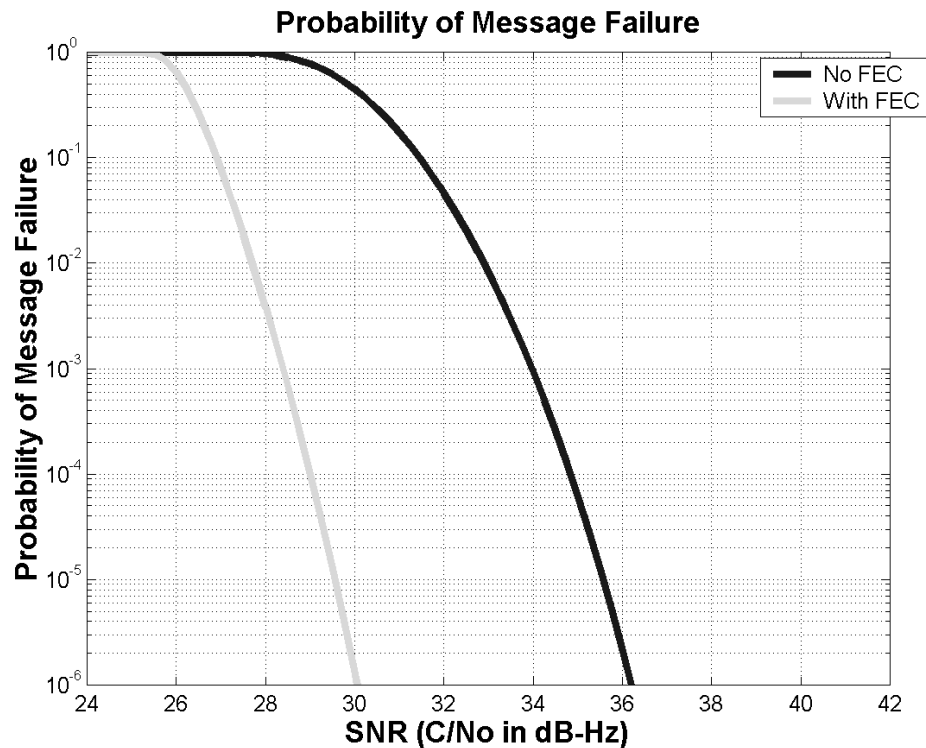
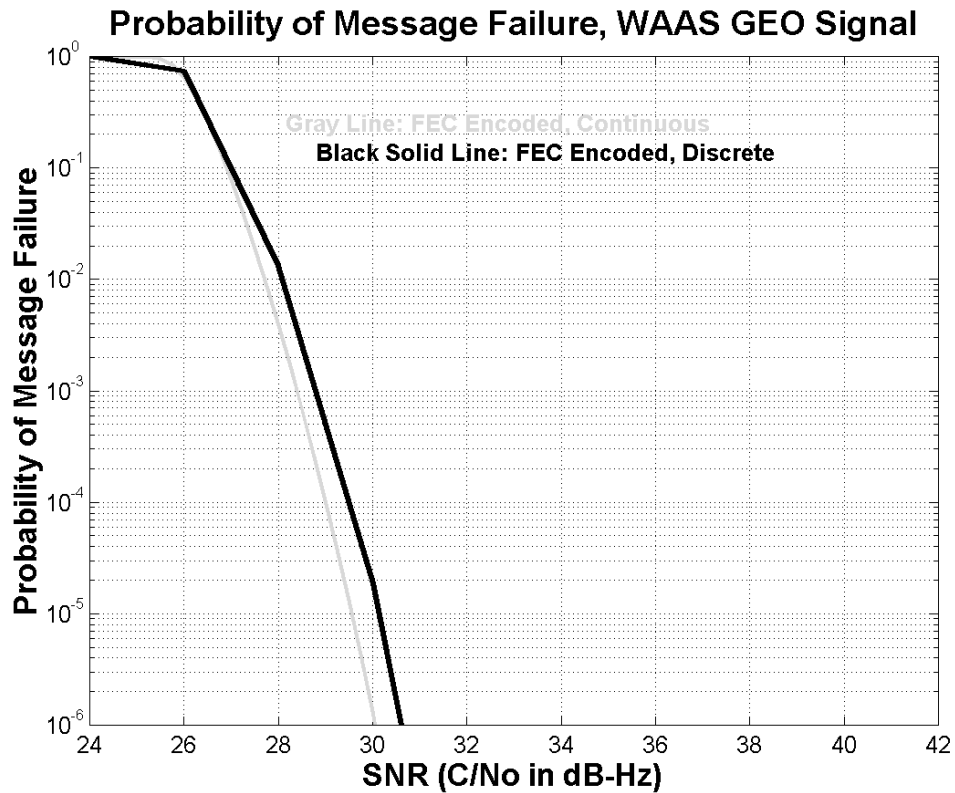


Figure 5.10: Probability of Message Failure without FEC and with FEC for  $R_{\text{tot}}=250$  and  $M=250$

Figure 5.10 shows the plot of probability message failure without and with FEC for an  $R_{\text{tot}}=250$  and  $M=250$ . The dramatic influence of the FEC is evident. At 30 dB-Hz the loss rate without FEC is 45% and when using FEC the loss rate is 0.00001%. This allows much lower power levels to be used for the same message loss failure rate [Enge97].



**Figure 5.11: Theoretical Message Loss Rate for FEC Signal Versus SNR**

Figure 5.11 shows the probability of message failure over a range of carrier-to-noise ratios. The gray curve is formed from the discrete version of Equation (5.8). To match data collected in the next chapter, this equation is integrated over bins of carrier-to-noise ratio 2 dB-Hz wide. Integrating Equation (5.8) from one carrier-to-noise ratios to another results in the equation:



$$\alpha = \frac{C}{R_{\text{tot}} N_0}$$

$$\int_a^b \Pr(\epsilon) d\alpha \leq 825.5(b-a) - (\Xi(b) - \Xi(a)) \quad (5.9)$$

where:

$$\begin{aligned} \Xi(x) = & 18 \cdot x \cdot \text{erf}(\sqrt{5x}) - \frac{36}{5} \left( -\frac{1}{2} \frac{\sqrt{5x}}{\exp(5x)} + \frac{1}{4} \sqrt{\pi} \cdot \text{erf}(\sqrt{5x}) \right) \Big/ \sqrt{\pi} \\ & + \frac{211}{2} \cdot x \cdot \text{erf}(\sqrt{6x}) - \frac{211}{6} \left( -\frac{1}{2} \frac{\sqrt{6x}}{\exp(6x)} + \frac{1}{4} \sqrt{\pi} \cdot \text{erf}(\sqrt{6x}) \right) \Big/ \sqrt{\pi} \\ & + 702 \cdot x \cdot \text{erf}(\sqrt{7x}) - \frac{1404}{7} \left( -\frac{1}{2} \frac{\sqrt{7x}}{\exp(7x)} + \frac{1}{4} \sqrt{\pi} \cdot \text{erf}(\sqrt{7x}) \right) \Big/ \sqrt{\pi} \end{aligned} \quad (5.10)$$

$$\text{erf}(y) = \frac{2}{\sqrt{\pi}} \cdot \int_0^y \exp(-\eta^2) d\eta$$

Chapter 6 compares the result from Equation (5.10) to collected data from the WAAS message stream stored in discrete bins.

The following section looks at a simulation of a WAAS receiver that addresses realistic performance considerations.

### 5.3.2 SIMULATED MESSAGE LOSS VERSUS SNR: CASCADE PLOT

Schnauffer simulated a realistic WAAS channel to establish a link budget for the WAAS aircraft user [Schnauffer]. The purpose of this work was to utilize existing receiver models to verify the reasonability of the [RTCA159] signal conditions.

Figure 5.12 shows the original curves of Figure 5.11 with the addition of one of the simulation results from [Schnauffer]. The new curve from their simulation includes effects for: 1) clock errors; 2) LOS dynamics; 3) tracking loop errors; and 4) data demodulation and Viterbi decoding (FEC). Clock errors and LOS dynamics contribute to short-term carrier tracking errors by adding accelerations not compensated for by the tracking loop.

These error components become part of the GPS navigation solution [Schnauffer]. More importantly, they influence the decoding of the signal bits.

The noise equivalent bandwidth (NEB) of the Phase-Locked-Loop (PLL) [Schnauffer] in Figure 5.12 is 15 Hz. This is a relevant curve because the receiver used to validate the tracking of actual GEO signals in the following chapter has a PLL with a NEB roughly equal to 15 Hz.

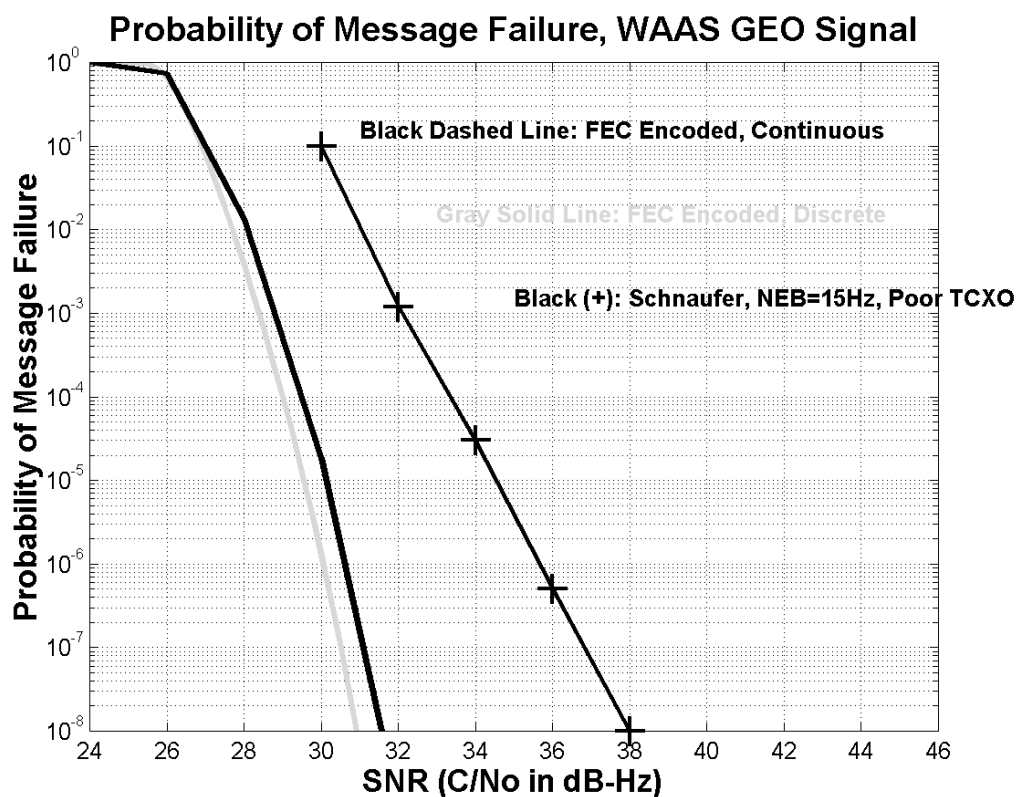


**Figure 5.12: Simulated Receiver Message Loss Rate versus SNR for 15 Hz NEB**

These relationships are based on independent message losses (i.e., when one message is lost it does not affect subsequent losses). However, the dynamics of the aircraft cause losses to be grouped: flight message losses occur in bursts (i.e. a burst of errors may persist through the duration of an aircraft bank).

The next chapter expands on the information presented here. Actual message loss performance was verified by tracking real GEO signals such that performance curves were met for a stationary receiver. Flight message loss data was collected and a model was fit to it such that these results could be extended to the NSTB. The impact on availability will be assessed for independent message losses as well as modeled flight losses at various sites in the US.



# **Chapter 6**

## **WAAS Messaging Performance In the Presence of Burst Errors**

The previous chapter introduced the expected performance of the GEO data link. This chapter shows the results for both a fixed receiver and a flight receiver and compares this to the theoretical and simulated message loss. To verify the message loss rate of a stationary receiver, a NovAtel MiLLenium™ receiver was utilized to collect messages in October and November 1999.

The WAAS message structure is not particularly sensitive to independent loss rates below 0.001 as specified in [RTCA159]. The results in this chapter show that even groups of missed messages (burst-mode) can be tolerated provided that the total message loss rate does not exceed a rate of 0.005.

Flight tests were conducted in California and Alaska to establish actual message loss profiles for aircraft. The flight data is used to develop a Markov model for the observed burst-mode errors. Using the model, the effects of burst-mode errors on the availability of the WAAS solution are analyzed. The flight test model is used in conjunction with the NTSB reference station data to establish availability of WAAS solutions for various locations in the US. This latter exercise studies the impact of the combined effects of

aircraft orientation and flight maneuvers on availability over the entire WAAS coverage region without conducting extra flight operations.

## 6.1 OBSERVED MESSAGE LOSSES

The NovAtel MiLLenium receiver is a specially modified version with the capability to track a GEO signal and decode 250 bit messages with FEC encoding as described in Chapter 5. The signal power levels measured by the receiver were collected along with the WAAS message packets.

Figure 6.1 shows the four Inmarsat GEO satellites currently planned for two of the Space-Based Augmentation Systems: WAAS and the European Geostationary Navigation Overlay System (EGNOS). EGNOS is a system under development in Europe that will provide GPS and GLONASS corrections [Benedicto, Traveset-Ventura]. Coordination of a standard wide-area correction message interface between WAAS and EGNOS will be overseen by the International Civil Aviation Organization (ICAO). This coordinated message structure has been published in [SARPS].

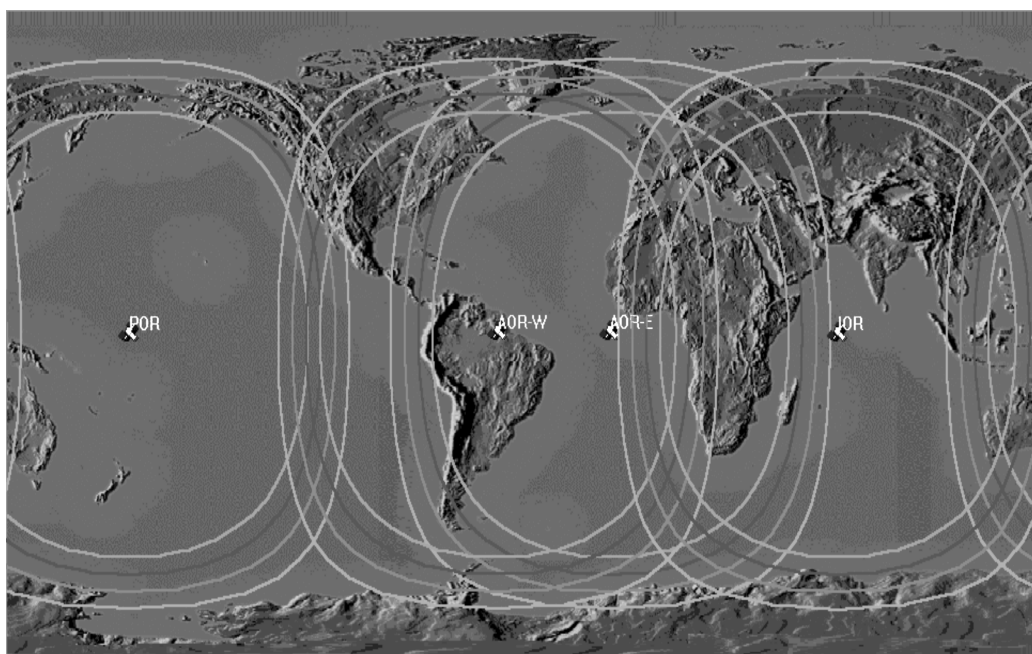


**Figure 6.1: Geostationary Satellites Utilized for Satellite Based Augmentation Systems (WAAS and EGNOS). Contours of the User Elevations for 5, 10, 15, and 20 Degrees**

EGNOS will be using Inmarsat's Atlantic Ocean Region-East (AOR-E) and Indian Ocean Region (IOR) satellites and WAAS is currently employing the Pacific Ocean Region (POR) and Atlantic Ocean Region-West (AOR-W) satellites. Both POR and AOR-W were used in this study. The contours represent the observation limits for users who employ 5, 10, 15 and 20 mask angles. The elevation of POR (PRN 134) at the Stanford University test location is about 15 degrees, while the elevation for AOR-W (PRN 122) is about 9 degrees.

During the period of the tests in October and November 1999, the GEO signals for both POR and AOR-W were often taken down to service the ground uplink system or to improve the messaging software. Many times the signal went down suddenly, without warning. For this reason, a test setup was required to differentiate between a lost message and a total absence of signal.

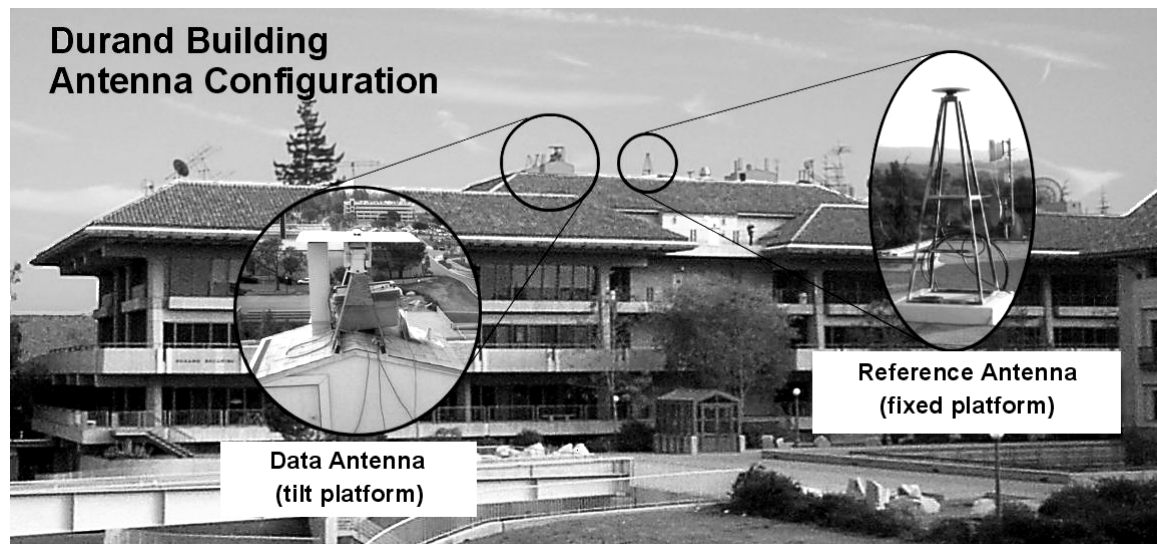


Figure 6.2: Rooftop Antenna Array Configuration

### 6.1.1 TEST SETUP AND EPOCH PROCESSING LOGIC

In order to make this differentiation, two identical receivers were used, comparing messages received at each epoch. Figure 6.2 shows the two antennas placed on top of the Durand Building at Stanford University. The fixed reference antenna is the same as that

used by the NSTB site at Stanford. The antenna mounted on the tilt platform was used as the test receiver and had the capability to use the gain pattern of the antenna itself to vary the power of the incoming signal.

Figure 6.3 shows the logic design to process the two message streams. If the data receiver (connected to the tilt platform antenna) does not record a message at a given epoch and the reference receiver (fixed reference antenna) does record the message, then there must have been a signal available for processing and therefore this is counted as a lost message. If neither receiver collects a message then it is assumed that there was no message broadcast and the event is not included in the statistics. If the test receiver records a valid message, the signal is assumed to be present and the message is counted as received. This method was implemented to reject the cases when there were no messages being broadcast by the satellite.

If neither the data receiver nor the reference receiver records a message, then it is likely that the signal was not present at that epoch (a satellite outage). This can be justified by the combined probability of dual message losses between two separate receivers. The level of message loss required to meet the requirements for WAAS [RTCA159] is  $\leq 10^{-3}$ . Assuming that the message losses between the two receivers are independent [Hsu, Leon-Garcia], then the chances of two receivers missing the same message is  $(\leq 10^{-3}) \cdot (\leq 10^{-3}) \leq 10^{-6}$ . The fraction of epochs ( $\approx 10^{-6}$ ) that are potentially excluded will place an insignificantly small bias on the results.



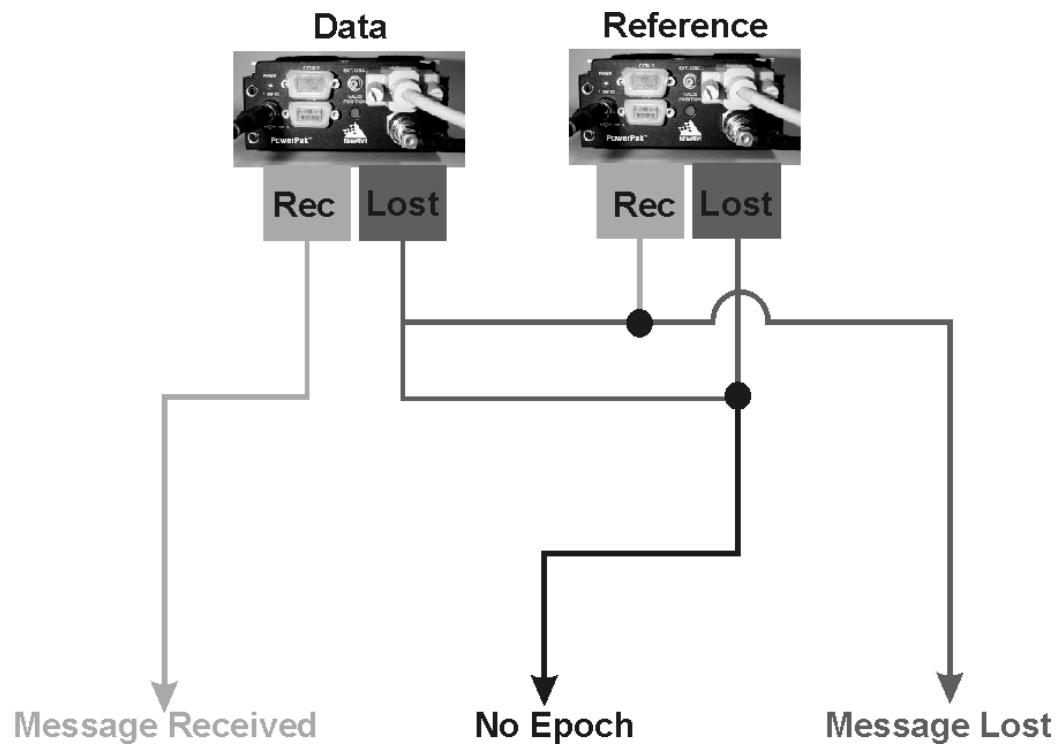


**Figure 6.3: Epoch Processing Logic for GEO Messages**

This method could have been used to track and capture messages for two GEOs simultaneously. However, there are processing limitations in the test receiver which made simultaneous tracking of the two GEOs difficult. It was apparent that the addition of a second GEO satellite to the tracking list of the receiver severely reduced the ability of both message streams to be decoded. The assumed reason for this problem was insufficient processing power in the receiver to compute the FEC decoding for two GEOs. Tracking of a single GEO satellite was observed to occupy as much as 15% of the receiver's CPU. The nominal margin without tracking any GEO satellites was about 20%. Flight test results that combined information from two GEO data streams were presented in [Fuller99]. Those results confirmed some degradation in the signal availability while tracking two GEO satellites.

### 6.1.2 OBSERVED MESSAGE LOSSES VERSUS SNR

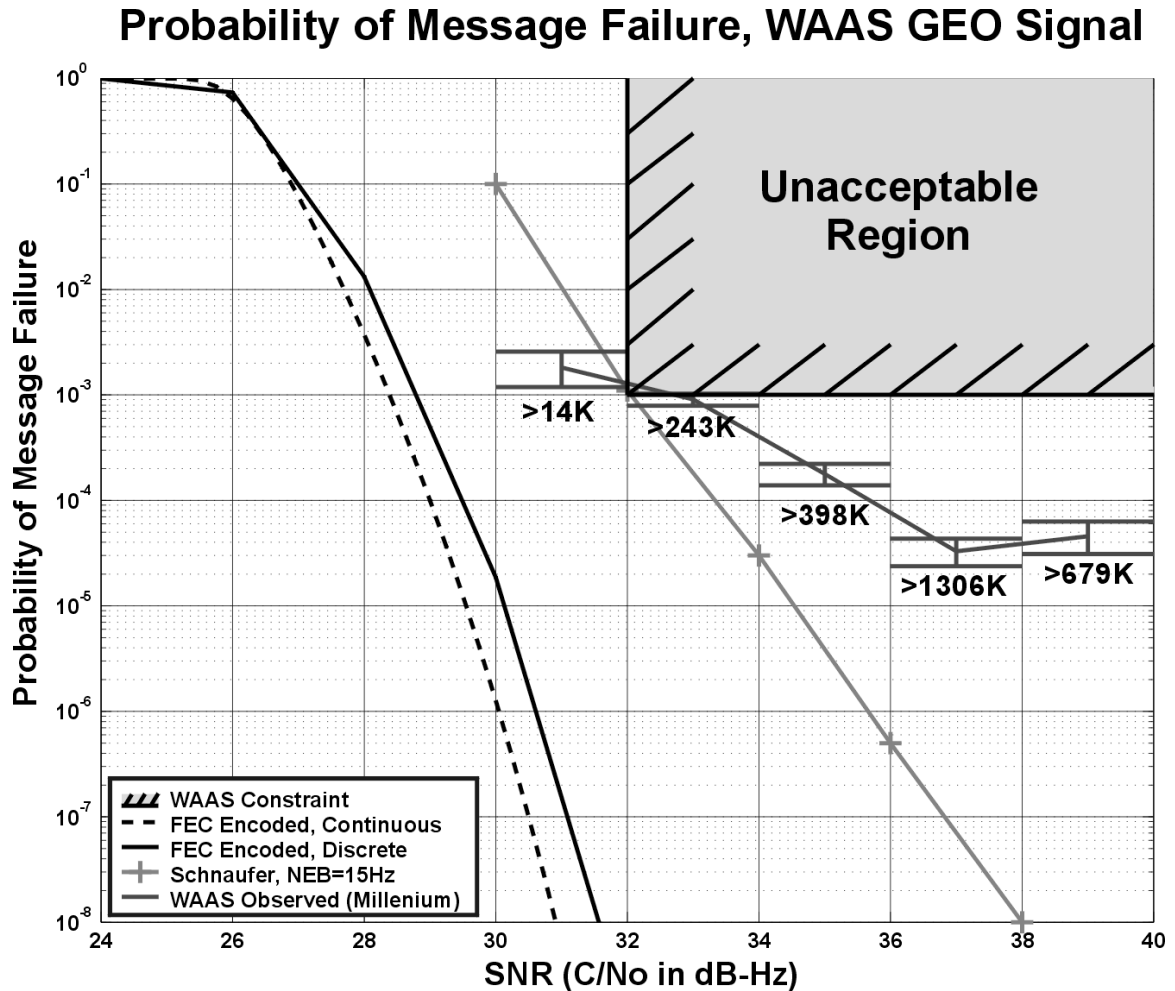
The WAAS specification for loss rate was established to meet aviation availability requirements. Since messages are repeated, a message loss rate of  $10^{-3}$  represents a probability  $10^{-3} * 10^{-3} = 10^{-6}$  for successive messages to be lost if the losses are independent. The chance of three successive losses is  $10^{-9}$  for independent losses. Hence, the probability of three successive key messages being lost is less than the  $10^{-8}$  integrity requirement. It will be shown in a later section of this chapter that the assumption of message loss independence is not correct and that flight message losses tend to occur in bursts. This is different than the assumption in the previous section where the losses between two receivers are assumed independent. The burst mode errors are correlated in time for a single receiver.

The 32 dB-Hz threshold was established by [Schnauffer] as a reasonable real-world limit for the minimum power level capable of achieving a  $10^{-3}$  loss rate. The gray shaded region shown in the upper right-hand corner of Figure 6.4 represents the intersection of the 32 dB-Hz threshold and the  $10^{-3}$  loss rate. No requirement is placed on a signal less than 32 dB-Hz; this is taken to be the minimum practical tracking level.

Using the method described in the previous section, 2.6 million data points were collected in the fall of 1999. The signal power levels measured by the receiver were collected along with the WAAS message packets. Slight adjustments in the angle on the tilt table were introduced to vary the power level going into the receiver. By tilting the antenna, power levels could be changed via the gain pattern.

The data was collected and grouped into bins that were 2 dB-Hz wide and the relative message losses for each bin are plotted in Figure 6.4. Also shown in Figure 6.4 are the theoretical and simulated results discussed in the previous chapter. The limiting region in the upper right-hand corner represents the specification for message loss given in [RTCA159]. The theoretical distribution presented in [Enge97] had a 3 dB-Hz margin versus the specification. [Schnauffer] and [Hegarty] presented results that had very little or no margin with respect to the specification.

For comparison to the data collected here, the curve from [Schnauffer] was chosen to nearly match the characteristics of the receiver used during the experiment. The error bars on each of the observed points are set at the width of the sampling interval in dB-Hz. The vertical extent error bars were determined from a Bernoulli distribution (the two-state case of the binomial distribution). The numbers below each observed point represent the number of samples taken in that bin.



The experimental data shows that the simulated, observed and specified levels are all approximately equal at 32 dB-Hz level. These results indicate that the message losses do meet the specification for the static receiver under these test conditions. However, there is

very little or no margin for the receiver characteristics in question. At higher power levels, the loss rates are better than the specification.

### 6.1.3 SNR FOR VARIOUS LOCATIONS ACROSS THE NSTB

To assess the significance of the low margin versus the specification, data were taken at a number of different locations across the US. These stations present a diversity of elevation angles to the GEO satellites. The station locations are shown in Figure 6.5. By measuring the received SNR values, comparison to the specified limit can be established.

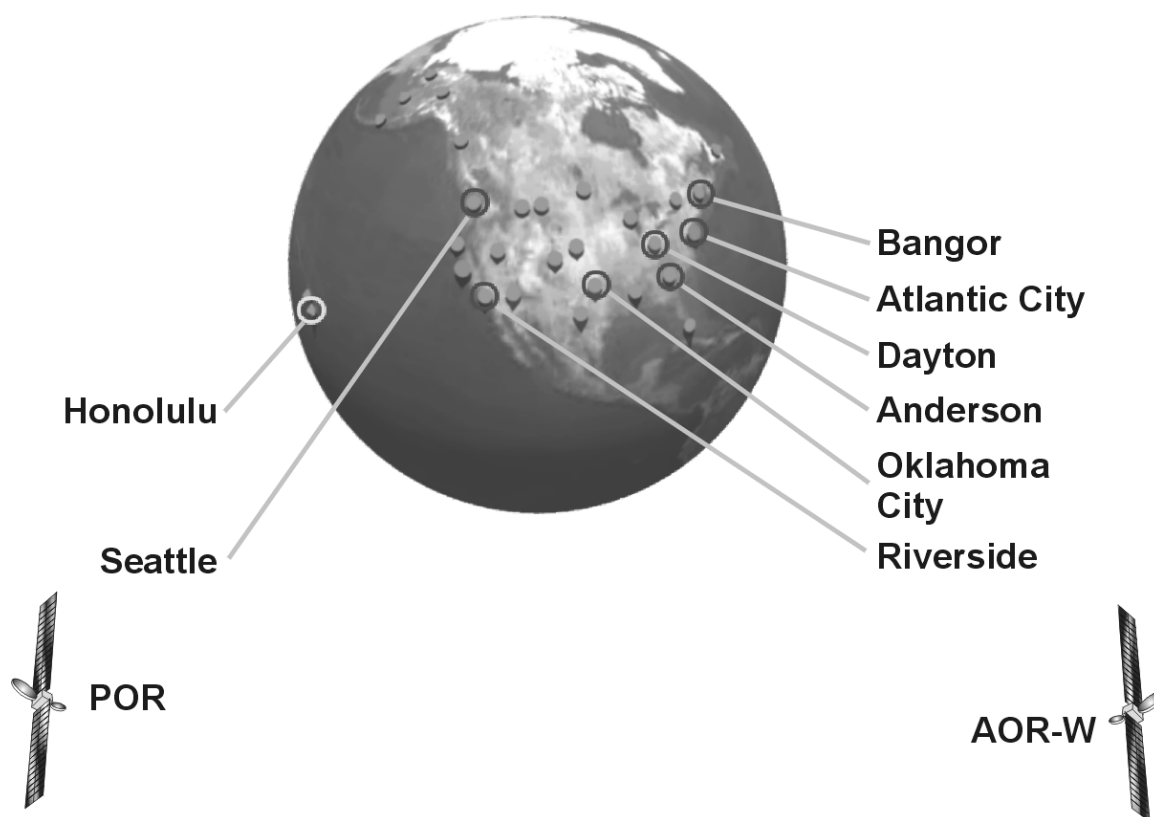


**Figure 6.5: NSTB Locations Used with GEO Tracking**

Figure 6.6 shows the SNR levels for eight stations located across the US. The majority of the stations in Figure 6.6 were tracking the satellite AOR-W or PRN 122. The labels for Honolulu and Seattle indicate the two stations were tracking POR or PRN 134. The

expected trend of higher SNR for higher elevation is observed. The results from PRN 134 bound the highest and lowest elevations and fit the general trend of PRN 122.

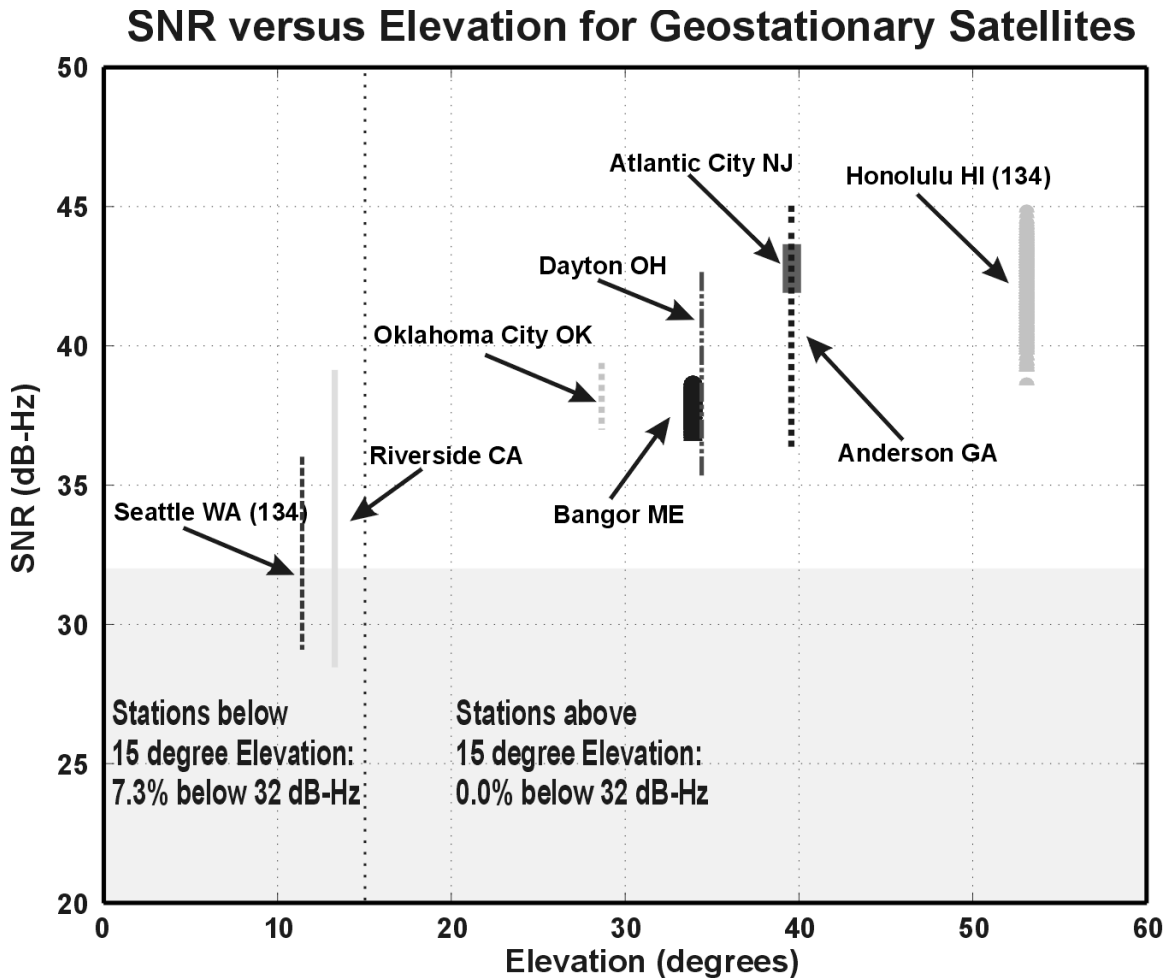


Figure 6.6: SNR Versus Elevation For Various Locations in the NSTB

For stations above a 15 degree elevation angle to the GEO, there were no recorded data points below 32 dB-Hz. For stations below a 15 degree elevation angle to the GEO, 7.3% of the points recorded below 32 dB-Hz.

As shown in Figures 6.4 and 6.6 a user can expect to meet or exceed the specified message loss rate of  $10^{-3}$  when the GEO satellite is in view above an elevation of 15 degrees. Below 15 degrees, the loss rate may not meet the specified level. The 7.3% of messages below 32

dB-Hz may have an impact on the availability of the WAAS solution for elevations between 10 and 15 degrees. While there is no data below 10 degrees of elevation, the trend in the data indicates that there may be a significant impact in message reception below 10 degrees.

The following section will examine the message loss results from flight tests. These flight tests were used as a basis for a Markov message loss model. This message loss model more accurately represents the burst-mode losses seen in flight as compared to independent losses assumed in previous work.

## 6.2 FLIGHT MESSAGE LOSSES

Over the course of June through December 1998 flight tests were conducted in Alaska and California to determine the message loss rate for an aircraft. Figure 6.7 shows the aircraft used in those flight tests. The aircraft used in the tests was equipped with multiple GPS-L1 antennas as well as a nose-mounted camera.

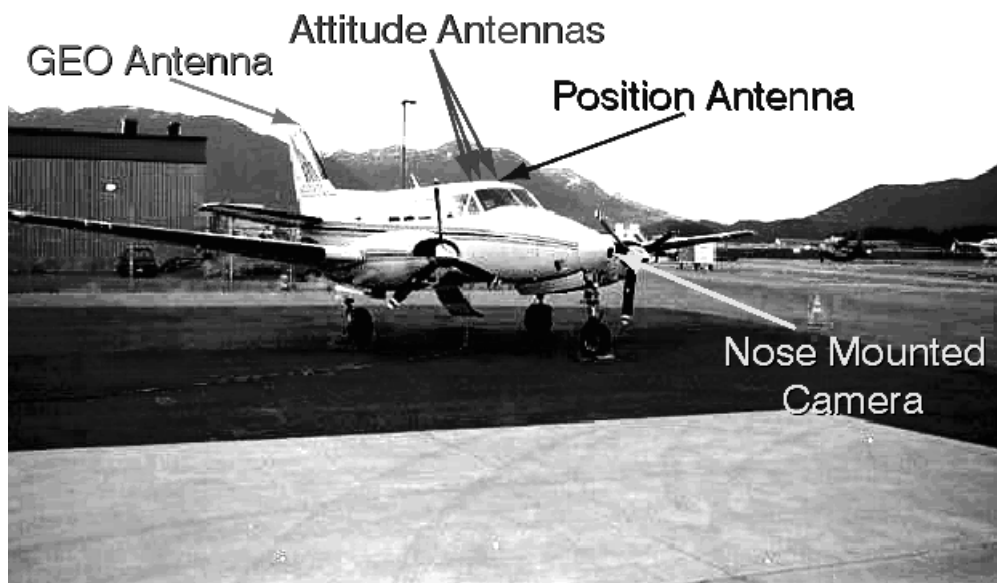
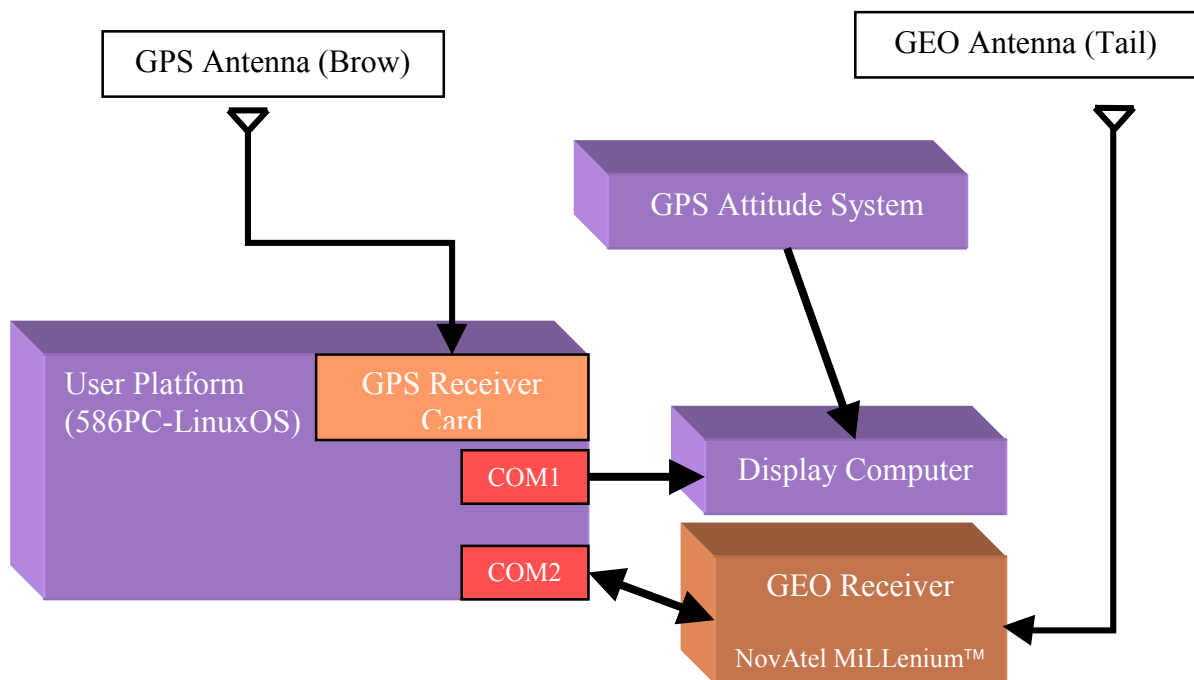


Figure 6.7: Flight Test Aircraft Used by Stanford University

The GPS-L1 antennas served multiple purposes. Three GPS-based experiments were usually conducted in parallel: 1) attitude determination, 2) flight displays, and 3) WAAS navigation. Attitude determination experiments used differential carrier phase measurements from three or four GPS antennas to precisely determine the orientation of the aircraft [Hayward]. The flight display research combined position and attitude information for presentation to the pilot. A representation of the data was projected on a small computer screen using 3D graphics to give the pilot increased situational awareness [Alter].



**Figure 6.8: Flight Test System Diagram**

Figure 6.8 shows the system diagram for the flight test equipment used on the aircraft. The receiver was the same NovAtel MiLLenium™ as utilized in Section 6.1. This test setup received the WAAS-compatible message stream broadcast by the Testbed Master Station (TMS) operating at Stanford University. This message stream was conveyed as shown in Figure 6.9. This figure shows the relay through network connection (ethernet) from

Stanford to the FAA Technical Center in New Jersey. The Technical Center has the capability of routing the message stream to the uplink station in Santa Paula, California.

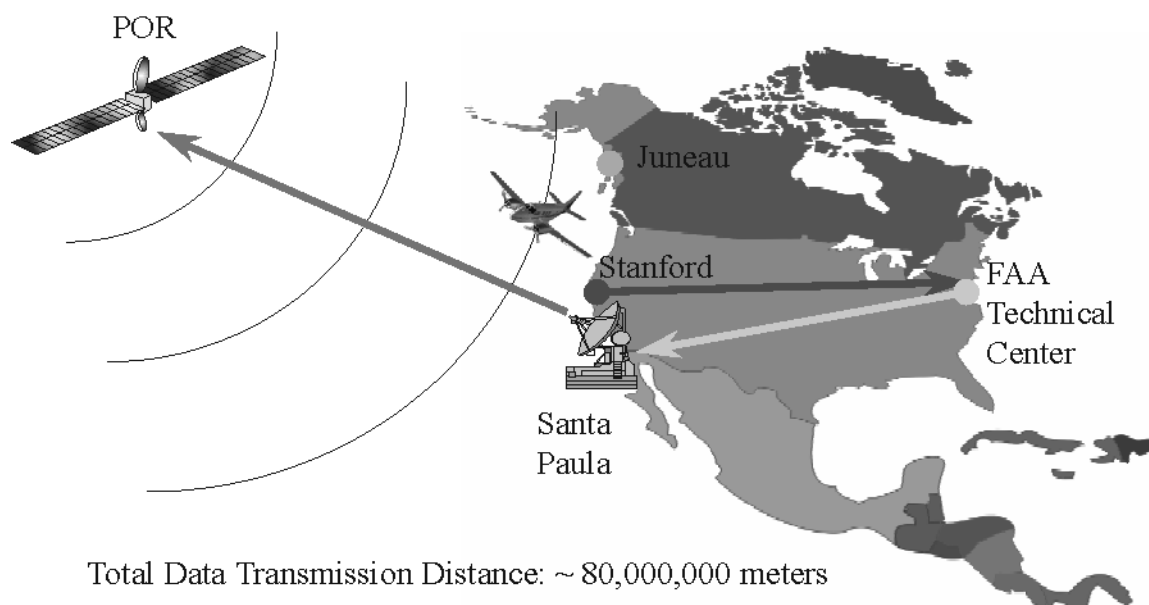


**Figure 6.9: Flight Test Data Link. Test Bed Master Station Located at Stanford University**

The message stream was used to correct the position solution yielding availability results that were presented in [Comp98, Fuller99]. The flight tests were conducted under a variety of flight modes from precision approach to en-route. In an effort to stress the GEO link some of the flight maneuvers included 60 degree banks from side-to-side. Using data collected during the flight tests, it was possible to ascertain the message loss rate for the GEO satellite message stream.

The following sections overview the data loss observed in flight and develop a Markov model (Appendix A) for characterizing message losses in flight. This model is then used to characterize the availability of WAAS solutions across the U.S. using NSTB data.



### 6.2.1 IN-FLIGHT MESSAGE LOSS OBSERVATIONS

Flight tests were conducted in August 1998 in the region around Juneau, Alaska and on various dates from October to December 1998 in and around Palo Alto, California. These flight tests recorded the messages lost over time. Figure 6.10 shows the distribution of the spacing between the messages. As a single WAAS message is sent every second, the nominal spacing is also one second. All other durations indicate that a certain number of messages have been lost. The data in Figure 6.10 indicate messages lost in all modes of flight; including periods of steep banks (up to 60 degrees) for short periods to determine the robustness of the signal tracking and re-acquisition [Comp98]. Even with these highly banked operations, the solution availability exceeded 98.5%. The data represents almost 11 hours of flight time (38644 one-second epochs).

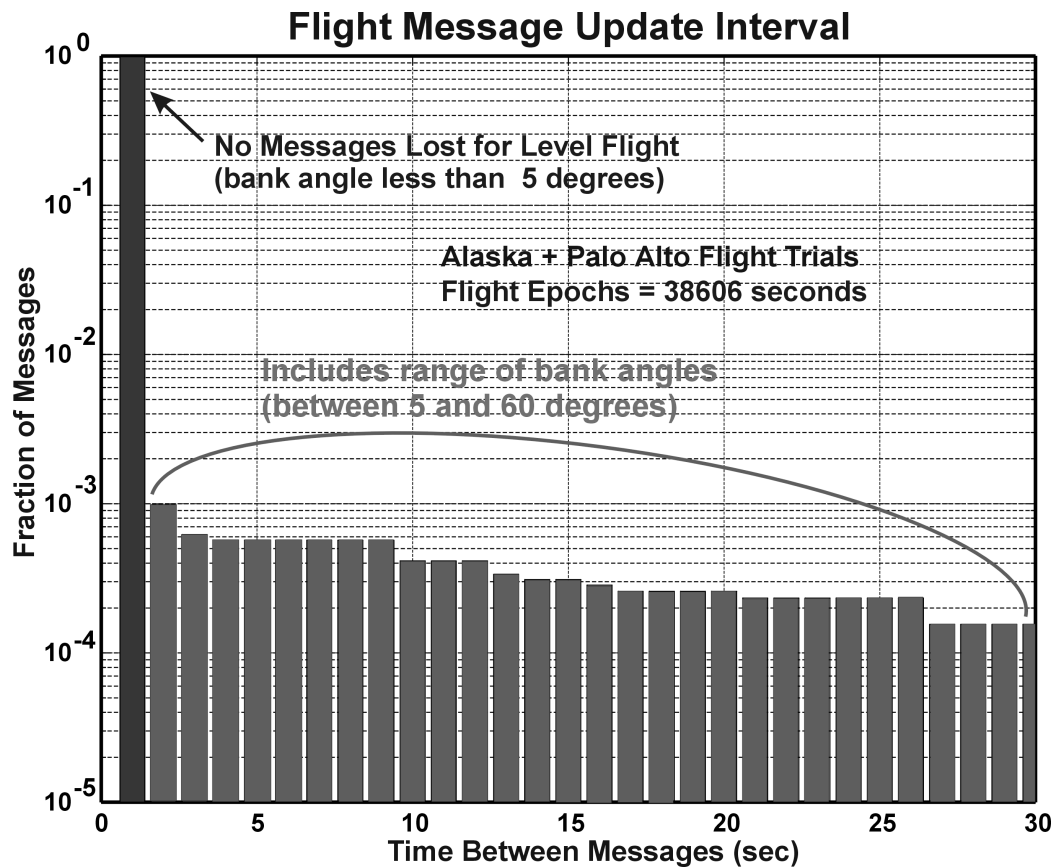


Figure 6.10: Message Loss Histogram. The Locally-Level Flight (< 5 degrees of bank) are All Contained in First Bar (Time Between Messages=1 sec)

Figure 6.10 is the message loss histogram from the flight tests. Using the symbol 0 to represent a received message, 1 to represent a lost message, and X to represent either a received or lost message, then the Figure 6.10 loss sequences can be written out. The bar to the farthest left (time between messages = 1) is the case for no losses, or 00. The next bar represents a single message loss, 01X, where the next message could be lost or received. The next bar (time between messages = 3) is the case for two sequential losses, 011X. The remaining sequences are 0111X, 01111X, 011111X, etc. These continue in this fashion up to 30 sequential losses.

As Figure 6.10 indicates, the overwhelming majority of the points fall into the bin which represents no loss (time difference between received messages = one second). All other outage durations are less probable than  $4 \times 10^{-3}$ . Of particular note is performance during near level flight. *With a bank angle less than 5 degrees, there were no message losses.* This level-flight result was true in both Alaska and California flight operations where the locally-level elevations to the GEO satellite were different; 15 degrees for Alaska (POR) and 9 degrees for California (AOR-W). Figure 6.1 gives the elevation angles versus geographic location. This differs from the results in Section 6.1.3 where message loss occurred at 12 degrees of elevation. It may indicate that proper siting of an antenna on an aircraft can help defray some of the losses incurred by low elevation satellites. Additionally, the observed GEO satellite power level of the receiver-in-flight for all wings-level conditions ( $< 5$  degrees of bank) always exceeded 40 dB-Hz and often exceeded 43 dB-Hz. This was true for both tracking GEO satellites AOR-W and POR in California as well as POR in Alaska.

For those times when the aircraft was not level, the message loss occurred in groups or ‘bursts.’ Since all of the burst-losses occurred when the aircraft was not level, a strong correlation exists between message losses and aircraft orientation. Since the bank angle of the aircraft does not change instantly, message losses tend to persist and create message loss burst. This is important in extending the static reference receiver results from the previous sections to users in flight.

The following sections establish a Markov model for the flight message loss and extend them to multiple locations across the US using NTSB data.

### 6.2.2 MODEL OF FLIGHT MESSAGE LOSSES (BURST-MODE ERRORS)

[Olsen] described a simple Markov channel model that could be used for the characterization of message loss in the presence of atmospheric noise. This work was an extension of [Fritchman], which used partitioned states to portray real communication channels. These methods suggested an approach that utilized a binary Markov chain to model the flight message losses. A brief introduction to random processes and Markov chains is given in Appendix B.

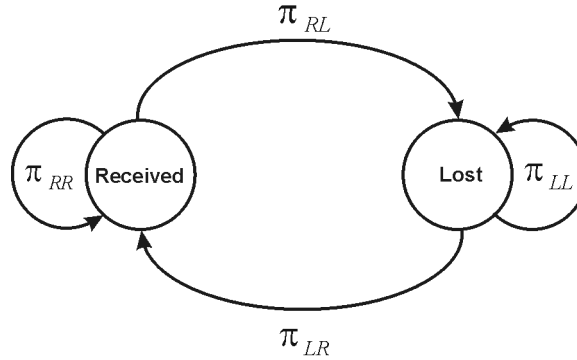


**Figure 6.11: Burst Model Diagram**

Figure 6.11 shows a transition probability diagram for a burst model which is a two-state Markov chain. The states are broken down into message received and message lost. This model is designed to capture the groups of messages lost. The transition probabilities are represented as described in Appendix B by the transition probability matrix:

$$P = \begin{bmatrix} \pi_{RR} & \pi_{RL} \\ \pi_{LR} & \pi_{LL} \end{bmatrix} \quad (6.1)$$

where:

$$\begin{aligned}\pi_{RR} + \pi_{RL} &= 1 \\ \pi_{LR} + \pi_{LL} &= 1\end{aligned}\tag{6.2}$$

Also known is the transition probability from the message-received state to message-lost,  $\pi_{RL}$ , which is simply the probability that a single message is lost. From inspection of Figure 6.10 this transition probability is on the order of 0.001, so for the Alaskan and California flight tests (including steep bank angles):

$$\pi_{RL} = 0.001\tag{6.3}$$

To solve for the other model parameters, we apply Bayes' rule [Leon-Garcia]:

$$P(A|B) = \frac{P(B|A)P(A)}{P(B)}\tag{6.4}$$

where  $P(A|B)$  is the conditional probability of event A given event B,  $P(B|A)$  is the conditional probability of event B given event A,  $P(A)$  is the total probability of event A and  $P(B)$  is the total probability of event B. Applying Bayes' rule to this model we have:

$$\pi_{LR} = \frac{\pi_{RL}P(R)}{P(L)}\tag{6.5}$$

where  $P(R)$  is the total probability of a message being received and  $P(L)$  is the total probability of a message being lost. For this data set the total probability of a message being lost was  $P(L) = 0.0106$ . The complementary total reception rate was  $P(R) = 1 - P(L) = 0.9894$ .

The full parameter set is solved by employing Equations (6.2), (6.3), (6.4) and (6.5) and the data in Figure 6.10:

$$\begin{aligned}
P(L) &= 0.0106 \\
P(R) &= 1 - P(L) = 0.9894 \\
\pi_{RL} &= 0.0010 \\
\pi_{RR} &= 1 - \pi_{RL} = 0.9990 \\
\pi_{LR} &= \frac{\pi_{RL} \cdot P(R)}{P(L)} = \frac{0.001 \cdot 0.9894}{0.0106} = 0.0922 \\
\pi_{LL} &= 1 - \pi_{LR} = 0.9078
\end{aligned} \tag{6.6}$$

The function to generate the flight model loss is:

$$P_L(n) = \begin{cases} 1 - P(L) = P(R) & n = 0 \\ \pi_{RL} & n = 1 \\ \pi_{RL} \cdot (\pi_{LL})^{(n-1)} & n > 1 \end{cases} \tag{6.7}$$

where  $P_L(n)$  represents the probability that  $n$  sequential messages are lost. Figure 6.12 is the comparison of the data to the model,  $P_L(n)$ , described in Equation (6.7).

These parameters form a good bound for short losses and slightly underestimate the longer losses as compared to actual losses. This forms a somewhat conservative estimate since part of the Alaska flight trials lowered the messaging performance by exercising very strong banking (60 degrees) during a period up to 15 minutes (900 seconds) in an alternating fashion. This high banking period represents less than 3% of the total flight data in Figures 6.10 and 6.12, so the influence is potentially large given the small overall percentages of loss. When the aircraft was operating at level or near-level flight (< 5 degrees), there were no recorded message losses. This near-level flight profile most closely represents approach to landing where the aircraft is less than 5 miles from touchdown.

The dashed line in Figure 6.12 represents independently distributed losses. The independent losses were treated as a Bernoulli distribution (see the next section) with a total probability of message loss,  $p=0.01$ . The burst model performs much better in comparison to independently distributed message losses in terms of its correspondence to the flight data.

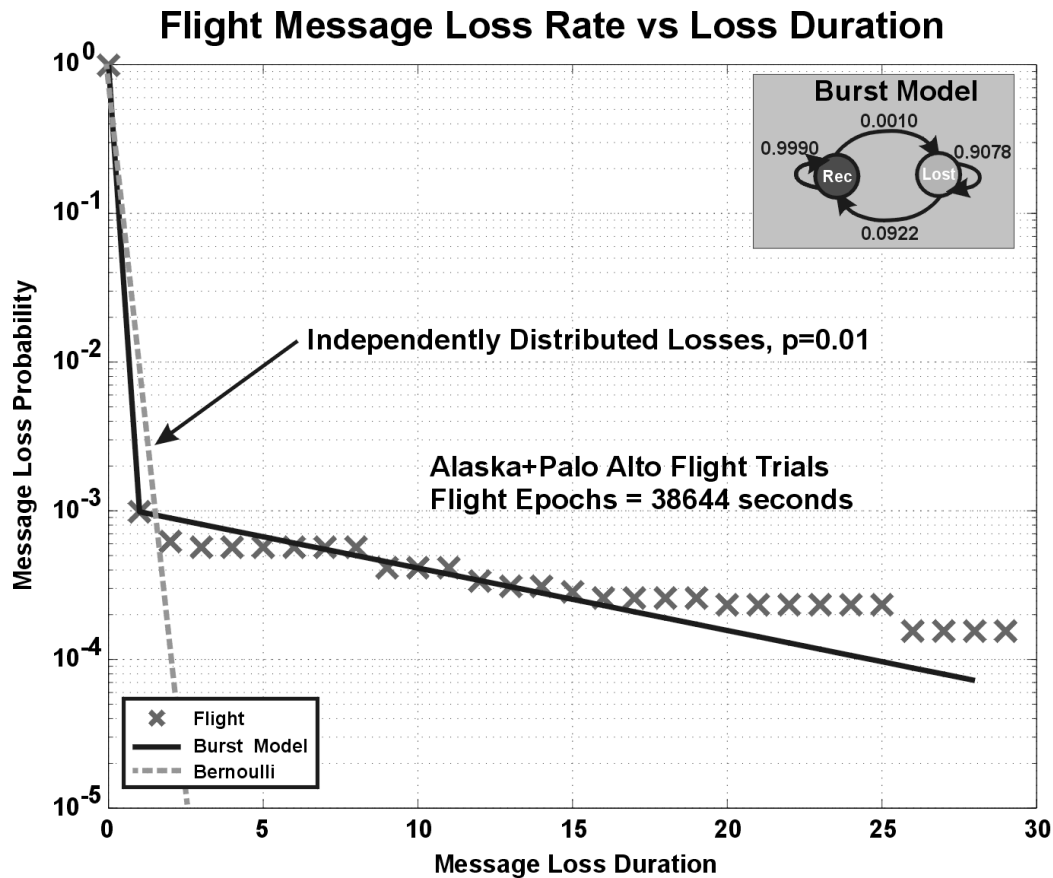


Figure 6.12: Flight Message Loss Compared to Burst Model Realization (3% of Data Including 60 Degree Bank Angles)

With a model for the flight message losses, the effects on integrity and availability can be established. The following section looks at the influence of the burst loss model on the overall integrity of the WAAS message signal compared to the assumption that the losses are independently distributed.

### 6.2.3 BURST LOSS EFFECT ON INTEGRITY

As stated in the previous chapter, the assumption is that three repeats are used for critical alarm messages or changes in the correction bounds (UDRE, GIVE). With independent message losses and a specification for those individual losses set at 0.001, the integrity level of  $10^{-8}$  is achieved ( $(10^{-3} \cdot 10^{-3} \cdot 10^{-3} = 10^{-9}) < 10^{-8}$ ). However, the preceding sections have shown that flight message losses are not independent. In order to determine the

integrity of the alarm message for the burst model, the probability distribution from Equation (6.7) was used to estimate the probability that three successive messages are lost. By fixing the value of  $\pi_{RL} = 0.001$ , the total probability of message loss,  $P(L)$ , was adjusted between loss rates of  $10^{-4}$  and  $10^{-1}$  and new model parameters were determined from Equations (6.2), (6.3), (6.4) and (6.5) and used in Equation (6.6) to develop the second line in Figure 6.13. The dotted line in Figure 6.13 represents the probability that three independent message losses have occurred.

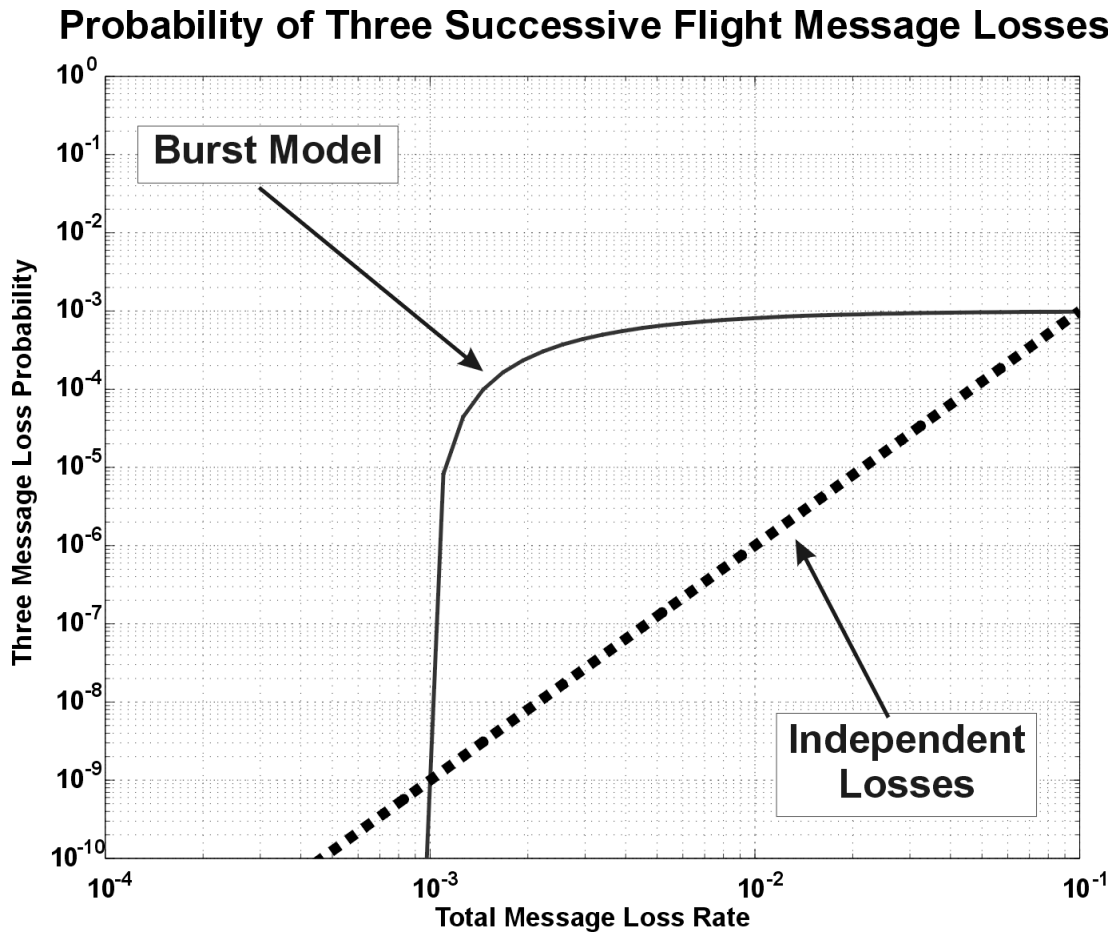


Figure 6.13: Comparison of Burst Model and Independent Loss Assumptions on the Probability that Three Successive Messages are Lost

The total message loss rate must be less than  $1.01 \times 10^{-3}$  using the burst model to meet the requirement that the probability of loss of three successive messages is less than  $10^{-8}$ . This

is very close to the requirement set forth in the MOPS [RTCA159] where independent losses were assumed at a  $1 \times 10^{-3}$  loss rate. However, the burst model has a very high slope near the critical message loss rate due mainly to the value of  $\pi_{RL} = 0.001$ . Slightly higher or lower losses could dramatically impact this result. Additionally, different values of  $\pi_{RL}$  have a strong effect on the results. The results from Section 6.1.2, Figure 6.4, suggest that message loss rates at least an order of magnitude better than  $1.01 \times 10^{-3}$  can be achieved if the power level for the receiver exceeds 36 dB-Hz. Significant margin in the message loss rate may even be attained even at 34 dB-Hz.

With a highly conservative flight message loss burst model in hand, the flight test values can be extended to multiple fixed sites across the US to assess the availability of the WAAS solution under general flight conditions.

### 6.3 MESSAGE LOSS IMPACT ON AVAILABILITY

The following two sections look at the availability of WAAS solutions for four sites across the US utilizing the burst message loss model developed in the previous section. The data was processed by the Stanford TMS program using data from the NTSB with models implemented to simulate message loss. The first section will assume a random message loss, with each loss uncorrelated to the others. It is important to note that each of the stations used in this study was set as passive, i.e., the station in question was *not* used in the formulation of the correction message. The independent loss results serve as the reference for burst message losses on availability.

#### 6.3.1 INFLUENCE OF RANDOM MESSAGE LOSS

The Stanford TMS software was modified to simulate random message losses. The loss model was simulated as a Bernoulli distribution [Hsu]. A Bernoulli distribution is a two-state version of the binomial random variable [Leon-Garcia]. The probability mass function (pmf) of a Bernoulli random variable,  $X$ , is defined by:

$$p_X(k) = P(X = k) = p^k (1 - p)^{1-k} \quad k = 0, 1 \quad (6.8)$$



where  $0 \leq p \leq 1$ . The cumulative distribution function (cdf),  $F_X(x)$ , of the Bernoulli random variable,  $X$ , is given by:

$$F_X(x) = \begin{cases} 0 & x < 0 \\ 1 - p & 0 \leq x \leq 1 \\ 1 & x > 1 \end{cases} \quad (6.8)$$

Figure 6.14 shows the distribution of the VAL=20 meter availability from four stations in the NSTB network. The influence of the random, independently distributed message loss is non-existent for loss rates less than  $10^{-3}$  and there are no significant increases for less than a rate  $10^{-2}$ . This validates the assumption in the specification that independently distributed message losses in combination with a loss rate less than  $10^{-3}$ , do not affect the availability.

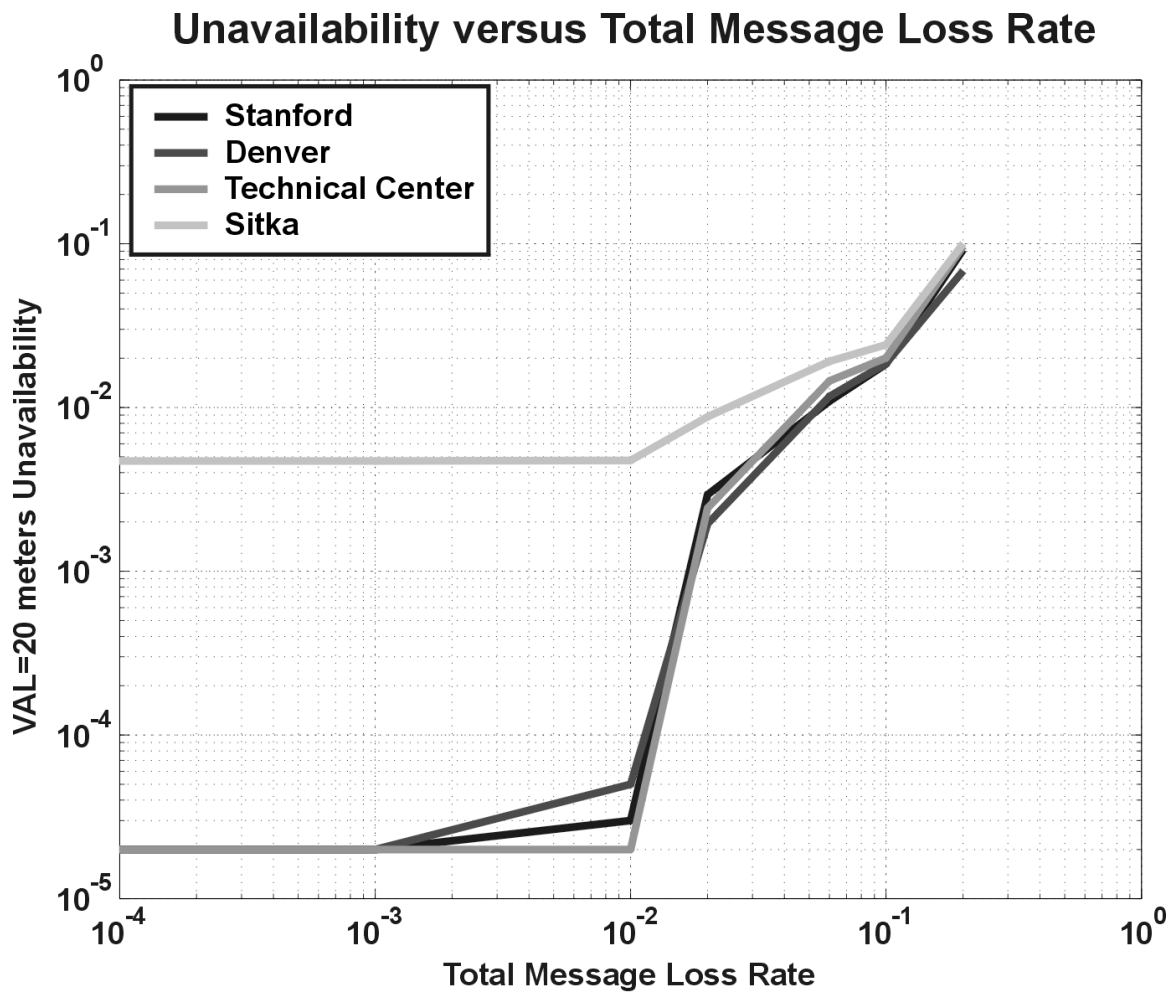


Figure 6.14: WAAS Correction Unavailability for Independently Distributed Message Loss at Four NSTB Locations (Bernoulli Random Variable)

Of particular note is that the Sitka Alaska station does not meet  $10^{-3}$  availability even with zero message loss. The extreme northern location of Sitka, Alaska limits the visibility of the GPS satellites (see Figure 1.7) and, therefore, severely limits navigation solution availability. Comp presented results showing that the availability of a GEO ranging signal could, in a specific case, improve the overall availability of the solution in Southeastern Alaska (i.e., the Juneau and Sitka area) [Comp98].

The following section shows the impact of applying the burst model to the availability of the WAAS solution.

### 6.3.2 BURST LOSS EFFECT ON AVAILABILITY

The previous results indicated that there were only subtle effects in availability under  $10^{-2}$  message loss rates. The parameters are modified for various total probability message loss rates,  $P(L)$ . As noted to in the previous section, the flight data had a total message loss probability of  $P(L) = 0.0106$ . This value, along with the transition probability in Equation (6.3), allowed the computation of all transition probabilities within the burst model by using Equations (6.2) and (6.5). By selecting different total probabilities of message loss, a higher or lower loss rate can be extrapolated from the same burst model. The transition probability in Equation (6.3) remained fixed in all cases. The total message loss probabilities tested were:

$$P(L) = \begin{cases} 0.0005 \\ 0.0010 \\ 0.0050 \\ 0.0106 \\ 0.0500 \end{cases} \quad \leftarrow \begin{array}{c} \text{flight result} \\ \hline \end{array} \quad (6.9)$$

Each of the total probabilities in Equation (6.9) was used to determine the burst model parameters subject to Equation (6.3). To calculate each of the transition probabilities:

$$\begin{aligned}
\pi_{RR} &= 0.9990 \\
\pi_{RL} &= 0.0010 \\
\pi_{LR} &= \frac{\pi_{RL} * P(L)}{P(R)} = \frac{0.0010 * P(L)}{1 - P(L)} \\
\pi_{LL} &= 1 - \pi_{LR}
\end{aligned} \tag{6.10}$$

The formulation in Equation (6.10) allows for the extension of the burst model along the horizontal axis shown in Figure 6.14 since that axis represents the total message loss rate. By constraining the solution to Equation (6.3), the transition probability from the ‘received’ state to the ‘lost’ state remains fixed. This causes the length of the outages to increase to accommodate the larger total loss probability. The ‘tail’ in Figure (6.12) is flattened as the total loss probability increases.

The message losses were simulated according to this burst model and processed with the TMS program using the NSTB data. This is the same data set used to generate Figure 6.14.

Figure 6.15 shows the results of the burst model on the WAAS solution availability for the various total message loss probabilities given in Equations (6.9) and (6.10). The horizontal axis represents the equivalent total message loss rate or  $P(L)$  from Equation (6.10). This shows that for three of the four stations, the impact on availability even at the lowest loss rates has been degraded by an order of magnitude. While the performance of the burst model message losses are significantly worse than with the independent loss assumption, the performance still meets 99.9% availability when the total message losses exceed 0.5%.

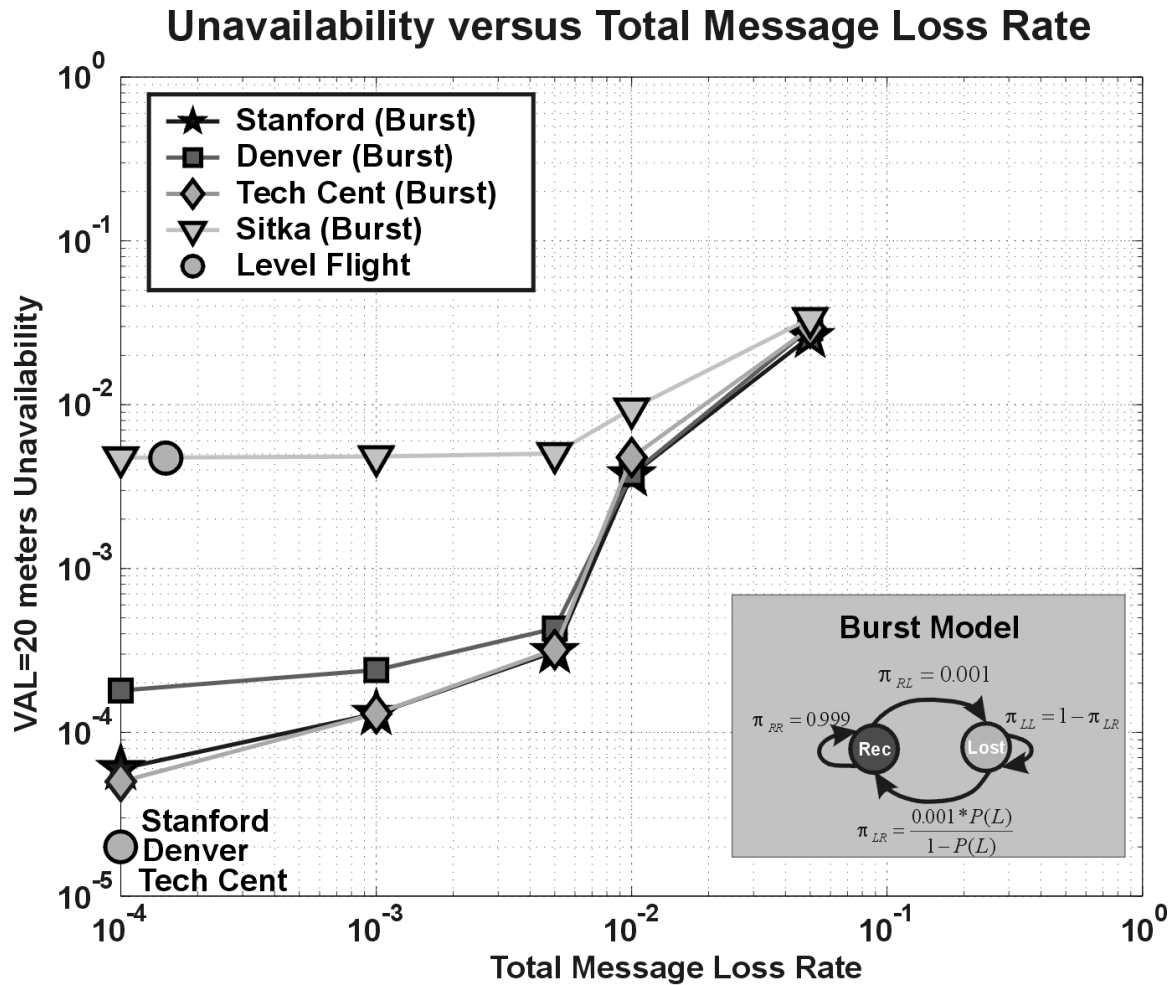


Figure 6.15: WAAS Correction Unavailability Versus Burst Model Equivalent Total Message Loss Rate at Four NSTB Locations

As in Figure 6.14, in Figure 6.15 the station at Sitka stands out. In this case, the burst model has a smaller relative influence on the performance in comparison to the other stations. This indicates that when the initial performance of a station (or an aviation user) is poor, then the influence of burst mode losses is less than when performance is initially good. When the loss rates approaches  $10^{-2}$ , the performance at all stations are nearly identical.

The large circles on the plot indicate the flight modes when the bank angles were small. This small bank-angle case corresponded to no message losses and hence the nominal performance at each of the reference stations. Three stations, Stanford, Denver and the

Technical Center are represented by the lower circle and Sitka is represented by the upper circle for no message loss.

As noted previously, these small bank angle cases model the critical approach phases of flight. Therefore, it may be deduced from this data that message loss performance for the aircraft on approach can be approximated by the stationary reference station availability profile and the burst model developed herein.

Of the total number of messages, roughly 3% represent a period when the aircraft was maneuvering in 60-degree banks back-and-forth. These maneuvers have a strong influence on the total message losses and make these results very conservative for estimating the availability of WAAS solutions during precision approaches. When preparing for final approach, bank angles are either kept small or range from 20-30 degrees for very short periods of time.

*These results show that the MOPS specification [RTCA159] for availability in a precision approach mode has been achieved even with a highly conservative model for flight message loss.*



# Chapter 7

## Conclusions and Suggestions for Future Work

The previous chapters studied the ranging and data link aspects of the geostationary satellite for application in WAAS. One of the most significant results of this work is that regardless of the maximum errors in the projection of the GPS satellite covariance matrix, the lowest satellite covariance is always in the vicinity of the reference stations. The GEO ranging contributions showed that availability improvements will only be seen when the number of GPS satellites drops below the nominal specified by [ICD200C] for users lower latitudes. Previous work [Comp98] showed that high latitude (i.e. Alaska) users could benefit from GEO ranging even with the current surplus of GPS satellites. Finally, it was demonstrated that while burst errors dominate the message loss profile in flight, the performance of the data link in flight is still meeting availability requirements.

This chapter reviews the results from this thesis and proposes future work to study satellite support for WAAS. Section 7.1 details the geostationary orbit determination conclusions and overviews the message loss conclusions. Section 7.2 looks at possible directions for future work with satellites and data links for WAAS.

While much of the WAAS infrastructure is already designed and in development, there is some room for flexibility in the future, especially when it comes to the satellite architecture. The satellites used in the WAAS architecture represent the greatest cost in

the long-term operation of the system. It is therefore important to make certain the best opportunities are utilized regarding future satellites. Over the next decade, scores of satellites will be launched; some may have direct benefit to the aviation navigation community or can be adapted to this use. Future work covers topics in Payloads, Satellite Orbits, Message Loss and SBAS Interoperability.

## **7.1 CONCLUSIONS**

The following two sections review the contributions made to the orbit determination and data link message loss for the geostationary satellite utilized by WAAS. While a great deal has been done in the past to establish the capabilities of the geostationary satellite in WAAS, this work verifies that real-time ranging to the satellite will improve the performance of the aviation user. Additionally, flight verification of the message loss rate was performed and provides the most extensive results to date validating the data link.

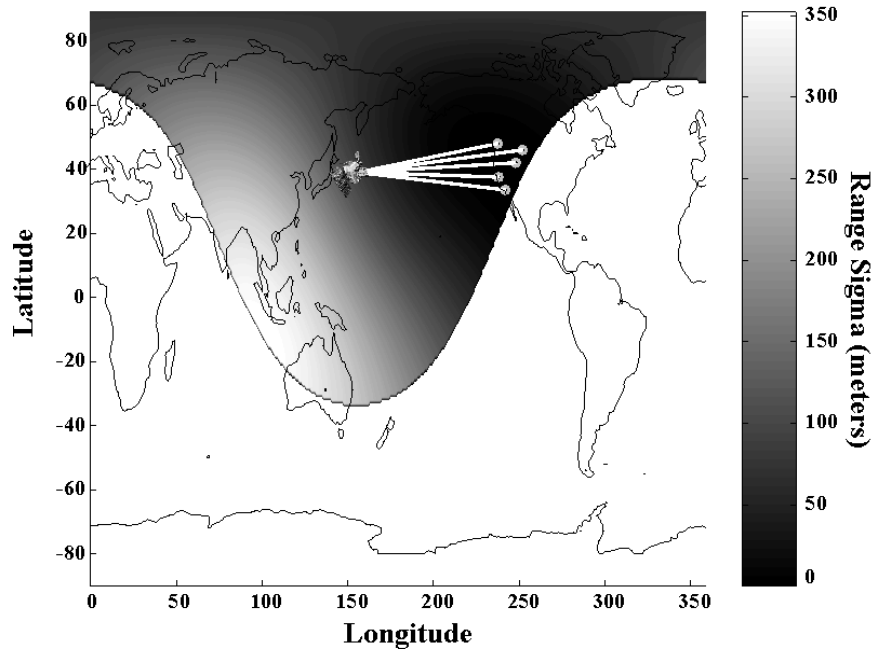
### **7.1.1 ORBIT DETERMINATION**

The first contribution of this thesis, as described in Chapter 3, showed three examples of orbit determination techniques were used to derive user position solutions from the Stanford University Testbed Master Station (TMS). The results from the three techniques were compared for their overall accuracy in the user position domain. They showed that while different techniques have widely different orbit determination accuracy the resultant user position domain solutions are very similar. This highlights the point that high accuracy and integrity for the user domain position solution is not determined by accurate satellite ephemeris estimation.

The subsequent contribution in Chapter 3 showed an analysis of the covariance distribution for a Wide-Area Reference Network. This contribution showed the relationship between a satellite location and its covariance projection upon a user. This is critical in establishing the required orbit determination accuracy necessary for a satellite to be helpful in user position computations. Figure 7.1 shows the projection of the satellite ephemeris estimate covariance from the network observations to the satellite footprint.



**User Worst-Case Sigma (m) for SV Located at Lat=39N, Lon=156E**



**User Worst-Case Sigma (m) for SV Located at Lat=39N, Lon=264E**

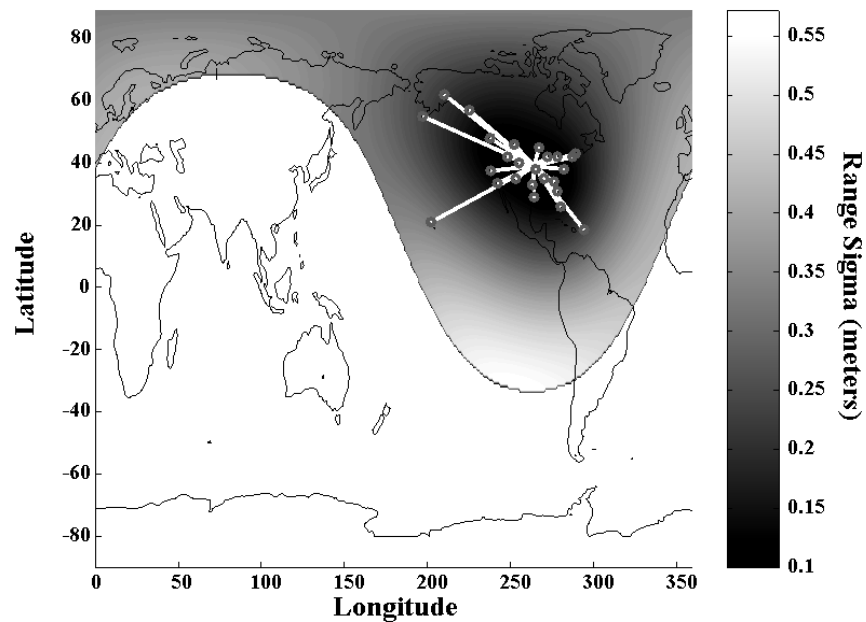


**Figure 7.1: Satellite Ephemeris Covariance Projections Upon Aircraft Users' Positions for Both Poor (Upper Plot) and Good (Lower Plot) Geometry Between the Satellite and Reference Stations**

In Chapter 4, a method was introduced to augment the approach used for GPS ephemeris estimation. [Tsai99] showed how a kinematically smoothed orbit determination technique

could be applied to GPS orbits. However, the GPS orbits nominally only vary by several meters from the projected ephemeris. This assists in defining a linear system that degrades gracefully when the ephemeris errors exceed the linear region. In fact, the errors cannot be corrected by the WAAS messages when they are larger than about 256 meters and therefore have to be removed from ranging consideration. This technique was extended to handle the geostationary satellite location variation that exceeds the linear limit assumed in Tsai's development.

This work solved the more difficult geostationary orbit determination problem. Figure 7.2 shows a typical improvement in availability and accuracy after the geostationary post orbit-fit solution was included in the user aircraft's position solution. The increase from 99.882% to 99.964% availability for a VAL of 20 meters represents an improvement from 102 seconds of unavailability per day to only 31 seconds per day. There was a corresponding accuracy increase from 4.1 meters to 2.9 meters (99.9%).

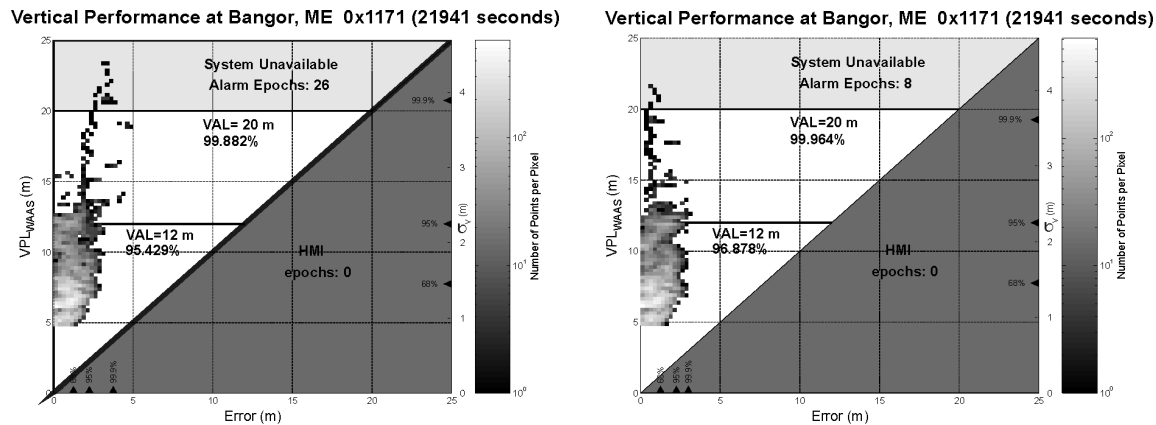


**Figure 7.2: Improvement in WAAS Availability and Accuracy With GEO Ranging. Left: Without GEO Ranging; Right: With GEO Ranging**

In addition to the orbit determination routines, an adaptive *a-priori* orbit estimator covariance propagator was developed. An overview of the orbit error covariance propagation is shown in Figure 7.3.

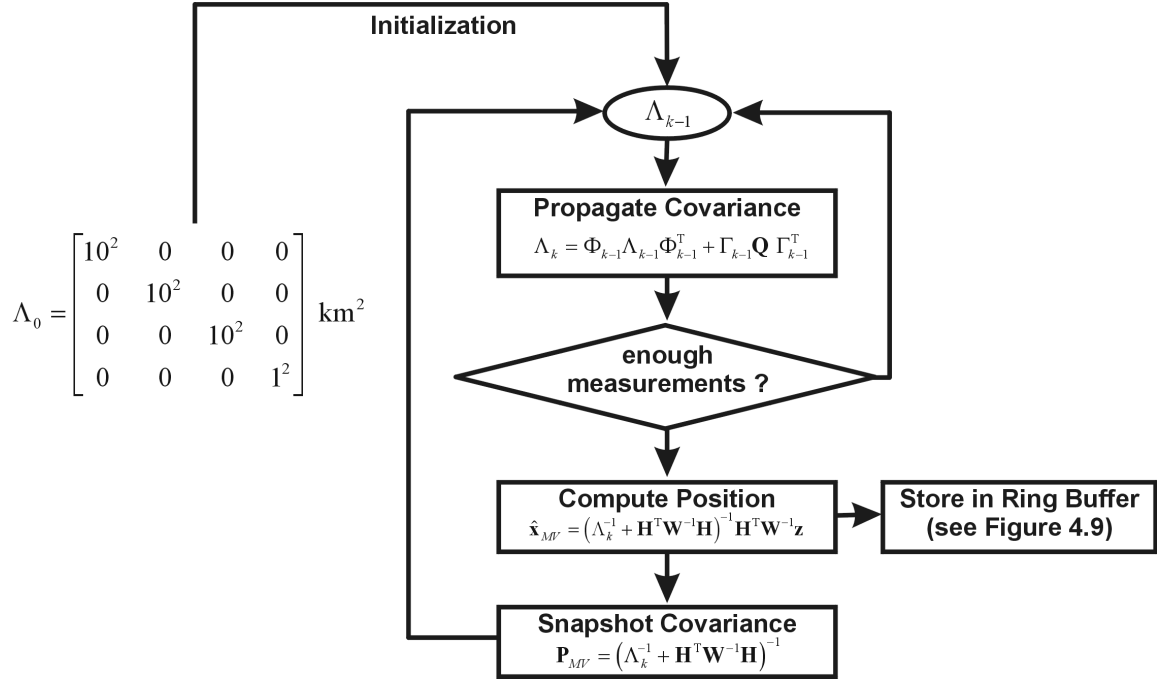


Figure 7.3: Orbit Error Covariance Propagation

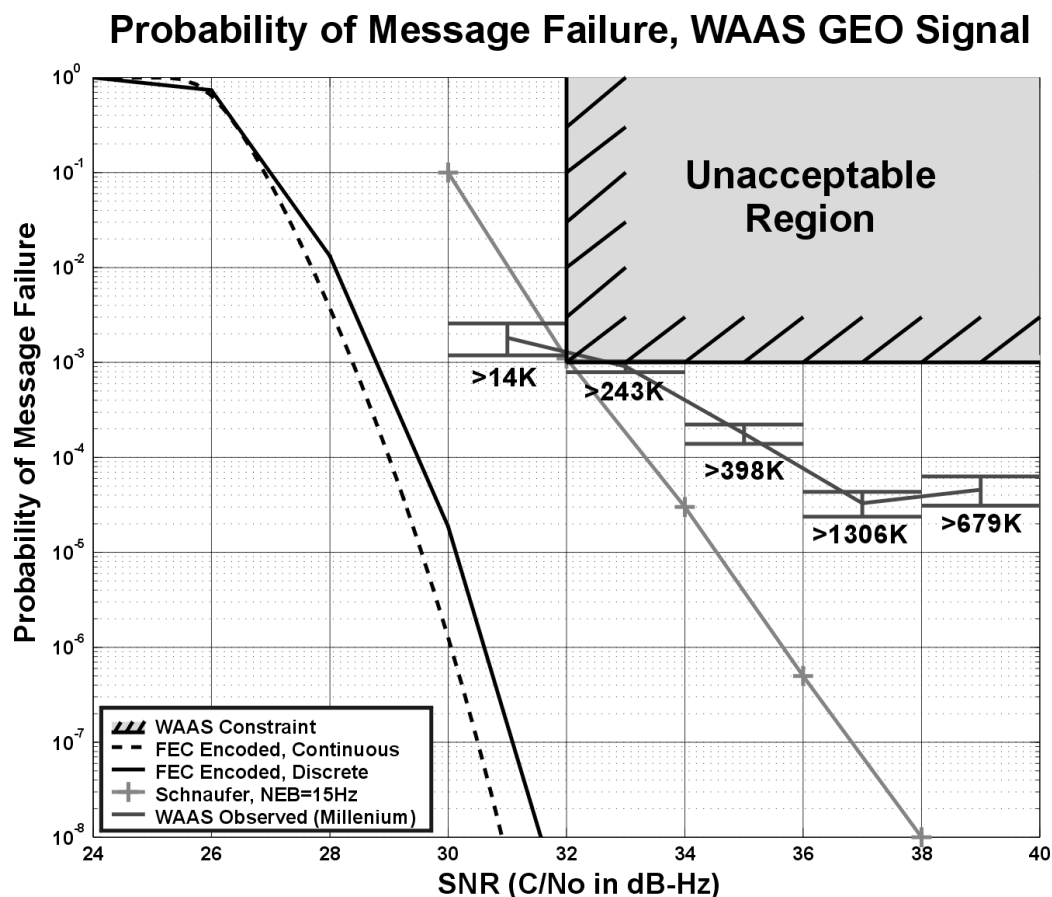
This technique is designed to provide high integrity performance in the user position domain and operates in real-time. This estimator was validated using real data from the FAA's National Satellite Test Bed (NSTB).

### 7.1.2 MESSAGE LOSS

Even more important than the geostationary satellite as an additional ranging source, the satellite data link must remain in near constant contact with the user to ensure that the GPS corrections are valid, due to time-limits for their application. This work evaluated the WAAS geostationary data link under a variety of airborne operations at different geographic locations.

Chapter 6 showed an experimental verification of the theoretical message loss rates for the geostationary satellite link for WAAS. Substantial work had been done on establishing the theoretical loss rate expected for a WAAS user [Enge97, McGraw]. This contribution verified and demonstrated the theoretical message loss rates for given signal power levels

by using a stationary reference receiver as shown in Figure 7.4. This figure also shows that the WAAS requirements are being met for a stationary receiver.



Also in Chapter 6, a new method was demonstrated for the characterization of burst-mode influence on message loss. Aircraft maneuvers, such as a bank away from a satellite, will cause message losses. These losses tend to be grouped together for multiple seconds during these maneuvers. Therefore, the loss characteristics will have a ‘burst mode’ characteristic. Flight data was collected and a method for modeling the losses was developed to predict the burst nature of the dropped messages and their impact on WAAS performance as shown in Figure 7.5. Since the bank angle of the aircraft does not change instantly, message losses tend to persist and create a message loss burst as shown in the

figure. These burst outages disprove the assumption that the message losses are independent and have a deleterious impact on the availability of WAAS. A burst message loss model was developed from a Markov process and is shown in Figure 7.5 to match the observed message losses well.

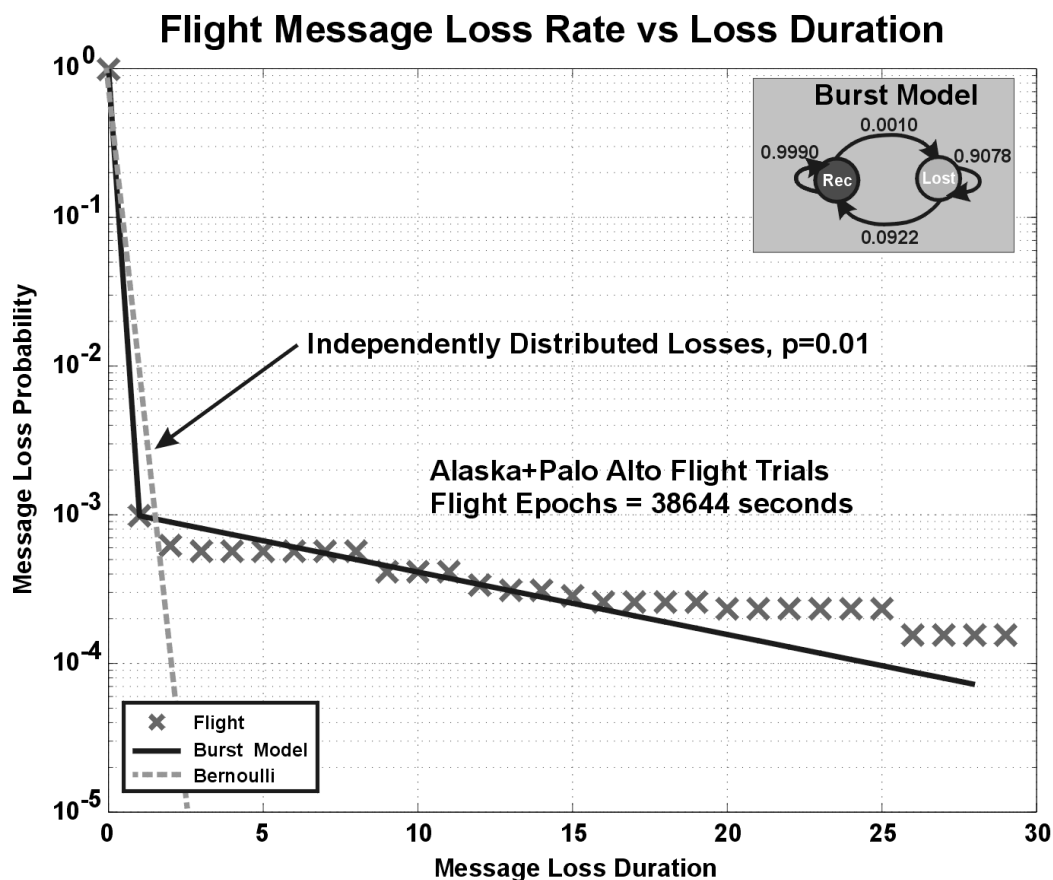


Figure 7.5: Message Loss From Flight Tests

The final result in this thesis showed the application of the burst message loss model to data collected at various NTSB reference sites. The burst model derived from flight data was applied to data from stationary reference sites around CONUS. This result is used to predict WAAS availability in flight for a wide geographic region as in Figure 7.6.

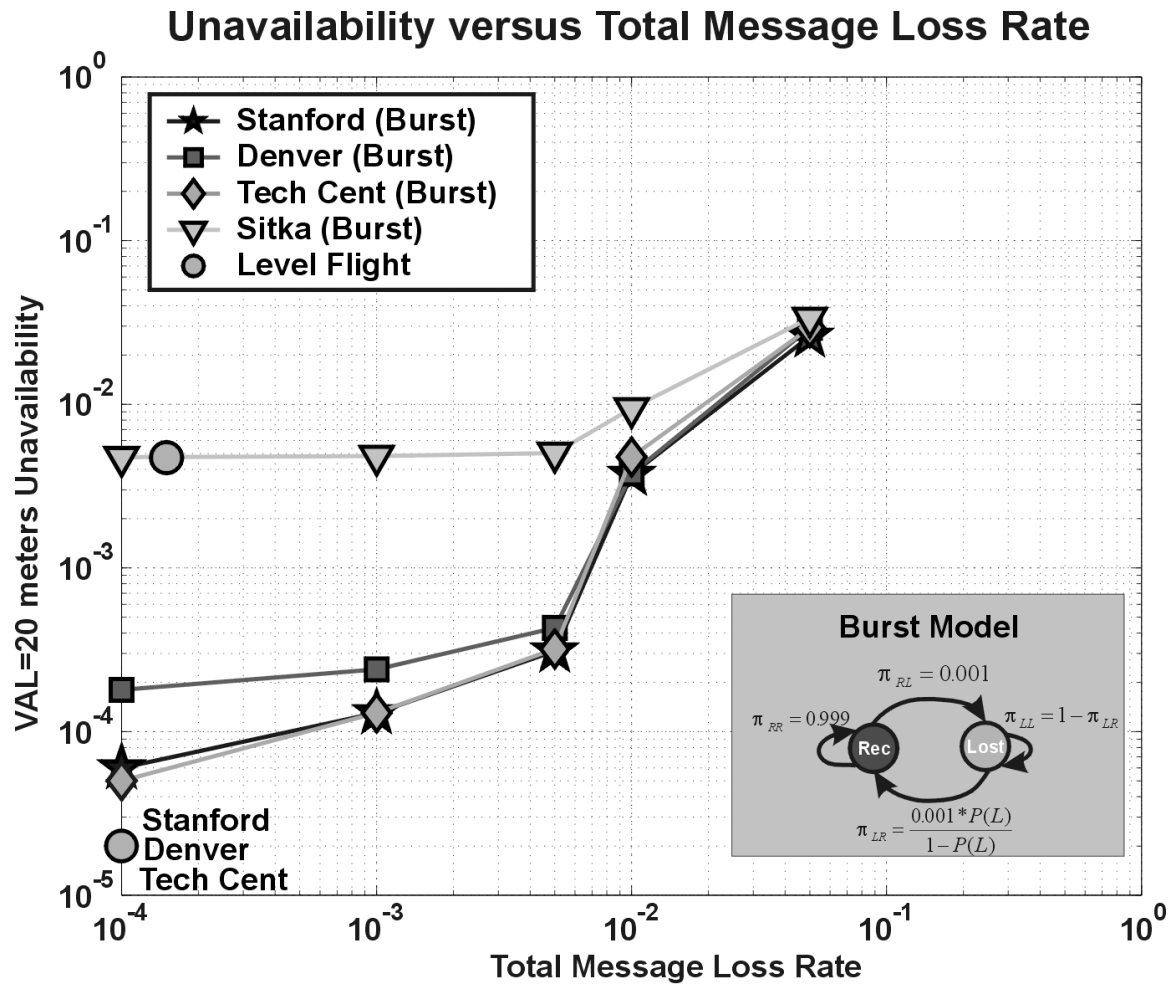


Figure 7.6: Flight Message Loss Extended to NSTB Sites

Roughly 3% of the flight data represents aircraft operations when maneuvering in 60-degree banks back-and-forth. These maneuvers have a strong influence on the total message losses and make these results very conservative for estimating the availability of WAAS solutions during precision approaches. Bank angles are either kept small or have bank angles of 20-30 degrees for very short periods of time during the landing phase of flight.

Using a highly conservative model for flight message loss, the results presented in Figure 7.6 show that the MOPS [RTCA159] availability for precision approach mode has been achieved.

## **7.2 SUGGESTIONS FOR FUTURE WORK**

The following sections detail various suggestions for future work with the geostationary satellite both for ranging and data link. These analyses are extensions of this work or previous work that will help bring the system to completion and potentially add cost benefits in future operations of WAAS.

### **7.2.1 PAYLOADS**

The payload is the device that is located on the satellite that takes the modulated signal from the ground and broadcasts it to the user. The payload is a transponder; a device that takes a given input signal and rebroadcasts or retransmits it based on the downstream requirements. The following sections explore different options with transponders. These options include adding a second transponder, coupling a stable clock to the transponder or adding frequencies to the transponder to aid in ionospheric disturbance mitigation.

### **7.2.2 SATELLITES WITH A SECOND TRANSPONDER**

The addition of a second Space-Based Augmentation System (SBAS) transponder allows for a second data signal on the same satellite. By using dual transponder satellites on the borders between two SBASs, the cost for a primary or backup satellite may be reduced. Figure 7.7 shows two SBASs sharing a satellite with two transponders. The figure indicates that SBAS A does not share satellite A, while, satellite B is shared by both SBAS A and B.

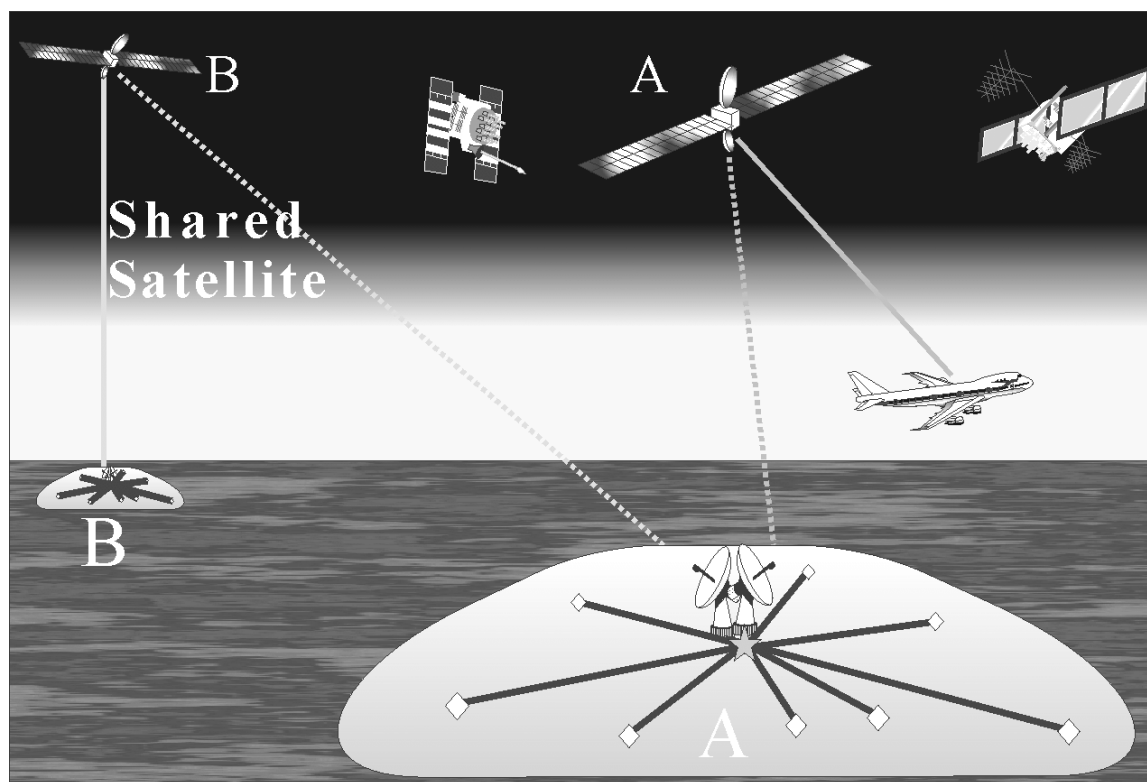


**Figure 7.7: Payload Sharing Between SBASs**

By placing an additional transponder on a satellite there could be an opportunity for an active backup in the case of transponder failure or even the ability to share the cost of satellite access with another SBAS. This could lead to substantial cost savings over the life of the program.

A geostationary satellite represents a great resource that has a correspondingly high expense. All satellites launched to geostationary orbit today perform multi-mission tasks incorporating many hundreds, if not thousands, of individual transponder channels. Each additional transponder is a small incremental cost to the overall satellite ( $< 5\%$ ) [Nagle90]. However, a single additional transponder could dramatically increase the usefulness of a satellite by: 1) allowing for a shared satellite; 2) providing a backup in case of satellite or transponder failure; or 3) adding coverage at the periphery of a region.

Future work will concentrate on evaluating various case-study scenarios that will help identify the advantages and limitations to satellites with a second transponder. A baseline



case will be created that will include complete single-string CONUS coverage with geostationary satellites having little or no overlap. Three variations will be considered:

1. The addition of satellites on either or both borders that could be co-operated with neighboring SBAS hosts as a full-time satellite;
2. The use of the additional border satellites as a backup for an individual satellite failure; and
3. The impact on the number and optimal placement of geostationary assets with shared border satellites.

### 7.2.3 USE OF A NAVIGATION PAYLOAD RATHER THAN A BENT-PIPE TRANSPONDER

The current WAAS architecture calls for the precise clock to be on the ground. This ‘bent-pipe’ architecture requires a ranging signal to be monitored on the ground in order to stabilize the ranging link. The GPS architecture, in comparison, has the precise clock on the satellite. These two architectures are shown in Figure 7.8.

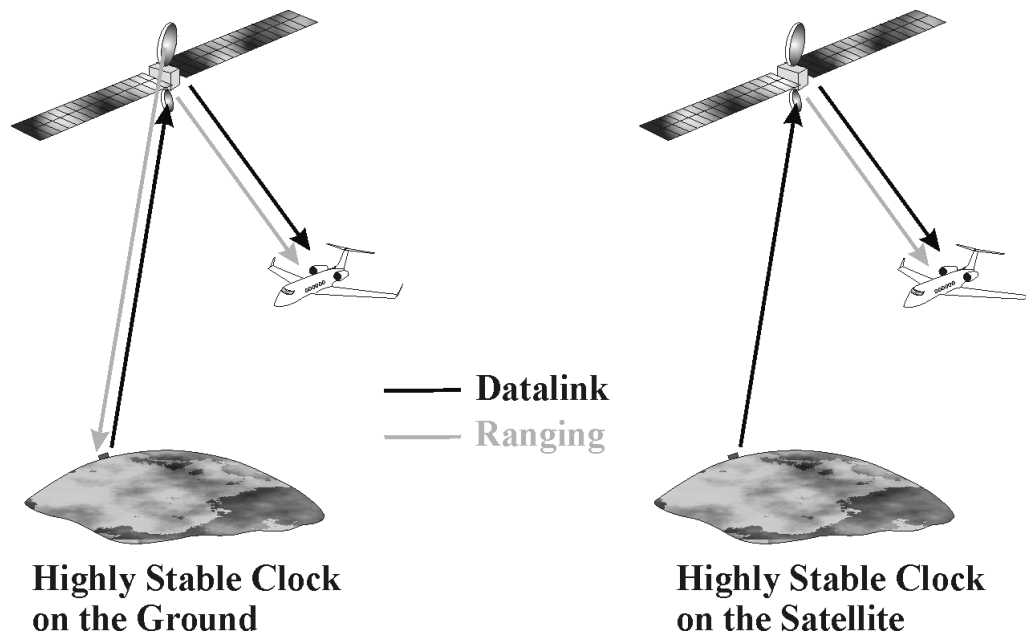


Figure 7.8: Comparison between a Clock on the Ground versus on the satellite

The difference in these two architectures is not readily apparent for the case of the geostationary satellite except for some extra requirements on the Geostationary Uplink Station (GUS) to close a fairly fast clock loop from the satellite. Since the motion of the geostationary satellite does not cause it to go out of view and the contact with the ground is necessary to send the WAAS message stream, it is not unreasonable to expect the fast clock loop to be closed in this manner. However, when the orbit is not geostationary, the satellite will not always be in view causing the fast clock loop to revert to open loop for certain periods.

Future research will analyze the requirements on satellite clocks for different types of orbits (LEO, MEO, etc.). Satellites in orbits that are not in constant view require time after acquisition by the network of ground-stations to stabilize the clock signal and then be verified before a satellite is made active for WAAS ranging. WAAS data transmission is less sensitive to clock uncertainties but large clock discrepancies could affect the signal. The nominal path would be that a satellite remains in view for a certain period of time and then goes out of view. If the signal is sufficiently stable before the satellite goes out of view, then the long-term stability of the satellite clock directly affects the potential magnitude of the clock error when the satellite is reacquired some time later. The time to stabilize the clock signal after reacquisition will be a function of the long-term stability of the satellite clock and the length of time the satellite was out-of-view.

The GPS constellation employs atomic clocks on the satellites to minimize the impact of clock drift on the user solutions under the circumstance when the satellite is not observed. This is important if the ground monitoring equipment for GPS should fail leaving the GPS satellites semi-autonomous for periods up to several weeks. As the geostationary satellites in WAAS are used as a real-time data link, it is not possible to fully automate the satellite signal content. Therefore, the geostationary satellites must remain in constant contact with the ground to continue to deliver the WAAS message content. This dramatically reduces the need for a semi-autonomous clock on the satellite.

However, other orbital satellite platforms that are not in constant contact with the control network (and thus not always seen in the service volume) will require tighter control of

their clocks than is generally afforded by standard satellite buses. By understanding the requirements on the payloads necessary for different orbit types, better decisions can be made for future satellite service acquisition.

Research should apply clock models for different clock types (rubidium, cesium, OCXO, etc.) to establish the advantages of more stable clocks for use with WAAS. These results should be combined with Section 7.2.5 below that studies various orbit types and the requirements on the clock package for each of these options. Studies should be performed for various clock qualities and different orbit types to evaluate the useful combinations for WAAS.

#### **7.2.4 MULTIPLE FREQUENCY TRANSPONDERS**

Two and three frequency transponders for WAAS have the following potential benefits: 1) higher integrity against L1 interference; 2) additional ionospheric measurements from reference stations; and, 3) compatibility with future GPS second and third frequencies for civilian use.

Recently, the JPO announced that a second civil frequency was being added as part of the first Block IIF satellites. Also plans were underway to establish a third civil frequency on the latter part of the Block IIF program. The satellite launch history and schedule is given in Table 7.1. Multiple frequencies will allow for greater tolerance to single-frequency interference, intentional or otherwise. Additionally, the coincident signals will allow for direct monitoring of the ionospheric delays on the measurements, thus increasing the accuracy and integrity of the raw GPS signal. By considering additional frequencies for the satellite signals for WAAS it prepares for future compatibility with the GPS signals. Additional frequencies also provide both the WMS and aircraft users additional measurements that could be utilized for improved integrity and availability.

<b>Block I</b>	First generation of GPS satellites. These were launched from 1978 until 1985
<b>Block II/IIA</b>	Follow-on to the first GPS satellite. These were launched from 1989 until 1996
<b>Block IIR</b>	Replenishment satellites for the Block II/IIA. These were first launched in 1996 and will continue being launch until about 2005
<b>Block IIF</b>	These are the follow-on satellites for the Block II/IIA constellation. These are due to begin launching in 2005

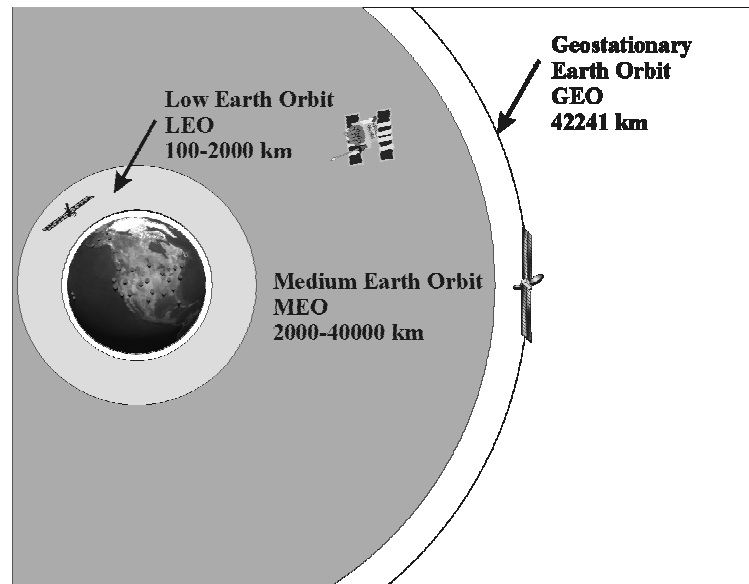
**Table 7.1: GPS Satellite Block History**

This future study should establish the advantage to both the WMS and the WAAS users when two or three frequencies are available for broadcast by the geostationary satellites only, as well as when two and three frequencies are available on both WAAS and GPS. This will be done by considering both the direct improvement in ionospheric estimation made possible by multiple frequencies (as with GPS), and the integrity improvement assuming some interference is present.

### 7.2.5 SATELLITE ORBITS

Geostationary satellites offer the highly advantageous feature of constantly being at the same location versus a fixed point on the surface of the Earth guaranteeing constant contact with the ground stations. However, their main disadvantage is their relatively high cost and limited number. Many other satellites with orbits varying from Low-Earth-Orbit (LEO) to beyond the orbit of a geostationary satellite, could be viable for signals to augment GPS.

The purpose of future work in this area would be to analyze the utilization of various types of satellites or satellite constellations. Potentially compatible satellite infrastructure, in existence or in development, will be identified with regard to their ability to carry WAAS signals.



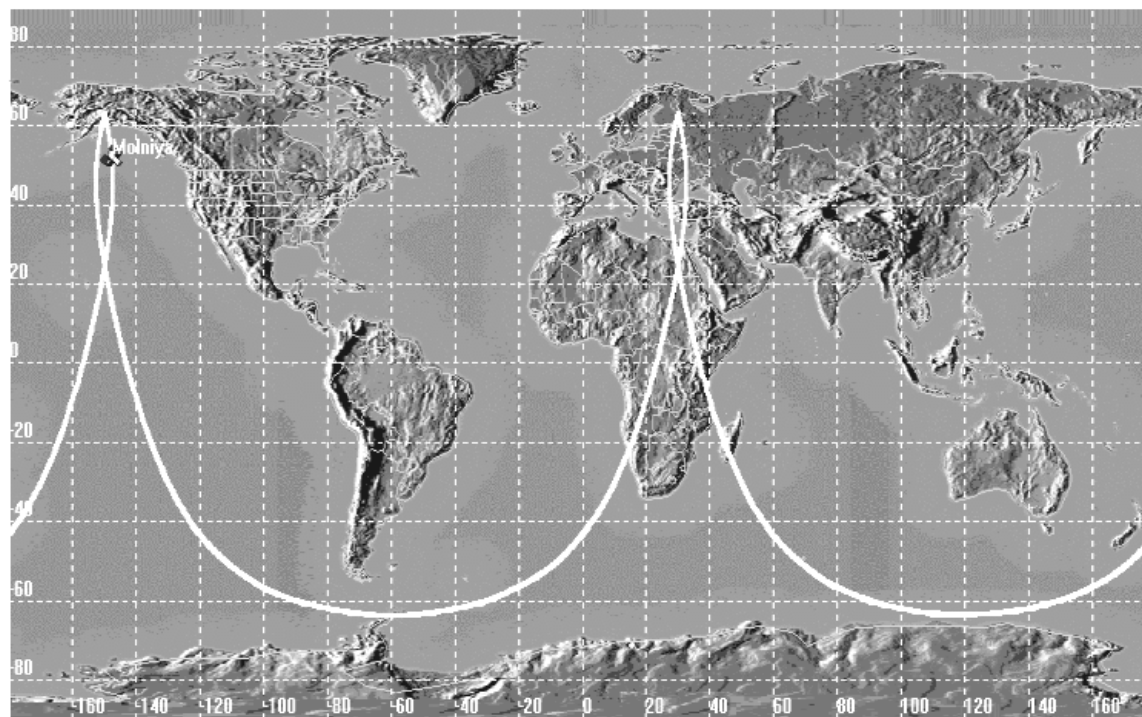
**Figure 7.9: Various Orbit Types**

Figure 7.9 shows several types of orbits that could be used for WAAS: LEO, MEO and GEO. As mentioned, the obvious choice when the ranging clock is not on the satellite is to use a GEO satellite since it is in constant view and the fast clock loop is easiest to close. However, the larger number and smaller costs of LEO satellites make them an important consideration for WAAS. Similarly, MEO orbits could offer advantages in satellite power consumption.

A number of LEO satellite constellations are being launched currently and the plans are for this trend to continue well into the future. A major advantage of a LEO satellite is its proximity to the surface of the Earth which lowers the broadcast power requirements substantially. The major disadvantages to using a LEO satellite are its relatively short time in view by surface and aviation users (on the order of single to dozens of minutes) and the large number of satellites necessary for continuous coverage over a given geographic area.

MEO satellites have longer in-view times relative to LEO satellites and have some power advantages over their GEO counterparts. Also, an interesting orbit class called Molniya, offer a long dwell times similar to a GEO satellite over either a northern or southern region. Figure 7.10 shows the ground track of a Molniya orbit that is an example of a MEO type. The orbit shown has the characteristic of being in view of Alaska and Hawaii for 10 hours per day. Additionally, 10 hours of observation in Eastern Europe and Northern Africa is

afforded each day that would be beneficial in a shared configuration (see Section 7.2.10 below).



**Figure 7.10: Ground Trace for a Molniya Orbit**

The goal of this research will be to build a satellite simulator that allows for evaluations of various combinations of satellites or satellite constellations. This simulation will enable the evaluation of these satellite options to determine relative cost, performance and complexity.

### **7.2.6 MESSAGE LOSS**

The geostationary satellite data link was investigated in Chapter 6. This research should be followed with its application to the forward prediction of WAAS availability across the intended service area. Since the performance of the data link was such a strong function of the tracking capability of the user for low elevation GEO signals, a critical concern is the design of GPS/WAAS antennas which have good low elevation tracking while maintaining excellent interference rejection characteristics. This work can be extended by showing that

with more than one WAAS satellite in view, the WAAS solution availability could be further improved.

### **7.2.7 SERVICE VOLUME MODEL**

A Service Volume Model (SVM) can have at least two functions: 1) a time-invariant version (using long-term averaging) can be used to plan assets such as reference stations and satellite links; and 2) a time-varying version can form a short-term prediction for WAAS solution availability. The message loss results presented in Chapter 6 can impact both types of the SVM by reducing the signal availability for a given elevation, and consequently, the power level.

### **7.2.8 ANTENNA DESIGN**

As the results from Chapter 6 indicated, the stations in the NSTB that had a relative elevation angle to the GEO satellite above 15 degrees each had sufficient power level to guarantee that the message losses will be below the WAAS specified level of one part in one-thousand. However, the burst losses that are prevalent in aviation operations reduced that level significantly. Burst losses, coupled with the fact that the initial WAAS operational system will use two satellites that generally have low elevations over a substantial portion of CONUS, create a situation in which careful tracking of very low elevation satellites has increased importance over standard GPS applications.

This dependence on low elevation satellites places extra pressure on the WAAS antenna design. Nominally, interference will come from terrestrial or ground-based sources. One of the most straightforward techniques for reducing the risk of interference from the ground on aircraft would be to eliminate any low elevation sensitivity to signals. That technique works in contrast to the needs of the early WAAS system. Therefore an antenna design, when integrated with an aircraft structure, must have good sensitivity down to nearly the horizon with a drastic decrease in sensitivity below the horizon. Achieving this drastic roll-off is no simple task and will require significant effort and research to accomplish. A potentially novel antenna design concept is presented in [Padros].

### 7.2.9 COPROBABILITY DISTRIBUTION

As shown in Figure 7.11, the use of a second WAAS satellite in parallel by a user would reduce the sensitivity to the loss of a single satellite due to an aircraft maneuver. Some operational benefits have been explored in [Fuller99]. However, a more complete study that extends the work presented in Chapter 6 along with specific operational situations could help clarify the true benefit of tracking more than one WAAS satellite at once.

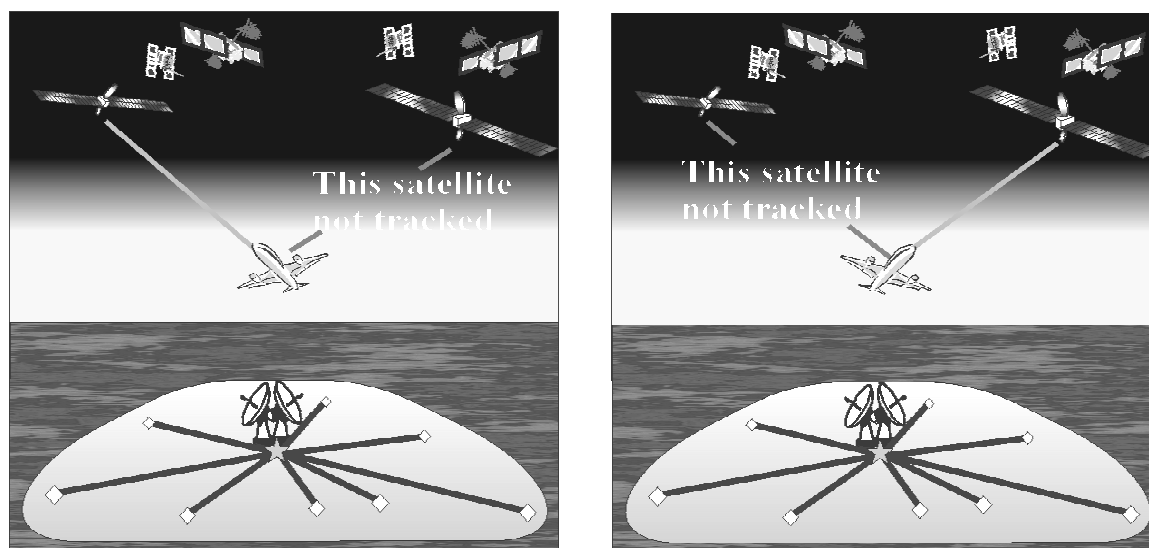


**Figure 7.11: Influence of Aircraft Maneuver (bank) on the Satellite Tracking Capability**

### 7.2.10 SBAS INTEROPERABILITY

WAAS is one of three systems currently under development around the world to augment GPS and GLONASS. Various papers including [Fernow97, Fuller98, and Fernow99] have addressed some of the issues that will present themselves when trying to implement a seamless worldwide navigation augmentation system for aviation. As indicated in Figure 7.12, there are three main areas where research in SBAS interoperability will be focused: 1) avionics (user equipment); 2) reference station data sharing; and 3) shared satellites. Active research continues in this field for the purpose of understanding the requirements in each of these options and their application in augmentation systems.



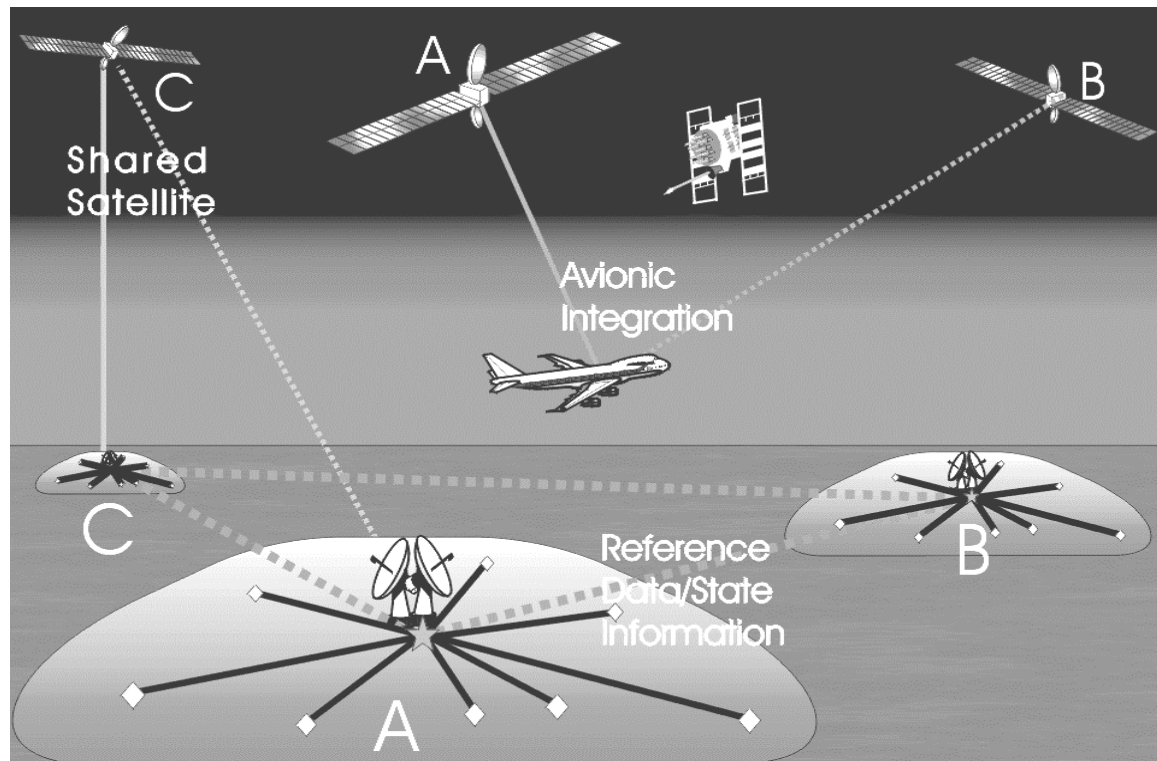


**Figure 7.12: Interoperability Options**

### 7.2.11 AVIONICS

This type of exchange assumes that the user hardware is the primary medium for SBAS data sharing. Figure 7.12 shows the user employing corrections from both SBAS A and B. Coordinating interoperation at the user level requires knowledge of the difference in the master clock terms between SBAS A and B if pseudorange correction data is to be combined and is compatible with both generated signals. Types of interoperability in this category can have the following characteristics [Fernow99]:

- The User Equipment conforms to a compatible signal specification [RTCA159, ICAO]
- The user equipment performance is the same across different SBASs
- The transition from one SBAS to another should be automatic and seamless
- The corrections and integrity information received from two different SBASs can be used simultaneously for user position solutions

The following subsets of interoperability correspond to the amount or other characteristics of information provided in the SBAS SIS and the degree of information sharing between SBASs. Some of the types of interoperability in this group require a connection between SBAS ground segments. The types of interoperability in the SIS include [Fernow97]:

- The broadcast navigation message information from one SBAS can be used safely in an airspace outside that SBAS's service volume, for en-route through non-precision approach operations. (In particular, the issue is in airspace outside of which monitoring stations exist.)
- The SBAS Network Time of one SBAS is steered within a certain threshold of the SBAS Network Time of another SBAS.
- Corrections and integrity information are provided in the broadcast message of one SBAS on the ranging signals of geostationary satellites belonging to other SBASs (for those GEOs visible from the service volume of the first SBAS).
- All GEOs from both SBASs provide corrections and integrity information on any satellite or ionospheric grid point (IGP) monitored by either SBAS. This level of interoperability requires explicit information exchange between SBAS ground segments
- Notices to Airmen (NOTAMs), or information used in generating NOTAMs, is shared and used in a common way by SBASs.

### **7.2.12 DATA SHARING**

This exchange mode suggests some connection between SBASs to allow for the information transfer. In this mode, SBASs A, B and C of Figure 7.12 are connected through some data link in which reference station measurements, status messages or the high-level state information from the master station process are transmitted. As it will be discussed below, the high-level state information (i.e. states of dynamic ephemeris estimator, grid ionospheric delay, etc.) offers the best economy of data transfer however the low level reference data represents the highest possible integrity protection.

### **7.2.13 SHARED SATELLITES**

A shared satellite may be supposed in the case where two (or more) SBASs distribute the cost of a geostationary satellite for use as a backup to a primary satellite failure. Similarly, two SBASs could share an active satellite by transmitting signals on mutually orthogonal

codes or at a frequency other than L1. The most likely method of satellite sharing would involve installing a second transponder on the satellite. As reported in [Nagle90], this would add a small cost to the production of a satellite, but add redundancy for a single SBAS using the satellite. This could also offer the ability for two SBASs to share the substantial cost of a satellite.



# Appendix A

## MESSAGE LOSS PROBABILITY

This appendix will introduce the concept of a random (or stochastic) process. The theory of random processes was first developed in connection with the study of fluctuations and noise in physical systems. A random process is the mathematical model of an empirical process whose development is governed by probability laws. Random processes provide useful models for the studies of such diverse fields as statistical physics, communication and control, time series analysis, population growth, and management sciences.

### A.1 RANDOM PROCESSES

A *random process* is a family of random variables  $\{X(t), t \in T\}$  defined on a given probability space, indexed by the parameter  $t$ , where  $t$  varies over an index set  $T$ .

A random variable is a function defined on the sample space  $S$ , where the sample space is the set of all possible outcomes of a random experiment [Hsu]. Thus, a random process  $\{X(t), t \in T\}$  is really a function of two arguments  $\{X(t, \zeta), t \in T, \zeta \in S\}$ . For a fixed  $t$  ( $t=t_k$ ),  $X(t_k, \zeta) = X_k(\zeta)$  is a random variable denoted by  $X(t_k)$  as  $\zeta$  varies over the sample space  $S$ . On the other hand, for a fixed sample point  $\zeta_i \in S$ ,  $X(t, \zeta_i) = X_i(t)$  is a single function of time  $t$ , called a *sample function* or a *realization* of the process. The totality of all sample functions is called an *ensemble*.

Of course if both  $\zeta$  and  $t$  are fixed,  $X(t_k, \zeta_l)$  is simply a real number. In the following sections, the notation  $X(t)$  will be used to represent  $X(t, \zeta)$ .

In a random process  $\{X(t), t \in T\}$ , the index set  $T$  is called the *parameter set* of the random process. The values assumed by  $X(t)$  are called *states*, and the set of all possible values forms the *state space*  $E$  of the random process. If the index set  $T$  of a random process is discrete, then the process is also called a *random sequence* and is denoted by  $\{X_n, n = 1, 2, 3, \dots\}$ . If  $T$  is continuous, then we have a *continuous-parameter* (or *continuous-time*) process. If the state space  $E$  of a random process is discrete, then the process is called a *discrete-state* process, often referred to as a *chain*. In this case, the state space  $E$  is often assumed to be  $\{0, 1, 2, 3, \dots\}$ . If the state space  $E$  is continuous, then we have a *continuous-state* process.

A complex random process  $X(t)$  is defined by:

$$X(t) = X_1(t) + jX_2(t) \quad (\text{A.1})$$

where  $X_1(t)$  and  $X_2(t)$  are (real) random processes and  $j = \sqrt{-1}$ . Throughout this book, all random processes are real random processes unless specified otherwise.

## A.2 CHARACTERIZATION OF A RANDOM PROCESS

Consider a random process  $X(t)$ . For a fixed time  $t_1$ ,  $X(t_1) = X_1$  is a random variable and its cumulative density function (CDF)  $F_x(x_1; t_1)$  is defined as:

$$F_x(x_1; t_1) = P\{X(t_1) \leq x_1\} \quad (\text{A.2})$$

$F_x(x_1; t_1)$  is known as the *first-order distribution* of  $X(t)$ . Similarly, given  $t_1$  and  $t_2$ ,  $X(t_1) = X_1$  and  $X(t_2) = X_2$  represent two random variables. Their joint distribution is known as the *second-order distribution* of  $X(t)$  and is given by:

$$F_x(x_1, x_2; t_1, t_2) = P\{X(t_1) \leq x_1, X(t_2) \leq x_2\} \quad (\text{A.3})$$

In general, the  $n$ th-order distribution of  $X(t)$  is defined by:

$$F_x(x_1, \dots, x_n; t_1, \dots, t_n) = P\{X(t_1) \leq x_1, \dots, X(t_n) \leq x_n\} \quad (\text{A.4})$$

If  $X(t)$  is a discrete-time process, then  $X(t)$  is specified by a collection of probability mass functions (PMF) [Leon-Garcia]:

$$p_x(x_1, \dots, x_n; t_1, \dots, t_n) = P\{X(t_1) = x_1, \dots, X(t_n) = x_n\} \quad (\text{A.5})$$

If  $X(t)$  is a continuous-time process, then  $X(t)$  is specified by a collection of PDFs:

$$f_x(x_1, \dots, x_n; t_1, \dots, t_n) = \frac{\partial^n F_x(x_1, \dots, x_n; t_1, \dots, t_n)}{\partial x_1 \dots \partial x_n} \quad (\text{A.6})$$

The complete characterization of  $X(t)$  requires knowledge of all the distributions as  $n \rightarrow \infty$ . Fortunately, often much less is sufficient.

As in the case of random variables, random processes are often described by using statistical averages. The mean of  $X(t)$  is defined by:

$$\mu_x(t) = E[X(t)] \quad (\text{A.7})$$

where  $X(t)$  is treated as a random variable for a fixed value of  $t$ . In general,  $\mu_x(t)$  is a function of time, and it is often called the *ensemble average* of  $X(t)$ . A measure of dependence among the random variables of  $X(t)$  is provided by its autocorrelation function, defined by:

$$R_x(t, s) = E[X(t)X(s)] \quad (\text{A.8})$$

Note that:

$$R_x(t, s) = R_x(s, t) \quad (\text{A.9})$$

and

$$R_x(t, t) = E[X^2(t)] \quad (\text{A.10})$$

The *autocovariance function* of  $X(t)$  is defined by:

$$\begin{aligned} K_x(t, s) &= \text{Cov}[X(t), X(s)] = E[(X(t) - \mu_x(t))(X(s) - \mu_x(s))] \\ &= R_x(t, s) - \mu_x(t)\mu_x(s) \end{aligned} \quad (\text{A.11})$$

It is clear that if the mean of  $X(t)$  is zero, then  $K_x(t, s) = R_x(t, s)$ . Note that the *variance* of  $X(t)$  is given by:

$$\sigma_x^2(t) = \text{Var}[X(t)] = E[(X(t) - \mu_x)^2] = K_x(t, t) \quad (\text{A.12})$$

If  $X(t)$  is a complex random process, then its autocorrelation function  $R_x(t, s)$  and autocovariance function  $K_x(t, s)$  are defined, respectively, by:

$$R_x(t, s) = E[X(t)X^*(s)] \quad (\text{A.13})$$

and

$$K_x(t, s) = E[(X(t) - \mu_x(t))(X(s) - \mu_x(s))^*] \quad (\text{A.14})$$

where  $*$  denotes the complex conjugate.

### A.3 CLASSIFICATION OF RANDOM PROCESSES

If a random process  $X(t)$  possesses some special probabilistic structure, we can specify less to characterize  $X(t)$  completely. Some simple random processes are characterized completely by only the first- and second-order distributions.

A random process  $\{X(t), t \in T\}$  is said to be *stationary* or *strict-sense stationary* if, for all  $n$  and for every set of time instances  $(t \in T, i = 1, 2, 3, \dots, n)$ :



$$F_x(x_1, \dots, x_n; t_1, \dots, t_n) = F_x(x_1, \dots, x_n; t_1 + \tau, \dots, t_n + \tau) \quad (\text{A.15})$$

for any  $\tau$ . Hence, the distribution of a stationary process will be unaffected by a shift in the time origin, and  $X(t)$  and  $X(t + \tau)$  will have the same distributions for any  $\tau$ . Thus, for the first-order distribution:

$$F_x(x; t) = F_x(x; t + \tau) = F_x(x) \quad (\text{A.16})$$

and

$$f_x(x; t) = f_x(x) \quad (\text{A.17})$$

Then the mean will be:

$$\mu_x(t) = E[X(t)] = \mu \quad (\text{A.18})$$

and the variance:

$$\text{Var}[X(t)] = \sigma^2 \quad (\text{A.19})$$

where  $\mu$  and  $\sigma^2$  are constants. Similarly, for the second-order distribution:

$$F_x(x_1, x_2; t_1, t_2) = F_x(x_1, x_2; t_2 - t_1) \quad (\text{A.20})$$

and

$$f_x(x_1, x_2; t_1, t_2) = f_x(x_1, x_2; t_2 - t_1) \quad (\text{A.21})$$

Nonstationary processes are characterized by distributions depending on the points  $t_1, t_2, \dots, t_n$ .

If stationary condition (A.15) of a random process  $X(t)$  does not hold for all  $n$  but holds for  $n \leq k$ , then we say that the process  $X(t)$  is *stationary to order k*. If  $X(t)$  is stationary to

order 2, then  $X(t)$  is said to be *wide-sense stationary* (WSS) or *weak stationary*. If  $X(t)$  is a WSS random process, then we have:

$$E[X(t)] = \mu \text{ (constant)} \quad (\text{A.22})$$

$$R_x(t, s) = E[X(t)X(s)] = R_x(|s - t|) \quad (\text{A.23})$$

Note that a strict-sense stationary process is also a WSS process, but, in general, the converse is not true.

In a random process  $X(t)$ , if  $X(t_i)$  for  $i=1, 2, \dots, n$  are independent random variables, so that for  $n = 2, 3, \dots$ ,

$$F_x(x_1, \dots, x_n; t_1, \dots, t_n) = \prod_{i=1}^n F_x(x_i; t_i) \quad (\text{A.24})$$

then we call  $X(t)$  an *independent random process*. Thus, a first-order distribution is sufficient to characterize an independent random process  $X(t)$ .

A random process  $\{X(t), t \geq 0\}$  is said to have *independent increments* if whenever  $0 < t_1 < t_2 < t_3 < \dots < t_n$ :

$$X(0), X(t_1) - X(0), X(t_2) - X(t_1), \dots, X(t_n) - X(t_{n-1}) \quad (\text{A.25})$$

are independent. If  $\{X(t), t \geq 0\}$  has independent increments and  $X(t) - X(s)$  has the same distribution as  $X(t + h) - X(s + h)$  for all  $s, t, h \geq 0, s < t$ , then the process  $X(t)$  is said to have *stationary independent increments*.

Let  $\{X(t), t \geq 0\}$  be a random process with stationary independent increments and assume that  $X(0) = 0$ . Then:

$$E[X(t)] = \mu_1 t \quad (\text{A.26})$$

where  $\mu_1 = E[X(1)]$  and:

$$\text{Var}[X(t)] = \sigma_1^2 t \quad (\text{A.27})$$

where  $\sigma_1^2 = \text{Var}[X(1)]$ .

From Equation (A.25), we see that processes with stationary independent increments are nonstationary. Examples of processes with stationary independent increments are Poisson processes and Wiener processes, which are discussed in [Hsu, Leon-Garcia, Gelb, Bryson].

A random process  $\{X(t), t \in T\}$  is said to be a *Markov process* if:

$$P\{X(t_{n+1}) \leq x_{n+1} | X(t_1) = x_1, X(t_2) \leq x_2, \dots, X(t_n) = x_n\} = P\{X(t_{n+1}) \leq x_{n+1} | X(t_n) = x_n\} \quad (\text{A.28})$$

whenever  $t_1 < t_2 < t_3 < \dots < t_n < t_{n+1}$ .

A discrete-state Markov process is called a *Markov chain*. For a discrete-parameter Markov chain  $\{X_n, n \geq 0\}$  we have for every  $n$ :

$$P\{X_{n+1} = j | X_0 = i_0, X_1 = i_1, \dots, X_n = i\} = P\{X_{n+1} = j | X_n = i\} \quad (\text{A.29})$$

Equation (A.28) or (A.29) is referred to as the *Markov property* (which is also known as the *memoryless property*). This property of a Markov process states that the future state of the process depends only on the present state and not on the past history. Clearly, any process with independent increments is a Markov process.

Using the Markov property, the  $n$ th-order distribution of a Markov process  $X(t)$  can be expressed as:

$$F_x(x_1, \dots, x_n; t_1, \dots, t_n) = F_x(x_1; t_1) \prod_{k=2}^n P\{X(t_k) < x_k | X(t_{k-1}) < x_{k-1}\} \quad (\text{A.30})$$

Thus, all finite-order distributions of a Markov process can be expressed in terms of the second-order distributions.

A random process  $\{X(t), t \in T\}$  is said to be a *normal* (or *Gaussian*) process if for any integer  $n$  and any subset  $\{t_1, t_2, \dots, t_n\}$  of  $T$ , the normal random variables  $X(t_1), X(t_2), \dots, X(t_n)$  are jointly normally distributed in the sense that their joint characteristic function is given by:

$$\begin{aligned}\Psi_{X(t_1), \dots, X(t_n)}(\omega_1, \dots, \omega_n) &= E[\exp j[\omega_1 X(t_1) + \dots + \omega_n X(t_n)]] \\ &= \exp \left[ j \sum_{i=1}^n \omega_i E[X(t_i)] - \frac{1}{2} \sum_{i=1}^n \sum_{k=1}^n \omega_i \omega_k \text{Cov}[X(t_i), X(t_k)] \right] \quad (\text{A.31})\end{aligned}$$

where  $\omega_1, \omega_2, \dots, \omega_n$  are any real numbers. Equation (A.31) shows that a normal process is completely characterized by the second-order distributions. Thus, if a normal process is wide-sense stationary, then it is also strictly stationary.

Consider a random process  $\{X(t), -\infty < t < \infty\}$  with a typical sample function  $x(t)$ . The time average of  $x(t)$  is defined as:

$$\langle x(t) \rangle = \lim_{T \rightarrow \infty} \frac{1}{T} \int_{-T/2}^{T/2} x(t) dt \quad (\text{A.32})$$

Similarly, the time autocorrelation function  $R_x(\tau)$  of  $x(t)$  is defined as:

$$R_x(\tau) = \langle x(t)x(t+\tau) \rangle = \lim_{T \rightarrow \infty} \frac{1}{T} \int_{-T/2}^{T/2} x(t)x(t+\tau) dt \quad (\text{A.33})$$

A random process is said to be *ergodic* if it has the property that the time averages of sample functions of the process are equal to the corresponding statistical or ensemble averages. The subject of *ergodicity* is extremely complicated. However, in most physical applications, it is assumed that stationary processes are ergodic.

**A.4 DISCRETE-PARAMETER MARKOV CHAINS**

If  $X_n = i$ , then the Markov chain is said to be in state  $i$  at time  $n$  (or the  $n$ th step). A discrete-parameter Markov chain  $\{X_n, n \geq 0\}$  is characterized by Equation (A.29):

$$P\{X_{n+1} = j | X_0 = i_0, X_1 = i_1, \dots, X_n = i\} = P\{X_{n+1} = j | X_n = i\} \quad (\text{A.34})$$

where  $P\{X_{n+1} = j | X_n = i\}$  are known as one-step transition probabilities. If  $P\{X_{n+1} = j | X_n = i\}$  is independent of  $n$ , then the Markov chain is said to possess *stationary transition probabilities* and the process is referred to as a *homogeneous* Markov chain. Otherwise the process is known as a *nonhomogeneous* Markov chain. Note that the concepts of a Markov chain's having stationary transition probabilities and being a stationary random process should not be confused. The Markov process, in general, is not stationary. Only homogeneous Markov chains have been used in this thesis.

Let  $\{X_n, n \geq 0\}$  be a homogeneous Markov chain with a discrete infinite state space  $E = \{0, 1, 2, \dots\}$ . Then:

$$p_{ij} = P\{X_{n+1} = j | X_n = i\} \quad i \geq 0, j \geq 0 \quad (\text{A.35})$$

regardless of the value of  $n$ . A transition probability matrix of  $\{X_n, n \geq 0\}$  is defined by

$$P = [p_{ij}] = \begin{bmatrix} p_{00} & p_{01} & p_{02} & \cdots \\ p_{10} & p_{11} & p_{12} & \cdots \\ p_{20} & p_{21} & p_{22} & \cdots \\ \vdots & \vdots & \vdots & \ddots \end{bmatrix} \quad (\text{A.36})$$

where the elements satisfy:

$$p_{ij} \geq 0 \quad \sum_{j=0}^{\infty} p_{ij} = 1 \quad i = 0, 1, 2, \dots \quad (\text{A.37})$$

In the case where the state space  $E$  is finite and equal to  $\{1, 2, \dots, m\}$ ,  $P$  is  $m \times m$  dimensional; that is:

$$P = [p_{ij}] = \begin{bmatrix} p_{11} & p_{12} & \cdots & p_{1m} \\ p_{21} & p_{22} & \cdots & p_{2m} \\ \vdots & \vdots & \ddots & \vdots \\ p_{m1} & p_{m2} & \cdots & p_{mm} \end{bmatrix} \quad (\text{A.38})$$

where:

$$p_{ij} \geq 0 \quad \sum_{j=1}^m p_{ij} = 1 \quad i = 0, 1, 2, \dots, m \quad (\text{A.39})$$

a square matrix whose elements satisfy Equation. (A.37) or (A.39) is called a *Markov* matrix or *stochastic* matrix.

# Bibliography

- [Alter] Alter, K.W., Barrows, A.K., Enge, P.K., Jennings, C.W., Parkinson, B.D., Powell, J.D., "In-flight Demonstrations of Curved Approaches and Missed Approaches in Mountainous Terrain," Proceedings of the ION GPS 98, The Institute of Navigation, September 1998
- [Andrewes] Andrewes, W.J.H. (editor), *The Quest for Longitude*, The Proceedings of the Longitude Symposium Harvard University, Cambridge, MA, November 4-6, 1993
- [Baker] R.M.L, Jr., *Astrodynamics: Applications and Advanced Topics*, New York, Academic Press, 1967
- [Bate] Bate, R.R., Mueller, D.D., White, J.E., *Fundamentals of Astrodynamics*, Dover Publications, Inc., New York, 1971
- [Battin] Battin, R., *An Introduction to the Mathematics and Methods of Astrodynamics*, AIAA Educational Series, American Institute of Aeronautics and Astronautics, 1991
- [Benedicto] Benedicto, J., Michael, P., Ventura-Traveset, J., "EGNOS, the European Regional Augmentation to GPS and GLONASS," Proceedings of the fifth ESA International Workshop on DSP Techniques Applied to Space Communications, Noorwijk, The Netherlands, 23-25 September 1998
- [Berry] Berry, A., *A Short History of Astronomy*, New York, 1962
- [Bevington] Bevington, P.R., Robinson, D.K., *Data Reduction and Error Analysis for the Physical Sciences*, Second Edition, McGraw-Hill, 1992
- [Bowditch] Bowditch, N., *American Practical Navigator*, United States Hydrographic Office, Washington, 1938

- [Brouwer] Brouwer, D., "Solution of the Problem of Artificial Satellite Theory Without Drag," *Astronautical Journal*, Vol. 64, No. 9, Nov. 1959, pp. 378-397
- [Bryson] Bryson, A.E., Ho, Y.C., *Applied Optimal Control: Optimization Estimation and Control*, Hemisphere Publishing Corporation, 1975
- [Calahan] Calahan, H.A., *The Sky and the Sailor*, Harper & Brothers, New York, 1952
- [Ceva] Ceva, J.C., *Real-Time Dynamical GPS Ephemeris Prediction for WAAS Applications*, Department of Aeronautics and Astronautics Thesis, Stanford University, 1995
- [Clark00] Clark, L., "Ancient Navigation," Nova Online, 2000
- [Clark81] Clark, G.C., Cain, J.B., *Error Correction Coding for Digital Communication*, New York, NY, Plenum, 1981
- [Chao97] Chao, Y.C., *Real Time Implementation of the Wide Area Augmentation System for the Global Positioning System with an Emphasis on Ionospheric Modeling*, Department of Aeronautics and Astronautics Thesis, Stanford University, 1997
- [Chou] Chou, H.T., *An Adaptive Correction Technique for Differential Global Positioning System*, Thesis, Stanford University, 1991
- [Christie98] Christie, J., Ko, P., Pervan, B., Enge, P., Parkinson, B., "Analytical and Experimental Observations of Ionospheric and Tropospheric Decorrelation Effects for Differential Satellite Navigation during Precision Approach," Proceedings of ION-GPS 98, The Institute of Navigation, September 1998
- [Christie99] Christie, J., Ko, P.Y., Hansen, A., Pullen, S., Pervan, B., Parkinson, B., "The Effects of Local Ionospheric Decorrelation on LAAS: Theory and Experimental Results," Proceedings of the ION National Technical Meeting 1999, The Institute of Navigation, January 1999
- [Cohen] Cohen, C.E., *Attitude Determination Using GPS*, Department of Aeronautics and Astronautics Thesis, Stanford University, 1992
- [Colombo] Colombo, O.L., "Ephemeris Errors of GPS Satellites," *Bulletin Geodetica*, Vol. 60, 1986, pp. 64-84
- [Comp97] Comp, C., Gazit, R., Walter, T., Enge, P., "Improving WAAS Integrity and Availability: UDRE and GIVE Time Updates," Proceedings of ION GPS 97, The Institute of Navigation, September 1997



- [Comp98] Comp, C., Walter, T., Fuller, R., Barrows, A., Alter, K., Gebre, D., Hayard, R., Jennings, C., Hansen, A., Phelts, R.E., Archdeacon, D., Enge, P., Powell, J.D., Parkinson, B., "Demonstration of WAAS Approach and Landing in Alaska," Proceedings of ION GPS 98, The Institute of Navigation, September 1998
- [Dai97] Dai, D., Walter, T., Comp, C.J., Tsai, Y.J., Ko, P.Y., Enge, P., Powell, J.D., "High Integrity Multipath Mitigation Techniques for Ground Reference Stations," Proceedings of ION GPS-97, The Institute of Navigation, September 1997
- [Dai99] Dai, D., Walter, T., Enge, P., Powell, J.D., "Satellite-Based Augmentation System Signal-In-Space Integrity Performance Analysis, Experience and Perspectives," Proceedings of ION GPS-99, The Institute of Navigation, September 1999
- [Davidson] Davidson, G., Unpublished notes on geostationary ranging, Stanford University, June 1996
- [Davis] Davis, G.W., *GPS-Based Precision Orbit Determination for Low Altitude Geodetic Satellites*, Thesis, The University of Texas at Austin, May 1996
- [El-Arini] El-Arini, M.B., Conker, R.S., Albertson, T.W., Reagan, J.K., Klobuchar, J.A., Doherty, P., H., "Comparison of Real-Time Ionospheric Algorithms for a GPS Wide-Area Augmentation System (WAAS)," *Selected Papers on the Wide-Area Augmentation System: Volume VI*, The Institute of Navigation, 1999
- [Enge96] Enge, P., "Wide Area Augmentation of the Global Positioning System," Proceedings of the IEEE, 84(8):1063-1088, August 1996
- [Enge97] Enge, P., "WAAS Messaging System: Data Rate, Capacity, and Forward Error Correction," *Navigation: Journal of the Institute of Navigation*, Vol. 44, No. 1, Spring 1997
- [Escobal] Escobal, P.R. *Methods of Orbit Determination*, Krieger, Malabar, FL, 1965
- [FAA97] FAA Specification WAAS FAA-E-2892 B, October 1997
- [FarAim] "Far Aim 99: Federal Aviation Regulations Aeronautical Information Manual", Air USA, 1999
- [Fernow97] Fernow, J.P., O'Laughlin, D., Hsiao, T.T., Reagan, J., "Interoperability Between SBASs," Proceedings of the ION Annual Meeting, The Institute of Navigation, June 1997

- [Fernow99] Fernow, J.P., O’Laughlin, D., Hsiao, T.T., Reagan, J., Fuller, R., Walter, T., Dai, D., Enge, P., and Powell, J.D., “Interoperability of Satellite-Based Augmentation Systems,” *Selected Papers on the Wide-Area Augmentation System: Volume VI*, Institute of Navigation, 1999
- [Fritchman] Fritchman, B.D., “A Binary Channel Characterization Using Partitioned Markov Chains,” *IEEE Transactions on Information Theory*, Vol. IT-13, No. 2, April 1967
- [Fuller98] Fuller, R., Dai, D., Walter, T., Comp, C., Enge, P., Powell, J.D., “Interoperation and Integration of Satellite Based Augmentation Systems,” *Proceedings of ION GPS 98*, The Institute of Navigation, September 1998
- [Fuller99] Fuller, R.A., Walter, T., Houck, S., and Enge, P., “Flight Trials of a Geostationary Satellite Based Augmentation System at High Latitudes and for Dual Satellite Coverage,” *Proceedings of the Institute of Navigation 1999 National Technical Meeting*, January, 1999
- [Gelb] Gelb, A. ed., *Applied Optimal Estimation*, The MIT Press, 1974
- [Goad] Goad, C., “Optimal filtering of pseudoranges and phases from single-frequency GPS receivers,” *The Journal of Navigation*, Vol. 37, No. 3, The Institute of Navigation, Fall 1990
- [Goldstein] Goldstein, H., *Classical Mechanics*, 2<sup>nd</sup> ed., Addison-Wesley, Reading, MA, 1980
- [Golub] Golub, G.H., Van Loan, C.F., *Matrix Computations, Third Edition*, Johns Hopkins University Press, 1996
- [GPSWorld99] *GPS World Showcase: Technology and Product Innovation for the Global Positioning System*, Advanstar Communications, December 1999
- [Grewal97] Grewal, M.S., *Kalman Filtering Theory and Practice*, Prentice Hall 5<sup>th</sup> Printing, June 1997
- [Grewal99] Grewal, M.S., Brown, W., Lucy, R., Hsu, P., “Test Results of Geostationary Satellite (GEO) Uplink Sub-Station (GUS) Using GEO Navigation Payloads,” *Selected Papers on Satellite Based Augmentation Systems (SBASs): Volume VI*, The Institute of Navigation, 1999

- [Haas94] Haas, F., Lage, M., Kalinowski, S. "GPS Wide Area Augmentation System (WAAS) – Phase 1D Testbed Results", Proceedings of the ION National Meeting, The Institute of Navigation, June 1994
- [Haas95] Haas, F., Lage, M., "Analysis of Recent Wide Area Augmentation System (WAAS) Flight Tests," Proceedings of the ION National Technical Meeting, The Institute of Navigation, January 1995
- [Hansen99] Hansen, A.J., Walter, T.F., Enge, P.K., "Real-Time Ionospheric Tomography Using Terrestrial GPS Sensors," *Selected Papers on Satellite Based Augmentation Systems (SBASs): Volume VI*, The Institute of Navigation, 1999
- [Hansen00] Hansen, A.J., Real Time Ionospheric Tomography Using Terrestrial GPS Sensors, Department of Electrical Engineering Thesis, Stanford University, 2000
- [Hayward] Hayward, R.C., Powell, J.D., "Real Time Calibration of Antenna Phase Errors for Ultra Short Baseline Attitude Systems," Proceedings of the ION GPS 98, The Institute of Navigation, September 1998
- [Hegarty] Hegarty, C.J., "Analytical Derivation of Maximum Tolerable In-Band Interference Levels for Aviation Applications of GNSS," *Selected Papers on the Wide-Area Augmentation System: Volume VI*, The Institute of Navigation, 1999
- [Heller] Heller, J.A., Jacobs, I.M., "Viterbi Decoding for Satellite and Space Communication," IEEE Transactions on Communication Technology, Vol. COM-19, No. 5, October 1971
- [Hernandez] Hernandez, J., Nieto, C., "Technical Note on Out-of-Zone UDRE Degradation," GMV Technical Memo, Oct. 15, 1998
- [Hofmann-Wellenhof] Hofmann-Wellenhof, B., Lichtenegger, H., and Collins, J., *GPS Theory and Practice*, Third Edition, Springer Verlag, 1994
- [Hsu] Hsu, H.P., *Probability, Random Variables, & Random Processes*, McGraw-Hill, New York, 1997
- [ICAO] Satellite-Based Augmentation System (SBAS) Standards and Recommended Practices (SARPS), Draft 7, August 1998, International Civil Aviation Organization (ICAO)
- [ICD200C] *Navstar GPS Space Segment/User Interfaces*, IRN-200C-002, Navstar GPS JPO, 25 September 1997

- [Izsak] Izsak, I., "A Theory of Satellite Motion About an Oblate Planet—I. A Second Order Solution of Vinti's Dynamical Problem," Smithsonian Institution Astrophysical Observatory, Special Report No. 52, November 1960
- [Kaplan] Kaplan, M.H., *Modern Spacecraft Dynamics & Control*, Wiley, New York, 1976
- [Kaula] Kaula, W.M., *Theory of Satellite Geodesy*, Blaisdell Publishing Company, Waltham, Massachusetts, 1966
- [Kee90] Kee, C., and Parkinson, B.W., "Wide Area Differential GPS," National Technical Meeting of the Institute of Navigation, San Mateo, California, January 1990
- [Kee91] Kee, C., Parkinson, B.W., and Axelrad, P., "Wide Area Differential GPS," *Navigation*, Journal of the Institute of Navigation, Vol. 38, No. 2, Summer 1991
- [Kee92] Kee, C., and Parkinson, B.W., "Algorithms and Implementations of Wide Area Differential GPS," Proceedings of ION GPS-92, Albuquerque, September, 1992
- [Kee93a] Kee, C., and Parkinson, B.W., "High Accuracy GPS Positioning in the Continent: Wide Area Differential GPS," Differential Satellite Navigation Systems 93 (DSNS-93) Conference, Amsterdam, The Netherlands, April 1993
- [Kee93b] Kee, C., *Wide Area Differential GPS (WADGPS)*, Department of Aeronautics and Astronautics Thesis, Stanford University, 1993
- [Kayton] Kayton, M., Fried, W.R., *Avionics Navigation Systems*, John Wiley & Sons, Inc., 1997
- [Klobuchar86] Klobuchar, J., "Design and Characteristics of the GPS Ionospheric Time Delay Algorithm for Single Frequency Users," IEEE PLANS 1986, Position Location and Navigation Symposium, Las Vegas, November 4, 1986
- [Lage] Lage, M., Elrod, B., "Flight Testing and Evaluation of Wide Area Differential GPS," Proceedings of the ION National Technical Meeting, January 1993
- [Leon-Garcia] Leon-Garcia, A., *Probability and Random Processes for Electrical Engineers*, 2nd Edition, Addison Wesley, 1997
- [Loh] Loh, R., Wulschleger, V., Elrod, B., Lage, M., Haas, F., "The U.S. Wide-Area Augmentation System (WAAS)", *Selected Papers on the Wide-Area Augmentation System: Volume VI*, Institute of Navigation, 1999
- [Matchett] Matchett, G., "Stochastic Simulation of GPS Selective Availability Errors," Technical Memorandum, TASC, June 1985

- [McHugh] McHugh, T., Private communication, March 2000
- [Nagle90] Nagle, J.R. and Kinal, G.V., "Geostationary Repeaters: A Low Cost Way to Enhance Civil User Performance of GPS and GLONASS," Proceedings of the IEEE Position, Location and Navigation Symposium, Las Vegas, NV, March 1990
- [Nagle93] Nagle, J.R., Van Dierendonck, A.J., and Hua, Q.D., "Inmarsat-3 Navigation Signal C/A Code Selection and Interference Analysis," *Navigation: Journal of the Institute of Navigation*, Vol. 39, No. 4, Winter 1992-93
- [Nichols99] Nichols, J., Hansen, A., Walter, T., Enge, P., "High Latitude Measurements of Ionospheric Scintillation Using the NSTB", Proceedings of the ION National Technical Meeting, The Institute of Navigation, January 1999
- [NAVSYS] "WAAS Dual Frequency Ranging and Timing Analysis Design Report, NAVSYS Corporation Report, November 11, 1996
- [Olsen] Olson, K.E., Enge, P.K., "Forward Error Correction for an Atmospheric Noise Channel," *IEEE Transactions on Communications*, Vol. 40, No. 5, May 1992
- [Padros] Padros, N., Ortigosa, J.I., Baker, J., Iskander, M.F., Thornberg, B., "Comparative Study of High-Performance GPS Receiving Antenna Designs", *IEEE Transactions on Antennas and Propagation*, Vol. 45, No. 4, April 1997
- [Parkinson95] Parkinson, B.W., Stansell, T., Beard, R., Gromov, K., "A History of Satellite Navigation," *Navigation: Journal of The Institute of Navigation*, Vol. 42, No. 1, Special Issue, The Institute of Navigation, 1995
- [Parkinson96] Parkinson, B.W., Spilker, J.J., Axelrad, P., Enge, P., *Global Positioning System: Theory and Applications, Volumes I and II*, Progress in Astronautics and Aeronautics, American Institute of Aeronautics and Astronautics, 1996
- [Parkinson97] Parkinson, B.W., "Origins, Evolution, and Future Satellite Navigation," *Journal of Guidance, Control and Dynamics*, American Institute of Aeronautics and Astronautics, Vol. 20, No. 1, January-February 1997
- [Pogorelc97a] Pogorelc, S., Cashin, T., Lage, M., "Test Results of GPS and Geostationary Satellite Orbit Determination", Proceedings of the ION National Technical Meeting, The Institute of Navigation, January 1997
- [Pogorelc97b] Pogorelc, S., Enge, P., DiMeo, M., Kalinowski, S., Dehel, T., "Flight and Static Test Results for the NSTB", Proceedings of ION GPS 97, September 1997.

- [Pullen] Pullen, S., Parkinson, B., "Optimal Augmentation of GPS Using Inexpensive Geosynchronous Navigation Satellites", Proceedings of the ION GPS 97, September 1997
- [Rosborough] Rosborough, G.W., "Gravitational Effects on Low-Earth Orbiters," 14<sup>th</sup> Annual American Astronautical Society Guidance and Control Conference, Conference Proceedings, Keystone Colorado, 1991
- [RTCA159] "Minimum Operational Performance Standards for Global Positioning System/Wide Area Augmentation System Airborne Equipment," RTCA Document No. RTCA/DO-229A, June 1998, prepared by RTCA SC-159
- [RTCM104] "RTCM Recommended Standards for Differential NAVSTAR GPS Service," Version 2.1, Radio Technical Commission for Maritime Services, 1994
- [SARPS] Satellite-Based Augmentation System (SBAS) Standards and Recommended Practices (SARPS), Draft 7, Aug. 1998, International Civil Aviation Organization (ICAO)
- [Schnauffer] Schnauffer, B.A., McGraw, G.A., "WAAS Receiver Carrier Tracking Loop and Data Demodulation Performance in the Presence of Wideband Interference," *Navigation: Journal of the Institute of Navigation*, Vol. 44, No. 1, Spring 1997
- [Seidelmann] Seidelmann, P.K., *Explanatory Supplement to the Astronomical Almanac*, University Science Books, Mill Valley, California, 1992
- [Sobel] Sobel, D., *Longitude: The True Story of a Lone Genius Who Solved the Greatest Scientific Problem of His Time*, Walker and Company, New York, 1995
- [Spilker] Spilker, J.J., "GPS Signal Structure and Performance Characteristics," Global Positioning System papers published in *Navigation*, Vol. I, 1980
- [Stengel] Stengel, R.F., *Optimal Control and Estimation*, Dover Publications Incorporated, New York, 1994
- [Strang] Strang, G., *Linear Algebra and Its Applications, Third Edition*, Harcourt Brace Jovanovich, 1988
- [TMSLIVE] TMSLIVE Website. <http://waas.stanford.edu/tmslive>
- [TRSICD] "Testbed Reference Station to Testbed Master Station Interface Control Document", Version 3.2, Federal Aviation Administration William J. Hughes Technical Center, 31 August 1998

- [Tsai95a] Tsai, Y., Chao, Y.C., Walter, T., Kee, C., Powell, D., Enge, P., Parkinson, B., "Evaluation of Orbit and Clock Models for Real-Time WAAS," Proceedings of the National Technical Meeting, The Institute of Navigation, Anaheim, California, 1995
- [Tsai95b] Tsai, Y., Enge, P., Chao, Y.C., Walter, T., Kee, C., Evans, J., Barrows, A., Powell, D., Parkinson, B., "Validation of the RTCA Message Format for WAAS," Proceedings of ION GPS 95, The Institute of Navigation, September 1995
- [Tsai99] Tsai, Y., *Wide Area Differential Operation of the Global Positioning System: Ephemeris and Clock Algorithms*, Department of Aeronautics and Astronautics Thesis, Stanford University, 1999
- [USDOD&T] U.S. Departments of Defense and Transportation, *1994 Federal Radionavigation Plan*, DOT-VNTSC-RSPA-95-1/DOD-4650.5, Washington DC, 1994
- [USDOT] U.S. Department of Transportation, U.S. Coast Guard, *Omega Navigation System User's Guide*, COMDTPUB P1656.3 Washington DC, 29 May 1990
- [Van Dierendonck94] Van Dierendonck, A.J., and Elrod, B., "Ranging Signal Control and Ephemeris/Time Determination for Geostationary Satellite Navigation Payloads," Proceedings of the 1994 National Technical Meeting of the ION, San Diego, CA, January 1994
- [Ventura-Traveset] Ventura-Traveset, J., *et al.*, "A technical review of SBAS interoperability issues from the EGNOS perspective," Proceedings of 2nd European Symposium of Global Navigation Satellite Systems (GNSS98), Toulouse, France, 20-23 October 1998
- [Vinti61] Vinti, J.P., "Theory of an Accurate Intermediary Orbit for Satellite Astronomy," Journal of Research of the National Bureau of Standards, Vol. 65B, July-Sept. 1961, pp. 169-201
- [Vinti98] Vinti, J.P., Der, G.J.(ed.), Bonavito, N.L.(ed.), *Orbital and Celestial Mechanics*, American Institute of Aeronautics and Astronautics, Reston, VA, 1998
- [Walter94] Walter, T., Kee, C., *et. al.*, "Flight Trials of the Wide Area Augmentation System (WAAS)," Proceedings of the ION GPS 94, The Institute of Navigation, September 1994

- [Walter99] Walter, T., Enge, P., Hansen, A., "Integrity Equations for WAAS MOPS", *Selected Papers on Satellite Based Augmentation Systems (SBASs): Volume VI*, The Institute of Navigation, 1999
- [Walter00] Walter, T., WAAS Ionosphere Grid Graphic, 2000
- [Wertz] Wertz, J.R., Larson, W.J., ed., *Space Mission Analysis and Design*, Kluwar Academic Publishers, 1991
- [Wessel] Wessel, P., and Smith, W.H.F., "New Version of the Generic Mapping Tools Released," EOS Transactions American Geophysical. Union, Vol. 76, pp. 329, 1995
- [Wulschleger] Wulschleger, V., O'Laughlin, D., Haas, F., "FAA Flight Test Results for GPS Wide Area Augmentation System (WAAS) Cross-Country Demonstration," Proceedings of the ION Annual Meeting, June 1994
- [Yunck] Yunck, T., et. al., "A Prototype WADGPS System for Real Time Sub-Meter Positioning Worldwide," Proceedings of ION GPS 96, The Institute of Navigation, September 1996
- [Zumberge] Zumberge, J.F., Neilan, R.E., Beutler, G., "The International Service for Geodynamics – Benefits to Users," Proceedings of the ION GPS 94, Salt Lake City, UT, 1994